School of Natural Sciences

Doctoral Thesis in Physics

Naturalness at the LHC

Raffaele Tito D'Agnolo

SCUOLA
NORMALE
SUPERIORE
PISA

Advisors
Prof. Gigi Rolandi
Prof. Riccardo Barbieri

Abstract

Particle physics is confronted by deep questions at the weak scale and the LHC can shed light on them. In this work we propose strategies to understand from its data if electroweak symmetry breaking is natural. We describe a search performed with the CMS detector in a yet unexplored area of natural LHC parameter space and we propose measurements in the Higgs boson sector that can discriminate between natural and unnatural theories.

Contents

Notation and acronyms

This section contains the conventions, notational choices and acronyms used in this work. Letters from the middle of the greek alphabet ($\mu, \nu, \rho, \sigma, ...$) represent four-vector indexes. We define the covariant position and momentum of a particle as

$$x^{\mu} = (t, \vec{x}) \ , \quad p^{\mu} = (E, \vec{p})$$

and we take for the Minkowski metric the convention

$$\eta_{\mu\nu} = \mathrm{diag} \left(1, -1, -1, -1\right)$$

that implies $p^2 \equiv p^{\mu} p_{\mu} = m^2$ for an on-shell particle of mass m.

Spinor indexes are labelled by greek letters from the beginning of the alphabet ($\alpha, \beta, ...$) and we distinguish between the two types of indexes with a dot ($\alpha = 1, 2$ and $\dot{\alpha} = 1, 2$). In our convention a generic Dirac spinor reads

$$\Psi = \left(\begin{array}{c} \xi_{\alpha} \\ \chi^{\dagger \dot{\alpha}} \end{array} \right) .$$

We conclude this short summary of conventions by reminding the reader that we always use natural units ($c = \hbar = 1$). We do so also in the chapters containing the experimental part of this work.

In this section we also collect acronyms used throughout the text. A more detailed definition of each of them can be found the first time that they are used in the main body of the thesis. The list is purposefully incomplete. Here we have included only those acronyms that appear multiple times across different chapters, often far removed from their original definition. We have omitted those that are used only in a few contiguous sections that would have made the list too long to be helpful for the reader.

ATLAS. A Toroidal LHC apparatus. One of the four major experiments at the LHC (see below for the definition of LHC).

BSM. Beyond the Standard Model. It refers to particle physics models extending the current reference theory for particle interactions.

CMS. Compact Muon Solenoid. One of the four major experiments at the LHC (see below for the definition of LHC). The CMS detector was used to collect the data needed for the original experimental part of this work.

CSV. Combined Secondary Vertex. A CMS algorithm used to identify jets originating from the fragmentation of b-quarks.

EW. ElectroWeak. It refers to two of the fundamental forces of nature (electromagnetic and weak) that in the SM (see below) have a unified description.

HLT. High Level Trigger. The last step of the CMS trigger. It is software based and capable of reconstructing physics objects extremely close to their offline counterparts (including quantities requiring tracking).

JES. Jet Energy Scale. It is used in the text referring to the uncertainties associated to its determination with the CMS detector.

LEP. Large Electron Positron Collider. Built at CERN in the 27 km circular tunnel now occupied by the LHC (see below) is the highest energy lepton collider ever constructed. It allowed to realize precision measurements at the Z resonance that are still of great importance for BSM physics.

LHC. Large Hadron Collider. Proton-proton (pp), proton-ion and ion-ion collider built at CERN with a design center of mass energy of $\sqrt{s} = 14$ TeV for pp collisions. It was operated from 2010 to 2012 at energies $\sqrt{s} = 7, 8$ TeV. A more complete description can be found in chapter 4.

LSP. Lightest SuperPartner. The lightest supersymmetric particle in a given spectrum, excluding SM (see below) particles.

MC. Monte Carlo. It refers to a class of computational algorithms that rely on repeated random sampling to obtain numerical results. This technique is used at the LHC to generate simulated event samples.

MVA. MultiVariate Analysis. Based on the principle of multivariate statistics [1], in LHC experiments it is used to optimize searches across multiple dimensions while taking into account the effects of all variables on the response to a certain signal.

PF. Particle Flow. Reconstruction algorithm used by CMS for almost all physics objects, described at the end of chapter 4.

PU. Pile-Up. In a pp collision selected by the experiments at the LHC, other than the vertex where the hard scattering took place several softer interactions occur (an average of 20 in 2012 running conditions). The contributions to the event from this additional interactions are generically denoted as pile-up.

PV. Primary Vertex.The reconstructed vertex in a pp collision where the hard scattering process took place. The identification techniques used by CMS are described in chapter 5.

QCD. Quantum CromoDynamics. The theory of strong interactions, describing one of the fundamental forces of the SM (see below).

QED. Quantum ElectroDynamics. The theory of electromagnetic interactions.

RPV. R-Parity Violation (Violating). It refers to supersymmetric theories in which a discrete symmetry know as R-parity is broken. More details can be found in chapter 3.

SM. Standard Model. The reference theory of particle physics, now established up to energies of a few hundred GeVs. It is described in chapter 1.

SUSY. Supersymmetry (but also supersymmetric). The most generic space-time symmetry of the S matrix consistent with local quantum field theory (see chapter 3).

UV. UltraViolet. It refers to high energy completions of effective low energy theories or more in

general to high energy regimes.

Introduction

Since the Large Hadron Collider (LHC) [2] started its operations, particle physics has entered a new data-driven era. Today we are offered the unique opportunity to answer questions that have been the object of speculation for decades. In this work we address the one that we consider the deepest confronting us at the new energy frontier: Is electroweak symmetry breaking natural?

The gauge symmetry describing electromagnetic and weak interactions must be spontaneously broken to be consistent with experimental observations. The most widely adopted mechanism realizing the breaking (strongly favored by recent LHC findings [3, 4] and indirectly also by LEP precision measurements [5]) introduces in the theory a mass parameter quadratically sensitive to quantum corrections. Current data point to a value for this parameter close to the Fermi scale. Therefore if new physics is present only at much higher energies we have to rely on an accidental cancellation to explain its smallness.

Particle physics is at a fork in the road, confronted by the choice between two paradigms. We could take the side of naturalness and imagine that new particles and possibly a new dynamics are lurking just around the corner, ready to make electroweak symmetry breaking natural. However it is equally legitimate to adopt the opposite point of view and accept the fine-tuning of the new mass parameter as a consequence of an analogue of Weinberg's anthropic argument for the smallness of the cosmological constant [6].

Neither of the two choices leads automatically to sharp predictions for the phenomenology of the TeV scale. The goal of this work is precisely to identify measurements that can distinguish between natural and unnatural theories, confirming or excluding whole classes of models. We follow two complementary approaches documented in the second and third part of the thesis. We design and perform a search for new physics on LHC data based on generic features of natural theories (in particular natural supersymmetric theories). Furthermore we study the couplings to known particles of the new state recently discovered by the two largest LHC experiments [3, 4] that is likely to have a key role in electroweak symmetry breaking.

The thesis is divided into three parts. The first part is introductory. It covers the theoretical aspects of particle physics needed to understand the original contributions contained in the second and third parts. In chapter 1 we discuss the reference theory of the field, known as the Standard Model of particle physics. In chapter 2 we treat in detail the Higgs mechanism for electroweak symmetry breaking and define the question of naturalness more precisely. We conclude the first part in chapter 3, with a phenomenological discussion of natural supersymmetric theories.

In the second part of the thesis we describe a search for new physics performed with the Compact Muon Solenoid (CMS) detector [7] on 2012 LHC data. We begin in chapter 4 by describing the experimental apparatus, we then discuss jet reconstruction and b-jet tagging with CMS in chapter 5. The last chapter of this second part is devoted to the search for new physics itself that targets a previously unexplored area of parameter space.

The third and last part of the thesis contains original theoretical work previously published in [8, 9, 10]. Always focussing on the question of naturalness we adopt a complementary approach with respect to the direct search discussed in the second part. We assume that the new state discovered at the LHC plays the role of the Higgs boson in electroweak symmetry breaking and study its couplings. In chapter 7 we give a detailed account of the deviations with respect to the Standard Model that we expect in natural supersymmetric models, showing that sharp predictions can be formulated and tested against the data. In chapter 8 we present measurements that can rule out vast classes of unnatural theories. We conclude by summarizing our findings and the status of naturalness after almost three years of LHC data-taking.

Part I

In the beginning

Chapter 1

The Standard Model of Particle Physics

> Let us raise a standard to which
> the wise and honest can repair;
> the rest is in the hands of God.
>
> *George Washington*

The reference theory of particle interactions has been extensively tested from atomic frequencies to the TeV scale, the highest energies that we can currently probe. Its continuos predictive successes have made of what is now called the Standard Model (SM) of particle physics the unavoidable starting point of any experimental or theoretical investigation of higher energies. In this chapter we outline the main features of the theory together with its open problems. In several sections of this chapter we follow [11, 12].

1.1   Matter and Forces

The SM describes three interactions (strong, electromagnetic and weak) between twelve fermionic fields. As we will see in the following, twelve bosonic fields mediate the interactions. In our current understanding these are the relevant degrees of freedom of particle physics in the few hundreds of GeV range.

The fermions can be divided into two subsets of six particles each: quarks and leptons. The division has been made in view of the fact that quarks feel the strong force while leptons do not. Each of the two groups can be organized into three families as shown in figure 1.1. In particle physics jargon the different families are said to have different flavors. The upper and lower components of each family have the same quantum numbers, so we can further subdivide the matter fields into up-quarks, down-quarks, charged leptons and neutrinos. Ordinary matter is composed only of u and d quarks, that form protons and neutrons, and of electrons. Here we do not discuss in detail the properties of each particle, however in section 1.5 we give their complete quantum numbers that are sufficient to fully deduce their phenomenology.

Three generations
of matter (fermions)
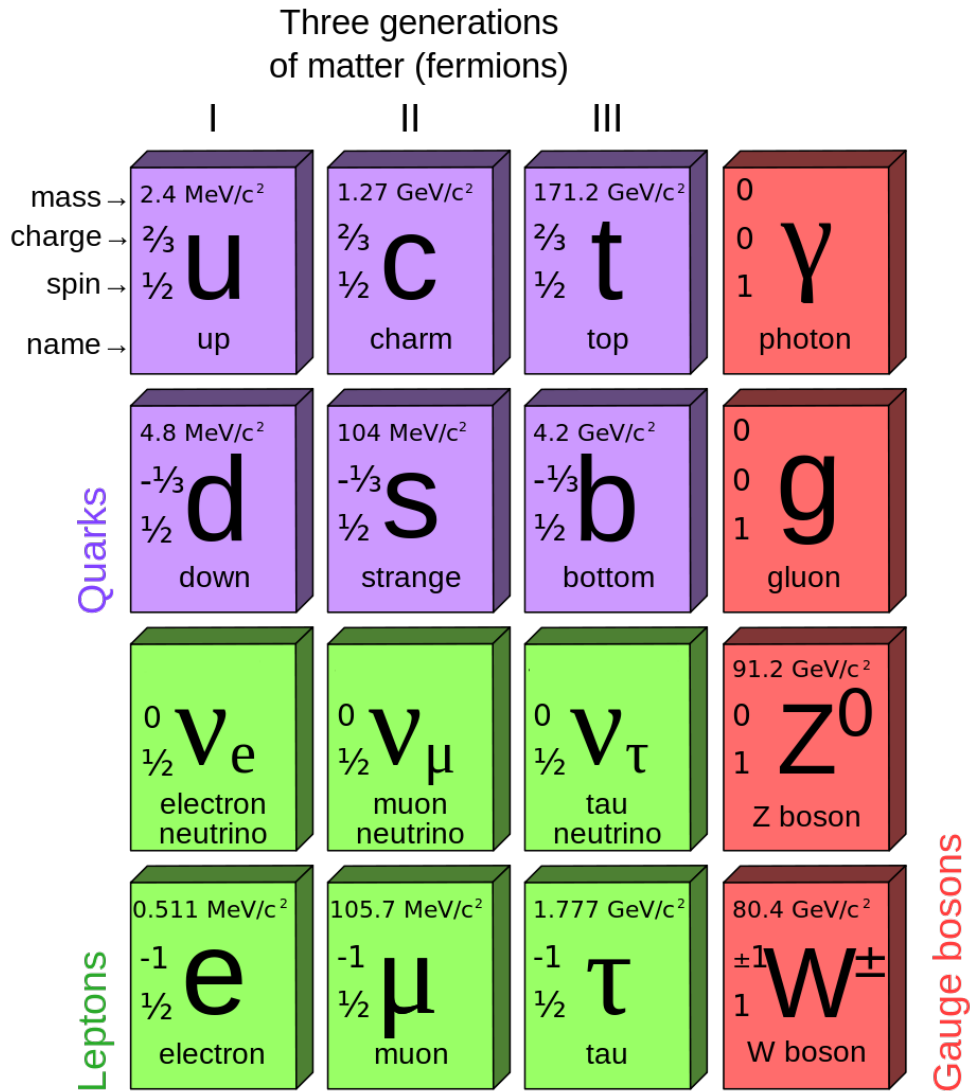
Figure 1.1: The particle content of the Standard Model, including matter and force carriers. Mass, electromagnetic charge and spin are included in the table.

We can now turn to the forces described by the SM. The three interactions mentioned above do not have all the same intensity, as their names suggest. At energies close to the W mass electromagnetic and weak interactions are comparable while the intensity of the strong interaction is roughly larger by a factor of 3. The situation changes dramatically at lower energies were the strong interaction is confining and the mass of the heavy mediators of the weak force suppress its

effect. For instance in the few MeV range

$$\frac{\text{strong}}{\text{electromagnetic}} \approx 100\,, \quad \frac{\text{electromagnetic}}{\text{weak}} \approx 10^9\,. \tag{1.1.1}$$

To complete this introductory picture of fields and interactions we just need to list the spin-1 bosonic degrees of freedom of the SM. Those mediating the strong force are called gluons, the photon carries the electromagnetic interactions, while the W and Z bosons are responsible for the weak ones, figure 1.1 contains a summary table.

So far we have neglected gravity. The reason is that at the energies we can currently probe its effects are not measurable

$$\text{gravity} \sim \frac{M_W^2}{M_P^2} \approx 10^{-34}\,, \quad M_W \sim 100 \text{ GeV}, \quad M_P \sim 10^{19} \text{ GeV}\,. \tag{1.1.2}$$

Several attempts have been made to formulate a quantum theory of gravitation and all of them are confronting serious conceptual difficulties. In addition to that they are clearly still far to obtain any experimental confirmation.

Before writing down the SM Lagrangian in sections 1.4 and 1.5, we need to introduce Yang-Mills theories in the next section. We then describe briefly the concept of effective field theory to put the SM in a more modern perspective.

1.2   Yang-Mills theories

When Yang and Mills wrote their seminal paper on Isotopic spin [13] it was already known that the electromagnetic interaction could be thought of as stemming from the invariance of the Lagrangian under local phase transformations (see for instance [14] and references therein)

$$\psi'(x) = e^{i\alpha(x)}\psi(x) \ \rightarrow \mathcal{L}\left(\psi(x)\right) = \mathcal{L}\left(\psi'(x)\right)\,. \tag{1.2.1}$$

Said invariance can be obtained introducing the photon field A_μ and adding the new interaction $\bar{\psi}\gamma_\mu\psi A^\mu$ to the kinetic Lagrangian,

$$\bar{\psi}\left(i\slashed{\partial} - m\right) \rightarrow \bar{\psi}\left(i\slashed{\partial} - m - e\gamma_\mu A^\mu\right)\psi\,. \tag{1.2.2}$$

The right hand side of 1.2.2 is invariant provided that A_μ transforms as

$$A'_\mu = A_\mu - \frac{1}{e}\partial_\mu\alpha(x) \tag{1.2.3}$$

that is nothing more than the gauge transformation of the vector potential under which classical Maxwell equations are invariant.

Yang and Mills enlarged this picture to more general internal [1] symmetries. Today the dynamics generating all known forces is derived from local gauge invariance principles. However this mathematical picture of Lagrangian invariance hides some simple physical arguments. At the end of the section we briefly comment on how this complexity arises from some redundancy. First it is good to introduce a more general form of local invariance, following the original Yang and Mills proposal.

We can start by imagining to have a Lagrangian which is a polynomial in fields and their derivatives

$$\mathcal{L} = \mathcal{L}\left(\partial_\mu \phi, \phi\right) \tag{1.2.4}$$

and that is invariant under a global Lie group transformation that does not act on space-time coordinates

$$
\begin{aligned}
\mathcal{L}\left(\partial_\mu \phi, \phi\right) &= \mathcal{L}\left((\partial_\mu \phi)', \phi'\right), & (1.2.5) \\
\phi_i'(x) &= U_{ij}(\alpha)\phi_j(x) = \left(e^{i\alpha^a \lambda^a}\right)_{ij} \phi_j(x), & (1.2.6) \\
(\partial_\mu \phi(x))_i' &= U_{ij}(\alpha)(\partial_\mu \phi(x))_j, & (1.2.7) \\
U &\in G,
\end{aligned}
$$

where λ^a are the generators of the group G, satisfying

$$\left[\lambda^a, \lambda^b\right] = if^{abc}\lambda^c, \quad \mathrm{Tr}\left[\lambda^a \lambda^b\right] = c\delta^{ab}, \quad c > 0. \tag{1.2.8}$$

The last identity, corresponding to the normalization of the generators with respect to the Cartan inner product, is valid only for compact Lie algebras. Even though there are many examples of non-compact Lie groups in physics, as the Lorentz group, we will restrict in the following to compact and simple groups without losing any of the internal symmetries of the SM. Note that the chosen normalization makes the structure constants of the group f^{abc} completely antisymmetric in the three indices.

At this point we would like to generalize the global invariance of the Lagrangian to a local (gauge) invariance, that is, we are searching for a new Lagrangian invariant under

$$
\begin{aligned}
\phi_i'(x) &= U_{ij}(\alpha(x))\phi_j(x) = U_{ij}(x)\phi_j(x) = \left(e^{i\alpha^a(x)\lambda^a}\right)_{ij} \phi_j(x), & (1.2.9) \\
(\partial_\mu \phi(x))_i' &= U_{ij}(x)(\partial_\mu \phi(x))_j + (\partial_\mu U(x))_{ij}\phi_j(x). & (1.2.10)
\end{aligned}
$$

The only difficulty is due to the gradients of the fields. If they transformed as the field themselves, local invariance would be automatically ensured by global invariance. So we would like to cancel the last term of the previous equation, adding a non-trivial part to the derivative. If we include a new component that transforms according to the adjoint representation of the group

$$D_\mu = \partial_\mu + iG_\mu, \quad G_\mu = \sum_a G_\mu^a \lambda^a \tag{1.2.11}$$

---

[1]That leave the space-time coordinates untouched.

we have

$$(D_\mu \phi(x))' = U(x)(D_\mu \phi(x)), \tag{1.2.12}$$

provided that G_μ transforms as

$$G'_\mu = U G_\mu U^\dagger + i \left(\partial_\mu U \right) U^\dagger. \tag{1.2.13}$$

This can be easily proven by exploiting the continuity properties of simple, compact Lie groups that allow us to consider only transformations that differ infinitesimally from the identity:

$$(\partial_\mu \phi)'_i(x) \approx (\partial_\mu \phi(x))_i + (i\partial_\mu \alpha^a(x)\lambda^a)_{ij}\phi_j(x) \,. \tag{1.2.14}$$

A complete proof can be found in any elementary field theory textbook (see for instance [15]).

In conclusion if $\mathcal{L}(\partial_\mu \phi, \phi)$ is invariant under the global symmetry,

$$\mathcal{L}(D_\mu \phi, \phi) \tag{1.2.15}$$

will be invariant under the gauge symmetry. Choosing the appropriate gauge groups, $\bar{\psi} D_\mu \psi$ can contain all SM fermion interactions. In section 1.4 we specify the form of D_μ and introduce the kinetic part of the Lagrangian for the gauge bosons G_μ.

As promised at the beginning of this section, before introducing the SM gauge groups, we want to make the physics of gauge invariance slightly more transparent. The truth behind the symmetry is that the form of the interactions above is unavoidable once Lorentz invariance is required. The gauge symmetry itself is just a consequence of the redundancy of the four component notation. We can take electromagnetism as an example to make this point more clear. It is well known that the photon (read a massless spin-1 field) has only two polarizations, so the field A_μ, with four components, can not be unique. In this sense the gauge transformation $A'_\mu = A_\mu - \frac{1}{e}\partial_\mu \alpha$ is not truly a symmetry linking two physical states, but rather it tells us that the two gauge potentials are physically equivalent. This is the consequence of having adopted a four component notation for a two component object.

1.3   Effective field theories

The SM is an effective field theory, valid only up to some yet unknown energy scale. Before introducing its particle content and gauge structure it is appropriate to review the modern definition of effective theory that will be useful also while discussing spontaneous symmetry breaking and the generation of particle masses in the SM. In this section we partially follow [16].

1.3.1   The basics

The idea of an effective theory is implicit in the human description of reality that brings order by neglecting effects that are far removed from our perception. In this case by neglecting what is "far" in energy.

The common intuition that the dynamics at low energies does not depend on the details of the theory at high energies (small distances) can be turned into a quantitative statement. To this end we can consider the example of the Hydrogen atom. We can calculate its energy levels to a certain degree of accuracy through the Schrödinger equation, knowing just the mass and the charge of the proton and the electron. If we want to refine our analysis, including the hyperfine splitting, we need additional information, such as their spins and magnetic moments. Moving towards higher precision demands the knowledge of QCD and the underlying structure of the proton.

To better quantify this progression and the level of accuracy achieved at each step, it is necessary to introduce the typical momentum scale of the problem. Through the Bohr radius $r_0 = 1/m_e\alpha$, where $\alpha \approx 1/137$ is the structure constant, it is easy to give an estimate

$$p_0 \approx \frac{1}{r_0} = m_e\alpha \,. \tag{1.3.1}$$

The Hydrogen atom has actually two separate scales since the typical energy scale is the Rydberg $\sim m_e\alpha^2$. Ignoring this detail we can estimate the error involved in neglecting an interaction at $p \sim \Lambda$. It is obvious that this error can be expressed in powers of $m_e\alpha/\Lambda$. As an example the energy levels can be computed to an accuracy of $(m_e\alpha/M_W)^2$ while ignoring the weak interactions (the value of M_W can be found in figure 1.1).

Now we have an intuitive picture of the the effective field theory approach, but we still need to render our initial statement more precisely. Ignoring the high energy dynamics means that its only effects are symmetry constraints on the low-energy theory and modifications of the low-energy coupling constants. For instance α depends crucially on the top quark mass

$$m_t \frac{d}{dm_t} \frac{1}{\alpha} = -\frac{1}{3\pi} \tag{1.3.2}$$

and the same is true for the proton mass

$$m_p \propto m_t^{2/27} \tag{1.3.3}$$

However in the Schrödinger picture we can still treat them as free parameters whose value will be obtained fitting experimental results. In this sense m_t is irrelevant as far as atomic properties are concerned, but in the higher energy theory it relates two parameters that are free in the effective one.

Turning to the symmetry constraints, a beautiful example is the spin-statistics theorem. In non-relativistic quantum mechanics the quantization of integer and non-integer spin degrees of freedom can proceed in exactly the same way without undermining the consistency of the theory. Nonetheless the full relativistic theory demands the respect of causality, which enforces the Fermi and Bose pictures also in low-energy observables.

In summary we can always find low-energy degrees of freedom that describe physics to a finite, but calculable precision. The only effect of the high-energy dynamics is to impose symmetry relations between them. In the process we do not need to know anything about the ultraviolet (UV) theory, but we loose some predictive power, in the sense that some parameters that are calculable in the complete theory might be free in our low-energy description.

1.3.2   Renormalization and Scaling

The main ideas behind effective field theories are now in place, however to actually construct an effective Lagrangian we need first a brief digression on the renormalization group equations. For the sake of simplicity we study the ϕ^4 theory which allows to introduce all the relevant information without wasting precious time on technical details.

The free theory in D dimensions is described by the action

$$S = \int d^D x \left[\frac{1}{2} (\partial_\mu \phi(x))^2 - \frac{1}{2} m^2 \phi^2(x) \right]. \tag{1.3.4}$$

We are interested to study the low-momentum behavior of the correlation functions,

$$G_n(x_1, ...x_n) = \langle \phi(x_1)...\phi(x_n) \rangle_S, \tag{1.3.5}$$

to this end we operate the change of variables

$$x' = sx, \quad \phi(x) = s^{(2-D)/2} \phi'(x'), \tag{1.3.6}$$

that recasts the action into

$$S' = \int d^D x \left[\frac{1}{2} (\partial_\mu \phi(x))^2 - \frac{1}{2} s^2 m^2 \phi^2(x) \right]. \tag{1.3.7}$$

where, for brevity we have renamed x'. This operation makes manifest the scaling behavior of Green functions

$$\langle \phi(sx_1)...\phi(sx_n) \rangle_S = s^{n(2-D)/2} \langle \phi'(x_1)...\phi'(x_n) \rangle_{S'} \tag{1.3.8}$$

At low energies i.e. $s \to \infty$ the mass term dominates the action, for this reason ϕ^2 is called a relevant operator. If we perform the same scaling on an interacting theory (suppressing the primes for brevity) we obtain

$$S' = \int d^D x \left[\frac{1}{2} (\partial_\mu \phi(x))^2 - \frac{1}{2} s^2 m^2 \phi^2(x) - \frac{\lambda}{4!} \phi^4(x) - \frac{\lambda_6}{6! s^2} \phi^6(x) \right]. \tag{1.3.9}$$

In this case ϕ^4 is a marginal operator whereas ϕ^6 an irrelevant operator, whose contribution vanishes in the limit $s \to \infty$. Nonetheless we are interested in the low-energy behavior of the theory and not to its zero-energy form, hence, depending on their matrix elements, irrelevant operators can play an important role through corrections that might be not so small.

All previous considerations arise from dimensional analysis, operators of dimension d scale as s^{D-d} and to retain all corrections up to order $1/s^r$ we should keep all operators of dimension $\leq D + r$. Until now it seems overly simple to construct an effective theory to an arbitrary degree of accuracy, we just need to keep operators up to a given dimension. However we have not yet taken into account the regularization and renormalization procedures of the interactions that in general can change the dimension of an operator.

In the presence of a cutoff Λ the relation between correlation functions becomes

$$G_n(sx; m^2, \lambda, \lambda_6; \Lambda) = s^{n(2-D)/2} G_n(x; s^2 m^2, \lambda, s^{-2}\lambda_6; \Lambda s) \tag{1.3.10}$$

and to obtain the infrared behavior of the left-hand side, we need to replace Λs on the right-hand side with Λ. To this end we exploit the standard renormalization group equations

$$\left[\Lambda \frac{\partial}{\partial \Lambda} + \beta_i \frac{\partial}{\partial c_i} + n\gamma_\phi \right] G = 0. \tag{1.3.11}$$

Here we have denoted with c_i the couplings of the interacting theory, with β_i the corresponding β-functions and with γ_ϕ the anomalous dimension[2] of the field ϕ. The latter two quantities depend on the couplings. The solution of (1.3.11) is well known [17, 18, 19]

$$\Lambda \frac{\partial}{\partial \Lambda} c_i(\Lambda) = \beta_i(c_i(\Lambda)) \tag{1.3.12}$$

and for the Green functions it means

$$G_n(x; c_i(\Lambda_1); \Lambda_1) = e^{-n \int_{\Lambda_1}^{\Lambda_2} \gamma_\phi(\Lambda) d\log \Lambda} G_n(x; c_i(\Lambda_2); \Lambda_2), \tag{1.3.13}$$

which leads us to

$$G_n(sx; c_i(\Lambda); \Lambda) = e^{-n \int_{\Lambda/s}^{\Lambda} \gamma_\phi(\Lambda') d\log \Lambda'} s^{n(2-D)/2} G_n(x; s^{d_i} c_i(\Lambda/s); \Lambda), \tag{1.3.14}$$

where d_i is the dimension of the coupling c_i. To illustrate the effect of renormalization on operators dimensions we take the simple case of an infrared stable fixed point

$$\beta(g^*) = 0 \quad g \to g^* \quad \text{as} \quad \mu \to 0, \tag{1.3.15}$$

where μ is the energy scale at which we are renormalizing the couplings. In this situation the renormalization group scaling for $s \to \infty$ is dominated by $g \approx g^*$, hence

$$\mu \frac{\partial}{\partial \mu} c_i = \gamma_{ij}(g^*) c_j, \tag{1.3.16}$$

$$\gamma_\phi(\mu) \to \gamma_\phi(g^*). \tag{1.3.17}$$

Without loss of generality we can ignore operators mixing $\gamma_{ij} = \gamma_i \delta_{ij}$ and adopt the more compact notation $\gamma_i(g^*) \equiv \gamma_i^*, \gamma_\phi(g^*) \equiv \gamma^*$. The solution of the renormalization group equations will then read

$$\frac{c_i(\mu_1)}{c_i(\mu_2)} = \left[\frac{\mu_1}{\mu_2} \right]^{\gamma_i^*}, \tag{1.3.18}$$

---

[2]The correction to the operator dimension arising from quantum effects.

$$e^{-\int_{\mu_2}^{\mu_1} \gamma_\phi(\mu) d \log \mu} = \left[\frac{\mu_1}{\mu_2}\right]^{-\gamma^*}, \qquad (1.3.19)$$

so that (1.3.14) becomes

$$G_n(sx; c_i(\Lambda); \Lambda) = s^{n(2-D)/2} s^{n\gamma^*} G_n(x; s^{d_i - \gamma_i^*} c_i(\Lambda/s); \Lambda). \qquad (1.3.20)$$

This equation shows that scale invariance is recovered at an infrared stable fixed point. However operators now have dimensions $D - d_i + \gamma_i^*$, their coefficients have dimensions $d_i - \gamma_i^*$ and scalar fields have dimensions $(D-2)/2 - \gamma^*$.

In weakly coupled theories anomalous dimensions can be computed in perturbation theory and are small. Therefore their effect is at most to turn marginal operators into relevant or irrelevant ones. The situation is completely different for strongly coupled theories. For instance in walking Technicolor it is believed that the operator $\overline{\psi}\psi$, with classical dimension 3, behaves at the quantum level as a dimension 1 scalar field, thus having an anomalous dimension of -2. The results obtained so far can be summarized as follows:

1. Select a set of variables that well describe the dynamics.

2. Write the effective Lagrangian as a sum of operators $\sum_i c_i \mathcal{O}_i$.

3. The scaling is $c_i \to s^{d_i - \gamma_i} c_i$. Where d_i is the naive dimension and γ_i the anomalous dimension of the operator. The most important operators are those of lowest dimension.

4. To compute a physics observable with an accuracy of order $1/s^r$ we must include all operators with dimensions $\leq D + r$.

1.3.3   Aside on the predictive power of effective theories

It is often argued in elementary field theory textbooks that a theory must be renormalizable to exhibit any predictive power. A non-renormalizable theory, it is said, would contain an infinite number of operators and, hence, of free parameters, that would make the physicist powerless in the description of nature. Nonetheless this statement is not completely correct, in a way that appears obvious after the previous discussion. If we consider a generic effective Lagrangian

$$\mathcal{L} = \mathcal{L}_{ren} + \mathcal{L}_{D+1} + \mathcal{L}_{D+2} + ... \qquad (1.3.21)$$

while it is clear that a computation to an arbitrary degree of accuracy is possible only in the limit $s \to \infty$, in which

$$\mathcal{L} = \mathcal{L}_{ren}, \qquad (1.3.22)$$

it is almost as obvious that we can compute any physical quantity to the desired (finite) accuracy retaining the correct number of operators in the effective theory.

As long as one is satisfied with a finite accuracy a non-renormalizable theory is as good as a renormalizable one. This is always the case, since, even though exact computations are nice,

no one knows the correct theory to arbitrary high energies. The only realistic results are always obtained in a, sometimes implicit, effective field theory framework. So in the next section we do not consider only dimension ≤ 4 operators for the sake of renormalizability, but in view of the fact that our description holds at sufficiently low energies.

1.4   The Standard Model gauge groups

We are now ready to discuss the application of the ideas treated in the previous sections to physical reality.

The full gauge group of the SM is

$$G = SU(3)_C \times SU(2)_L \times U(1)_Y \,. \tag{1.4.1}$$

The first factor describes strong interactions (or Quantum CromoDynamics, QCD), while the latter two electroweak ones. In the following we briefly account for the experimental and group theoretic reasons that lead to this structure of gauge symmetries.

1.4.1   Strong interactions

The selection of the $SU(3)$ gauge group is unique, in view of [20]

(a) The group must admit complex representations to account for both quarks and anti-quarks and distinguish them. There are mesons which can be conveniently described as $q\bar{q}$ bound states, but not any qq bound state.

(b) There must be a color singlet completely antisymmetric representation made up of qqq in order to solve the statistics puzzle of the low-lying baryons of spin $1/2$ and $3/2$.

(c) Given the number of quark flavors, the number of colors[3] must be in agreement with the data on the total e^+e^- hadronic cross section and the $\pi^0 \to \gamma\gamma$ decay rate.

Within simple groups, (a) restricts the choice to $SU(N)$ with $N \geq 3$, $SO(4N + 2)$ with $N > 1$ ($SO(6)$ is homomorphic to $SU(4)$) and $E(6)$. The remaining prescriptions lead unambiguously to $SU(3)$ with each flavor of quarks in a fundamental representation.

The kinetic Lagrangian of the six quarks is already invariant under a global $SU(3)$ (enlarged to $SU(3)_L \times SU(3)_R$ if m_f is independent of the flavor):

$$\mathcal{L}_D = \sum_{f=1}^{6} \bar{q}_f \left(i\gamma^\mu \partial_\mu - m_f \right) q_f. \tag{1.4.2}$$

---

[3]As the $SU(3)$ quantum number is denoted.

Gauging the global $SU(3)$, under which each quark carries an additional color index q^a, we obtain the complete QCD Lagrangian

$$
\begin{aligned}
\mathcal{L}_{QCD} &= \sum_{f=1}^{6} \overline{q}_f \left(i\gamma^\mu D_\mu - m_f \right) q_f - \frac{1}{4} \sum_{a=1}^{8} G^a_{\mu\nu} G^{\mu\nu}_a, \\
D_\mu q_f &= \left(\partial_\mu + ig_s \sum_{a=1}^{8} \lambda^a G^a_\mu \right) q_f, \\
G^a_{\mu\nu} &= \partial_\mu G^a_\nu - \partial_\nu G^a_\mu - g_s f^{abc} G^b_\mu G^c_\nu,
\end{aligned} \tag{1.4.3}
$$

where we accounted for the fact that the generators of $SU(N)$ are $N^2 - 1$ and we have included an additional term which is allowed by the symmetry. This is nothing but the kinetic term of the gluons, mediating the strong interactions. If we had omitted the last term in the first line, resumming quark loops would have made it reappear.

The symmetry insures that the constant g_s is unique for all flavors of quarks and all additional boson fields described by G^a_μ. As can be seen by direct inspection of (1.4.3) g_s is the coupling constant of the theory. This Lagrangian, as it is very well known, describes a dynamics of confined quarks and gluons, reproducing at high-energies the asymptotic freedom required by experimental evidence. Accounting for its complete phenomenology is beyond the scope of this very brief introduction. However it is worth to mention that $\mathcal{L}_{QCD}$ is not the most general Lagrangian consistent with the gauge symmetry. We have purposefully omitted

$$
\mathcal{L}_{CP} = -\frac{\alpha_s \theta}{8\pi} \widetilde{G}^a_{\mu\nu} G^{\mu\nu}_a , \quad \widetilde{G}^a_{\mu\nu} \equiv \epsilon_{\mu\nu\delta\lambda} \left(G^{\delta\lambda} \right)^a , \quad \alpha_s \equiv \frac{g_s^2}{4\pi} . \tag{1.4.4}
$$

Even if this term can be rewritten as a total derivative, in a non-Abelian gauge theory it can contribute to the action with boundary terms. The reason we could omit it is that direct measurements limit $|\theta| \lesssim 10^{-10}$ [21]. The operator, in fact, is not CP invariant and induces a non-zero electric dipole moment for the neutron. The smallness of θ is known as the "strong CP problem". A possible solution would be to introduce a global $U(1)_{PQ}$ spontaneously broken at high energies [22].

After this aside on the strong sector, we can turn to the electroweak sector, that is the real protagonist of the rest of this work.

1.4.2   Electroweak interactions

If we had to describe only the electromagnetic interactions, the task would be exceedingly simple. The first and only step is to notice that different fields interact with the photon with different strengths, according to their charge. The only possible choice for Quantum ElctroDynamics (QED) is then an abelian group. Otherwise the coupling would be universal as in QCD. Without practically any effort we could then rebuild QED from the free Dirac Lagrangian in analogy with QCD. This discussion implies that even if we were to describe electromagnetic and weak

interactions as two aspects of a unified force we would still need an abelian factor in the full gauge group. To see how this is realized in practice we need to build the weak part of the picture, that first emerged consistently in [23, 24]. We adopt a more modern and concise perspective, following [11].

The Fermi theory for β-decay is known to describe well weak interactions at nuclear energies

$$\mathcal{L}_F = \frac{G_F}{\sqrt{2}} \cos\theta_C \left[\overline{p}\gamma^\mu(1 - \alpha\gamma_5)n\right]\left[\overline{e}\gamma_\mu(1 - \gamma_5)\nu_e\right] . \tag{1.4.5}$$

Here p, n, e and ν_e are the fields of the proton, neutron, electron and neutrino, respectively. The factor $\cos\theta_C$ is close to one and is due to the lack of alignment between quark mass eigenstates and the states feeling the electroweak interaction. To our trained eyes this appears as the low energy limit of a gauge theory, where the gauge degrees of freedom have been integrated out. The interaction part of the theory would be written as

$$\mathcal{L}_{int} = \frac{g}{\sqrt{2}}W_\mu^+(J^-)^\mu + \text{h.c.} \tag{1.4.6}$$

where

$$\frac{G_F}{\sqrt{2}} = \frac{g^2}{8m_W^2}. \tag{1.4.7}$$

The W boson of mass m_W plays the role interpreted in QCD by the gluon fields. Therefore if we are able to find the currents that reproduce the Fermi theory for $p^2 \ll m_W^2$, where p is the relevant momentum of the process, we will reconstruct the symmetry group through their algebra. We begin by introducing the doublets

$$Q_L = (1 - \gamma_5)\begin{pmatrix} u \\ d \end{pmatrix}, \quad L_L = (1 - \gamma_5)\begin{pmatrix} \nu_e \\ e \end{pmatrix} \tag{1.4.8}$$

Here u and d are the quark fields making up neutrons and protons. If we assume that the factor α in (1.4.5) is due to the composite nature of the nucleons, we can immediately write

$$J_\mu^\pm = \overline{Q}_L\gamma_\mu\frac{\sigma^\pm}{2}Q_L + \overline{L}_L\gamma_\mu\frac{\sigma^\pm}{2}L_L \tag{1.4.9}$$

and from the commutation relations of the Pauli matrices

$$\left[\frac{\sigma^+}{2}, \frac{\sigma^-}{2}\right] = i\frac{\sigma^3}{2}, \quad \left[\frac{\sigma^3}{2}, \frac{\sigma^\pm}{2}\right] = \pm i\frac{\sigma^\pm}{2}, \tag{1.4.10}$$

we can deduce that the group we were searching for is $SU(2)_L$. It is clear that a unified description of the electroweak interactions requires a larger group. Even if we assumed that electromagnetic charges were the same for all the SM fields, we would still have problems with $SU(2)$ as can be seen by taking for example,

$$\lambda^\pm = \frac{\sigma^\pm}{2}, \quad \lambda^0 = \begin{pmatrix} 0 & 0 \\ 0 & 1 \end{pmatrix}. \tag{1.4.11}$$

In this case J^0_μ reproduces the electromagnetic current, but the algebra of the generators does not close to give a Lie group.

However a first, easy guess, that satisfies all our needs is $SU(2)_L \times U(1)_Y$ where $Q = T_3 + Y$ and T_3 is the eigenvalue of $\sigma_3 \left(1 - \gamma_5\right)/2$. This turns out to be the correct choice and gives us the gauge bosons Lagrangian

$$\mathcal{L}_{EW} = -\frac{1}{4}\hat{W}_{\mu\nu}\hat{W}^{\mu\nu} - \frac{1}{4}B_{\mu\nu}B^{\mu\nu}\,, \tag{1.4.12}$$

where $\hat{W}_{\mu\nu}$ and $B_{\mu\nu}$ are the, so called, field strengths

$$\hat{W}_{\mu\nu} = \sum_{a=1}^{3} W^i_{\mu\nu}T^i, \quad T^i = \text{Generator of } SU(2)_L \text{ in the adjoint representation} \tag{1.4.13}$$
$$B_{\mu\nu} = \partial_\nu B_\mu - \partial_\mu B_\nu. \tag{1.4.14}$$

The gauge bosons interact with the weak currents,

$$\sum_\psi \bar{\psi}\gamma_\mu \frac{1}{2}\left(1 - \gamma_5\right)T_i^{R_\psi}\psi W^\mu_i\,, \quad \sum_\psi \bar{\psi}\gamma_\mu Y_\psi\psi B^\mu\,, \quad i = 1,..,3\,, \tag{1.4.15}$$

as in (1.4.9). Each fermion enters differently in the current, according to its hypercharge Y_ψ and its $SU(2)_L$ representation R_ψ. In the next section we specify the quantum numbers of all SM fermions.

In the spirit of section 1.3, in the discussion above we have included only operators of dimension ≤ 4, confident that at sufficiently low energy our description holds. What "sufficiently" means for the SM is a deep question, discussed in detail in the following chapters.

1.5   The Standard Model gauge Lagrangian

The symmetry groups described above are not enough to define a complete theory. In order to write the SM Lagrangian we need to specify its particle content. As discussed in section 1.1 we have twelve fermions, organized in three families of leptons and quarks. It is convenient to define a vector $\boldsymbol{\Psi}$, that contains all SM fermions

$$\boldsymbol{\Psi} = \left(Q_L(3,2)_{1/6}, L_L(1,2)_{-1/2}, u^c(\bar{3},1)_{-2/3}, d^c(\bar{3},1)_{1/3}, e^c(1,1)_1, N(1,1)_0\right)\,. \tag{1.5.1}$$

The first number in brackets indicates the transformation properties under the color $SU(3)$ group, the second number those pertaining to $SU(2)_L$ and the subscript shows the hypercharge Y. With ψ^c we have denoted, as usual, the left-handed spinor $\overline{\psi}_R$. We have included also the neutral field N, that plays the role of the right-handed neutrino. Its presence can explain the smallness of light-neutrino masses through a see-saw mechanism and allow flavor mixing in the lepton sector.

The theory depicted so far contains the three gauge couplings of $SU(3)_C \times SU(2)_L \times U(1)_Y$. As mentioned above, only the couplings arising from a non-abelian symmetry are universal. The

values of the hypercharges, on the contrary, are arbitrary and have been fixed experimentally to reproduce the observed electric charges.

At this point we can write the SM gauge Lagrangian,

$$\mathcal{L}_{SMg} = -\frac{1}{4}\hat{W}_{\mu\nu}\hat{W}^{\mu\nu} - \frac{1}{4}B_{\mu\nu}B^{\mu\nu} - \frac{1}{4}G_{\mu\nu}G^{\mu\nu} + i\overline{\mathbf{\Psi}}\gamma^\mu D_\mu \mathbf{\Psi}, \tag{1.5.2}$$

where

$$G_{\mu\nu} = \sum_{a=1}^{8} G_{\mu\nu}^a \lambda^a, \quad \lambda^a = \text{Generators of } SU(3)_C \text{ in the adjoint representation.} \tag{1.5.3}$$

The Lagrangian above contains only renormalizable interactions and describes massless fields. This is true both for the matter fields and the gauge bosons. Including by hand gauge boson masses or fermion masses would spoil gauge invariance, making the theory inconsistent. It is appropriate to point out, though, that while the gauge boson masses are forbidden by the local nature of the symmetry itself, the fermion masses are ruled out by the *chiral* nature of the weak interactions (in $\mathcal{L}_{QCD}$ we had included the quark masses). A mass term would read

$$m\overline{\psi}\psi = m(\overline{\psi}_R\psi_L + \overline{\psi}_L\psi_R) \tag{1.5.4}$$

and it would be manifestly invariant if left-handed and right-handed components transformed in the same way, since any representation of a compact and simple Lie group is equivalent to a finite dimensional unitary representation.

1.6   Completing the picture

The Lagrangian in (1.5.2) does not describe nature. The first obvious problem with it is the masslessness of all fields mentioned in the previous section. This is in contrast both with direct measurements of the elementary particle masses and with the observed range of the weak force that semiclasically should scale as $\sim e^{-M_W r}/r$. Besides, as a consequence of the reducibility of $\mathbf{\Psi}$ under the gauge symmetry, the fermions enjoy a large $SU(3)^5 \times U(1)^4$ global symmetry whose selection rules are not observed experimentally.

These problems can not be solved by breaking explicitly the gauge symmetry, otherwise we would run into inconsistencies in perturbation theory. An elegant solution is provided by the Higgs mechanism [25, 26, 27, 28]. The first step consists in introducing the scalar doublet

$$\phi = \left(\begin{array}{c} \phi_1 + i\phi_2 \\ \phi_3 + i\phi_4 \end{array} \right), \tag{1.6.1}$$

with transformation properties under the gauge group given by

$$\phi = (1, 2)_{1/2}. \tag{1.6.2}$$

The idea of doing without any extra fields, although interesting, can be immediately excluded. The only term we would be able to add without renouncing gauge invariance, would be a mass for the right-handed neutrinos

$$\mathcal{L}_{M_N} = -\frac{1}{2} N_i M_{ij} N_j + \text{h.c.}, \tag{1.6.3}$$

which does not influence the other degrees of freedom in any way, unless we add at least the scalar doublet ϕ. In this case, in fact, we have new possible interaction terms that change dramatically the SM picture. First and foremost we are able to write a Yukawa-like Lagrangian

$$\mathcal{L}_Y = -\phi \left(\overline{Q}_i \left(Y_u \right)_{ij} u_j^c + \overline{L}_i \left(Y_n \right)_{ij} N_j \right) - \phi^\dagger \left(\overline{Q}_i \left(Y_d \right)_{ij} d_j^c + \overline{L}_i \left(Y_e \right)_{ij} e_j^c \right) + \text{h.c.} . \tag{1.6.4}$$

Furthermore we have to describe the dynamics of the new field. The most general invariant Lagrangian for a complex scalar field with operators of dimension ≤ 4 is

$$\mathcal{L}_H = |D_\mu \phi|^2 - \mu^2 \phi^\dagger \phi - \lambda \left(\phi^\dagger \phi \right)^2 . \tag{1.6.5}$$

Adding $\mathcal{L}_Y$ and $\mathcal{L}_H$ to the *minimal* Lagrangian (1.5.2) has important phenomenological consequences. We consider first the Yukawa sector. Its introduction has reduced the global symmetries of the system. To notice this we first have to eliminate the redundancy in the Y matrices through appropriate field redefinitions

$$Y_a \to (U_L^a)^\dagger Y_a U_R^a \tag{1.6.6}$$

This rotation does not affect the other terms in the full Lagrangian because of its global invariance properties. The Yukawa sector, instead, becomes

$$\mathcal{L}_Y \to -\phi \left(\overline{Q} V^\dagger Y_u^D u^c + \overline{L} U^\dagger Y_n^D N \right) - \phi^\dagger \left(\overline{Q} Y_d^D d^c + \overline{L} Y_e^D e^c \right) + \text{h.c.} . \tag{1.6.7}$$

The matrices Y^D are in diagonal form and we have defined

$$V \equiv U_L^u \left(U_L^d \right)^\dagger \tag{1.6.8}$$

$$U \equiv U_L^n \left(U_L^e \right)^\dagger . \tag{1.6.9}$$

It is manifest now that the overall baryon and lepton numbers are conserved. If we neglect right-handed neutrinos also the individual lepton numbers L_e, L_μ, L_τ are conserved. However we have clearly lost the large flavor symmetry. This can be easily seen with the further redefinition

$$u_L \to u_L V^\dagger, \tag{1.6.10}$$

which brings the current coupled to the W boson in the form

$$J_\mu^- = \overline{u}_L V \gamma_\mu d_L. \tag{1.6.11}$$

This vertex is the source of the successful predictions of the SM in flavor physics and one of the element of the matrix V is precisely $\cos \theta_C$ introduced in the Fermi Lagrangian.

1.6.1   Mass generation

If the parameter μ^2 is positive the potential (note the conventional change of sign with respect to (1.6.5))

$$V(\phi) = -\mu^2 \phi^\dagger \phi + \lambda \left(\phi^\dagger \phi\right)^2 \tag{1.6.12}$$

has a circle of minimums corresponding to

$$\phi = v e^{i\theta}, \quad v = \frac{\mu}{\sqrt{2\lambda}}, \quad \theta \in [0, 2\pi]. \tag{1.6.13}$$

To construct a perturbative expansion we have to make a single choice for the vacuum state. Because of the symmetry, the physics will be completely equivalent regardless of the choice. So without loss of generality, we can fix it to the value

$$\langle \phi \rangle = \begin{pmatrix} 0 \\ v \end{pmatrix}. \tag{1.6.14}$$

We have just found a way to break the gauge symmetry and hence generating masses, without spoiling the invariance of the vertexes of the theory. In fact, the dynamics is still completely symmetric, but there are generators T^a, $a = 1, .., r$ of the ElectroWeak (EW) gauge group, that do not leave the vacuum invariant $T^a \langle \phi \rangle \neq 0$, the *broken* generators. The remaining T^i that annihilate the vacuum, $T^i \langle \phi \rangle = 0$ are *unbroken* and still associated with massless gauge bosons.

To examine the consequences of the breaking we parametrize the field ϕ non-linearly

$$\phi(x) = e^{i\pi^a(x)T^a/v} \left(\frac{h(x)}{\sqrt{2}} + v \right). \tag{1.6.15}$$

This is particularly convenient, since, with a gauge transformation we get

$$\phi(x) \rightarrow \left(\frac{h(x)}{\sqrt{2}} + v \right). \tag{1.6.16}$$

Once ϕ acquires a vacuum expectation value it is easy to introduce the gauge bosons masses. Using (1.6.16) we have

$$|D_\mu \phi|^2 = \frac{v^2}{4} \left[g^2 \sum_{i=1}^{2} \left(W_\mu^i\right)^2 + \left(-g W_\mu^3 + g' B_\mu\right)^2 \right] + ... , \tag{1.6.17}$$

where g is the $SU(2)_L$ coupling while g' the $U(1)_Y$ coupling. Rotating to the mass eigenstates basis we are left with a massive charged vector,

$$W_\mu^\pm = \frac{W_\mu^1 \pm W_\mu^2}{\sqrt{2}}, \quad m_W = \frac{gv}{\sqrt{2}}, \tag{1.6.18}$$

a neutral massive boson

$$Z_\mu = \cos\theta_W W_\mu^3 - \sin\theta_W B_\mu, \quad \theta_W = \arctan\frac{g'}{g}. \tag{1.6.19}$$

of mass

$$m_Z = \frac{\sqrt{(g')^2 + g^2}}{\sqrt{2}} v \tag{1.6.20}$$

and a neutral massless degree of freedom (the photon),

$$A_\mu = \sin\theta_W W_\mu^3 + \cos\theta_W B_\mu. \tag{1.6.21}$$

The Yukawa Lagrangian (1.6.4) provides masses to fermions, in the usual $m_\psi \bar{\psi}\psi$ form, once the vacuum expectation value of ϕ is plugged in. The fermion masses are free parameters of the theory, that are fixed once the Yukawa couplings are measured,

$$m_i^u = \left(Y_u^D\right)_{ii} v, \quad m_i^d = \left(Y_d^D\right)_{ii} v, \quad m_i^e = \left(Y_e^D\right)_{ii} v. \tag{1.6.22}$$

Here we have redefined the left-handed components of the u quarks as in (1.6.10) and neglected light-neutrino masses.

Before mentioning some general aspects of spontaneous symmetry breaking and discussing the open problems of the SM, it is useful to notice an approximate accidental symmetry. There is a tree-level relation between the masses of the W and Z bosons

$$\frac{m_W^2}{m_Z^2 \cos\theta_W^2} \equiv \rho = 1. \tag{1.6.23}$$

In particular they become degenerate when $g' \to 0$ or $\cos\theta_W \to 1$. This is not a consequence of the gauge symmetry, but rather of the $SO(4)$ invariance of the potential of the scalar field ϕ. If we rewrite the scalar doublet as 2×2 matrix

$$\mathcal{H} = \left(i\sigma_2\phi^*, \phi\right), \tag{1.6.24}$$

the action of $SO(4)$ becomes

$$\mathcal{H}' = e^{-i\omega_L^i \sigma^i/2} \mathcal{H} e^{i\omega_R^i \sigma^i/2}, \tag{1.6.25}$$

where $\omega_{L,R}$ are the parameters of two independent $SU(2)$ transformation, one of which is the gauged $SU(2)_L$. Hence the group under which (1.6.12) is left invariant is $SU(2)_L \times SU(2)_R$ isomorphic to $SO(4)$. Furthermore the vacuum expectation value of the scalar doublet $\langle\mathcal{H}\rangle = I_{2\times 2} v$ is left invariant only by $SU(2)_{L+R}$. This explains the degeneracy of the two masses in the limit $g' \to 0$, that is the leading coupling breaking this symmetry.

$SU(2)_L \times SU(2)_R$ is often called *custodial* symmetry. It is not only broken by g', but also by the Yukawa interactions described in the previous section. So ρ at one-loop receives a correction proportional to m_t^2 that allowed to predict the top mass within a few GeV of the currently measured value using LEP precision measurements.

1.6.2   Spontaneous symmetry breaking

The Higgs mechanism described in the previous sections is just an application of the more general concept of spontaneous symmetry breaking first introduced by Anderson in 1962 [29]. Spontaneous symmetry breaking is a fascinating topic in quantum field theory and here we have just scratched the tip of the iceberg. However it is worth to spend some more words on a few aspects of the mechanism described above.

First of all spontaneous symmetry breaking is possible only with infinitely many degrees of freedom, as in quantum field theory. In quantum mechanics we encounter all the time Hamiltonians with multiple vacua linked by a symmetry transformation. The true vacuum however is unique and determined by one of their superpositions. This is due to the finite probability of tunneling between these states that scales as e^{-cV}, with c a positive constant and V the spatial volume of the system. Only as $V \to \infty$ the Hamiltonian has no off-diagonal elements connecting the different vacua, that become all degenerate. It is also easy to show that in this limit a small perturbation that breaks the symmetry can only select a ground state among the degenerate vacua, but not mix them [30].

Second and not less important, when the potential has a flat direction, as in this case, we would expect the presence of massless fields in the physical spectrum due to the Goldstone theorem. The fields $\pi^a(x)$ have the right quantum numbers to play this role, however they have been eliminated by a gauge transformation. Nonetheless the overall number of degrees of freedom must not have changed. In fact, they now constitute the longitudinal polarizations of the massive gauge bosons. If we consider, for a moment, a generic gauge group with generators λ^a, the covariant derivative of the field ϕ can be formally written as

$$D_\mu = \partial_\mu + ig\lambda^a A_\mu^a. \tag{1.6.26}$$

When ϕ acquires a vacuum expectation value, its covariant kinetic term gives rise to the mass matrix of the gauge bosons, in the form

$$\frac{1}{2}m_{ab}^2 A_\mu^a (A^b)^\mu \quad m_{ab}^2 = g^2(\lambda^a\langle\phi\rangle)_a(\lambda^b\langle\phi\rangle)_a. \tag{1.6.27}$$

So only the bosons associated to broken generators acquire a mass and eat up the corresponding Goldstone boson.

Another aspect, that is worth noticing, is the fact that we have chosen a scalar field. Imagine we had picked a vector field to acquire a vacuum expectation value, in this case we would have had

$$\langle 0|A_\mu(0)|0\rangle \neq 0 \tag{1.6.28}$$

but under a Lorentz transformation

$$\langle 0|A_\mu'(0)|0\rangle = \Lambda_\mu^\nu \langle 0|A_\nu(0)|0\rangle. \tag{1.6.29}$$

Lorentz invariance would then be lost. The same would have occurred for any non-trivial representation of the Lorentz group. In principle this is not a problem. There are many examples in the

literature of deformed or broken Lorentz symmetry at the Planck scale, due to quantum gravity effects (space-time foams, space time discretization, space time non-commutativity,...). However, the scale of the electroweak symmetry breaking is set by the Fermi constant, through equation (1.6.18),

$$v = \left(G_F 2\sqrt{2}\right)^{-1/2} \approx 246 \text{ GeV} \tag{1.6.30}$$

This value would be largely incompatible with experimental data if this was the scale at which the breaking of the Lorentz symmetry occurred.

1.6.3   Rise and fall

The predictive successes of the SM are endless, span many aspects of particle physics and phenomena taking place at very different energies. An incomplete list includes gauge coupling universality, precision flavor physics, atomic parity violation and precision tests of electroweak observables (see [31, 5] for reviews). Here we refrain from discussing even a small subset of them, contenting ourselves with the statement that the Lagrangian derived in this chapter is by now established up to energies of about one hundred GeVs. The only exception is its EW symmetry breaking sector. We will see in the next chapter how adding the Higgs scalar doublet has several theoretical advantages, but that we are still awaiting a complete experimental confirmation of the above picture. Recent LHC results seem to avail it, but even with a full proof, we would know that the SM Lagrangian is certainly not the whole story.

First and foremost, at some scale, possibly $M_P \sim 10^{19}$ GeV, gravitational effects have to be taken into account. Probably this implies abandoning quantum field theory altogether. Second and not less important the SM does not have a dark matter candidate and, as it is, can account only for 5% of the observed universe. Furthermore CP violation in the theory is not sufficient to account for the observed baryon asymmetry [32]. Another conceptual issue of this kind is the observed equality between the electron and the proton charges (currently a part in 10^{20} [31]). In the SM they are unsatisfactorily fixed by hand, but said equality could be justified in a grand unified picture implying a larger gauge group at higher energies. These facts are unavoidable, but are not linked unambiguously to an energy scale, they might be explained at scales we can not even start imagining to probe. Equivalently they could imply the existence of new particles extremely hard to detect with tiny observable effects in all other sectors of the theory.

There is only one hint for physics Beyond the SM (BSM) that is inextricably linked to the weak scale. It is related to the instability under quantum corrections of the mass m_h of the fourth component of the Higgs doublet. If there is a new neutral boson and it is light, in the SM only an accidental cancellation could push the cut-off of the theory much above m_h itself. An accidental cancellation of several orders of magnitude is not exactly the best explanation for a natural phenomenon, but it is appropriate to stress that the theory would be perfectly consistent also if it took place.

In the next chapter we introduce explicitly the interactions of the fourth neutral component of the doublet, discuss its theoretical relevance and current experimental results of its searches. This

will allow us to state the fine-tuning problem more precisely and eventually propose solutions to it.

Chapter 2

The Higgs boson

Manifest plainness,
Embrace simplicity,
Reduce selfishness,
Have few desires.

Lao Tzu

The Higgs doublet introduced in the previous chapter contains three degrees of freedom that become the longitudinal polarizations of the W and the Z bosons. The fourth component is a neutral field whose existence might just have been proved by the LHC. In this chapter we show that its presence is not indispensable to have a phenomenologically viable EW symmetry breaking mechanism, but that introducing it allows to extrapolate the SM to arbitrarily high energies and to obtain a good agreement with LEP precision EW measurements. We then describe its phenomenology at hadron colliders and summarize the experimental results of the LHC. In several sections we follow [11, 12].

2.1   Introduction

Throughout the previous chapter we have ignored the effect of the gauge fixing procedure

$$\phi \rightarrow \left(\frac{h}{\sqrt{2}} + v \right) \tag{2.1.1}$$

on the last degree of freedom of the scalar doublet. While the three Goldstone bosons are eaten up by the W and the Z, a fourth neutral boson remains. We denote it by $h(x)$. Its kinetic term comes from the covariant derivative $|D_\mu \phi|^2$, while its mass and self-interactions arise from the potential in (1.6.12),

$$V = \mu^2 \left(0, v + h\right) \begin{pmatrix} 0 \\ v + h \end{pmatrix} + \lambda \left| (0, v + h) \begin{pmatrix} 0 \\ v + h \end{pmatrix} \right|^2. \tag{2.1.2}$$

32

This gives for the complete Lagrangian,

$$\mathcal{L}_h = \frac{1}{2}\left(\partial_\mu h\right)^2 - \sqrt{\frac{\lambda}{2}} m_h h^3 - \frac{1}{2} m_h^2 h^2 - \frac{\lambda}{4} h^4, \tag{2.1.3}$$

with

$$m_h = 2\sqrt{\lambda}\, v = \sqrt{2}\mu. \tag{2.1.4}$$

In the same way we can derive the Higgs boson coupling to vectors

$$\mathcal{L}_{hV} = -\left[m_w^2 W_\mu^+ (W^-)^\mu + \frac{1}{2} M_Z^2 Z_\mu Z^\mu \right] \left(1 + \frac{h}{v\sqrt{2}}\right)^2 \tag{2.1.5}$$

and fermions

$$\mathcal{L}_{hf} = -\sum_f m_f \overline{\psi}_f \psi_f \left(1 + \frac{h}{v\sqrt{2}}\right). \tag{2.1.6}$$

By inspecting the Lagrangians above it is clear that all the physics of this neutral field can be expressed in terms of a single unknown parameter: m_h. We see this in more detail in section 2.6, while discussing its phenomenology at hadron colliders. However first it is appropriate to review its role in EW symmetry breaking.

2.2   A life without Higgs

The Higgs doublet has a key role in the SM. It allows to account for the masses of gauge bosons and fermions without renouncing gauge invariance and it solves brilliantly the problem of unitarity of the weak bosons scattering, as we will see in the next section. Furthermore its existence is in agreement with LEP ElectroWeak Precision Tests (EWPTs) and recent LHC results seem to confirm its existence. However it is worth to point out that, at least theoretically, the full doublet is not needed for electroweak symmetry breaking and a viable phenomenological Lagrangian can be written introducing only the EW Goldstone bosons.

To see this we can begin with the chiral $SU(2)_L \times SU(2)_R$ symmetry of the SM Higgs potential. In the familiar notation of the SM this symmetry manifest itself as an $SO(4)$ rotational invariance

$$H = \begin{pmatrix} \phi_1 + i\phi_2 \\ \phi_3 + i\phi_4 \end{pmatrix}, \quad r^2 = \phi_1^2 + \phi_2^2 + \phi_3^2 + \phi_4^2, \quad V(H) = V(r^2).$$

To simplify the chiral description it is convenient to reparametrize the Higgs doublet as

$$\mathcal{H} = \left(\frac{h}{2} + v\right) U, \quad U \equiv e^{\frac{i\pi^a \sigma^a}{2v}}. \tag{2.2.1}$$

Equation (2.2.1) allows us to ignore the Higgs boson altogether. The symmetry group now acts uniquely on U,

$$U' = g_L U g_R^\dagger, \quad g_{L,R} \in SU(2)_{L,R} \tag{2.2.2}$$

which contains the Goldstone bosons π^a. To construct gauge invariant functions of U we first introduce some fundamental building blocks:

$$\begin{align}
T &= U\sigma_3 U^\dagger \tag{2.2.3}\\
V_\mu &= (D_\mu U)U^\dagger \tag{2.2.4}\\
\hat{W}_{\mu\nu} &= W_{\mu\nu}^a \sigma^a/2 = W_{\mu\nu}^a T^a, \tag{2.2.5}
\end{align}$$

among them we can recognize the usual field strengths $\hat{W}_{\mu\nu}$ and a vector V_μ involving the covariant derivative

$$D_\mu U = \left(\partial_\mu - i\hat{B}_\mu\right)U + iU\hat{W}_\mu, \quad \hat{W}_\mu = gT^a W_\mu^a, \quad \hat{B}_\mu = g'T^3 B_\mu. \tag{2.2.6}$$

All these fields denoted collectively by Γ transform under $SU(2)_L$ as

$$\Gamma' = g_L \Gamma g_L^\dagger. \tag{2.2.7}$$

The question is now to find a guiding principle to construct the Lagrangian. In this picture, in fact, the operator dimension counting criterion fails, due to the fact that U is dimensionless. However if we accept the framework of effective field theories it is natural to adopt an expansion in momenta. Hence the *electroweak chiral* Lagrangian up to $O(p^2)$ is

$$\mathcal{L}_{EWc} = -\frac{1}{2}Tr\left[\hat{W}_{\mu\nu}\hat{W}^{\mu\nu}\right] - \frac{1}{2}B_{\mu\nu}B^{\mu\nu} + \frac{v^2}{4}Tr\left[D_\mu U(D^\mu U)^\dagger\right] + a_0\frac{v^2}{4}\left\{Tr\left[TV_\mu\right]\right\}^2. \tag{2.2.8}$$

The last term of $\mathcal{L}_{EWc}$ is responsible for a redefinition of the gauge boson masses and it is often not included exploiting custodial invariance. It is obvious that this Lagrangian describes massive W and Z together with a massless photon. The coefficient a_0 is arbitrary as are arbitrary all the coefficients of the ten terms that appear at the next order in the momentum expansion. If we adopt the point of view of considering $\mathcal{L}_{EWc}$ as a low-energy effective theory of which the SM with the Higgs boson is the UV completion, all these coefficients can be uniquely determined in terms of m_h.

We could also introduce fermion masses in the theory, using just the fields in U. For quarks we would have

$$\mathcal{L}_{Yc} = -\overline{Q}_i\left(Y_u\right)_{ij}U u_j^c - \overline{Q}_i\left(Y_d\right)_{ij}U^\dagger d_j^c + \text{h.c.} \tag{2.2.9}$$

We have just shown that we can construct the SM also without introducing the field h. However this description breaks down at $\Lambda \sim 4\pi v$, where the one-loop contribution to $\pi\pi \to \pi\pi$ becomes comparable to the tree-level amplitude. Adding h is the most economical extension of the EW chiral Lagrangian that can be extrapolated to arbitrarily high energies.

2.3   Perturbative unitarity

The interactions of the longitudinal components of the massive gauge bosons grow with their momenta. This can be seen by considering the polarization of the EW gauge bosons in their rest

frame

$$\epsilon_{T_1}^{\mu} = (0,1,0,0), \quad \epsilon_{T_2}^{\mu} = (0,0,1,0), \quad \epsilon_L^{\mu} = (0,0,0,1). \tag{2.3.1}$$

A boost along the z direction leaves the two transverse components untouched, whereas, for the longitudinal polarization, it gives

$$\epsilon_L^{\mu} = \left(\frac{|\vec{p}|}{m_V}, 0, 0, \frac{E}{m_V} \right) \to \frac{p_\mu}{m_V}, \ E \gg m_V. \tag{2.3.2}$$

This polarization is proportional to the gauge bosons momentum and it dominates the scattering at high energies. Processes involving W_L and Z_L have cross sections that grow with the energies and that, at some stage violate unitarity. We consider as an example the scattering process $W^+W^- \to W^+W^-$, if we do not include h exchange, at tree-level, in the high energy limit $s \gg m_W^2$, we have [33]

$$\mathcal{A}(W^+W^- \to W^+W^-) \to \frac{1}{v^2} \left[s + t \right], \tag{2.3.3}$$

where s and t are the usual Mandestalm variables. It is clear that the corresponding cross section grows with s, finally violating its unitarity bounds. To see this explicitly, we follow [34] and expand the amplitude into partial waves of definite angular momentum l

$$\mathcal{A} = 16\pi \sum_{l=0}^{\infty} (2l+1)P_l(\cos\theta)a_l, \tag{2.3.4}$$

where P_l are the Legendre polynomials and θ is the scattering angle. Since the cross section for a $2 \to 2$ process is given by

$$\frac{d\sigma}{d\Omega} = \frac{|\mathcal{A}|^2}{64\pi^2 s}, \tag{2.3.5}$$

we can immediately write, using the orthogonality of Legendre polynomials,

$$\sigma = \frac{8\pi}{s} \sum_{l'=0}^{\infty} \sum_{l=0}^{\infty} (2l'+1)(2l+1)a_{l'}a_l \int_{-1}^{1} d\cos\theta \, P_{l'}(\cos\theta) P_l(\cos\theta) = \tag{2.3.6}$$

$$= \frac{16\pi}{s} \sum_{l=0}^{\infty} (2l+1)|a_l|^2. \tag{2.3.7}$$

To impose the unitarity condition on σ, we invoke the optical theorem, which tells us that the cross section must be proportional to the imaginary part of the forward scattering amplitude,

$$\sigma = \frac{1}{s} \mathrm{Im}\left[\mathcal{A}(\theta = 0) \right]. \tag{2.3.8}$$

This implies

$$|a_l|^2 = \mathrm{Im}(a_l) \quad \Rightarrow \quad [\mathrm{Re}(a_l)]^2 + [\mathrm{Im}(a_l)]^2 = \mathrm{Im}(a_l) \tag{2.3.9}$$

$$\Rightarrow \quad [\mathrm{Re}(a_l)]^2 + \left[\mathrm{Im}(a_l) - \frac{1}{2} \right]^2 = \frac{1}{4}, \tag{2.3.10}$$

which is the equation of a circle of radius $1/2$ and center $(0, 1/2)$. Therefore the real part lies in the interval

$$|\text{Re}(a_l)| \leq \frac{1}{2}. \tag{2.3.11}$$

The strongest bound comes from the $l = 0$ partial wave

$$a_0 \approx -\frac{s}{32\pi v^2} \tag{2.3.12}$$

and with the condition $|\text{Re}(a_0)| \leq \frac{1}{2}$, one has

$$\sqrt{s} \lesssim 1.7 \text{ TeV}. \tag{2.3.13}$$

This means that at the TeV scale, if the Higgs boson is not present in the theory, either

1. Some new physics appears to cut-off the growth, or

2. The unitarity breakdown is canceled by higher-order terms whose importance signals the loss of perturbativity in the SM.

If on the contrary we include h exchange, the growth is cut-off by m_h, giving

$$a_0 = \frac{1}{16\pi s} \int_s^0 dt |\mathcal{A}| = -\frac{m_h^2}{16\pi v^2} \left[2 + \frac{m_h^2}{s - m_h^2} - \frac{m_h^2}{s} \log \left(1 + \frac{s}{m_h^2} \right) \right]. \tag{2.3.14}$$

In the limit $s \gg m_h^2$

$$a_0 \to -\frac{m_h^2}{8\pi v^2}. \tag{2.3.15}$$

So the unitarity condition (2.3.10), favors a relatively light Higgs boson

$$m_h \lesssim 870 \text{ GeV}. \tag{2.3.16}$$

This argument was carried out at tree-level, but for large Higgs boson masses, its quartic coupling becomes strong, leading to non-negligible radiative corrections. Thus to apply the previous analysis to set a bound on m_h one has to assume that the SM remains perturbative. Nonetheless we are just interested in showing that the addition of a lightish h can cure the high energy behavior of gauge boson scattering. For this same reason we have ignored that the scattering channel considered so far can be coupled to other neutral channels and that also charged channels such as $W_L^+ H \to W_L^+ H$ contribute to set a more stringent bound on m_h. For a complete treatment we should consider the eigenvalues of the matrix mixing

$$\left(W_L^+ W_L^-, \ \frac{1}{\sqrt{2}} Z_L Z_L, \ \frac{1}{\sqrt{2}} HH, \ Z_L H, \ W_L^+ H_L, \ W_L^+ Z_L \right). \tag{2.3.17}$$

This is not the only advantage of adding h to the SM. It also brings it back in agreement with the LEP precision measurements that we discuss in the next section.

2.4   Electroweak precision tests

Some of the parameters entering the EW gauge Lagrangian are known to sufficient accuracy to probe SM loop corrections. The three observables measured with the greatest precision are [35]

$$
\begin{aligned}
G_F &= \frac{g^2 \sqrt{2}}{8 m_W^2}, \quad \alpha(m_Z^2) \equiv \frac{e^2(m_Z^2)}{4\pi}, \quad m_Z, \\
G_F &= (1.166378 \pm 0.000050)\, 10^{-5}\ \text{GeV}^{-2}, \\
\alpha(m_Z^2) &= 0.0077550 \pm 0.0000029, \\
m_Z &= 91.1875 \pm 0.0021\ \text{GeV}.
\end{aligned}
\tag{2.4.1}
$$

Rather than directly computing the one-loop corrections to these quantities, we first recast the problem in a more theoretically convenient way [36, 37, 38]. The measurements above constrain significantly only gauge bosons two-point functions. Therefore we start by considering

$$
\mathcal{L}_{vp} = -\frac{1}{2}(W^3)^\mu \Pi_{33}(q^2) W^3_\mu - \frac{1}{2} B_\mu \Pi_{00}(q^2) B^\mu - W^3_\mu \Pi_{30}(q^2) B^\mu - W^+_\mu \Pi_{WW}(q^2)(W^-)^\mu.
\tag{2.4.2}
$$

We neglect longitudinal terms, proportional to $(q_\mu A_\mu)^2$, since they are irrelevant for physical amplitudes with external fermion lines. Even with the high accuracy achieved experimentally we can not hope to reconstruct the full functional form of $\Pi(q^2)$. Besides we are only interested in studying the contributions from the Higgs boson to see if they are in agreement with experiment and the leading ones affect only the first orders in the momentum expansion

$$
\Pi(q^2) = \Pi(0) + \Pi'(0)\, q^2 + \Pi''(0)\, q^4 + \dots,
\tag{2.4.3}
$$

namely $\Pi(0)$ and $\Pi'(0)$ are the only terms sensitive to $\log m_h$. There is no quadratic dependence on m_h due to the custodial symmetry of the Higgs potential. $SU(2)_R \times SU(2)_L$ insures that m_h^2 corrections appear only at two-loops, being completely negligible for $m_h < 1$ TeV.

To see the effect of h we should first notice that some of these two-point functions are already fixed by gauge couplings or other parameters of the theory. We can start with the $\Pi'(0)$s. Two of them can be traded for g and g', the remaining two can be compared to the data

$$
\hat{S} \equiv \frac{g}{g'} \Pi'_{30}(0), \quad \hat{U} \equiv \Pi'_{33}(0) - \Pi'_{WW}(0).
\tag{2.4.4}
$$

Turning to the $\Pi(0)$s, the masslessness of the photon gives two conditions $\Pi_{\gamma\gamma}(0) = \Pi_{\gamma Z}(0) = 0$ and the knowledge of v can be used to fix $\Pi_{ZZ}(0)$. Therefore we end up with a single prediction

$$
\hat{T} \equiv \frac{\Pi_{33}(0) - \Pi_{WW}(0)}{m_W^2}.
\tag{2.4.5}
$$

The form of $\hat{T}$ and $\hat{U}$ is such that they are zero in the limit of exact $SU(2)_R \times SU(2)_L$. So the main contributions we expect in the SM are proportional to its largest breaking spurions y_t and g'. The
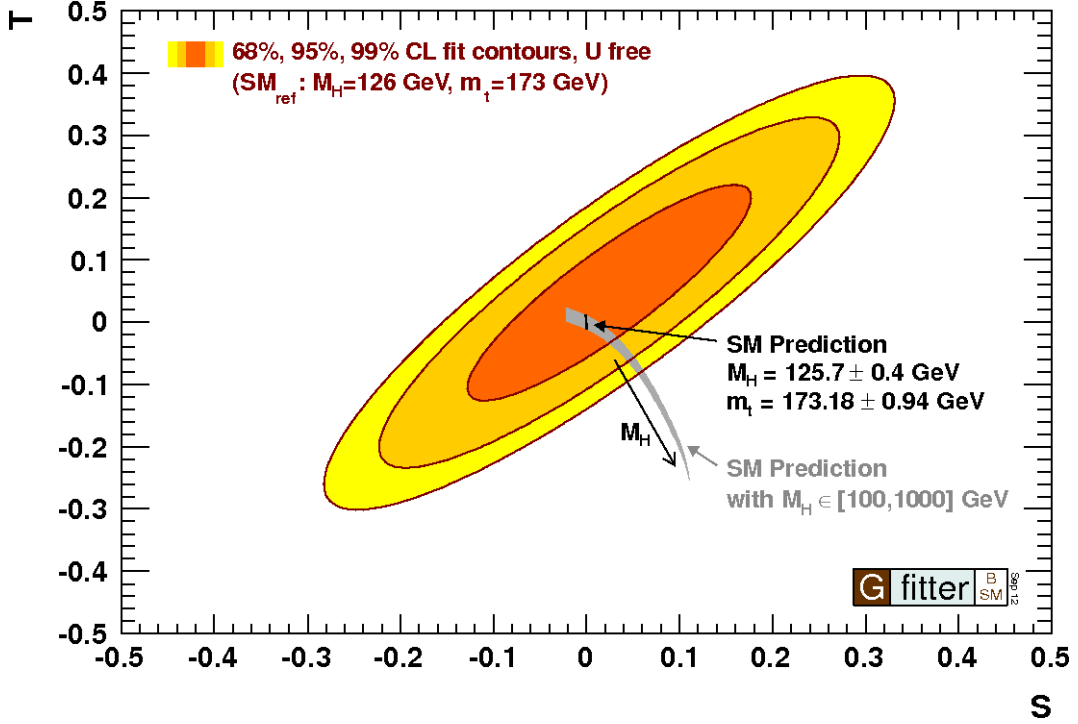
Figure 2.1: Contours of 68%, 95% and 99% experimental confidence level in the $S-T$ plane. The gray band corresponds to varying m_h taking into account the current experimental uncertainty on m_t. The black line is result in the SM assuming that the new boson discovered at the LHC is the Higgs. Note that the axes are scaled with respect to our definition in the text $S = \frac{4s_W^2 \hat{S}}{\alpha}$, $T = \frac{\hat{T}}{\alpha}$.

y_t^2 corrections to T are well known and allowed to predict the top mass with good accuracy before its discovery at the Tevatron. Here we are mainly interested in the Higgs boson contribution and we ignore them in what follows.

The effect of adding the Higgs boson to the EW chiral Lagrangian is

$$\hat{S} \approx \frac{G_F m_W^2}{12\sqrt{2}\pi^2} \log m_h$$

$$\hat{T} \approx -\frac{3G_F m_W^2}{4\sqrt{2}\pi^2} \log m_h \,. \tag{2.4.6}$$

As mentioned above these terms grow with m_h making manifest the effect of decoupling the Higgs boson from the theory. In figure 2.1 we can see that precision measurements favor a light h and that already $m_h \approx 500$ GeV is outside of the 2σ ellipse. Taking it out from the theory requires the introduction of new degrees of freedom cutting off the growth of $\hat{S}$ and $\hat{T}$, in order to fall back inside the experimentally allowed contour.

We have seen that the Higgs boson, albeit not needed for EW symmetry breaking, cures the high energy behavior of gauge boson scattering and at the same time puts the SM in agreement with electroweak precision measurements. In principle the SM $+ h$ can be extrapolated to arbitrarily high energies.

Eliminating h altogether requires the addition of new fields to solve these same problems. Typically the ensuing theories are much more involved and succeed in delaying the loss of perturbativity only up to a few TeV or tens of TeV at most. There are nonetheless possibilities of extending the SM while keeping the Higgs boson in the theory. The reason why such theories have been thought of at all is discussed in the next section.

2.5   Naturalness

We have seen that EW precision observables favor the presence of a light Higgs boson, that would also regulate the high-energy behavior of VV scattering amplitudes. However the Higgs mass is quadratically sensitive to the cut-off of the theory. At one-loop we have

$$m_h^2 = (m_h^0)^2 + \frac{3\Lambda^2}{8\pi^2 v^2} \left(m_h^2 + 2m_W^2 + m_Z^2 - 4m_t^2 \right), \tag{2.5.1}$$

where m_h^0 is the bare mass and we have taken into account only the main contributions (self-interactions, vector bosons and top quark). Without accidental cancellations it is reasonable to define a naturalness scale of the SM[1], Λ_N, at which the dominant of these contributions exceeds the physical Higgs boson mass by the amount $\sqrt{\Delta}$. For an Higgs boson mass well below 350 GeV, favored also by the LHC results that we examine in the next sections, the top contribution dominates and leads to

$$\Lambda_N < \frac{2\pi v}{\sqrt{3}m_t}\sqrt{\Delta} \approx 430 \text{ GeV} \frac{m_h}{125 \text{ GeV}} \sqrt{\Delta}. \tag{2.5.2}$$

$1/\Delta$ is the percentage of cancellation that can occur between the top contribution and any other term in the complete expression for m_h^2. The larger is Δ the more we are relying on accidental cancellations to explain the lightness of the Higgs boson. This is known as the *hierarchy problem*[2] and has unquestionably been the main driving motivation for extensions of the SM in the past few decades. The question is why the Higgs boson is so light if new physics is present only at the Planck scale or at the GUT scale ($\Lambda_{GUT} \approx 10^{16}$ GeV). In a new theory, differing from the SM only at such high energies, the calculation of the Higgs boson mass would require a huge amount of fine tuning if m_h falls in a range compatible with the EW precision observables.

This might be taken as an indication that new physics is lurking just around the corner, ready to make the SM natural. However in the past decades a vast array of precision measurements

---

[1] Here we follow [11].

[2] The first works pointing out the problem were [39, 40, 41, 42, 43].

has been performed and they all gave null results for new physics. This can be interpreted as the sign that BSM physics has an highly non-trivial structure, appearing at a low scale, but not contributing significantly to observables that we have measured precisely. Then the null results give themselves some guidance to model builders. Alternatively we can be agnostic about the characteristics of the physics stabilizing the Higgs mass. In this case there is a tension between Λ_N needed to to eliminate fine tuning and Λ_{NP}, the scale at which new operators extending the SM Lagrangian are generated. This is known as the *little* hierarchy problem [44].

We can illustrate this point with two concrete examples: EW precision observables and meson mixing. In the first case, we can imagine adding to the SM Lagrangian the two operators

$$
\begin{aligned}
O_{WB} &= gg' \frac{c_{WB}}{\Lambda_{NP}^2} \left(H^\dagger \sigma^a H \right) W_{\mu\nu}^a B^{\mu\nu}, \\
O_H &= gg' \frac{c_H}{\Lambda_{NP}^2} \left| H^\dagger D_\mu H \right|^2
\end{aligned}
\tag{2.5.3}
$$

$$
\tag{2.5.4}
$$

that correct $\hat{S}$ and $\hat{T}$

$$
\begin{aligned}
\hat{S} &= 4\frac{m_W^2}{\Lambda_{NP}^2} c_{WB}, \\
\hat{T} &= -2\frac{m_W^2}{g^2\Lambda_{NP}^2} c_H.
\end{aligned}
\tag{2.5.5}
$$

Provided that we assume $c_{WB} \sim c_H \sim 1$, living inside the 2σ ellipse in figure 2.1 requires $\Lambda_{NP} \gtrsim$ 5 TeV that for m_h around 100 GeV would imply a 1% fine tuning.

The situation is way more dramatic if we consider precision flavor observables. In this sector of the SM there would be a large number of measurements relevant for this discussion and in general crucial to build realistic models. We consider a single operator, just to illustrate the point

$$
O_{KK} = \frac{c_{KK}}{\Lambda_{NP}^2} \left(\bar{Q}_L \gamma_\mu Q_L \right)^2 .
\tag{2.5.6}
$$

O_{KK} contributes to the mixing between K^0 and $\bar{K}^0$. This is not the only operator we could write, but we have chosen the same already generated in the SM by integrating out the W. This choice avoids enhanced contributions in the matrix element that would make the bound on Λ_{NP} stronger. From the measurement of the $K - \bar{K}$ mass difference Δm_K and that of CP violation in the mixing ϵ_K we can set a bound on the real and imaginary parts of the contribution from O_{KK} [45]

$$
\text{Re} : \Lambda_{NP} \gtrsim 10^3 \text{ TeV} , \quad \text{Im} : \Lambda_{NP} \gtrsim 10^4 \text{ TeV} ,
\tag{2.5.7}
$$

where we have taken c_{KK} to be unity.

As stated above it is possible to model build around the little hierarchy problem and these arguments do not suggest that we should live with the fine tuning of the SM. An obvious consideration to relax the tension is to consider new physics that contributes only at loop level to

the operators above, this for a weak coupling $\sim g$ would reduce by a factor of more than 10 the bounds on Λ_{NP}. Another possibility would be to extend some of the approximate symmetries of the SM to the new physics. Assuming for instance that the new dynamics respects the custodial $SU(2)_L \times SU(2)_R$ or that some of the large flavor invariance of the SM gauge Lagrangian $SU(3)^5 \times U(1)^4$ is preserved. In summary we can take the hierarchy problem as an indication that new physics can appear around the TeV scale to mitigate the SM fine tuning and the little hierarchy problem as an hint to the structure of this new physics. Completely different attitudes are also present in the particle physics community accepting the fine-tuning as a fact of nature explained by arguments similar to Weinberg's anthropic treatment of the cosmological constant problem.

2.6   Production and decays at Hadron Colliders

In recent years the Higgs boson has been searched for at LEP, the Tevatron and the LHC. The experimental settings and conditions were different in the three cases and different phenomenological aspects were relevant. In this section we focus on the most important production and decay modes at the LHC, that are more closely related to this work. Most of the discussion applies also to a general hadron collider, with the largest differences determined by the parton distribution functions of the colliding particles.

2.6.1   Production modes at the LHC

The most important production modes for a SM Higgs boson at the LHC are

- Gluon Fusion (GF) production : Two gluons annihilate to form an Higgs through a triangle loop of top quarks. $gg \to h$.

- Vector Boson Fusion (VBF) production : Two initial state quarks emit two EW gauge bosons that annihilate to the Higgs. $qq \to hqq$.

- Associated Production (AP) : An intermediate EW gauge boson radiates an Higgs in association with another gauge boson V. $qq \to hV$.

- tth production: The Higgs is produced in association with two top quarks as a result of a double gluon splitting. $gg \to t\bar{t}h$.

The relevant diagrams are schematically depicted in figure 2.2 while the values of the cross sections for different Higgs masses and two different center of mass energies are in figure 2.3. The relative importance of the production mechanisms is reflected by the order in which they are listed above. For a light Higgs, around 120 GeV at $\sqrt{s} = 8$ TeV, we have $GF/VBF \approx 10$, $VBF/Wh \approx 2$ and $Wh/tth \approx 5$. However to design a search we must also take into account the very different backgrounds and fold in the decay we are interested in. So depending on the details of the final
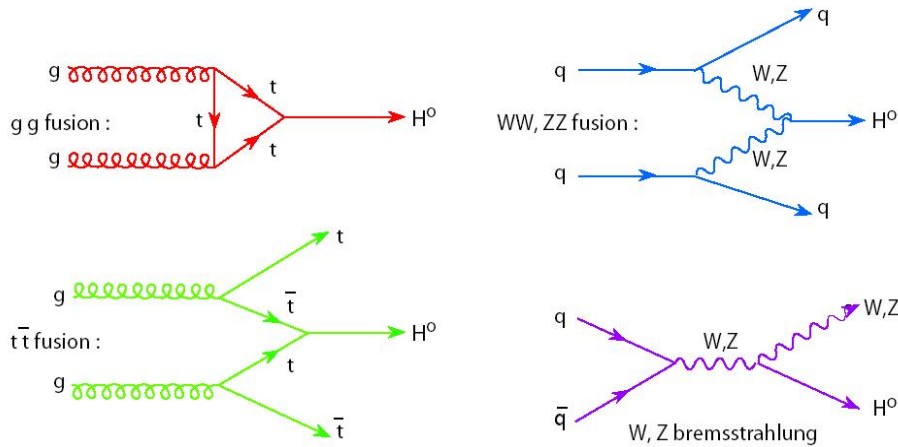
Figure 2.2: Schematic representation of the Feynman diagrams for the main Higgs production mechanisms at the LHC.

state, VBF production or even AP might be more important than GF. We see this in more detail in the next sections.

The theoretical uncertainties on the cross sections are also shown in figure 2.3, they became relevant in view of extracting Higgs couplings and possibly find deviations from the SM predictions. EW processes do not suffer from large errors, while GF production is known at the 10% level due to higher order QCD corrections.

2.6.2   Decays

As we have seen at the beginning of this chapter, the SM Higgs boson coupling to a field is proportional to the field mass. So the Higgs will decay preferentially to the heaviest particle that is kinematically allowed. For this reason a Higgs boson with a mass below the $2m_W$ threshold predominantly decays to b quarks, that at $m_h \approx 126$ GeV, account for $\approx 56\%$ of its width. For higher masses decays to WW and ZZ dominate. However, even in this low mass region, they can not be neglected giving 27% of the total width and proceeding mainly through a virtual boson: WW^*, ZZ^*. Also the decay to τ leptons is relevant for the LHC, even if they make up only 7% of the width at $m_h \approx 126$ GeV. It is the only accessible mode that probes Higgs couplings to leptons. These considerations are summarized in figure 2.4 that shows Higgs branching ratios as a function of its mass.

Next to these three level decays there are two loop-induced widths that are of the utmost importance for LHC searches. Namely $h \to gg$ and $h \to \gamma\gamma$. The decay to gluons is not observable at the LHC, due to the overwhelming QCD dijet background, but it is generated by the same diagram as the GF production process. $h \to \gamma\gamma$, instead, even if it has an almost negligible branching ratio, is one of the golden search modes due to the relative purity of the final state and
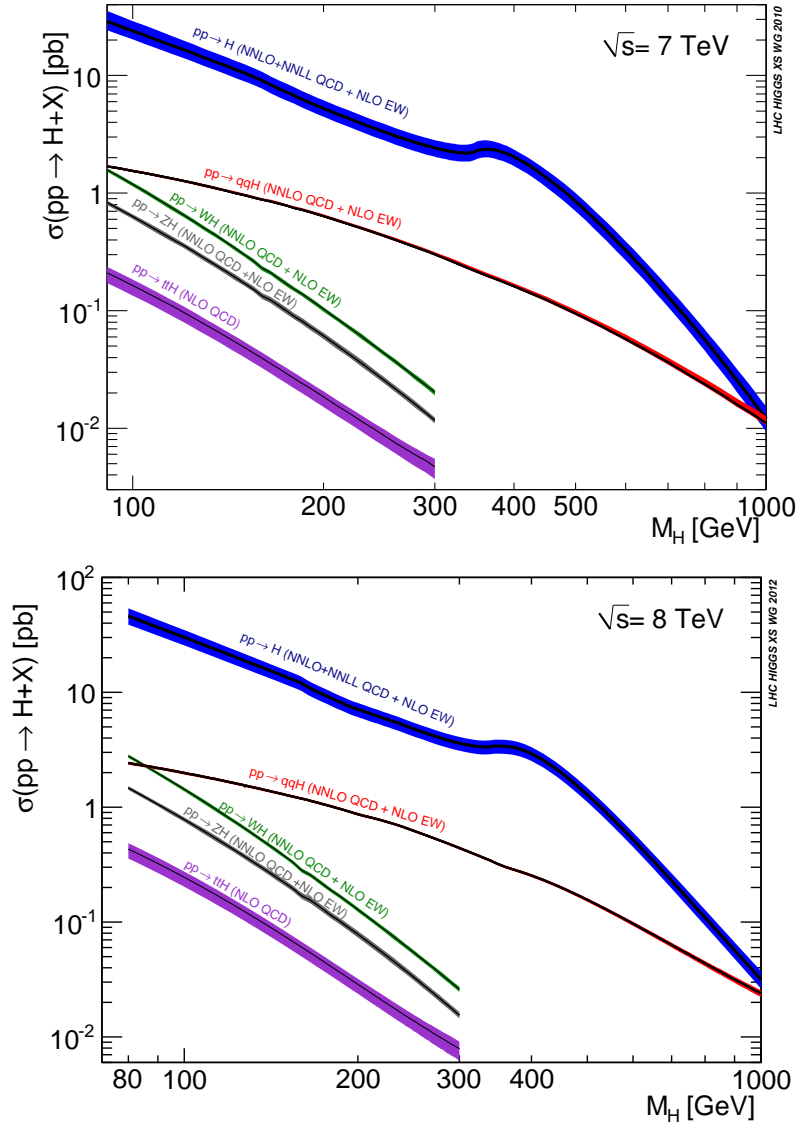
Figure 2.3: Higgs boson production cross sections at the LHC. Top $\sqrt{s} = 7$ TeV, Bottom $\sqrt{s} = 8$ TeV. The bands correspond to the current theoretical uncertainty. We have GF production in blue, VBF production in red, Wh associated production in green, Zh associated production in gray and tth production in purple.

the good energy resolution achievable on photons that allows to reconstruct the mass peak. The only other mode with good enough energy resolution is $h \to ZZ \to 4l$. For these reasons we show here the Higgs widths to gluons and photons that will be useful also in the last part of this work, while considering modification of Higgs couplings with respect to the SM. The Higgs decay width

to gluons is [46, 47]

$$\Gamma\left(h \to gg\right) = \frac{G_F \alpha_s^2 m_h^3}{36\sqrt{2}\pi^3} \left| \frac{3}{4} \sum_q F_{1/2}\left(x_q\right) \right|^2, \quad x_i \equiv \frac{m_h^2}{4m_i^2}, \tag{2.6.1}$$

while for photons we have [48]

$$\Gamma\left(h \to \gamma\gamma\right) = \frac{G_F \alpha^2 m_h^3}{128\sqrt{2}\pi^3} \left| \sum_f N_c^f Q_f^2 F_{1/2}\left(x_f\right) + F_1\left(x_W\right) \right|^2. \tag{2.6.2}$$

The loop functions are

$$\begin{aligned}
F_1(x) &= -\left(2x^2 + 3x + 3(2x-1)f(x)\right)x^{-2}, \\
F_{1/2}(x) &= 2\left(x + (x-1)f(x)\right)x^{-2}, \\
f(x) &= \begin{cases} \arcsin^2\sqrt{x} & x \le 1 \\ -\frac{1}{4}\left(\log\frac{1+\sqrt{1-x^{-1}}}{1-\sqrt{1-x^{-1}}} - i\pi\right)^2 \end{cases}.
\end{aligned} \tag{2.6.3}$$

These expressions are valid only at leading order, we do not show explicitly the QCD corrections to the gluon width for which we refer to [34]. In all numerical studies in the following of the thesis they are taken into account.

In the SM the top quark gives the most important fermion contribution to the two loops with its y_t^2 dependence. This is basically the only relevant term in the gluon width. The photon loop is dominated by the W contribution that is ≈ 5 times larger that the t quark term and has an opposite sign. These general considerations could also have been derived from the so called Higgs low energy theorem [49, 50]. It is easy to show that the leading contribution to the Higgs loop couplings to gluons (photons) is proportional to the particle mass and QCD (QED) β-function.

2.7   Experimental evidence

Each of the two largest LHC experiments (ATLAS and CMS) has collected approximately 5 fb^{-1} of 7 TeV data during the 2011 run and 20 fb^{-1} of 8 TeV data during last year run. Higgs analyses have not yet been updated to the full 2012 dataset, but most of them include up to 12 fb^{-1} of 2012 data. A new state has been observed with more than 5σ of global significance and its couplings to fermions and gauge bosons are broadly in agreement with those predicted in the SM for an Higgs boson [51, 52]. In this section we discuss this discovery and its compatibility with the Higgs boson hypothesis without entering into the finest experimental details.

LHC searches are currently sensitive to the processes listed in table 2.1. The column of the table approximately correspond to the production mechanisms described in the previous section, but due to finite experimental precision they are not pure. For instance the untagged category
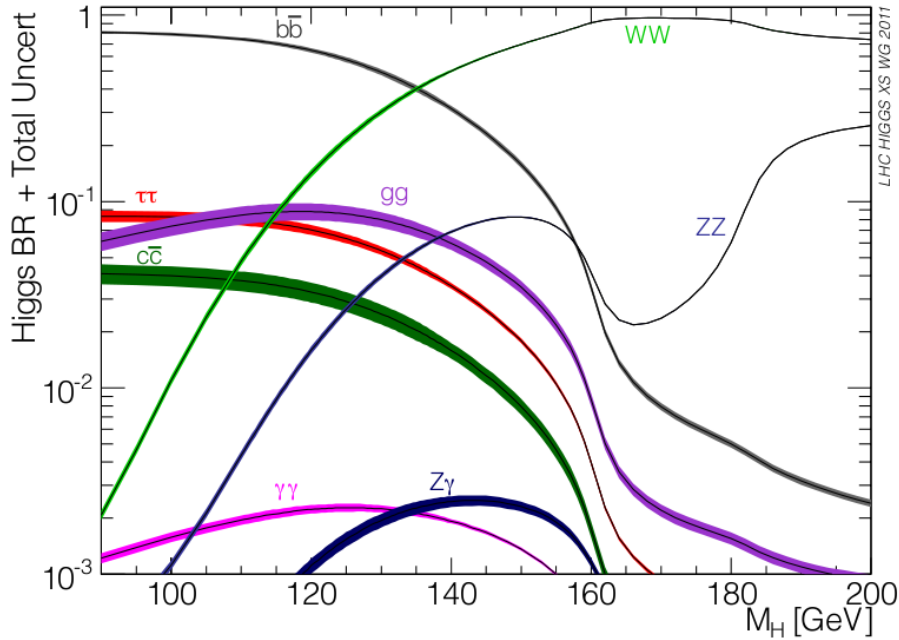
Figure 2.4: Higgs boson branching fractions as a function of its mass. The theoretical uncertainty is represented as a colored band around the central value.

is an admixture of GF and VBF production modes with relative fractions given approximately by the ratio between cross-sections. Instead the dijet tagged category was designed to isolate VBF production, but still retains a $\sim 20\%$ GF contamination. The last two categories can be considered as pure and in one-to-one correspondence with the equivalent production mode. The approximate contaminations quoted are the same for ATLAS and CMS within a few %. Note that table 2.1 is good only for illustrative purposes, as for example a $Wh \to WWW \to 3l\nu$ search might be ongoing, but the corresponding one with one hadronic W might not be. So the decay modes considered do not cover all possible final states, for a complete list of the current searches we refer to [53, 54] that are kept up to date by the two collaborations.

Combining searches in these channels ATLAS and CMS can separately exclude at 95% C.L. a broad range of masses for the SM Higgs boson, going from the LEP limit $m_h \gtrsim 114$ GeV up to more than 600 GeV. This is illustrated in figure 2.5, where we show the CMS result. The exclusion spares a small window around 126 GeV where evidence for a new state was found.

The significance of the discovery is presented in figure 2.6 separately for the two experiments. In the same figure it is possible to appreciate the very different mass resolution and sensitivity of the different channels. These two characteristics single out untagged $h \to \gamma\gamma$ and untagged $h \to ZZ \to 4l$ analyses as the main source of sensitivity, with a local p-value of up to $4-5\sigma$ each for both experiments and a mass resolution of $\mathcal{O}(1-2\%)$.

Table 2.1: Higgs decay modes to which the LHC is currently sensitive. The columns correspond to exclusive experimental categories, approximately corresponding to a production mode.

	untagged	dijet tagged	Vh	tth
$h \to \gamma\gamma$	✔	✔	✔	
$h \to WW$	✔	✔	✔	
$h \to ZZ$	✔	✔		
$h \to \tau\tau$	✔	✔	✔	
$h \to b\bar{b}$			✔	✔
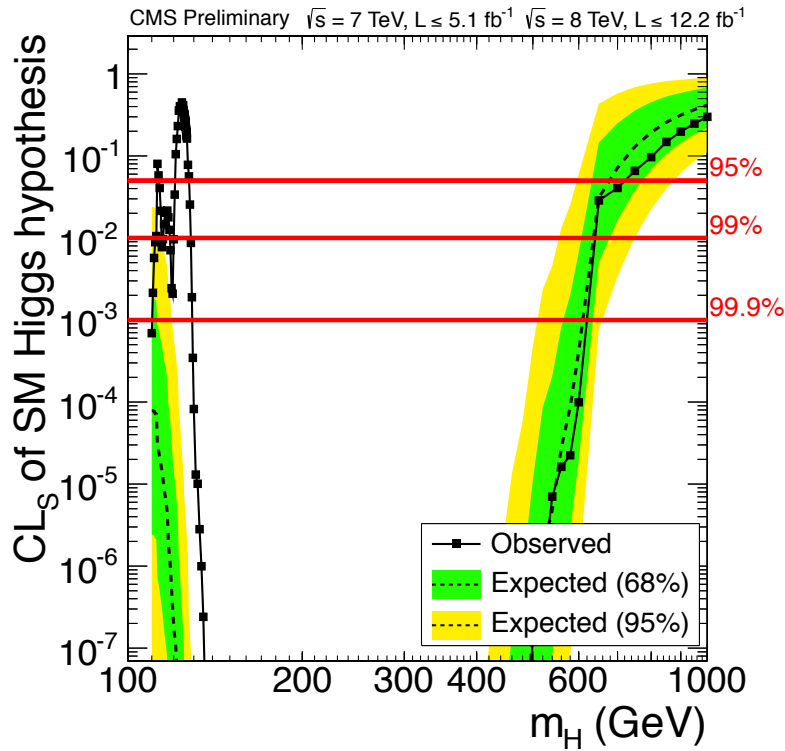
Figure 2.5: CMS limit on the Higgs boson production cross section, obtained combining 5 fb^{-1} of 7 TeV data and 12.2 fb^{-1} of 8 TeV data.

Here we are not going to enter into the details of the experimental effort leading to this result that can be found in [53, 54], where references to the single analyses are listed. However there is at least one comment that can not be omitted. The spin and CP quantum numbers of this new state have not yet been measured at the 5σ level, even if several attempts are ongoing in the $ZZ \to 4l$
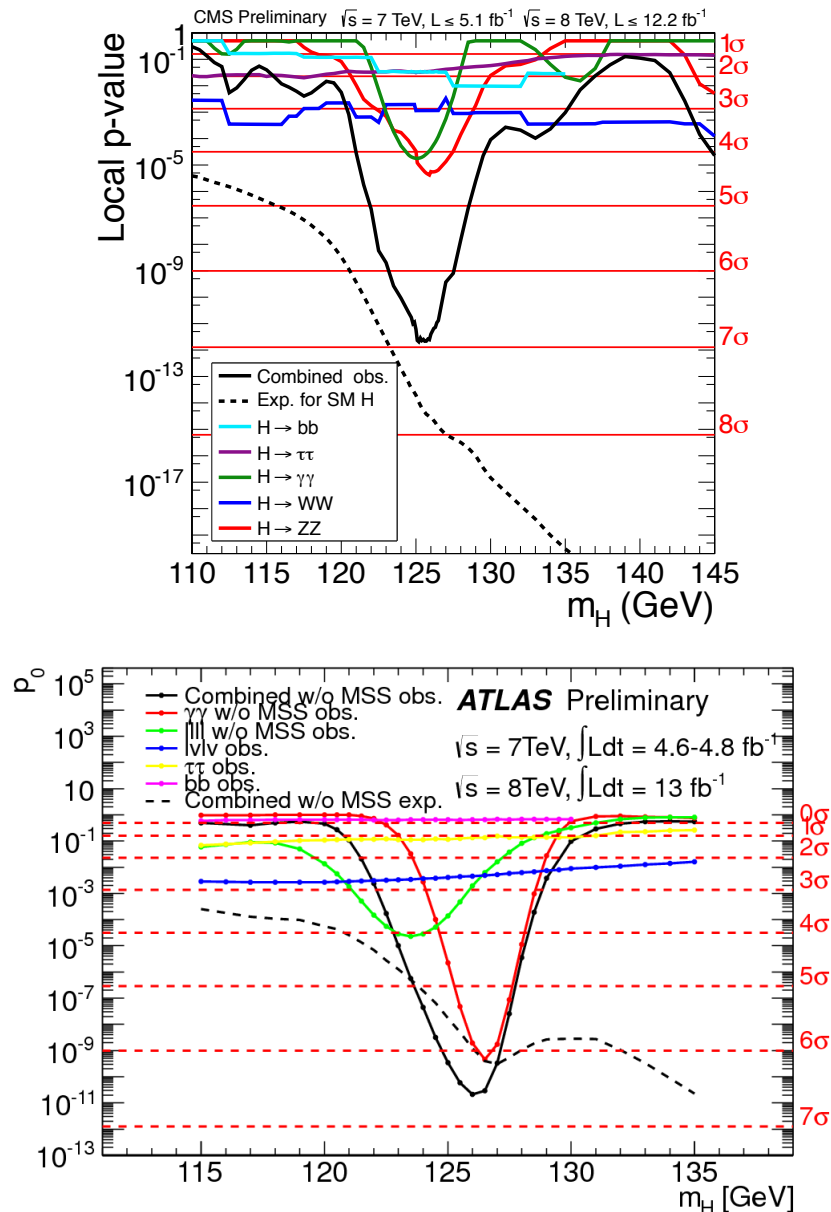
Figure 2.6: Local *p*-value for the background only hypothesis to be compatible with the 126 GeV excess in the CMS (top) and ATLAS (bottom) Higgs analyses. The combined significance was obtained assuming an Higgs boson with SM couplings.

channel [55]. Nonetheless the excess was found in analyses that were optimized to the extreme for a SM Higgs boson signal, often employing neural networks trained on the SM Higgs. In addition
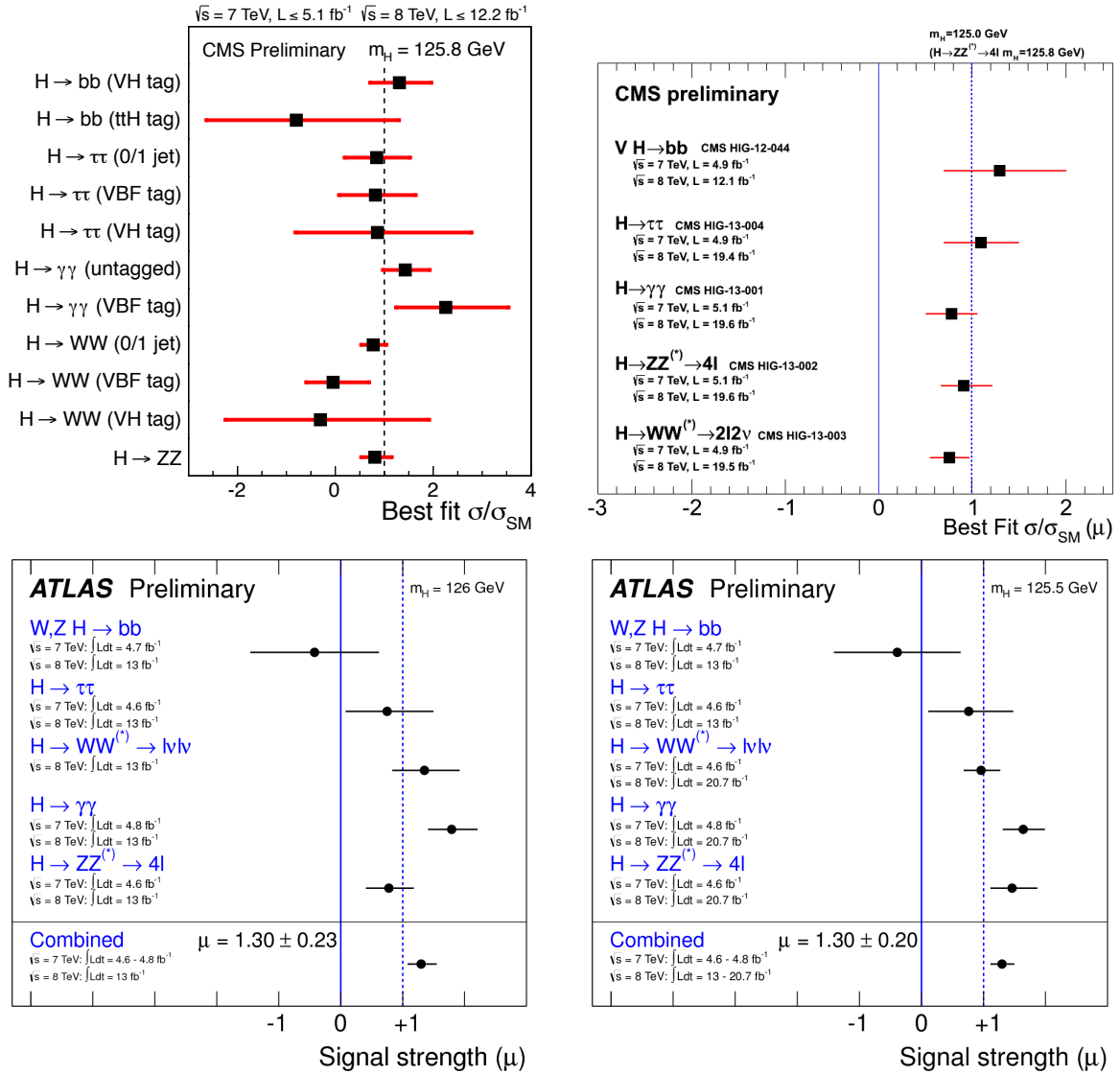
Figure 2.7: Observed production and decay rates of the new state, relative to their SM Higgs boson values. Top: CMS, Bottom: ATLAS. The results in the left column have been obtained combining the 2011 and part of the 2012 dataset, corresponding approximately to 5 fb^{-1} collected at $\sqrt{s} = 7$ TeV and 13 fb^{-1} collected at $\sqrt{s} = 8$ TeV. Most of those on the right column were produced using the full 2011 and 2012 datasets (an addition of ≈ 7 fb^{-1} at 8 TeV) and were made public in March 2013 in occasion of the *Recontres de Moriond*.

to that, measurements of its rates are all in good agreement with the SM, with tensions in single channels below the 2σ level, as can be seen from figure 2.7.

To conclude this section we note that also Tevatron experiments have found evidence for this new state at the 3σ level in the Vh, $h \to b\bar{b}$ channels [56].

While this work was being completed ATLAS and CMS updated most of their Higgs searches in occasion of the *Recontres de Moriond* showing results on the full 2012 dataset. The most notable differences with respect to the results presented in the previous set of publications are the decrease in the $h \to \gamma\gamma$ rate (now very close to its SM value) reported by the CMS experiment and the 1.5σ discrepancy in the mass determination observed by the ATLAS collaboration between the $h \to ZZ \to 4l$ and $h \to \gamma\gamma$ channels. The third difference worth to point out is that the ATLAS $h \to ZZ \to 4l$ is now slightly more than 1σ above the SM prediction while before it was below by roughly the same amount. For the most recent results we refer again to [53, 54].

Chapter 3

Supersymmetry

Supersymmetry (SUSY) is the most general spaceti me symmetry of the S-matrix consistent with relativistic quantum field theory [57, 58]. It is one of the most studied topics of the past decades in theoretical physics.

In this chapter we introduce it from a phenomenological point of view, having necessarily to leave out some of its most exciting formal developments. We start by discussing the main phenomenological for TeV scale supersymmetry, the solution of the hierarchy problem. This was not the historical reason for its development [59, 60, 61, 62, 63] , but it is the natural starting point for the LHC searches that we discuss in the second part of the thesis and the main drive behind the theoretical work treated in the third part. We then introduce all the necessary ingredients to build a supersymmetric model, including a short discussion of supersymmetry breaking, describe the minimal extension of the SM with supersymmetry and some of its extensions. We also discuss general features of natural supersymmetric theories that inspired the search for new physics in chapter 6.

3.1   The hierarchy problem

As we have seen in the previous chapter a fermion coupled to the Higgs boson through the Yukawa interaction $y_f H \bar{f} f$, gives a loop correction to the Higgs mass of the form

$$\delta m_h^2 = -\frac{N_c \left| y_f \right|^2}{8\pi^2} \Lambda^2 + \dots .$$ (3.1.1)

The ellipses represent terms that grow at most logarithmically with Λ. In dimensional regularization the Λ^2 term would be absent, but we would like to interpret Λ as the physical cut-off of the theory, in which case m_h^2 is quadratically sensitive to it. In general m_h is sensitive to the highest scale in the theory. Even if the heaviest degree of freedom does not couple directly to h we would still have a two loop correction that could be sizeable. For instance a fermion with EW quantum numbers and a large vector-like mass $m_F \bar{F} F$ gives

$$\delta m_h^2 \propto \left(\frac{g^2}{16\pi^2} \right)^2 \left[a\Lambda^2 + 24 m_F^2 \log \left(\frac{\Lambda}{m_F} \right) \right] . \tag{3.1.2}$$

The coefficient a depends on the renormalization scheme adopted, but even in dimensional regularization the m_F^2 term can be large requiring additional fine-tuning.

This observation suggests that the fine-tuning problem can not have a trivial solution, based on the cancellation of one-loop corrections. However thinking about one-loop is a good starting point towards an elegant symmetry answer. A scalar with coupling $y_\phi |H|^2 |\phi|^2$ and mass m_ϕ gives a contribution opposite in sign with respect to a fermion

$$\delta m_h^2 = \frac{N_c y_\phi}{8\pi^2} \left[\Lambda^2 + ... \right] , \tag{3.1.3}$$

the two quadratic terms would exactly cancel for $y_\phi = |y_f|^2$. If this occurrence was not accidental, but rather the consequence of a symmetry relating fermions and bosons, the cancellation might be extended to higher loops, reducing or eliminating the sensitivity of m_h on the cut-off of the theory. Such a symmetry exists and has much deeper consequences than the simple cancellation above, it is known in particle physics under the name of supersymmetry.

3.2   The supersymmetry algebra

Supersymmetry not only has the potential to solve the fine-tuning problem above, but, in a sense, it is unavoidable. As anticipated in the introduction it is the most general symmetry of the S-matrix, realized as a graded Lie algebra, consistent with relativistic quantum field theory. The generator algebra is

$$\begin{aligned}
\left\{ Q_\alpha^A, \bar{Q}_{\dot{\beta}}^B \right\} &= 2\sigma_{\alpha\dot{\beta}}^\mu P_\mu \delta^{AB}, \quad \sigma^\mu = \left(1, \sigma^i \right) , \\
\left\{ Q_\alpha^A, Q_\beta^B \right\} &= \left\{ \bar{Q}_{\dot{\alpha}}^A, \bar{Q}_{\dot{\beta}}^B \right\} = 0 , \\
\left[P_\mu, Q_\alpha^A \right] &= \left[P_\mu \bar{Q}_{\dot{\alpha}}^A \right] = 0 \\
\left[P_\mu, P_\nu \right] &= 0 .
\end{aligned} \tag{3.2.1}$$

Here the generators $Q(\bar{Q})$ have spin 1/2, they transform bosonic states into fermionic states and vice versa. α and β are spinorial indexes, while μ and ν run over the spacetime coordinates

(P_μ is the four-momentum generator of spacetime translations). The capital letters refer to an internal space and go from 1 to some integer N. The $N = 1$ case is the most relevant for the phenomenology of the TeV scale and is known as the supersymmetry algebra *tout court*. The algebra above is invariant under an $U(N)_R$ rotation of the Q^A, that for $N = 1$ reduces to a phase transformation.

In order to construct a supersymmetric theory we first need to discuss the representations of the algebra. The first key observation is that particles in a supersymmetric multiplet (supermultiplet) have the same mass. This descends from the fact the the Q's and P_μ commute. Therefore it is easy, by just inspecting the algebra, to conclude that $P_\mu P^\mu$ is a Casimir operator. This is already an hint that supersymmetry is indeed a possible solution to the hierarchy problem. Radiative corrections to fermion masses are known to diverge at most logarithmically in any renormalizable field theory, so the same must be true for scalar masses, if supersymmetry is unbroken.

A second point that can be easily proven is that supermultiplets contain an equal number of bosons and fermions. We can show it by introducing the fermion number operator $(-1)^{N_F}$ that has eigenvalue $+1$ on bosonic states and -1 on fermionic ones. From the definition it is clear that $(-1)^{N_F} Q = -Q(-1)^{N_F}$. If we then assume to be working with a finite dimensional representation, for which the trace is well defined, we have

$$\text{Tr}\left[(-1)^{N_F}\left\{Q^A_\alpha, \bar{Q}^B_{\dot{\beta}}\right\}\right] = \text{Tr}\left[-Q^A_\alpha\left\{Q^A_\alpha, \bar{Q}^B_{\dot{\beta}}\right\}\bar{Q}^B_{\dot{\beta}} + Q^A_\alpha\left\{Q^A_\alpha, \bar{Q}^B_{\dot{\beta}}\right\}\bar{Q}^B_{\dot{\beta}}\right] = 0\,, \qquad (3.2.2)$$

where we have used the cyclic property of the trace. Introducing the algebra we find

$$\text{Tr}\left[(-1)^{N_F}\left\{Q^A_\alpha, \bar{Q}^B_{\dot{\beta}}\right\}\right] = 2\sigma^\mu_{\alpha\dot{\beta}}\delta^{AB}\text{Tr}\left[(-1)^{N_F}P_\mu\right]\,. \qquad (3.2.3)$$

That for a non-zero momentum P_μ, together with (3.2.2) implies

$$\text{Tr}\left[(-1)^{N_F}\right] = 0\,, \qquad (3.2.4)$$

proving our statement about the equal number of bosonic and fermionic states in a supermultiplet. After these general considerations we can build the representations. We start with massive one-particle states. Going to the rest frame $P_\mu = (-m, 0, 0, 0)$ we find

$$\begin{aligned}
\left\{Q^A_\alpha, \bar{Q}^B_{\dot{\beta}}\right\} &= 2\delta_{\alpha\dot{\beta}}\delta^{AB} \\
\left\{Q^A_\alpha, Q^B_\beta\right\} &= \left\{\bar{Q}^A_{\dot{\alpha}}, \bar{Q}^B_{\dot{\beta}}\right\} = 0\,,
\end{aligned} \qquad (3.2.5)$$

that after the rescaling

$$\begin{aligned}
a^A_\alpha &= \frac{1}{\sqrt{2m}}Q^A_\alpha\,, \\
\left(a^A_\alpha\right)^\dagger &= \frac{1}{\sqrt{2m}}\bar{Q}^A_{\dot{\alpha}}\,,
\end{aligned} \qquad (3.2.6)$$

$$(3.2.7)$$

is isomorphic to the algebra of $2N$ fermionic creation and annihilation operators, whose representations can be built from a Clifford vacuum Ω defined by $a_\alpha^A \Omega = 0$ and for which $P^\mu P_\mu \Omega = -m^2 \Omega$. The particle states are then constructed applying creation operators

$$|n\rangle = \frac{1}{\sqrt{n!}} \prod_{i=1}^{n} \left(a_{\alpha_i}^{A_i} \right)^\dagger \Omega \,. \tag{3.2.8}$$

In the case $N = 1$, if the vacuum has spin 0, we have the states

$$\Omega \,, \quad (a_\alpha)^\dagger \, \Omega \,, \quad \frac{1}{\sqrt{2}} \, (a_\alpha)^\dagger \, (a_\beta)^\dagger \, \Omega \,. \tag{3.2.9}$$

The first and last have spin-0 and form a complex scalar, while the second one describes a spin-1/2 Majorana fermion. If we had started with a spin-1/2 vacuum the first and last state would correspond to two Majorana fermions, while the intermediate states would have contained a massive spin-1 vector and a real scalar.

In the massless case it is convenient to go to a light-like reference frame $P_\mu = (-E, 0, 0, E)$, obtaining

$$\left\{ Q_\alpha^A, \bar{Q}_{\dot{\beta}}^B \right\} = 2 \begin{pmatrix} 2E & 0 \\ 0 & 0 \end{pmatrix} \delta^{AB}$$
$$\left\{ Q_\alpha^A, Q_\beta^B \right\} = \left\{ \bar{Q}_{\dot{\alpha}}^A, \bar{Q}_{\dot{\beta}}^B \right\} = 0 \,. \tag{3.2.10}$$

The operators Q_2^A and $\bar{Q}_{\dot{2}}^A$ are totally anticommuting and hence must be zero. So rescaling just Q_1 and $\bar{Q}_{\dot{1}}$

$$a^A = \frac{1}{2\sqrt{E}} Q_1^A \,,$$
$$\left(a^A \right)^\dagger = \frac{1}{2\sqrt{E}} \bar{Q}_{\dot{1}}^A \,, \tag{3.2.11}$$

$$\tag{3.2.12}$$

we find a creation and annihilation algebra, consisting of N operators

$$\left\{ a^A, \left(a^B \right)^\dagger \right\} = \delta^{AB} \,,$$
$$\left\{ a^A, a^B \right\} = \left\{ \left(a^A \right)^\dagger, \left(a^B \right)^\dagger \right\} = 0 \,. \tag{3.2.13}$$

These operators raise and lower the helicities of states and starting from the one of lowest helicity Ω_λ, we can construct all other states

$$|\lambda + n/2\rangle = \frac{1}{\sqrt{n!}} \prod_{i=1}^{n} \left(a^{A_i} \right)^\dagger \Omega_\lambda \,. \tag{3.2.14}$$

For $N = 1$ and $\lambda = 0$ we have

$$\Omega_0 \, , \quad a^\dagger \Omega_0 \, , \quad \Omega_{-1/2} \, , \quad a^\dagger \Omega_{-1/2} \, , \tag{3.2.15}$$

a massless Weyl fermion and a complex scalar. Note that the extra states with $\lambda \to -\lambda$ are required by CPT invariance. Starting from $\Omega_{1/2}$ we have a massless Weyl fermion and a massless spin-1 vector

$$\Omega_{1/2} \, , \quad a^\dagger \Omega_{1/2} \, , \quad \Omega_{-1} \, , \quad a^\dagger \Omega_{-1} \, . \tag{3.2.16}$$

This concludes the group-theoretic discussion needed to introduce the phenomenological implications of supersymmetry at the TeV scale. For a more complete, but still elementary, treatment of the supersymmetry algebra and of its representations, in particular $N > 1$, we refer to [64, 65].

3.3   Lagrangians and superpotentials

Now that we have the algebra and its representations we can start building complete theories. The simplest possible example consists of the free Lagrangian of a massless Weyl fermion and of a complex scalar

$$\mathcal{L}_{\mathrm{kin}} = |\partial_\mu \phi|^2 + i \psi^\dagger \bar{\sigma}^\mu \partial_\mu \psi \, , \quad \bar{\sigma}^\mu = \left(-1, \sigma^i \right) \, . \tag{3.3.1}$$

Under an infinitesimal supersymmetric transformation we have

$$\begin{aligned}
\phi &\to \phi + \delta\phi \, , \quad \delta\phi = \epsilon_\alpha \psi^\alpha \, , \\
\psi &\to \psi + \delta\psi \, , \quad \delta\psi_\alpha = -i(\sigma^\mu \epsilon^\dagger)_\alpha \partial_\mu \phi \, .
\end{aligned} \tag{3.3.2}$$

Here ϵ is a spinor with index α, which parametrizes supersymmetric transformations. From the first line above it must have spin $1/2$ and mass dimension $-1/2$. The choice for $\delta\phi$ is the simplest possible and can be verified to respect the algebra. The transformation of ψ is the only expression linear in $\epsilon^\dagger$ and ϕ consistent with dimensional arguments.

The Lagrangian above is invariant under this supersymmetry transformation, going to itself plus a total derivative. However the algebra closes only on-shell as can be seen by applying a commutator of two transformations to the fermion field[1]

$$\begin{aligned}
\left[\delta_{\epsilon_1}, \delta_{\epsilon_2} \right] \psi_\alpha &= -i \left(\epsilon_1 \sigma^\mu \epsilon_2^\dagger - \epsilon_2 \sigma^\mu \epsilon_1^\dagger \right) \partial_\mu \psi_\alpha + \\
&+ i \left(\epsilon_{1\alpha} \epsilon_2^\dagger \bar{\sigma}^\mu \partial_\mu \psi - \epsilon_{2\alpha} \epsilon_1^\dagger \bar{\sigma}^\mu \partial_\mu \psi \right) \, .
\end{aligned} \tag{3.3.4}$$

---

[1]We have left implicit the contraction of spinor indexes: $\epsilon\psi \equiv \epsilon^\alpha \boldsymbol{\epsilon}_{\alpha\beta} \psi^\beta$ with

$$\boldsymbol{\epsilon}_{\alpha\beta} = \begin{pmatrix} 0 & -1 \\ 1 & 0 \end{pmatrix} \, . \tag{3.3.3}$$

The last term of the above equation is zero on the solutions of the equation of motion, but off-shell it does not vanish. This can be equivalently stated as the reduction of the fermion degrees of freedom from four to two by the equation of motion, that in the frame $p_\mu = (p, 0, 0, p)$,

$$\bar{\sigma}^\mu p_\mu \psi = \begin{pmatrix} 0 & 0 \\ 0 & 2p \end{pmatrix} \begin{pmatrix} \psi_1 \\ \psi_2 \end{pmatrix}, \tag{3.3.5}$$

projects out two components of the spinor. We can make SUSY invariance manifest by adding an auxiliary spin-0 field F and the additional Lagrangian term

$$\mathcal{L}_F = FF^*. \tag{3.3.6}$$

F on-shell is, in general, just a function of the other fields, but if we give it the transformation properties

$$\delta F = -i\epsilon^\dagger \bar{\sigma}^\mu \partial_\mu \psi, \quad \delta F^* = i\partial_\mu \psi^\dagger \bar{\sigma}^\mu \epsilon \tag{3.3.7}$$

and change the fermion transformation to

$$\delta \psi_\alpha = -i(\sigma^\mu \epsilon^\dagger)_\alpha \partial_\mu \phi + \epsilon_\alpha F, \tag{3.3.8}$$

it closes the algebra off-shell

$$\begin{aligned} X &= \phi,\, \phi^*,\, \psi,\, \psi^\dagger,\, F,\, F^*, \\ [\delta_{\epsilon_1}, \delta_{\epsilon_2}] X &= -i\left(\epsilon_1 \sigma^\mu \epsilon_2^\dagger - \epsilon_2 \sigma^\mu \epsilon_1^\dagger\right) \partial_\mu X. \end{aligned} \tag{3.3.9}$$

The new Lagrangian $\mathcal{L}_{\text{kin}} + \mathcal{L}_F$ is invariant under SUSY transformations. The introduction of F, that from the equations above has mass dimension 2, is not only an useful trick for the free supersymmetric Lagrangian, but also helps in the construction of interacting models. If we introduce additional generations of supermultiplets, labelled by latin indexes, we can write the most general interaction Lagrangian in the form

$$\mathcal{L}_{\text{int}} = -\frac{1}{2} W^{jk}(\phi, \phi^*)\, \psi_j \psi_k + W^j(\phi, \phi^*)\, F_j + \text{h.c.}, \tag{3.3.10}$$

where, if we require renormalizability, W^{jk} is linear in (ϕ, ϕ^*) and W^j quadratic at most. We have omitted a term containing only ϕ and ϕ^*, because it would have a variation linear in ψ and $\psi^\dagger$ with no F's or derivatives and thus it could not be cancelled by the variation of $\mathcal{L}_{\text{int}}$.

Clearly the W functions can not be arbitrary. To see the consequences of SUSY invariance we can first consider the variation of $\mathcal{L}_{\text{int}}$ with four spinors

$$\delta \mathcal{L}_{\text{int}}^4 = -\frac{1}{2} \frac{\partial W^{jk}}{\partial \phi_n}\, (\epsilon \psi_n)\, \psi_j \psi_k - \frac{1}{2} \frac{\partial W^{jk}}{\partial \phi_n^*}\, \left(\epsilon^\dagger \psi_n^\dagger\right) \psi_j \psi_k. \tag{3.3.11}$$

The first term vanishes if and only if $\partial W^{jk}/\partial \phi_n$ is totally symmetric in the three indexes, since Fierz identities imply

$$(\epsilon \psi_n)\, \psi_j \psi_k + (\epsilon \psi_j)\, \psi_k \psi_n + (\epsilon \psi_k)\, \psi_n \psi_j = 0. \tag{3.3.12}$$

The second term cancels only if $\partial W^{jk}/\partial\phi_n^*$ vanishes, so W^{ij} must be holomorphic. Before going to the next part of the Lagrangian variation we find convenient to rewrite W^{jk} as

$$W^{jk} = \frac{\partial^2}{\partial\phi_j\partial\phi_k}W\,,\tag{3.3.13}$$

where, for renormalizable interactions,

$$W = \frac{1}{2}M^{jk}\phi_j\phi_k + \frac{1}{6}y^{jkn}\phi_j\phi_k\phi_n\,.\tag{3.3.14}$$

Note that we have omitted the linear term $E^i\phi_i$ to avoid a non-zero vacuum energy and the spontaneous breaking of SUSY. If $H|0\rangle \neq 0$, in fact, supersymmetry is broken (i.e. $Q_\alpha|0\rangle \neq 0$ for some α). This descends from the anticommutation relations in equation (3.2.1) that for $N = 1$, imply

$$H = P^0 = \frac{1}{4}\sum_{i=1}^{2}\left(Q_iQ_i^\dagger + Q_i^\dagger Q_i\right)\,.\tag{3.3.15}$$

We can now turn to the part of the Lagrangian variation containing derivatives

$$
\begin{aligned}
\delta\mathcal{L}_{\text{int}}^\partial &= -iW^{jk}\partial_\mu\phi_k\psi_j\sigma^\mu\epsilon^\dagger - iW^j\partial_\mu\psi_j\sigma^\mu\epsilon^\dagger + \text{h.c.} = \\
&= -i\partial_\mu\left(\frac{\partial W}{\partial\phi_j}\right)\psi_j\sigma^\mu\epsilon^\dagger - iW^j\partial_\mu\psi_j\sigma^\mu\epsilon^\dagger + \text{h.c.}\,.
\end{aligned}
\tag{3.3.16}
$$

If we want $\delta\mathcal{L}_{\text{int}}^\partial$ to be a total derivative we obtain

$$W^j = \frac{\partial W}{\partial\phi_j}\,,\tag{3.3.17}$$

that makes manifest the reason of the definition in equation (3.3.13). The remaining pieces of $\delta\mathcal{L}_{\text{int}}$ are linear in F, F^* and vanish if the conditions above are satisfied.

We have found that all renormalizable non-gauge supersymmetric interactions can be written in terms of W, a single holomorphic function of the scalar fields, known as the *superpotential*. Later in this section we comment on non-renormalizable interactions, after briefly introducing the superfield formalism. For the time being we simply give the expression of $\mathcal{L}_{\text{int}}$ by solving the Gaussian path integral for F, F^* (their action is quadratic)

$$F_j = -W_j^*,\quad F_j^* = -W_j\,,\tag{3.3.18}$$

which gives

$$\mathcal{L}_{\text{int}} = -\frac{1}{2}W^{jk}\left(\phi,\phi^*\right)\psi_j\psi_k + \text{h.c.} + V\left(\phi,\phi^*\right)\,,\quad V\left(\phi,\phi^*\right) = W^jW_j^* = F^jF_j^*\,.\tag{3.3.19}$$

3.3.1   Supersymmetric gauge theories

As we have seen while discussing SUSY representations, a gauge boson A_μ^a is accompanied by a fermion λ^a in the multiplet. In a theory where SUSY is unbroken the two must fall in the same representation of the gauge group. So λ^a is also in the adjoint representation of the gauge symmetry. Therefore for a group G with structure constants f^{abc} we have

$$
\begin{aligned}
\delta_G \lambda^a &= g f^{abc} \lambda^b \alpha^c \,, \\
D_\mu \lambda^a &= \partial_\mu \lambda^a - g f^{abc} A_\mu^b \lambda^c \,,
\end{aligned}
\tag{3.3.20}
$$

where α^c parametrizes the gauge transformations and g is the coupling constant of the gauge theory. Again the fermion equation of motion projects out two degrees of freedom, but off-shell we have four degrees of freedom from $\lambda^a, \lambda^{a\dagger}$ and only three in A_μ^a. So we perform the same addition as in the previous section introducing the auxiliary field D^a and writing the gauge Lagrangian as

$$
\mathcal{L}_{\mathrm{G}} = -\frac{1}{4} F_{\mu\nu}^a F^{\mu\nu a} + i \lambda^{a\dagger} \bar{\sigma}_\mu D^\mu \lambda^a + \frac{1}{2} D^a D^a \,,
\tag{3.3.21}
$$

where $F_{\mu\nu}^a$ are the usual field strengths, introduced in the first chapter. For completeness we list the SUSY transformations of all the fields

$$
\begin{aligned}
\delta A_\mu^a &= -\frac{1}{\sqrt{2}} \left[\epsilon^\dagger \bar{\sigma}_\mu \lambda^a a + \lambda^{a\dagger} \bar{\sigma}_\mu \epsilon \right] \,, \\
\delta \lambda_\alpha^a &= -\frac{i}{2\sqrt{2}} (\sigma^\mu \bar{\sigma}^\nu \epsilon)_\alpha F_{\mu\nu}^a + -\frac{1}{\sqrt{2}} \epsilon_\alpha D^a \,, \\
\delta D^a &= -\frac{i}{\sqrt{2}} \left[\epsilon^\dagger \bar{\sigma}^\mu D_\mu \lambda^a - D_\mu \lambda^{a\dagger} \bar{\sigma}^\mu \epsilon \right] \,,
\end{aligned}
\tag{3.3.22}
$$

more details on their derivation can be found in [64, 65]. To complete the gauge theory we must introduce the interactions between the gauge fields and the matter fields. Clearly we have the usual

$$
D_\mu \Phi = \partial_\mu \Phi + i g A_\mu^a T^a \Phi \,, \quad \Phi = (\phi, \psi) \,,
\tag{3.3.23}
$$

entering the kinetic terms, where T^a are the group generators in the representation of the matter fields. In addition to that, the enlarged field content allows the terms

$$
\phi^* T^a \psi \lambda^a \,, \quad \lambda^{a\dagger} \psi^\dagger T^a \phi \,, \quad \phi^* T^a \phi D^a \,.
\tag{3.3.24}
$$

These interactions are needed to insure gauge and SUSY invariance that fix their coefficients (and the full Lagrangian) to be

$$
\begin{aligned}
\mathcal{L} &= |D_\mu \phi|^2 + i \psi^\dagger \bar{\sigma}_\mu D^\mu \psi + \mathcal{L}_G + \mathcal{L}_{\mathrm{int}} - \\
&- \sqrt{2} g \left(\phi^* T^a \psi \lambda^a + \lambda^{a\dagger} \psi^\dagger T^a \phi \right) + g \phi^* T^a \phi D^a \,,
\end{aligned}
\tag{3.3.25}
$$

where $\mathcal{L}_{G(\text{int})}$ are defined in equations (3.3.21) and (3.3.19), respectively and $\mathcal{L}_{\text{int}}$ must be generated by a gauge invariant superpotential. The SUSY transformations of the fields seen above are easily generalized by replacing derivatives with covariant derivatives. The scalar potential can be simplified by using the equations of motion for F, in equation (3.3.18), and those for D^a

$$D^a = -g\phi^* T^a \phi \,, \tag{3.3.26}$$

that give for the scalar potential

$$V(\phi, \phi^*) = F_i^* F^i + \frac{1}{2} D^a D^a = W_i^* W^i + \frac{g^2}{2} \left(\phi^* T^a \phi\right)^2 \,. \tag{3.3.27}$$

If we want the vacuum to preserve SUSY we need $\langle V \rangle = 0$ (where $\langle \cdot \rangle$ represents the vacuum expectation value) and therefore $\langle F_i \rangle = \langle D^a \rangle = 0$.

3.3.2   Soft supersymmetry breaking

We have seen how to construct theories invariant under SUSY transformations, but any realistic model incorporating supersymmetry must break it, for the simple reason that we have not observed any partners of the SM fields. Nonetheless if we want to retain the cancellation of quadratic divergences that lead us to introduce the supersymmetry algebra, the breaking must be soft. Meaning that it must proceed only through operators with coefficients of positive mass dimension. If we included dimensionless SUSY-breaking couplings we would reintroduce into the theory quadratic divergences of the form

$$\delta m_h^2 = -\frac{|y_f|^2 - y_\phi^2}{8\pi^2} \Lambda^2 + ... \,, \tag{3.3.28}$$

while soft breaking terms associated to a mass scale m_{soft} would give correction that must vanish in the limit $m_{\text{soft}} \to 0$ and therefore cause at most logarithmic divergences

$$\delta m_h^2 \propto m_{\text{soft}}^2 \left[\log \frac{\Lambda}{m_{\text{soft}}} + ...\right] \,. \tag{3.3.29}$$

The presence of these logarithmic divergences is the reason why we expect at least top partners, that give the largest contribution to δm_h^2, $\sim y_t^2$, to have masses close to the Fermi scale.

Many explicit models that generate supersymmetry breaking terms dynamically have been proposed[2]. Here we do not focus on the dynamics generating SUSY breaking, but rather adopt a low energy perspective and write the general soft supersymmetry breaking Lagrangian

$$\begin{aligned}\mathcal{L}_{\text{soft}} &= -\left(\frac{1}{2} M_a \lambda^a \lambda^a + \frac{1}{6} a^{ijk} \phi_i \phi_j \phi_k + \frac{1}{2} b^{ij} \phi_i \phi_j + \text{h.c.}\right) - \\ &- m_{ij}^2 \phi_i^* \phi_j \,,\end{aligned} \tag{3.3.30}$$

---

[2]See [66] for a review and a detailed bibliography.

where all the gauginos corresponding to the same group have the same mass M_a and a runs over the different gauge groups. It has been proved that a supersymmetric theory with the breaking terms in (3.3.30) is free of quadratic divergences to all orders in perturbation theory [67]. We have omitted *tadpole* terms $t_i \phi_i$ and trilinear terms in the form $\phi^2 \phi^*$ or $\phi^{*2} \phi$ that can produce quadratically divergent graphs. Furthermore these terms can be generated only if a gauge singlet is present in the theory.

In theories with chiral supermultiplets in the adjoint representation of one of the gauge groups we can write also a supersymmetry breaking Dirac mass term for the gauginos

$$\mathcal{L}_{\text{soft}} \supset -M_D \lambda \psi + \text{h.c.}. \tag{3.3.31}$$

We report this possibility for completeness, but these terms do not enter the extensions of the SM treated in this work.

We conclude with the obvious remark that supersymmetry breaking terms are constrained by gauge invariance. Therefore the a^{ijk} and b^{ij} terms have the same restrictions as the y^{ijk} and M^{ij} operators in the superpotential. On the contrary gaugino masses M_a and scalar masses m_{ii}^2 are always allowed by gauge invariance.

3.3.3 Superfields

With the previous section we have exhausted the discussion of the basic ingredients needed to construct a phenomenologically viable supersymmetric model. Before introducing the minimal extension of the SM that includes supersymmetry we rederive some of the previous results using superfield methods.

The superspace notation was introduced for the first time in [68], it is an extremely useful tool that allowed to prove several theorems perturbatively and in general is convenient to deal with loop calculations and SUSY breaking. We start with two Grassmanian anticommuting spinors $\theta_\alpha, \bar\theta_{\dot\alpha}$

$$\left\{ \theta_\alpha, \bar\theta_{\dot\alpha} \right\} = 0 \tag{3.3.32}$$

and introduce the notation

$$\begin{aligned}
d^2\theta &\equiv -\frac{1}{4} d\theta^\alpha d\theta^\beta \boldsymbol{\epsilon}_{\alpha\beta}\,, \\
d^2\bar\theta &\equiv -\frac{1}{4} d\bar\theta_{\dot\alpha} d\bar\theta_{\dot\beta} \boldsymbol{\epsilon}^{\dot\alpha\dot\beta} \\
d^4\theta &\equiv d^2\theta d^2\bar\theta\,.
\end{aligned} \tag{3.3.33}$$

Then we can define the superspace coordinate $y^\mu = x^\mu - i\theta\sigma^\mu\bar\theta$ and organize the supermultiplets into superfields

$$\begin{aligned}
\boldsymbol{\Phi}(y) &\equiv \phi(y) + \sqrt{2}\theta\psi(y) + \theta^2 F\,, \\
V^a(y) &\equiv \theta\bar\sigma^\mu\bar\theta A_\mu^a(y) + i\theta^2\bar\theta\lambda^{a\dagger}(y) - i\theta\bar\theta^2\lambda^a(y) + \frac{1}{2}\theta^2\bar\theta^2 D^a(y)\,.
\end{aligned} \tag{3.3.34}$$

$\mathbf{\Phi}$ is often referred to as a chiral superfield and V^a as a vector or real superfield. The reason is that they can be defined as the superfields that satisfy the constraints

$$
\begin{aligned}
\frac{\partial}{\partial \theta_\alpha} \mathbf{\Phi}^\dagger &= 0 \,, \\
V^\dagger &= V \,.
\end{aligned}
\tag{3.3.35}
$$

It is worth to notice that the expression for the real superfield V^a is valid only in the Wess-Zumino gauge, for its general form we refer to [64].

The Lagrangians discussed in the previous section can be expressed in a compact form as a integrals over the Grassman spinors. Keeping in mind the usual integration rules for anticommuting variables, that in our case give, for example

$$
\int d^2\theta\, \theta^2 = 1 \,,
\tag{3.3.36}
$$

we obtain

$$
\begin{aligned}
\int d^4\theta\, \mathbf{\Phi}^\dagger \mathbf{\Phi} &= \mathcal{L}_{\text{kin}} + \mathcal{L}_F \,, \\
\int d^2\theta\, W\left(\mathbf{\Phi}\right) + \text{h.c.} &= \int d^2\theta\, \theta^2 W_2 + \text{h.c.} = \mathcal{L}_{\text{int}} \,, \\
W\left(\mathbf{\Phi}\right) &= W_0 + \theta W_1 + \theta^2 W_2 \,.
\end{aligned}
\tag{3.3.37}
$$

In the last two lines we have used the superpotential W formally written as a function of superfields and expanded it in the Grassman variable θ. For the gauge invariant kinetic terms of matter fields we have

$$
\int d^4\theta\, \mathbf{\Phi}^\dagger e^{g T^a V^a} \mathbf{\Phi} \,,
\tag{3.3.38}
$$

while we refer to [64, 65] for the complete gauge Lagrangian. Finally we note that, to allow the most general non-renormalizable SUSY interactions we can write an action of the form

$$
\int d^4 x\, d^4\theta\, K\left(\mathbf{\Phi}^\dagger, \mathbf{\Phi}\right) \,.
\tag{3.3.39}
$$

The function K is known as the Kähler potential.

3.4   The minimal supersymmetric standard model

As the name suggests the Minimal Supersymmetric Standard Model (MSSM) has the minimal particle content imposed by supersymmetry and experiment, with the notable exception of an

extra Higgs doublet. The relevant degrees of freedom are listed in table 3.1 and the naming convention can be summarized as follows

$$\text{quark} \Leftrightarrow \text{squark}: \quad \text{top} \leftrightarrow \text{stop, bottom} \leftrightarrow \text{sbottom, ...},$$
$$\text{gauge boson} \Leftrightarrow \text{gaugino}: \quad \text{gluon} \leftrightarrow \text{gluino, W} \leftrightarrow \text{wino, ...},$$
$$\text{Higgs boson} \Leftrightarrow \text{higgsino},$$
$$\text{lepton} \Leftrightarrow \text{slepton},$$
$$\text{fermion} \Leftrightarrow \text{sfermion}.$$

Table 3.1: MSSM field content. $\boldsymbol{Ad}$ indicates the adjoint representation of the gauge group.

	bosons	fermions	$SU(3)_C$	$SU(2)_L$	$U(1)_Y$
Q_i	$(\widetilde{u}_L, \widetilde{d}_L)_i$	$(u_L, d_L)_i$	$\boldsymbol{3}$	$\boldsymbol{2}$	$\frac{1}{6}$
u_i^c	$\widetilde{u}_{Ri}^*$	$\bar{u}_{Ri}$	$\bar{\boldsymbol{3}}$	$\boldsymbol{1}$	$-\frac{2}{3}$
d_i^c	$\widetilde{d}_{Ri}^*$	$\bar{d}_{Ri}$	$\bar{\boldsymbol{3}}$	$\boldsymbol{1}$	$\frac{1}{3}$
L_i	$\left(\widetilde{\nu}, \widetilde{l}_L\right)_i$	$(\nu, l_L)_i$	$\boldsymbol{1}$	$\boldsymbol{2}$	$\frac{1}{2}$
e_i^c	$\widetilde{e}_{Ri}^*$	$\bar{e}_{Ri}$	$\boldsymbol{1}$	$\boldsymbol{1}$	1
H_u	$\left(\widetilde{H}_u^+, \widetilde{H}_u^0\right)$	(H_u^+, H_u^0)	$\boldsymbol{1}$	$\boldsymbol{2}$	$\frac{1}{2}$
H_d	$\left(\widetilde{H}_d^0, \widetilde{H}_d^-\right)$	$\left(H_d^0, H_d^-\right)$	$\boldsymbol{1}$	$\boldsymbol{2}$	$-\frac{1}{2}$
G	G_μ^a	$\widetilde{G}^a$	$\boldsymbol{Ad}$	$\boldsymbol{1}$	0
W	$W_\mu^3, W_\mu^\pm$	$\widetilde{W}^3, , \widetilde{W}^\pm$	$\boldsymbol{1}$	$\boldsymbol{Ad}$	0
B	B_μ	$\widetilde{B}$	$\boldsymbol{1}$	$\boldsymbol{1}$	0

For each SM fermion we have a chiral supermultiplet containing a scalar partner. SM gauge bosons fall into vector supermultiplets with the corresponding gauginos. The two Higgs doublet form a chiral supermultiplet together with higgsinos. The introduction of a second Higgs is needed to write down-type Yukawa couplings in the superpotential, that would be forbidden by holomorphy if we had only one hypercharge 1/2 doublet. Its presence also avoids the $U(1)_Y^3$ and $U(1)_Y \times SU(2)_L^2$ gauge anomalies and the $SU(2)_L$ Witten anomaly, by making the number of fermion doublets even.

We can now write the MSSM superpotential

$$W_{\text{MSSM}} = QH_u Y_u u^c - QH_d Y_d d^c - LH_d Y_e e^c + \mu H_u H_d , \tag{3.4.1}$$

where flavor indexes have been left implicit. These terms generate the usual Yukawa interactions, cubic terms for scalars

$$\mathcal{L}_{\text{cubic}} = \mu^* (\widetilde{u_R^*} Y_u \widetilde{u}_L H_d^{0*} + \widetilde{d_R^*} Y_d \widetilde{d}_L H_u^{0*} + \widetilde{e_R^*} Y_e \widetilde{e}_L H_u^{0*}$$

$$+\widetilde{u_R^*}Y_u\widetilde{d}_L H_d^{-*} + \widetilde{d_R^*}Y_d\widetilde{u}_L H_u^{+*} + \widetilde{e_R^*}Y_e\widetilde{\nu}_L H_u^{+*}) + \text{h.c.} \tag{3.4.2}$$

and masses for higgses and higgsinos

$$-\mathcal{L}_{\widetilde{h}\text{m}} = \mu(\widetilde{H}_u^+\widetilde{H}_d^- - \widetilde{H}_u^0\widetilde{H}_d^0) + \text{h.c.}\,, \tag{3.4.3}$$

$$-\mathcal{L}_{h\text{m}} = |\mu|^2\big(|H_u^0|^2 + |H_u^+|^2 + |H_d^0|^2 + |H_d^-|^2\big). \tag{3.4.4}$$

Also quartic terms for scalars are generated in the form $\left(\widetilde{Q}_L Y_u \widetilde{u}_R^*\right)\left(\widetilde{Q}_L^* Y_u^\dagger \widetilde{u}_R\right)$, but here we do not list them explicitly for brevity.

These are not the most general interactions we can write given the field content and the symmetries. We have purposefully omitted the following lepton and baryon number violating parts of the superpotential

$$W_{\Delta\text{L}=1} = \frac{1}{2}\alpha^{ijk} L_i L_j \bar{e}_k + \beta^{ijk} L_i Q_j \bar{d}_k + \gamma^i L_i H_u\,, \tag{3.4.5}$$

$$W_{\Delta\text{B}=1} = \frac{1}{2}\delta^{ijk} \bar{u}_i \bar{d}_j \bar{d}_k\,, \tag{3.4.6}$$

where family indices $i = 1, 2, 3$ have been restored. These superpotentials can generate squark mediated proton decay with a lifetime given approximately by

$$\Gamma_p \approx \frac{|\beta\delta|^2}{m_{\widetilde{q}}^4}\frac{m_p^5}{8\pi}\,,$$

$$\tau_p = \frac{1}{\Gamma} \approx 2 \times 10^{-11}\frac{1}{|\beta\delta|^2}\left(\frac{m_{\widetilde{q}}}{1\ \text{TeV}}\right)^4\ \text{s}\,. \tag{3.4.7}$$

The current bound of 10^{32} years on the proton lifetime would impose $|\beta\delta| < 10^{-25}$. Even if we did not have baryon and lepton number violating interactions at the same time we would still have strong constrains on these couplings from $\Delta B = 2$ processes, $n - \bar{n}$ oscillations and dinucleon decays (see [69] for a comprehensive review).

Rather than fine-tuning the coefficients above we can impose a symmetry that forbids them. We can use the discrete subgroup of $B - L$ known as matter parity

$$P_M = (-1)^{3(B-L)} \tag{3.4.8}$$

or, equivalently, R-parity

$$R = (-1)^{3(B-L)+2s}\,, \tag{3.4.9}$$

where s is the particle spin. The latter choice has the interesting property of acting in the following way on MSSM fields

$$\text{SM} \rightarrow \text{SM}\,,$$
$$\text{SM partner} \rightarrow -(\text{SM partner})\,.$$

This implies that the lightest superpartner (LSP) is stable and can be a potential dark matter candidate. It also implies that superpartners are produced in pairs at colliders and decay to an odd number of LSPs. From now on we include R-parity in the definition of the MSSM, phenomenologically viable alternatives are discussed at the end of this chapter.

To complete the MSSM we need to introduce SUSY breaking. As anticipated in section 3.3.2 we include only soft supersymmetry breaking interactions

$$
\begin{aligned}
\mathcal{L}_{\text{soft}}^{\text{MSSM}} \;=\; & -\frac{1}{2}\left(M_3 \widetilde{g}\widetilde{g} + M_2 \widetilde{W}\widetilde{W} + M_1 \widetilde{B}\widetilde{B} + \text{h.c.}\right) \\
& -\left(\widetilde{\widetilde{u}}\,\mathbf{A_u}\,\widetilde{Q}H_u - \widetilde{\widetilde{d}}\,\mathbf{A_d}\,\widetilde{Q}H_d - \widetilde{\widetilde{e}}\,\mathbf{A_e}\,\widetilde{L}H_d + \text{h.c.}\right) \\
& -\widetilde{Q}^\dagger\,\mathbf{m_Q^2}\,\widetilde{Q} - \widetilde{L}^\dagger\,\mathbf{m_L^2}\,\widetilde{L} - \widetilde{u_R^*}\,\mathbf{m_{\widetilde{u}}^2}\,\widetilde{u_R^*}^\dagger - \widetilde{d_R^*}\,\mathbf{m_{\widetilde{d}}^2}\,\widetilde{d_R^*}^\dagger - \widetilde{e_R^*}\,\mathbf{m_{\widetilde{e}}^2}\,\widetilde{e_R^*}^\dagger \\
& - m_{H_u}^2 H_u^* H_u - m_{H_d}^2 H_d^* H_d - (bH_uH_d + \text{h.c.})\,.
\end{aligned}
\tag{3.4.10}
$$

We further need to assume that the squark and slepton masses squared are positive and large enough to ensure that their vevs are zero. Color, charge, baryon or lepton number breaking minima could be generated otherwise. Similarly we can find upper bounds on the trilinear couplings A. With this move we have added 105 more parameters to the SM, thus reducing considerably the possibility of unambiguous predictions in the MSSM. However the structure of many of the SUSY breaking terms is strongly constrained by precision measurements that, for instance, severely reduce the possible flavor structures of the A-terms and of the squarks and sleptons soft masses. We elaborate more on this point in section 3.4.2.

3.4.1   Electroweak symmetry breaking

To study electroweak symmetry breaking in the MSSM we need the full Higgs potential. So we add to the $|\mu|^2$ and breaking terms, shown above, also the gauge D-terms contribution, obtaining

$$
\begin{aligned}
V \;=\; & (|\mu|^2 + m_{H_u}^2)(|H_u^0|^2 + |H_u^+|^2) + (|\mu|^2 + m_{H_d}^2)(|H_d^0|^2 + |H_d^-|^2) + \\
& + [b\,(H_u^+ H_d^- - H_u^0 H_d^0) + \text{h.c.}] + \frac{1}{2}g^2|H_u^+ H_d^{0*} + H_u^0 H_d^{-*}|^2 + \\
& + \frac{1}{8}(g^2 + g'^2)(|H_u^0|^2 + |H_u^+|^2 - |H_d^0|^2 - |H_d^-|^2)^2\,.
\end{aligned}
\tag{3.4.11}
$$

First we have to check for the presence of charge breaking minima. If we fix $\langle H_u^+ \rangle = 0$ by an $SU(2)_L$ gauge transformation, we obtain

$$
\frac{\partial V}{\partial H_u^+} = bH_d^- + \frac{g^2}{2}H_d^{0*} H_d^- H_u^{0*}\,,
\tag{3.4.12}
$$

that vanishes only for $\langle H_d^- \rangle = 0$. So we can automatically select the correct vacuum by focussing on the neutral components of the two doublets. After setting $H_u^+ = H_d^- = 0$ it is easy to check that

the MSSM does not break spontaneously CP. At the minimum $\phi_{H_d^0} = -\phi_{H_u^0}$ (for real couplings in the potential), so the two phases can be set to zero by the same $U(1)_Y$ transformation.

After these preliminary considerations we can start to constrain Lagrangian parameters to obtain a phenomenologically viable electroweak symmetry breaking sector. For the potential not to be stable at the origin of the (H_u^0, H_d^0) plane, we require the matrix of second derivatives to have a negative eigenvalue there. This implies

$$b^2 > \left(|\mu|^2 + m_{H_u}^2\right)\left(|\mu|^2 + m_{H_d}^2\right) . \tag{3.4.13}$$

We have also an upper bound on b, coming from the flat direction in the quartic potential. For $H_u^0 = H_d^0$ the D-term potential vanishes and we have to impose

$$2b < 2|\mu|^2 + m_{H_u}^2 + m_{H_d}^2 . \tag{3.4.14}$$

These two conditions leave open only a rather narrow corridor in parameter space where $\mu \sim m_{\text{soft}}$. However a priori there is no good reason for μ to be roughly equal in magnitude to the soft breaking parameters b and $m_{H_{u,d}}$. This is known as the μ problem, typical solutions assume μ to vanish at tree-level and be generated as a consequence of SUSY-breaking [70, 71, 72, 73].

Assuming that the two conditions above are fulfilled we can introduce the vevs

$$\frac{\langle H_u^0 \rangle}{\sqrt{2}} = v_u , \quad \frac{\langle H_d^0 \rangle}{\sqrt{2}} = v_d , \quad v^2 = v_u^2 + v_d^2 = (246 \text{ GeV})^2 \tag{3.4.15}$$

and the parameter $\tan\beta$

$$\tan\beta \equiv \frac{v_u}{v_d} \tag{3.4.16}$$

that simplifies the expressions for the mass spectrum. Before discussing the mass matrices we need to impose the two minimum conditions $\partial V/\partial H_u^0 = \partial V/\partial H_d^0 = 0$ that are equivalent to

$$
\begin{aligned}
|\mu|^2 + m_{H_u}^2 &= b\cot\beta + \frac{m_Z^2 \cos 2\beta}{2} , \\
|\mu|^2 + m_{H_d}^2 &= b\tan\beta - \frac{m_Z^2 \cos 2\beta}{2} .
\end{aligned}
\tag{3.4.17}
$$

For simplicity we assume the absence of CP violation[3] and therefore we can divide the mass matrix in a CP-odd and a CP-even sector. There are two CP-odd states, one of which becomes the longitudinal polarization of the Z. Their mass matrix reads

$$\left(\text{Im}H_u^0, \ \text{Im}H_d^0\right)\begin{pmatrix} b\cot\beta & b \\ b & b\tan\beta \end{pmatrix}\begin{pmatrix} \text{Im}H_u^0 \\ \text{Im}H_d^0 \end{pmatrix} \tag{3.4.18}$$

---

[3]CP violating phases are severely constrained by measurements of the dipole moments of atoms [74, 75], molecules [76] and the neutron [77, 78]. That restrict them to be $\mathcal{O}\left(10^{-2} - 10^{-3}\right)$ over most of the MSSM parameter space [79, 80, 81].

and can be diagonalized with the rotation

$$\begin{pmatrix} \pi^0 \\ A^0 \end{pmatrix} = \sqrt{2} \begin{pmatrix} s_\beta & -c_\beta \\ c_\beta & s_\beta \end{pmatrix} \begin{pmatrix} \mathrm{Im}H_u^0 \\ \mathrm{Im}H_d^0 \end{pmatrix} , \qquad (3.4.19)$$

giving

$$\begin{aligned} m_{\pi^0} &= 0 \, , \\ m_A^2 &= \frac{2b}{s_{2\beta}} \, . \end{aligned} \qquad (3.4.20)$$

In the CP-even sector we have

$$\left(\mathrm{Re}H_u^0, \, \mathrm{Re}H_d^0\right) \begin{pmatrix} m_A^2 \sin^2\beta + m_Z^2 s_\beta^2 & -(m_A^2 + m_Z^2)c_\beta s_\beta \\ -(m_A^2 + m_Z^2)c_\beta s_\beta & m_A^2 \cos^2\beta + m_Z^2 c_\beta^2 \end{pmatrix} \begin{pmatrix} \mathrm{Re}H_u^0 \\ \mathrm{Re}H_d^0 \end{pmatrix} , \qquad (3.4.21)$$

that gives the mass eigenstates

$$\begin{pmatrix} h^0 \\ H^0 \end{pmatrix} = \sqrt{2} \begin{pmatrix} c_\alpha & -s_\alpha \\ s_\alpha & c_\alpha \end{pmatrix} \begin{pmatrix} \mathrm{Re}H_u^0 \\ \mathrm{Re}H_d^0 \end{pmatrix} , \qquad (3.4.22)$$

with eigenvalues

$$m_{h^0,H^0}^2 = \frac{1}{2}\left(m_A^2 + m_Z^2 \mp \sqrt{(m_A^2 - m_Z^2)^2 + 4m_Z^2 m_A^2 \sin^2(2\beta)}\right) . \qquad (3.4.23)$$

For $m_A \to \infty$, m_h reaches its maximum. Thus we obtain the tree-level upper bound

$$m_h^2 < m_Z^2 \cos^2 2\beta \, , \qquad (3.4.24)$$

in contradiction with LEP and LHC searches. Nonetheless there are large loop corrections, in particular from stops, that can solve the problem. We discuss them in chapter 7.

It is also appropriate to notice that in general $\alpha \neq \beta$

$$\frac{\tan 2\alpha}{\tan 2\beta} = \frac{m_A^2 + m_Z^2}{m_A^2 - m_Z^2} \, . \qquad (3.4.25)$$

This misalignment between the mass eigenstates and the vevs shifts the couplings of the lightest CP-even neutral Higgs to the SM particles with respect to the SM Higgs couplings. We recover an approximately SM light Higgs only in the decoupling limit

$$\alpha \to \beta - \pi/2 \, . \qquad (3.4.26)$$

Turning to the charged components we find

$$\left(H_u^{+*}, \, H_d^-\right) \begin{pmatrix} b\cot\beta + m_W^2 c_\beta^2 & b + m_W^2 c_\beta s_\beta \\ b + m_W^2 c_\beta s_\beta & b\tan\beta + m_W^2 s_\beta^2 \end{pmatrix} \begin{pmatrix} H_u^+ \\ H_d^{-*} \end{pmatrix} . \qquad (3.4.27)$$

Here we have the W longitudinal polarization π^+ plus one additional massive state

$$\begin{pmatrix} \pi^+ \\ H^+ \end{pmatrix} = \begin{pmatrix} s_\beta & -c_\beta \\ c_\beta & s_\beta \end{pmatrix} \begin{pmatrix} H_u^+ \\ H_d^{-*} \end{pmatrix}, \tag{3.4.28}$$

with eigenvalue

$$m_{H^\pm}^2 = m_A^2 + m_W^2. \tag{3.4.29}$$

We have now completed the introductory discussion of the MSSM Higgs sector and we can turn to the mass spectra of sfermions and partners of the EW gauge bosons (ewkinos).

3.4.2　Sfermions mass spectrum

We start for simplicity by assuming that there is no mixing between different generation of squarks and leptons. In this case we can use the stops as a prototype

$$- \begin{pmatrix} \widetilde{t}_L^* & \widetilde{t}_R^* \end{pmatrix} \mathcal{M}_{\widetilde{t}}^2 \begin{pmatrix} \widetilde{t}_L \\ \widetilde{t}_R \end{pmatrix}. \tag{3.4.30}$$

Their mass matrix reads

$$\mathcal{M}_{\widetilde{t}}^2 = \begin{pmatrix} m_{\widetilde{Q}}^2 + m_t^2 + \left(\frac{1}{2} - \frac{2}{3}s_w^2\right) m_Z^2 \cos 2\beta & m_t X_t \\ m_t X_t & m_{\widetilde{u}}^2 + m_t^2 + \frac{2}{3}s_w^2 m_Z^2 \cos 2\beta \end{pmatrix}. \tag{3.4.31}$$

where $X_t = A_t - \mu \cot \beta$. Corresponding expressions for down-type sfermions can be obtained from those above changing the definition of X to $X = A - \mu \tan \beta$ and noting that the contributions proportional to m_Z^2 arise from D-terms. Therefore for each sfermion they are given by

$$\delta_f = \left(T_f^3 - Q_f s_W^2\right) m_Z^2 \cos 2\beta. \tag{3.4.32}$$

With the convention we have adopted for the mass matrix, δ_f enters the upper diagonal element, while $\delta_{\bar{f}}$ the lower one.

If we introduce mixings between the different generations, through the soft masses or the A-terms, we will need to consider the full 6×6 mass matrices. However arbitrary flavor mixings can not be accommodated in the MSSM. In the lepton sector we would introduce dangerous contributions to several well measured observables. For example $\mu \to e\gamma$ receives a correction from the diagram in figure 3.1 that gives

$$\Gamma_{\mu \to e\gamma} \approx 8 s_W^2 \left(\frac{\alpha_W}{4\pi}\right)^3 \frac{\pi m_\mu^5}{m_{\widetilde{l}}^4} \left(\frac{\delta m_L^2}{m_{\widetilde{l}}^2}\right)^2 \tag{3.4.33}$$

where we have used a mass insertion approximation, assuming the off-diagonal entries of the sleptons mass matrix (that we have denoted generically with δm_L) to be much smaller than those on the diagonal. Current bounds, at 90% C.L., from the MEG experiment [82] require

$$\left(\frac{\delta m_L^2}{m_{\widetilde{l}}^2}\right)^2 \lesssim 10^{-4} \left(\frac{m_{\widetilde{l}}}{500 \text{ GeV}}\right)^2. \tag{3.4.34}$$
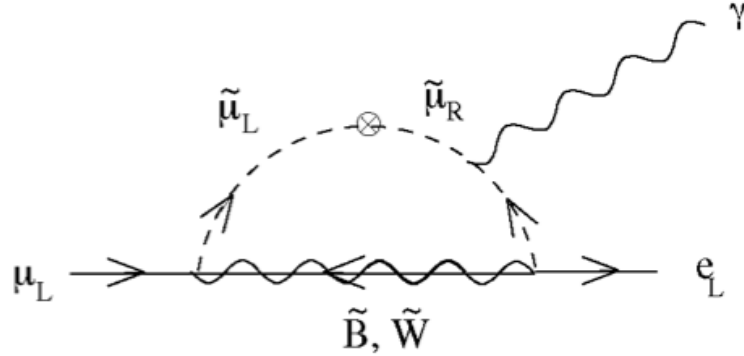
Figure 3.1: A possible contribution to $\mu \to e\gamma$ in the MSSM with arbitrary slepton mixings.

Gluino exchange in the squark sector is also dangerous phenomenologically, giving a correction to $K - \bar{K}$ mixing scaling parametrically with α_s

$$\mathcal{M}_{K-\bar{K}} \approx \frac{4\alpha_s^2}{m_{\tilde{q}}^2} \left(\frac{\delta m_Q^2}{m_{\tilde{q}}^2} \right)^2 \tag{3.4.35}$$

and just requiring it not to exceed the measured value $\epsilon_K^{\text{SM}} = (2.233 \pm 0.015)\,10^{-3}$ [31] (not even considering the small error on the measurement), would give

$$\left(\frac{\delta m_Q^2}{m_{\tilde{q}}^2} \right) \lesssim 4 \times 10^{-3} \frac{m_{\tilde{q}}}{500\ \text{GeV}}\,. \tag{3.4.36}$$

There are several popular solutions to the problem. We can fix the soft SUSY breaking squark and slepton masses to be proportional to the identity in the same basis where quark and lepton mass matrices are diagonal, then we have to further require that the A-term matrices be proportional to the Yukawa matrices and ask for no new nontrivial phases beyond the SM.

A second possibility is to assume that the only light superpartners are those most directly affecting naturalness: $\tilde{t}_L$, $\tilde{t}_R$, $\tilde{b}_L$, $\widetilde{H}_u$, $\widetilde{H}_d$. The first two generation squarks, instead, can go up to 20 TeV, suppressing the contributions to the most sensitive flavor observables (such as ϵ_K). Note that also the gluino can not be too heavy, since it feeds into the tuning of the Fermi scale at two loops (which would give $m_{\tilde{g}} \lesssim 1.3$ TeV for a 10% tuning and a SUSY breaking scale of 10^3 TeV). In this scenario approximate $U(2)$ symmetries for the first two generations of squarks considerably relax bounds on their masses, in some cases improving the agreement of the MSSM with flavor data [83, 84].

3.4.3   Charginos and Neutralinos

The mass eigenstates arising from the mixing between $\widetilde{W}^{\pm}$ and $\widetilde{H}^{\pm}$ are called charginos. In the notation $\psi = \left(\widetilde{W}^{+}, \, \widetilde{H}_u^{+}, \, \widetilde{W}^{-}, \, \widetilde{H}_d^{-} \right)^T$, the part of the Lagrangian relevant to the spectrum is

$$\mathcal{L}_c = -\frac{1}{2} \psi^T \mathcal{M}_{\widetilde{C}} \psi + \text{h.c.} \, , \tag{3.4.37}$$

with mass matrix

$$\mathcal{M}_{\widetilde{C}} = \begin{pmatrix} 0 & M^T \\ M & 0 \end{pmatrix} , \quad M = \begin{pmatrix} M_2 & \sqrt{2} s_\beta m_W \\ \sqrt{2} c_\beta m_W & \mu \end{pmatrix} . \tag{3.4.38}$$

The mixing comes from the wino-higgsino-Higgs coupling. Diagonalizing it using singular value decomposition

$$UMV = \begin{pmatrix} m_{\widetilde{\chi}_1^{\pm}} & 0 \\ 0 & m_{\widetilde{\chi}_2^{\pm}} \end{pmatrix} , \tag{3.4.39}$$

we obtain

$$\begin{pmatrix} \widetilde{\chi}_1^+ \\ \widetilde{\chi}_2^+ \end{pmatrix} = V^{-1} \begin{pmatrix} \widetilde{W}^+ \\ \widetilde{H}_u^+ \end{pmatrix} , \quad \begin{pmatrix} \widetilde{\chi}_1^- \\ \widetilde{\chi}_2^- \end{pmatrix} = U^* \begin{pmatrix} \widetilde{W}^- \\ \widetilde{H}_d^- \end{pmatrix} \tag{3.4.40}$$

and

$$m_{\widetilde{\chi}_{2,1}^{\pm}}^2 = \frac{1}{2} \left(|M_2|^2 + |\mu|^2 + 2 m_W^2 \pm \sqrt{(|M_2|^2 + |\mu|^2 + 2 m_W^2)^2 - 4 |\mu M_2 - m_W^2 \sin 2\beta|^2} \right) . \tag{3.4.41}$$

Higgsinos and winos become approximate mass eigenstates in the limit $|M_2 \pm \mu| \gg m_W$.

In analogy with the case just discussed, the neutral fermionic superpartners,

$$\psi^0 = \left(\widetilde{B}, \, \widetilde{W}^3, \, \widetilde{H}_u^0, \, \widetilde{H}_d^0 \right)^T , \tag{3.4.42}$$

all mix with each other

$$\mathcal{L}_n = -\frac{1}{2} \psi^{0T} \mathcal{M}_{\widetilde{N}} \psi^0 + \text{h.c.} \tag{3.4.43}$$

where

$$\mathcal{M}_{\widetilde{N}} = \begin{pmatrix} M_1 & 0 & -c_\beta s_W m_Z & s_\beta s_W m_Z \\ 0 & M_2 & c_\beta c_W m_Z & -s_\beta c_W m_Z \\ -c_\beta s_W m_Z & c_\beta s_W m_Z & 0 & -\mu \\ c_\beta c_W m_Z & -s_\beta c_W m_Z & -\mu & 0 \end{pmatrix} . \tag{3.4.44}$$

The off-diagonal terms come from the wino-higgsino-Higgs and bino-higgsino-Higgs couplings and in the limit $|M_{1,2} \pm \mu| \gg m_Z$ we have the mass eigenstates $\widetilde{B}, \, \widetilde{W}^3, \, \left(\widetilde{H}_u^0 \pm \widetilde{H}_d^0 \right) / \sqrt{2}$ with masses $(|M_1|, |M_2|, |\mu|, |\mu|)$.

In the following we denote neutralino mass eigenstates as $\widetilde{\chi}_i^0$ for $i = 1, ..., 4$, with $m_{\widetilde{\chi}_i^0} > m_{\widetilde{\chi}_j^0}$ if $i > j$.

3.4.4   Gauge coupling unification

Several phenomenological aspects of the MSSM made it appealing in the past few decades other than the solution of the hierarchy problem. Among them the improvement of gauge coupling unification over the SM and the presence of a viable dark matter candidate.

Since the 70's it was known that that a generation of SM fermions could be embedded in a $\bar{\mathbf{5}}$ and a $\mathbf{10}$ of $SU(5)$ and that under renormalization group evolution the SM gauge coupling approximately unified at high scales, suggesting a single Grand Unified gauge group [85]. Exploring this observation in the MSSM led to the conclusion that the unification of couplings is much more successful than in the SM [86, 87].

At the scale m_Z the SM gauge couplings have measured values

$$
\begin{aligned}
\alpha_1(m_Z) &= 0.016830 \pm 0.000007\,, \\
\alpha_W(m_Z) &= 0.03347 \pm 0.00003\,, \\
\alpha_s(m_Z) &= 0.1187 \pm 0.002\,,
\end{aligned}
\tag{3.4.45}
$$

where we have rescaled the hypercharge coupling $g_1 = \sqrt{5/3}g'$, that can not have an arbitrary normalization if embedded in a traceless generator of a non-Abelian group. The choice of the coefficient for the rescaling is the correct one for $SU(5)$ and larger groups in which the latter can be embedded.

The one-loop running of the couplings is given by

$$
\frac{dg_a}{d\log\mu} = -\frac{1}{16\pi^2}\beta_a g_a^3\,,
\tag{3.4.46}
$$

with β function coefficients

$$
\beta_a^{SM} = \left(-\frac{41}{10}, \frac{19}{6}, 7\right)
\tag{3.4.47}
$$

and

$$
\beta_a^{MSSM} = \left(-\frac{33}{5}, -1, 3\right)\,,
\tag{3.4.48}
$$

in the SM and the MSSM respectively. The difference is due to the fermionic superpartners (gauginos and higgsinos) and to the extra Higgs. Squarks and sleptons fall into complete $SU(5)$ multiplets and do not affect the differential running of the couplings. This is the reason why extensions of the minimal setting such as "Split Supersymmetry" [88, 89, 90], with the scalars decoupled from the Fermi scale, retain the MSSM success.

In the MSSM the key observation was that for a common threshold $\widetilde{m}$ for the superpartners,

$$
3\text{ GeV} < \widetilde{m} < 100\text{ TeV}\,,
\tag{3.4.49}
$$

the couplings unify at two-loops, within the error, around [86, 87]

$$
\Lambda_U \approx 2 \times 10^{16}\text{ GeV}\,.
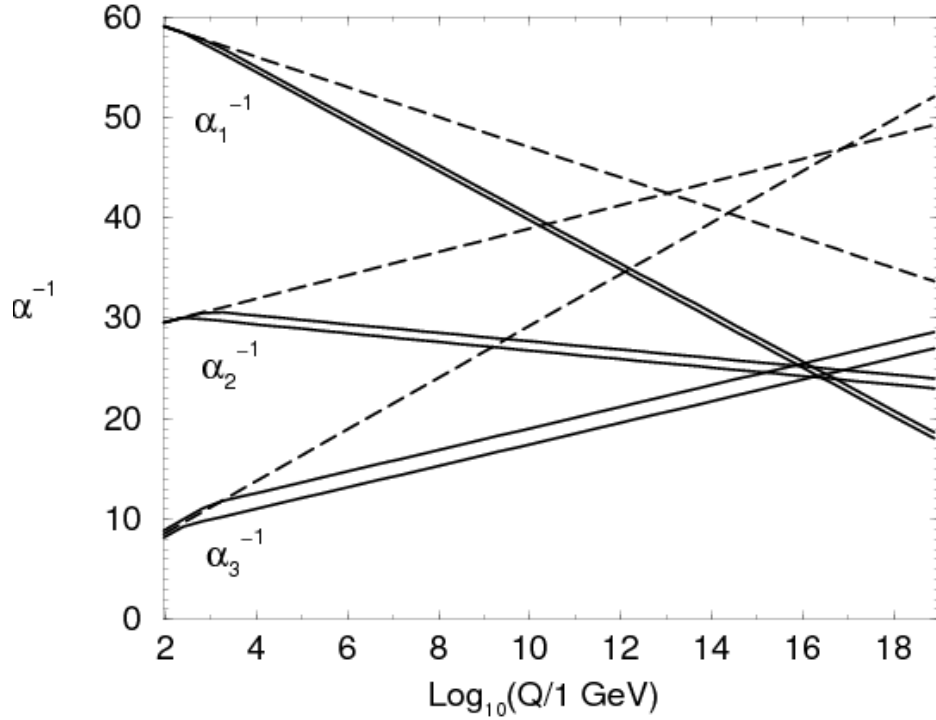\tag{3.4.50}
$$

Figure 3.2: Running at one-loop of the inverse gauge couplings in the SM (dashed lines) and in the MSSM (solid lines) [91]. It should be noted that the two-loop MSSM computation does not give exact unification within the couplings errors, as the one-loop result. However the MSSM retains a more successful gauge couplings unification than the SM also at two-loops.

In figure 3.2 we can see the difference between the approximate unification in the SM and in the MSSM at one-loop. Note that gauge coupling unification at two-loops in the MSSM is not exact within the couplings errors [86, 87] as it is the case at one-loop, but there is still a large improvement over the SM. For this reason the figure should be considered only for its illustrative purpose.

3.4.5   Dark matter in the MSSM

In many supersymmetric theories with R-parity, the LSP is a stable neutralino. In principle it can account for the observed dark matter (DM) in the Universe. Recent Planck observations are consistent with a relic abundance of DM given by [92]

$$\Omega_{DM} h^2 = 0.1196 \pm 0.0031 \,, \tag{3.4.51}$$

in agreement with the WMAP determination $\Omega_{DM} h^2 = 0.111 \pm 0.006$ [93], but exceeding it by some amount. If all the observed density is composed of neutralinos arising from thermal

freeze-out, it was shown that both wino-bino and higgsino-bino admixtures with masses in the few hundred of GeVs range can account for it [94]. Light higgsinos alone can not reproduce the observed relic density, but a tiny admixture of bino (that can be as heavy as $10^3 - 10^4$ TeV), can solve the problem [95, 96]. Clearly if we assume that non-thermal processes either deplete or enhance the abundance or that the DM is a multi-component object, theoretical constraints on the neutralino parameter space can be arbitrarily relaxed.

Currently the most stringent limits on spin-independent and spin-dependent nucleon-DM scattering cross sections, from XENON100 [97] and IceCube [98], do not rule out the possibility of reproducing the correct relic density in the MSSM. However the next generation of DM experiments, such as XENON1T [99], will probe most of the viable parameter space, with the exception of some narrow corners [100].

An alternative to neutralino DM in supersymmetry is gravitino dark matter. We know that gravity exists, therefore if supersymmetry is realized in nature it must be enlarged to include its effects. To this end supersymmetry can be promoted to a local symmetry with a massless supermultiplet of spin-3/2, the gravitino, and a spin-2 graviton. The gravitino $\widetilde{\psi}_\mu^\alpha$ transforms inhomogeneously

$$\delta\widetilde{\psi}_\mu^\alpha = -\partial_\mu\epsilon^\alpha + ... \tag{3.4.52}$$

and it can be considered the gauge particle of local SUSY transformations. Since supersymmetry must be spontaneously broken to be phenomenologically viable, the gravitino will acquire a mass eating the goldstone fermion associated to the global breaking. Its mass depends on the scale of SUSY breaking and on the Planck scale and can vary between a few eVs and some TeVs. If heavier than about 100 keV, the gravitino LSP is a natural candidate for cold dark matter [101] and it can be generated both through thermal production and through late decays of the next-to-LSP (NLSP).

The MSSM with R-parity has several interesting phenomenological consequences as it can solve the hierarchy problem, improve gauge coupling unification and provide a viable dark matter candidate. We can now turn to explore its collider signatures. However as we have seen in the previous sections there is a huge number of free parameters in the MSSM and its spectrum is virtually unconstrained by the requirements of gauge coupling unification or DM. Therefore we first use naturalness as a guiding principle to constrain the spectrum.

3.5 Supersymmetry at colliders

In this section, after introducing the main consequences of naturalness for the MSSM spectrum, we review the traditional arguments (and their drawbacks) for collider searches in final states with high ME_T arising from pair production of superpartners. We argue that final states with high (jets) multiplicities and no ME_T cuts are competitive in the search for natural spectra and allow to probe regions in theory space that the LHC and the Tevatron have left untouched.

3.5.1   Naturalness

The presence of soft breaking terms reintroduces some of the fine-tuning of the Higgs mass that exact supersymmetry was intended to cancel. This was proposed as a guidance to constrain the superpartner spectrum [102, 103]. The sparticles most affected by the minimization of the fine-tuning are stops, higgsinos and, to a lesser extent, gauginos. It is not surprising that these are the partners of the SM particles that more strongly contribute to the quantum corrections to the Higgs mass.

Since the relevant terms are those that determine the curvature of the potential in the direction of the Higgs vacuum expectation value, we can restrict the discussion of naturalness to the SM one-dimensional problem of correcting the bare parameters in [104]

$$V = m_H^2 |H|^2 + \lambda |H|^4 \,. \tag{3.5.1}$$

In general m_H is a combination of various masses and mixing angles (α and β) in the MSSM Higgs sector.

We would like each contribution to δm_H not to exceed by a large amount m_H itself. Otherwise different contributions would have to be fine-tuned to cancel each other. For this reason we define [104]

$$\Delta \equiv \left| \frac{2\delta m_H^2}{m_h^2} \right| \,, \tag{3.5.2}$$

where we have used the fact that $m_h^2 = -2m_H^2$, with m_h the lightest Higgs mass in the decoupling limit of the MSSM. This choice of fine-tuning measure can lead to a slight underestimate for $\tan \beta \lesssim 2 - 3$ in the presence of extra light Higgses. However it is sufficient for our intention of using fine-tuning as a guiding principle.

Requiring Δ not to exceed a fixed amount, at tree-level we can impose a bound on μ and therefore on higgsino masses

$$\mu \lesssim 300 \text{ GeV} \left(\frac{m_h}{126 \text{ GeV}} \right) \sqrt{\frac{10\%}{\Delta^{-1}}} \,. \tag{3.5.3}$$

The main effect at loop-level are the corrections to m_{H_u} proportional to the top Yukawa coupling, that, in the leading logarithmic approximation, are given by

$$\left(\delta m_{H_u}^2 \right)^{\widetilde{t}} = -\frac{3}{8\pi^2} y_t^2 \left(m_{\widetilde{Q}_3}^2 + m_{\widetilde{u}_3}^2 + |A_t|^2 \right) \log \left(\frac{\Lambda}{\text{TeV}} \right) \,. \tag{3.5.4}$$

Here Λ is the scale at which SUSY breaking effects are communicated to the MSSM. Through the soft parameters entering in the correction to m_{H_u} we can obtain an upper bound on the stop masses

$$\sqrt{m_{\widetilde{t}_1}^2 + m_{\widetilde{t}_2}^2} \lesssim 880 \text{ GeV} \frac{\sin \beta}{\sqrt{1 + x_t^2}} \sqrt{\frac{3}{\log \left(\Lambda/\text{TeV} \right)}} \left(\frac{m_h}{126 \text{ GeV}} \right) \sqrt{\frac{10\%}{\Delta^{-1}}} \,, \tag{3.5.5}$$

where $x_t = A_t / \sqrt{m_{\tilde{t}_1}^2 + m_{\tilde{t}_2}^2}$. From these equations we can deduce that naturalness not only prefers at least one stop to be light, but disfavors also an highly asymmetric spectrum, since A_t quadratically enters the correction to m_{H_u} and μ is bounded at tree-level. Enhancing the stop mixing $A_t - \mu \cot \beta$ using large $\cot \beta$ is not viable if we want to keep the top Yukawa perturbative up to high scales, which requires $\tan \beta \gtrsim 1$ [66].

Other radiative corrections pose much weaker bounds, in the range of tens of TeVs. The only exception is the gluino that at two-loops gives, always at leading log,

$$\left(\delta m_{H_u}^2 \right)^{\widetilde{g}} = -\frac{2}{\pi^2} y_t^2 \left(\frac{\alpha_s}{\pi} \right) |m_{\widetilde{g}}|^2 \log^2 \left(\frac{\Lambda}{\text{TeV}} \right) , \tag{3.5.6}$$

where we have neglected $A_t m_{\widetilde{g}}$ contributions. The corresponding naturalness bound reads

$$m_{\widetilde{g}} \lesssim 1.3 \text{ TeV} \sin \beta \frac{3}{\log \left(\Lambda / \text{TeV} \right)} \left(\frac{m_h}{126 \text{ GeV}} \right) \sqrt{\frac{10\%}{\Delta^{-1}}} . \tag{3.5.7}$$

The one-loop contribution of other gauginos gives a somewhat less stringent bound, which is almost irrelevant for the LHC, given the large difference in cross section between gluino pair production and ewkino pair production. However we show it here for completeness

$$(M_1, M_2) \lesssim (4.4 \text{ TeV}, 1.3 \text{ TeV}) \sqrt{\frac{3}{\log \left(\Lambda / \text{TeV} \right)}} \left(\frac{m_h}{126 \text{ GeV}} \right) \sqrt{\frac{10\%}{\Delta^{-1}}} . \tag{3.5.8}$$

In conclusion, asking for a moderate fine-tuning, even taking a relatively low SUSY breaking scale $\Lambda = 10^3$ TeV, requires stops to be in the few hundred GeVs range (600-700 GeV), the gluino to be lighter than approximately 1.3 TeV and μ not larger than $200 - 300$ GeV. A natural spectrum is schematically depicted in figure 3.3. A first look suggests that natural SUSY is well within the reach of the LHC. In the next sections we explore in more detail its collider phenomenology.

3.5.2   Collider phenomenology

Naturalness, if adopted to construct the spectrum with a bottom-up approach, has a strong impact on supersymmetry searches that we explore at the end of this section. First it is useful to review the consequences of R-parity conservation, that also heavily influences supersymmetric particles collider signatures. The main effect of R-parity is that superpartners are produced in pairs. We have both strong

$$gg \rightarrow \widetilde{g}\widetilde{g}, \ \widetilde{q}_i \widetilde{q}_j^*, \tag{3.5.9}$$

$$gq \rightarrow \widetilde{g}\widetilde{q}_i, \tag{3.5.10}$$

$$q\bar{q} \rightarrow \widetilde{g}\widetilde{g}, \ \widetilde{q}_i \widetilde{q}_j^*, \tag{3.5.11}$$

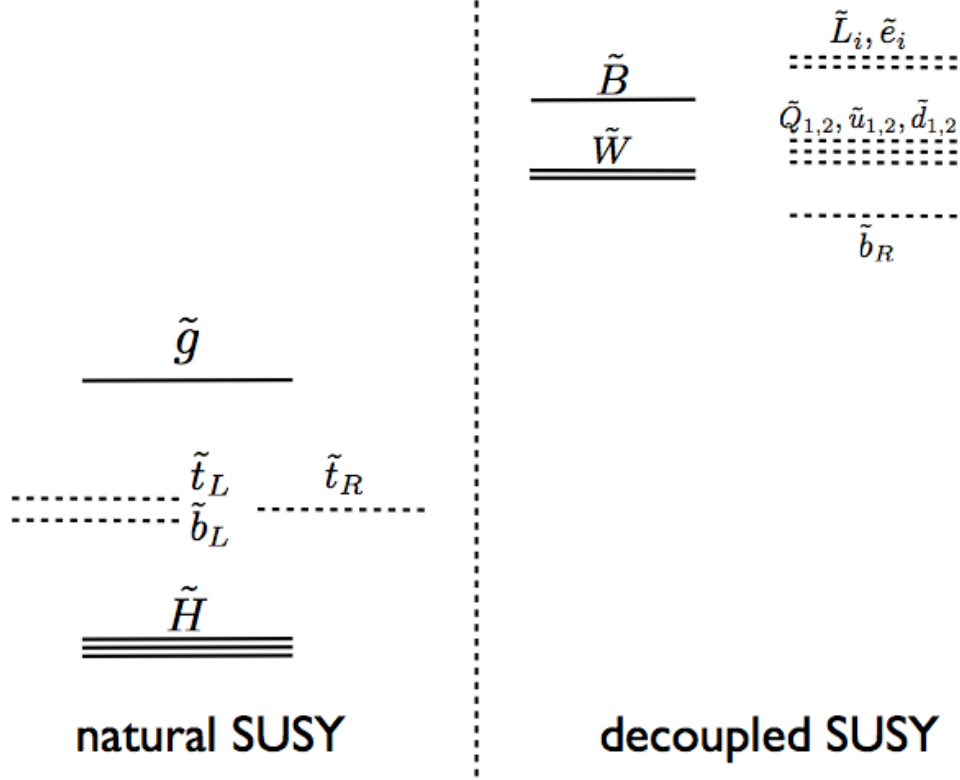$$qq \rightarrow \widetilde{q}_i \widetilde{q}_j, \tag{3.5.12}$$

Figure 3.3: Schematic view of a natural SUSY spectrum [105]. All superpartners on the right (except the winos) can be heavy $\widetilde{m} \gg 1$ TeV without considerably affecting the fine-tuning of the Higgs mass.

and electroweak

$$q\bar{q} \;\;\rightarrow\;\; \widetilde{\chi}_i^+ \widetilde{\chi}_j^-, \;\; \widetilde{\chi}_i^0 \widetilde{\chi}_j^0, \qquad u\bar{d} \rightarrow \widetilde{\chi}_i^+ \widetilde{\chi}_j^0, \qquad d\bar{u} \rightarrow \widetilde{\chi}_i^- \widetilde{\chi}_j^0, \qquad (3.5.13)$$

$$q\bar{q} \;\;\rightarrow\;\; \widetilde{\ell}_i^+ \widetilde{\ell}_j^-, \;\; \widetilde{\nu}_\ell \widetilde{\nu}_\ell^* \qquad u\bar{d} \rightarrow \widetilde{\ell}_L^+ \widetilde{\nu}_\ell \qquad d\bar{u} \rightarrow \widetilde{\ell}_L^- \widetilde{\nu}_\ell^*, \qquad (3.5.14)$$

production mechanisms. Typical production cross sections are shown in figure 3.4 for a $\sqrt{s} = 7$ TeV LHC. Generic production diagrams involve s-channel exchange of a SM gauge boson and t-channel exchange of a superpartner. The latter is often neglected at the LHC, where the experimental limits are presented in simplified settings in which only the superpartners directly involved in the decay chain are light and all the others decoupled. Other effects, such as the mixing between $\widetilde{t}_L$ and $\widetilde{t}_R$ have only recently started to be taken into account, even if it is known that the nature
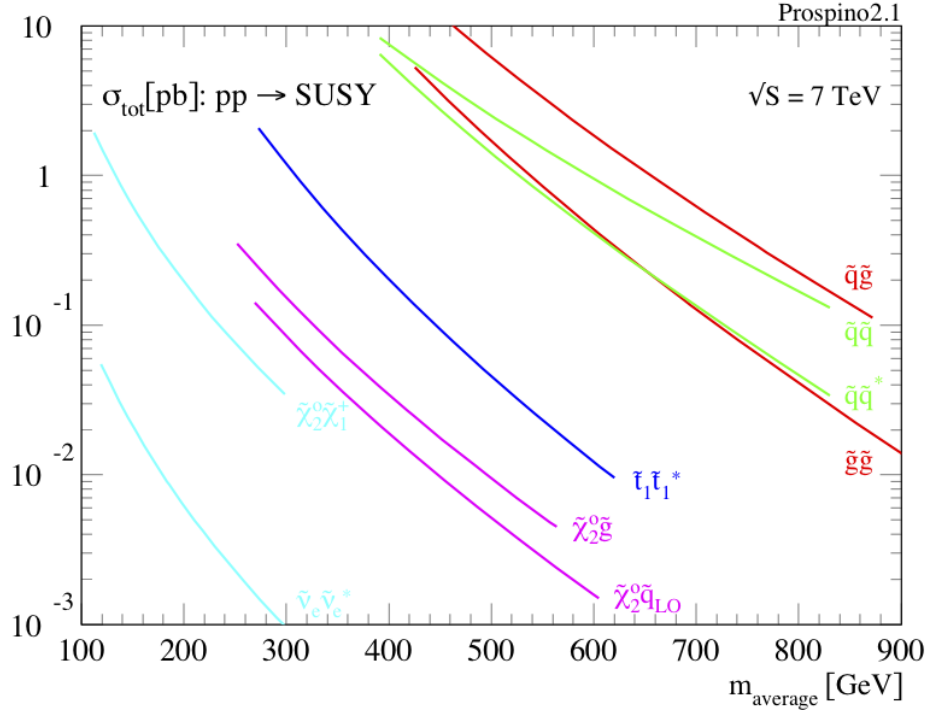
Figure 3.4: Production cross sections of supersymmetric particles computed at LO with `Prospino` [107] for the LHC at $\sqrt{s} = 7$ TeV. The figure was taken from [108].

of the pair produced stops influences the polarization of the decay products and can change by a factor of two the efficiency of current analyses [106].

These remarks are useful to keep in mind while looking at LHC exclusions. Currently they are in the ballpark of 1 TeV for strongly pair produced particles (gluinos and degenerate squarks), around 500-600 GeV for stops and 300 GeV for charginos and neutralinos decaying to gauge bosons [109, 110]. In figure 3.5 we show two exclusions in the mother particle-LSP masses plane for illustrative purposes.

These limits apply only under certain assumptions and heavily rely on the existence of a stable LSP well separated in mass from the pair produced mother particles, as can be seen also from figure 3.5. Going to mass splittings of $\mathcal{O}(100)$ GeV the limits are considerably weakened and completely vanish for certain final states. This is the case because LHC searches rely on the second consequence of R-parity conservation: the presence of a stable LSP. This is the only constant assumption in an otherwise varied analysis framework. Each of the production mechanisms listed above can give rise to many different decay chains of different length and complexity. Therefore supersymmetry is currently searched for in a topology-based framework, with the experiments distinguishing final states by the count of leptons, jets and the possible requirement of high hadronic activity in the event. These requirements are always accompanied by a ME_T cut.

However this is not necessarily the optimal way to search for natural supersymmetry and has the drawback of being completely insensitive to less than minimal supersymmetric scenarios (MSSM with R-parity violation, extra hidden sectors, moderately squeezed spectra). For these reasons we propose a change of paradigm in supersymmetry searches that we further argue in the next two subsections and apply to LHC data in the second part of this work.

Natural signatures

In a natural framework (see for instance the spectrum in figure 3.3) we can restrict the MSSM phenomenology to a relatively small number of final states [111], that are generically characterized by high jets and b-jets multiplicities and a reduction of ME_T due to the large mass of the top quark that often appears in the final state.

In this context the most copious process at the LHC will be gluino pair production, followed by two body decays into third generation squarks [111]

$$pp \to \tilde{g}\tilde{g}; \quad \tilde{g} \to \tilde{t}_1 \bar{t}, \; \tilde{t}_2 \bar{t}, \; \tilde{b}\bar{b} \tag{3.5.15}$$

and the corresponding conjugate modes with equal branching ratios. Gluino production dominates due to the color and spin factors in the amplitude that are larger than that of the squarks and are more important than the phase space suppression in most of the natural parameter space not yet excluded by direct searches.

In turn gluino decays are followed by the squark decays that are, when allowed by phase space and charge conservation,

$$\tilde{q} \to q\tilde{\chi} \tag{3.5.16}$$

$$\tilde{q} \to \tilde{q}V \tag{3.5.17}$$

$$\tilde{q} \to \tilde{q}S \tag{3.5.18}$$

where

$$\tilde{q} = \tilde{t}_1, \tilde{t}_2, \tilde{b}; \quad q = t, b; \quad \tilde{\chi} = \tilde{\chi}_1^0, \tilde{\chi}_2^0, \tilde{\chi}^\pm; \quad V = W, Z; \quad S = h, A, H^\pm \; . \tag{3.5.19}$$

If we want to understand which decay modes dominate we have first to identify the relevant parameters on which they depend and then find a range for them consistent with naturalness and flavor measurements. The decay chains listed above, once $m_{\tilde{g}}$ is fixed and thus the production cross section is known, involve only $m_{\tilde{t}_{1,2}}$, the angle θ_t that diagonalizes the stops mass matrix, μ and $\tan\beta$. We have already discussed naturalness bounds on the stop masses and on μ and also $\tan\beta$ can be constrained by phenomenological considerations. $\Delta F = 1$ transitions involving b quarks are enhanced at large $\tan\beta$. The most stringent limit in this sector is the one arising from $b \to s\gamma$ and it points to $\tan\beta \lesssim 10$. We can further restrict $\tan\beta \gtrsim 1$ without excluding any corner of parameter space interesting for phenomenology (besides in the MSSM and its D-term extensions $\tan\beta \gtrsim 5$ would be favored by the tree-level bound on the lightest Higgs mass). In

this range of $\tan \beta$ and with the neutralinos and charginos being mostly higgsinos[4] the dominant decays for the squarks are

$$\tilde{t}_{1,2} \to t \widetilde{\chi}^0, \quad \tilde{t}_{1,2} \to b \widetilde{\chi}^+, \quad \tilde{b} \to t \widetilde{\chi}^-, \tag{3.5.20}$$

thus limiting the full decay chain to the final states

$$\tilde{g} \to t\bar{t}\widetilde{\chi}^0; \quad \tilde{g} \to t\bar{b}\widetilde{\chi}^-; \quad \tilde{g} \to \bar{t}b\widetilde{\chi}^+, \tag{3.5.21}$$

where we have indicated with $\widetilde{\chi}^0$ both $\widetilde{\chi}_1^0$ and $\widetilde{\chi}_2^0$ and we have neglected $\tilde{b} \to b\widetilde{\chi}^0$ since it has a suppressed amplitude, relative to the other ones, by a factor $(m_b/m_t) \tan \beta$. The decays among the higgsinos of the heavier into the lighter ones via virtual W and Z are not crucial experimentally. They produce leptons, whose possible detection has been analyzed in [104], but their softness allows us to ignore them. It is easy to see that in this generic configuration of superpartners masses the phenomenology is characterized by the production of multitop and multibottom final states

$$pp \to \tilde{g}\tilde{g} \to tt\bar{t}\bar{t} + \widetilde{\chi}^0\widetilde{\chi}^0 \tag{3.5.22}$$

$$pp \to \tilde{g}\tilde{g} \to tt\bar{t}\bar{b}(\bar{t}\bar{t}\bar{t}b) + \widetilde{\chi}^0\widetilde{\chi}^0 \tag{3.5.23}$$

$$pp \to \tilde{g}\tilde{g} \to tt\bar{b}\bar{b}(\bar{t}\bar{t}bb) + \widetilde{\chi}^0\widetilde{\chi}^0 \tag{3.5.24}$$

$$pp \to \tilde{g}\tilde{g} \to t\bar{t}b\bar{b} + \widetilde{\chi}^0\widetilde{\chi}^0 \tag{3.5.25}$$

and it is governed by a single branching ratio B_{tb}

$$B_{tb} \equiv BR(\tilde{g} \to t\bar{b}\widetilde{\chi}^-) = BR(\tilde{g} \to \bar{t}b\widetilde{\chi}^+) \approx \frac{1}{2}(1 - BR(\tilde{g} \to t\bar{t}\widetilde{\chi}^0)), \tag{3.5.26}$$

$$B_{tt} \equiv BR(\tilde{g} \to t\bar{t}\widetilde{\chi}^0) \approx 1 - 2B_{tb}. \tag{3.5.27}$$

In the range of parameters that we have chosen B_{tb} can go from 25% to 50% reaching its maximum when $\tilde{t}_{1,2}$ become heavy enough to kinematically constrain $\tilde{g} \to \tilde{t}_{1,2}t$ or asymmetric enough to inhibit $\tilde{t}_1 \to t\widetilde{\chi}^0$. Notice that in this framework the simplified models in which the two experiments are interpreting their results (gluino pair production followed by $\widetilde{g} \to t\bar{t}\widetilde{\chi}_1^0$ and $\widetilde{g} \to b\bar{b}\widetilde{\chi}_1^0$) make up at most 25% and 4% of the gluino total width as can be seen from figure 3.6. Therefore exclusions such as the one in figure 3.5 must be taken with a grain of salt. A similar argument holds for the lightest stop that in most of the relevant parameter space has $0 \leq BR(\tilde{t}_1 \to t\widetilde{\chi}_1^0) \leq 20\%$, which reduces considerably the high mass reach in figure 3.5. Inclusive analysis would recover part of the lost sensitivity by combining different channels, but typically for gluino searches a $BR(\widetilde{g} \to t\bar{t}\widetilde{\chi}_1^0) = 100\%$ is the most favorable possibility, especially for the one-lepton CMS search [112] currently reaching almost up to $m_{\widetilde{g}} = 1.3$ TeV. Therefore, in general we expect a decrease in sensitivity with respect to the results presented in 3.5.

This together with the discussion at the beginning of section 3.5.2, allows us to conclude that LHC experiments are already sensitive to a large fraction of the relevant parameter space in this minimal natural scenario, but are still far from excluding natural supersymmetry, even in this simple realization. Nonetheless at the end of the 14 TeV run the reach on the gluino mass is likely to be extended to ≈ 2 TeV [113], thus covering a spectrum with $5 - 10\%$ fine-tuning.

---

[4]If we saturate the naturalness bound on $M_{1,2}$

High multiplicities

The signatures discussed in the previous sections are characterized by high jets and b-jets multiplicities, while the ME_T can be low if the top quarks are produced on-shell and $\Delta m_{\widetilde{g}-\widetilde{\chi}^0}$ is small. Other than the minimal natural SUSY spectrum, there are several generic scenarios, in the MSSM and its extensions, in which we expect large signals with many jets, little or no missing energy, and an occasional lepton, photon, or other relatively rare visible object. Following [114] we can identify four classes of models with this kind of signatures

- **Non standard LSP.** If supersymmetry breaking is communicated through low-scale gauge-mediation, the gravitino is the lightest R-parity-odd particle. The lightest SM superpartner can decay to it in association with its partner. For instance, a neutralino NLSP can decay to a gravitino plus a photon, Z or Higgs boson. Many of the other possible choices for the NLSP often produce jets and/or taus. The next-to-minimal supersymmetric standard model (NMSSM) can also accommodate a similar scenario. In this case the LSP can be dominantly a singlino and the NLSP will in general decay to it plus a pair of b-jets or τ's.

- **Cascade decays and/or squeezed spectrum.** If the MSSM spectrum is modestly squeezed or decays to W's or Z's carry off energy, the LSP can be left with a relatively low p_T and higher multiplicity final states can be produced.

- **Broken global symmetries.** In supersymmetry this is the case of R-parity violation, but similar situations can occur in little Higgs models (T-parity violation) [115] or in extra dimensional models with some amount KK-parity breaking. In supersymmetry R-parity breaking can lead to two or three-quark decays of the LSP (depending on its nature), with light or heavy flavors involved. This sends the ME_T content of the signal almost to zero (there could always be neutrinos in the final state) and increases the number of jets.

- **Top-rich final states.** Supersymmetric models with a "more minimal" spectrum as the one described previously, that contain light stops and sbottoms, can easily lead to final states with up to four top quarks. The same can happen in generic strong dynamics frameworks where the top is often the SM particle that couples more strongly to the composite sector [116, 117].

All these classes of models can easily accommodate also an high number of b-jets. In the case of top-rich signals the reason is apparent.

Independent considerations can point to high b-jet multiplicities also in the case of R-parity violating models or that of an LSP outside of the usual MSSM particle content. In the latter scenario an NMSSM-type framework can easily give rise to b-rich decays of the NLSP

$$\widetilde{\chi}_2^0 \rightarrow \widetilde{S}S \rightarrow \widetilde{S}b\bar{b}, \tag{3.5.28}$$

where we have indicated with $\widetilde{S}$ the fermionic partner of the extra singlet. In these models it is common for the mass eigenstate that is mainly singlet to decay to $b\bar{b}$ when it mixes predominantly

with H_d. This can happen naturally if, for instance, both S and H_d are parametrically heavier than H_u.

In the case of the R-parity violating MSSM, in general is harder to predict the size of all the new superpotential and Kähler potential couplings that will ultimately determine the b-content of the signal. However we expect high jet multiplicities and we can identify several models in which the dominant production and decay modes lead to signals with four or more b-quarks in the final state. An excellent example can be found in [118] where the R-parity violating couplings are determined by the SM Yukawa matrices, following a well motivated Minimal Flavor Violation (MFV) [119, 120, 121, 122] paradigm. In this model a stop, the sbottom left, a neutralino, a chargino or a gaugino can all be the LSP and their main decay modes are

$$
\begin{aligned}
\widetilde{t} &\to \bar{s}\bar{b}\,, \\
\widetilde{b}_L &\to \bar{s}\bar{t}\,, \\
\chi^0, \widetilde{g} &\to \bar{s}\bar{b}\bar{t}\,, \\
\chi^+ &\to \bar{s}\bar{b}\bar{b}\,.
\end{aligned}
\tag{3.5.29}
$$

There is also the possibility that the stau be the LSP in which case searches for displaced vertices are more effective. Another supersymmetric model that was developed along completely different lines, but gives interesting final states from the point of view adopted in this section can be found in [123, 124].

In the next section we discuss in more detail the RPV scenario anticipated here.

3.6   R-parity violation

R-parity is not necessary, small R-parity violating couplings can be added to the MSSM, changing dramatically its phenomenology at colliders, without any conflict with current experimental bounds (see [69] for a review). Furthermore we could still have a gravitino with a sufficiently long lifetime to account for dark matter, as we will discuss in more detail later in this section.

Nonetheless there are three theoretical considerations that make R-parity attractive. First it is rather unsatisfactorily to fix all R-parity violating couplings to be small by hand while R-parity provides a natural solution. Furthermore the MSSM already suffers from a proliferation of undetermined parameters, without adding to the count also the R-parity violating couplings. Last but not least R-parity violation accompanied by baryon number violation spoils the MSSM approximate gauge coupling unification. Nonetheless we can always include additional matter at higher scales to recover it. The other two arguments against R-parity violation (RPV) are essentially one of naturalness and one of predictivity.

In this section we show that imposing MFV in the superpotential, automatically generates RPV couplings of the correct size, solving at the same time the flavor problem discussed briefly in section 3.4.2. We are effectively replacing two assumptions (R-parity conservation and some

non-trivial flavor structure in the sfermions soft-terms) with the single MFV requirement. This is clearly not the only possible solution to accommodate RPV in the MSSM, however we find this scenario (introduced in [118]) particularly compelling from a theoretical point of view and at the same time interesting for LHC searches.

3.6.1   Minimal flavor violation in the superpotential

The basic assumption of minimal flavor violation is that the Yukawa couplings Y_u, Y_d and Y_e are the only spurions which break the $SU(3)^5$ flavor symmetry of the SM. So we can write flavor non-singlet terms in the superpotential and in the SUSY breaking part of the Lagrangian, but they are always accompanied by the appropriate powers of the SM Yukawas. New CP phases can still appear, since the MFV framework suppresses all new flavor-changing CP violating effects, but does not address the problem of flavor diagonal sources of CP violation. Here for simplicity we set these extra phases to zero.

Applying MFV to SUSY we need to assign the Yukawa to a SUSY representation. Since they appear in the superpotential, the most natural choice is to consider them as the vevs of some chiral superfields. With this choice the predictivity of the framework is enhanced considerably due to the constraints imposed by holomorphy. If we further impose the discrete Z_3 symmetry

$$L \to \omega L \,, \quad \bar{e} \to \omega^{-1}\bar{e} \,, \quad Y_e \to Y_e \quad \omega \equiv e^{2\pi i/3} \,, \tag{3.6.1}$$

no lepton number violating terms can be generated[5]. This assumption is made here only for simplicity and can be relaxed to allow neutrino mass generation, without any catastrophic phenomenological consequences [118]. The most notable constraint that applies removing this Z_3 symmetry is the one arising from the proton lifetime. In the scenario with no neutrino masses the proton is effectively stable, since, in the absence of light unflavored fermions, proton decay requires lepton number violation.

To construct the superpotential we recall that the quark Yukawas have flavor quantum numbers under $SU(3)_Q \times SU(3)_{u_R} \times SU(3)_{d_R}$

$$Y_u = (\bar{\mathbf{3}}, \mathbf{3}, \mathbf{1}) \,, \quad Y_d = (\bar{\mathbf{3}}, \mathbf{1}, \mathbf{3}) \,, \tag{3.6.2}$$

while Y_e transforms as a $(\bar{\mathbf{3}}, \mathbf{3})$ under $SU(3)_L \times SU(3)_{e_R}$. A simple spurion analysis is sufficient to conclude that only one additional term is generated in the superpotential

$$W_{\Delta B=1} = \frac{w}{2} \left(Y_u \bar{u}\right) \left(Y_d \bar{d}\right) \left(Y_d \bar{d}\right) \,, \tag{3.6.3}$$

where w is an $\mathcal{O}(1)$ coefficient. The Kähler potential, at the renormalizable level, has the structure

$$
\begin{aligned}
K &= Q^\dagger \left[1 + F_Q\left(Y_u Y_u^\dagger, Y_d Y_d^\dagger\right) + \text{h.c.}\right] Q + \bar{u}^\dagger \left[1 + F_u\left(Y_u Y_u^\dagger, Y_d Y_d^\dagger\right) + \text{h.c.}\right] \bar{u} + \\
&\quad + \bar{d}^\dagger \left[1 + F_d\left(Y_u Y_u^\dagger, Y_d Y_d^\dagger\right) + \text{h.c.}\right] \bar{d} + \\
&\quad + L^\dagger \left[1 + F_L\left(Y_e Y_e^\dagger\right) + \text{h.c.}\right] L + \bar{e}^\dagger \left[1 + F_e\left(Y_e Y_e^\dagger\right) + \text{h.c.}\right] \bar{e} \,,
\end{aligned} \tag{3.6.4}
$$

---

[5]With the exception of strongly suppressed dimension 8 Kähler $\Delta L = \pm 3$ interactions.

where the functions F are polynomials of their arguments. The new soft breaking terms are in one-to-one correspondence with the superpotential term, with additional non-holomorphic corrections suppressed by the smallness of the Yukawas for which we refer to the appendix of [118]

$$\mathcal{L}_{\text{soft}} \supset Y_u \left(1 + Y_u^\dagger Y_u + ...\right) \widetilde{u} \left(Y_d \widetilde{\overline{d}}\right) \left(Y_d \widetilde{\overline{d}}\right) + Y_d \left(1 + Y_d^\dagger Y_d + ...\right) \widetilde{\overline{d}} \left(Y_d \widetilde{\overline{d}}\right) \left(Y_u \widetilde{u}\right) + ... \quad (3.6.5)$$

The most interesting phenomenological consequences arise from the superpotential. In the basis where $Y_u \sim V^\dagger \text{diag}(y_u, y_c, y_t)$ its coefficients have the parametric form

$$W_{\Delta B=1} = \frac{1}{2}\lambda_{ijk}\bar{u}_i\bar{d}_j\bar{d}_k, \quad \lambda_{ijk} = wy_{u_i}y_{d_j}y_{d_k}\epsilon_{jkl}V_{il}^*, \quad (3.6.6)$$

where the antisymmetric tensor ϵ is a consequence of the only possible color contraction $\epsilon^{abc}\bar{u}^a\bar{d}^b\bar{d}^c$.

The largest coupling is $\lambda_{tbs} \sim \lambda^3 t_\beta^2 \frac{m_b m_s}{m_t^2}$[6] that even for $t_\beta \equiv \tan\beta = 45$ is still of $\mathcal{O}(10^{-4})$. As a consequence of MFV the couplings of first generations are the smallest, with $\lambda_{uds} \approx 10^{-12}$ (again for $t_\beta = 45$). This gives a feeling of how contributions to the most sensitive precision observables, from nucleons and light mesons, can be kept under control, while we expect an LHC phenomenology dominated by decays to third generation quarks. Here we do not discuss indirect constraints, that can be accommodated as shown in [118] and just review the LHC phenomenology of the model. It is only worth to mention that the contributions to $n - \bar{n}$ oscillation can easily be kept under control. The reason is that the RPV couplings are antisymmetric in the flavor indexes and the only tree-level diagram inducing the oscillation requires two RPV vertices. Thus to have the necessary flavor change we have to introduce two off-diagonal mass insertions, proportional to CKM matrix elements. In view of these considerations, the parametric dependence of the oscillation amplitude is

$$\mathcal{M}_{n-\bar{n}} \propto t_\beta^6 \lambda^8 \frac{m_u^2 m_d^2 m_b^4}{m_t^8}, \quad (3.6.7)$$

where we have shown only the most important contribution coming from $\widetilde{b}_R \to \widetilde{d}_L \sim y_b\lambda^3$. This leads to an approximate oscillation time of [118]

$$t_o \approx 9 \cdot 10^9 \text{ s} \left(\frac{45}{\tan\beta}\right)^6, \quad (3.6.8)$$

already for first and second generation squarks at $m_{\widetilde{q}} \approx 100$ GeV and $m_{\widetilde{g}} \approx 100$ GeV. We have further assumed the hadronic matrix element to be ≈ 250 MeV. This value is safely above the current lower bound $\tau_{n-\bar{n}} \geq 2.44 \cdot 10^8$ s [125].

3.6.2 LHC phenomenology

Not surprisingly the detailed LHC phenomenology of MFV RPV supersymmetry depends on its spectrum. So we are led to consider several possible scenarios depending on the nature of the LSP that we do not require to be charge and color neutral.

---

[6]Where $\lambda \approx 0.2$ is the Cabibbo angle.

The the spectrum is not completely random, being constrained by MFV. In the up-squarks sector the mass matrix reads

$$M_{\tilde{u}}^2 = \begin{pmatrix} m_{\tilde{Q}}^2 \left(1 + \alpha_u Y_u Y_u^\dagger + \alpha_d Y_d Y_d^\dagger \right) + \delta_u & X_u Y_u \\ X_u^* Y_u^\dagger & m_{\tilde{u}}^2 \left(1 + \beta_u Y_u^\dagger Y_u \right) + \delta_{\bar{u}} \end{pmatrix} + ... , \qquad (3.6.9)$$

where we have omitted higher orders in Y_u and Y_d, α_u and β_u are non-holomorphic parameters coming from the soft masses, the δ's are the usual D-term contributions and the X_u's are combinations of holomorphic parameters describing left-right mixing. The structure of the mass matrix is the same for down squarks and sleptons.

If we do not want to introduce additional fine-tuning all dimensionless parameters should be $\mathcal{O}(1)$. So the hierarchy between SM Yukawas strongly influences the spectrum. We can easily have a light stop, but all other up-squarks are nearly degenerate. The same is true for one of the sbottoms and the other down-squarks. In the sleptons and sneutrinos sector, on the contrary, the degeneracy is extended to all three generations unless $\tan\beta$ is large enough to make y_τ corrections sizeable.

It is therefore natural to have a stop or sbottom LSP. In the first case we would have decays to two down quarks governed by the superpotential coupling λ

$$\Gamma_{ij} \approx \frac{m_{\tilde{t}}}{8\pi} \sin^2\theta_{\tilde{t}} |\lambda_{tij}|^2 . \qquad (3.6.10)$$

Given the sizes of the λ_{ijk} in the previous section we have a 90% branching fraction to bs and an 8% one to bd. The lifetime is short enough not to produce displaced vertices[7] except for very small values of $\tan\beta$ or a very light stop

$$\tau_{\tilde{t}} \approx 2\,\mu\text{m} \left(\frac{10}{\tan\beta} \right)^4 \left(\frac{300\text{ GeV}}{m_{\tilde{t}}} \right) \left(\frac{1}{2\sin^2\theta_{\tilde{t}}} \right) . \qquad (3.6.11)$$

The situation is similar for the sbottom that goes 99% of the time to ts or td ($\Gamma \sim |\lambda_{ibk}|^2$), the main difference being the lifetime of the sbottom left, that has decay widths suppressed by the insertion of a left-right mixing, giving

$$\tau_{\tilde{b}_L} \approx 41\,\mu\text{m} \left(\frac{10}{\tan\beta} \right)^6 \left(\frac{300\text{ GeV}}{m_{\tilde{b}_L}} \right) . \qquad (3.6.12)$$

At low $\tan\beta$ we can have displaced vertices. The other candidates for the role of LSP are neutralinos, gluinos, charginos and sleptons. Each having a very different phenomenology. The decays of the former three are listed in equation (3.5.29). They all give rise to final states with high jets and

---

[7]The typical position resolution of ATLAS and CMS experiments on the primary vertex is $20-100\ \mu$m depending on the number of tracks associated to it (for this estimate: $N_{\text{tracks}} > 4$) and their momentum.

b-jets multiplicities and can also produce displaced vertices. For instance the neutralino width and lifetime scale as

$$\begin{aligned} \Gamma_{\widetilde{\chi}^0} &\approx \frac{m_{\widetilde{\chi}^0}}{128\pi^3}|\lambda_{tsb}|^2\,, \\ \tau_{\widetilde{\chi}^0} &\approx 12\,\mu\mathrm{m}\left(\frac{20}{\tan\beta}\right)^4\left(\frac{300\text{ GeV}}{m_{\widetilde{\chi}^0}}\right)\,. \end{aligned} \tag{3.6.13}$$

Therefore we expect the main signature at the LHC to be pair production of the LSP followed by the decays discussed above. For the sake of completeness we include also the case in which the stau is the LSP, that would give the four body decays $\widetilde{\tau}\to\tau\bar{t}\bar{s}\bar{b}$ or $\widetilde{\tau}\to\nu_\tau\bar{b}\bar{b}\bar{s}$ with

$$\begin{aligned} \Gamma_{\widetilde{\tau}} &\approx \frac{m_{\widetilde{\tau}}}{2048\pi^5}|\lambda_{tbs}|^2\,, \\ \tau_{\widetilde{\tau}} &\approx 44\,\mu\mathrm{m}\left(\frac{45}{\tan\beta}\right)^4\left(\frac{500\text{ GeV}}{m_{\widetilde{\chi}^0}}\right)\,. \end{aligned} \tag{3.6.14}$$

The lifetime is long enough to give displaced vertices in almost all the relevant parameter space. The signatures are again characterized by high jets multiplicities a large number of b-quarks and leptons in the final state.

As we have seen RPV couplings are small, therefore superpartner production proceeds mainly through R-parity conserving couplings and was already discussed in section 3.5.2. The constraints imposed by naturalness on the spectrum do not change and we can imagine scenarios with neutralino, chargino, stop or gluino LSPs. It is also appropriate to point out that traditional analyses retain some sensitivity for the displacements discussed here, since the lifetime distribution is exponential and a large fraction of long lived LSPs decays before the first layer of pixels.

3.6.3   Gravitino dark matter

Introducing R-parity violating couplings closes the possibility of having neutralino dark matter. In [126] it was found that the leading decay of a gravitino, too light to decay through RPV couplings, is $\widetilde{G}\to\gamma\nu$ with the width

$$\Gamma_{\widetilde{G}} \approx \frac{1}{32\pi}|U_{\gamma\nu}|^2\frac{m_{\widetilde{G}}^3}{M_P^2}\,. \tag{3.6.15}$$

$U_{\gamma\nu}$ is the photino-neutrino mixing due to the small vev that the sneutrino acquires if we introduce neutrino masses following [118]. In this case the mixing is related to a spurion bounded by the proton lifetime and the limit leads to [118]

$$\tau_{\widetilde{G}} \gtrsim 4\times10^{39}\text{ yr}\left(\frac{1\text{ GeV}}{m_{\widetilde{G}}}\right)^3\left(\frac{\tan\beta}{10}\right)^8\left(\frac{500\text{ GeV}}{m_{\widetilde{q}}}\right)^4\,, \tag{3.6.16}$$

where $m_{\widetilde{q}}$ is a common first-second generation squarks mass scale. This lifetime is large enough to make of the gravitino a potential dark matter candidate. However a gravitino heavier than ≈ 1

GeV can also decay through λ_{cbs} with a lifetime of order [118]

$$\tau_{\widetilde{G}} \approx 2 \times 10^{22} \text{ yr} \left(\frac{500 \text{ GeV}}{m_{\widetilde{q}}} \right)^4 \left(\frac{10}{\tan \beta} \right)^4 \left(\frac{100 \text{ GeV}}{m_{\widetilde{G}}} \right)^3 . \tag{3.6.17}$$

Also in this case the lifetime is larger than that of the universe and the gravitino makes a viable candidate. We do not elaborate further on the point leaving a more detailed study of relic abundance and detection cross section to future work. We only find appropriate to remark that if the gravitino is lighter than the LSP, we could have for instance $\widetilde{t} \to t\widetilde{G}$, but if we assume that the gravitino mass saturates the lower bound [118]

$$m_{\widetilde{G}} \gtrsim 300 \text{ KeV} \left(\frac{300 \text{ GeV}}{m_{\widetilde{q}}} \right)^2 \left(\frac{\tan \beta}{10} \right)^4 \tag{3.6.18}$$

coming from $p \to K^+\nu$ searches (that are sensitive also to $p \to K^+\widetilde{G}$), we have

$$\frac{\Gamma_{\widetilde{t} \to t\widetilde{G}}}{\Gamma_{\widetilde{t} \to SM}} \approx 7 \times 10^{-10} \left(\frac{m_{\widetilde{t}}}{300 \text{ GeV}} \right)^8 \left(\frac{10}{\tan \beta} \right)^{12} . \tag{3.6.19}$$

So the decays to gravitino are typically negligible, but strongly depend on $\tan \beta$ and the NLSP mass.

3.7   Conclusion

In this chapter we have given a brief review of the main phenomenological aspects of supersymmetry at the TeV scale. The discussion does not have any pretence of completeness and it is meant as an introduction to the LHC search described in the second part of the thesis and to a more detailed treatment of Higgs couplings and supersymmetry in the third part.

We have tried to give an account of some of the most phenomenologically appealing aspects of the MSSM, such as the solution to the fine-tuning problem, the improvement in gauge coupling unification and the presence of several viable dark matter candidates. This is balanced by the large number of free parameters that in most cases make any sharp prediction problematic. Both positive and negative aspects are important for the two following parts of the thesis.

The theoretical qualities of the MSSM and its extensions have inspired the search for new physics in the next part of the thesis. In particular the discussion of natural signatures of the MSSM, of the high multiplicity signatures and of the final states of MFV R-parity violating SUSY are relevant for the next chapters.

The difficulty in making sharp predictions, on the other hand, has opened the way to the work presented in the last part of the thesis. There we try to identify a small number of parameters relevant to the couplings of the lightest supersymmetric Higgs and to give simple predictions that can be tested at the LHC, both for supersymmetry as a prototype of a natural theory.

So in the next two parts of this work the real goal of this discussion is made manifest presenting ways to address, in the next few years, the question of naturalness.
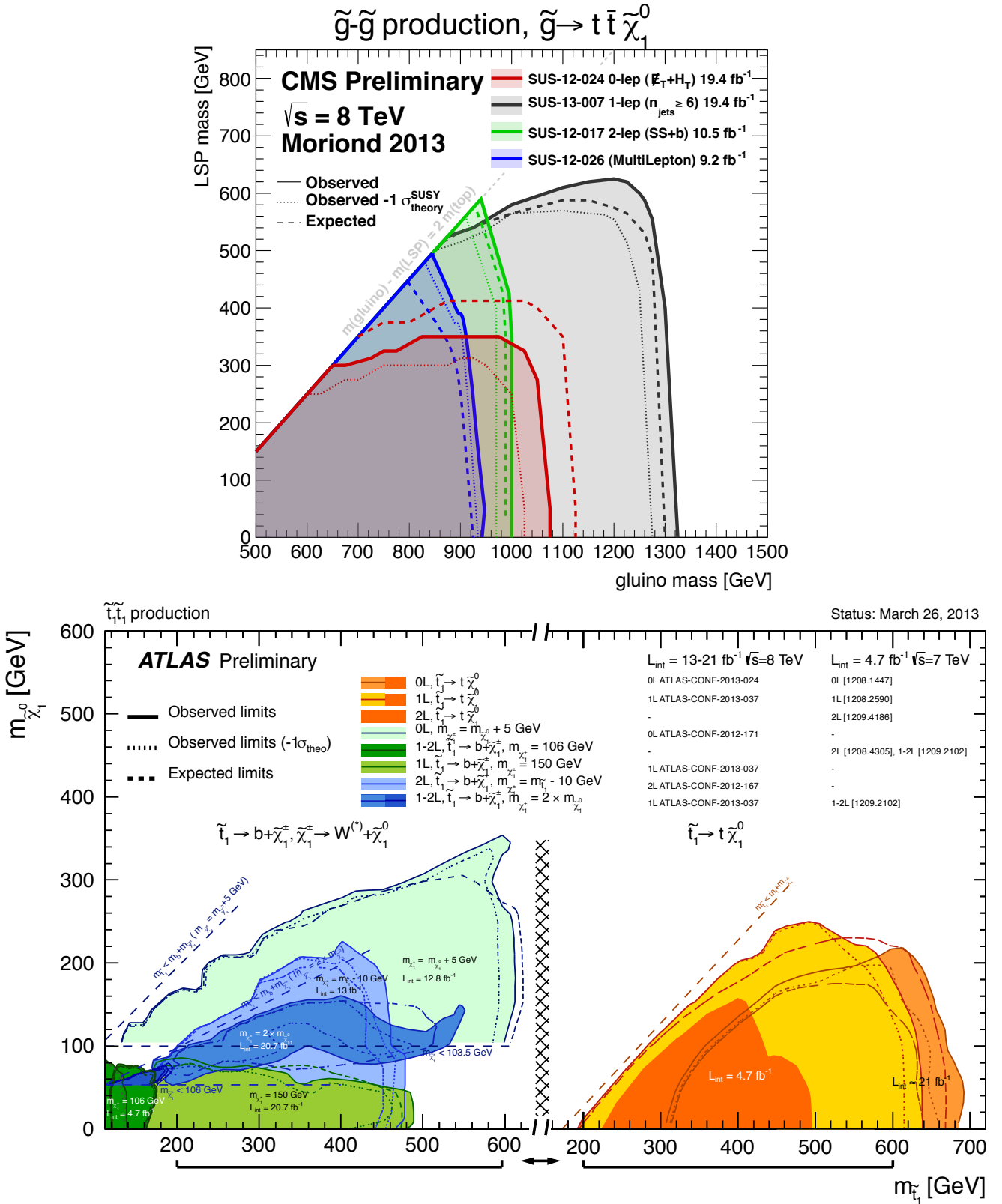
Figure 3.5: (Top) CMS exclusion in the gluino-neutralino plane for $pp \to \widetilde{g}\widetilde{g}$ and $\widetilde{g} \to t\bar{t}\widetilde{\chi}_1^0$. The different colors correspond to different searches described in [109]. (Bottom) ATLAS exclusion in the stop-neutralino plane for $pp \to \widetilde{t}_1\widetilde{t}_1^*$ and (Left) $\widetilde{t}_1 \to b\widetilde{\chi}_1^+ bW^{(*)}\widetilde{\chi}_1^0$ and (Right) $\widetilde{t}_1 \to t\widetilde{\chi}_1^0$. More details on the searches presented collectively in the plot can be found in [110].
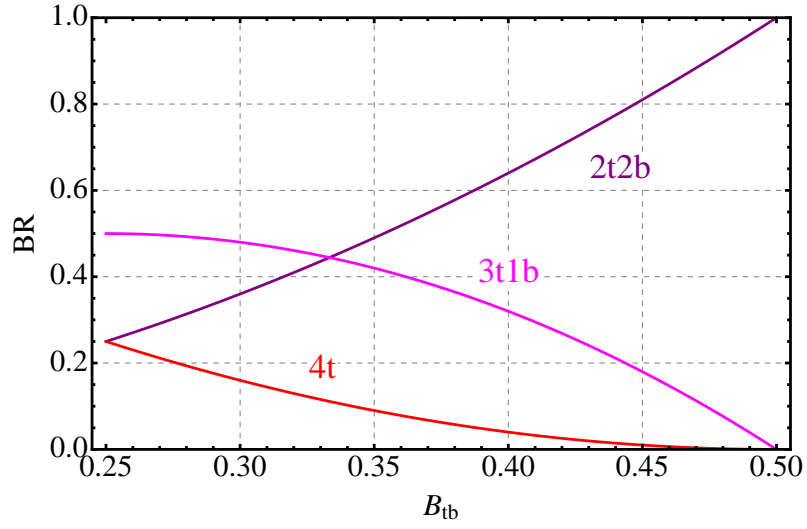
Figure 3.6: Inclusive gluino branching ratios in the model described in section 3.5.2 with the assumption $BR\left(\widetilde{g} \to b\bar{b}\widetilde{\chi}_1^0\right) = 0$ (valid a 4% in all the relevant parameter space). On the x axis we have $B_{tb} \equiv BR(\tilde{g} \to t\bar{b}\widetilde{\chi}^-)$. The inclusive final states are distinguished only by the number of t and b quarks.

Part II

A search for new physics inspired by naturalness

Introduction

Natural theories generically predict a large number of new particles at the Fermi scale, associated to the solution of the hierarchy problem. Therefore the most straightforward way to obtain a strong hint in favor of naturalness is to discover new physics at the LHC.

Unfortunately we do not have any generic indication of how natural new physics can manifest itself. Multilepton, multijet and high ME_T final states (just to mention a few) are all valid candidates for a quick discovery of naturalness. Nonetheless in the previous chapter we were able to identify some generic features of natural supersymmetric theories that can offer some guidance in the search.

First and foremost the top Yukawa always plays a central role. This is a general characteristic of natural theories determined uniquely from the requirement of reproducing the SM in the low energy limit. Therefore it is reasonable to expect production of top partners with decays to third generation quarks. The explicit examples in the literature are endless and do not include only supersymmetric theories, but also technicolor [127], universal extra dimensions [128] and top compositeness scenarios [116, 117], just to mention a few.

The second feature that emerges clearly is the frequency with which high jet multiplicity final states appear. Often this is a consequence of the abundance of top quarks and thus not specific to supersymmetry. However, in many of the examples seen in the previous chapter, the large number of jets could also be ascribed to long cascade decays determined by some features of the supersymmetric spectrum (moderate compression, singlino LSP, ...). In both cases the high multiplicities are also accompanied by a reduction of ME_T on which traditional SUSY searches cut strongly to suppress the background.

In conclusion if we are interested in detecting natural theories and in particular natural supersymmetry a good starting point would be to design an inclusive search on the tails of the jets and b-jets multiplicities. The presence of top quarks in the final state or the long decay chains typically allow for at least one rare object (lepton) to be produced and we can use it to reduce the background. This allows to avoid any ME_T requirement, making the analysis more inclusive and complementary to traditional searches. In chapter 6 we describe a search developed along these lines, after having introduced the experimental setting in chapter 4 and jets and b-jets reconstruction with the CMS detector in chapter 5.

Chapter 4

The experimental setting

Come, let us build ourselves a
city, with a tower that reaches
to the heavens, so that we may
make a name for ourselves;
otherwise we will be scattered
over the face of the whole earth

Genesis 11:4-5

In this chapter we describe the Large Hadron Collider [2] and the Compact Muon Solenoid
(CMS) experiment [129]. Their design and construction took several years and the combined effort
of a varied international community of thousand of researches. Therefore rather than aiming at
completeness we focus on the aspects of this experimental apparatus that made possible the search
for new physics presented in chapter 6.

4.1   The Large Hadron Collider

The Large Hadron Collider was built to accelerate and collide protons and atomic nuclei at design
center of mass energies of $\sqrt{s} = 14$ TeV and $\sqrt{s} = 5.52$ TeV, respectively (where the last value
refers to Pb-Pb collisions). It is hosted in the LEP tunnel, a circular cave 26.7 km long with an
approximately round inner chamber of radius 1.75 m. Here we highlight just the main features
of the machine, a more complete description can be found in [2]. The energy reached in the 2011
proton run was of 7 TeV, in 2012 it was raised to 8 TeV and it will get close to the nominal value
after the 2013-2014 long shutdown.

Two transfer tunnels link the LHC to the CERN accelerator complex that acts as an injector.
The protons start from the LINAC2 (that will be substituted in 2018 by the LINAC4) then pass
through the Proton Synchrotron Booster (PBS), followed by the Proton Synchrotron (PS) and
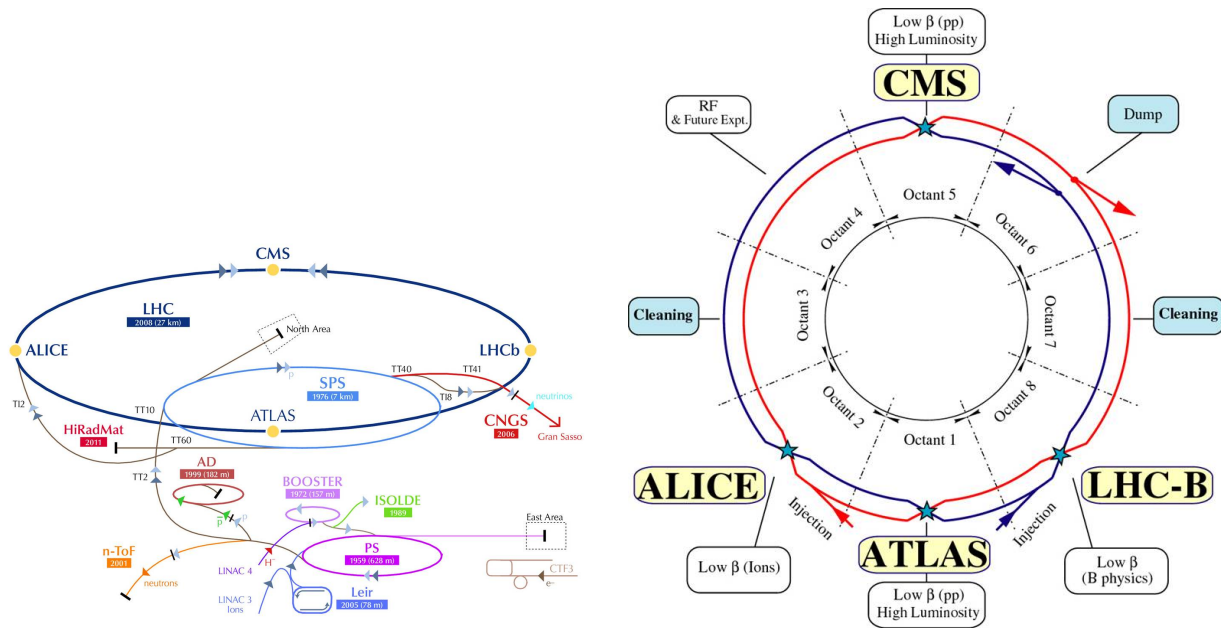the Super Proton Synchrotron (SPS) that injects them in the LHC. The chain followed by the

Figure 4.1: Left: the CERN accelerator complex. Note that the initial step of the proton acceleration chain in the figure is the LINAC4 that will become the source of proton beams for the LHC in 2018. Right: Schematic view of the two LHC rings and eight crossing points.

heavy ions differs only in the first two steps that are replaced by the LINAC3 and the Low Energy Ion Ring (LEIR). More details on the CERN accelerator complex can be found in [130] and a schematic representation is shown in the left panel of figure 4.1.

The LHC is composed of two rings with eight crossing points, flanked by long straight sections, as shown in the right panel of figure 4.1. The protons in the two rings can be made to collide at the crossing points. Each straight section has a length of 528 m and can serve as an experimental or utility insertion. Four of the crossing points are occupied by experiments. The ATLAS, ALICE, LHCb, CMS, TOTEM (that shares the CMS cavern) and LHCf (that shares the ATLAS cavern) detectors are accommodated there.

The particles traveling inside the accelerator are organized in bunches containing 10^{11} protons in nominal conditions, with a 25 ns spacing between them. Up to 3564 bunches could be contained in the machine, but the injection chain and, to a larger extent, the beam dump limit this number to 2808, again in design conditions. The acceleration takes place in radiofrequency cavities each delivering 2 MV (an accelerating field of 5 MV/m) at 400 MHz. They operate in a superconductive state at 4.5 K. A set of superconducting magnets is responsible for bending the particle trajectories and keeping the bunches focused. There are roughly 1600 magnets in the LHC tunnel, cooled down to a temperature of 1.9 K with superfluid helium, producing magnetic fields of approximately 8 T. A section of a LHC dipole bending magnet is shown in figure 4.2.
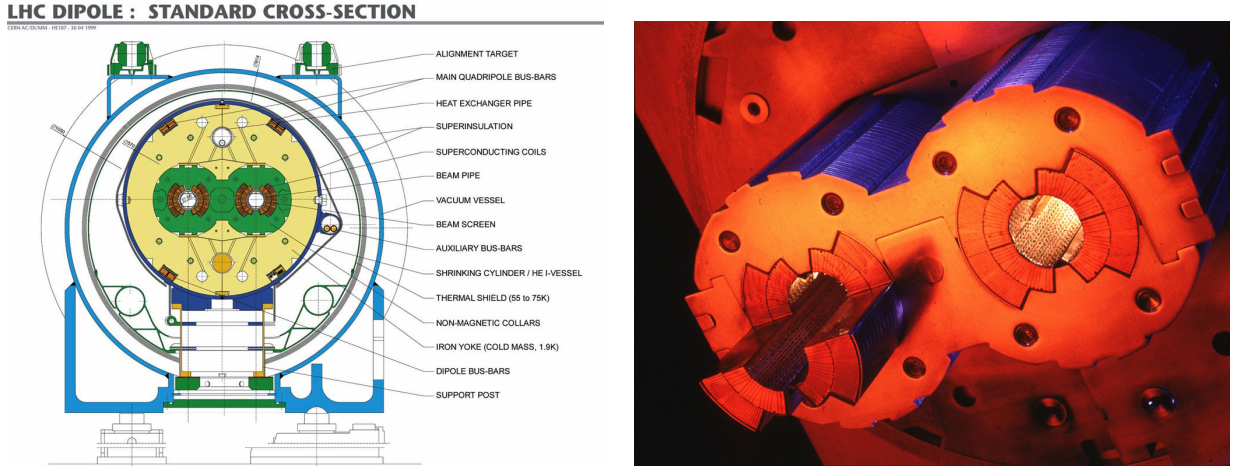
Figure 4.2: Left: Structural components of an LHC dipole magnet. Right: Close up on one of its Niobium Titanium superconducting coils.

The accelerator was designed to deliver high energy collisions at a rate of 40 MHz and this year it operated at 20 MHz. However rather than the collision rate, the relevant quantity measuring the number of interactions detected by the experiments is the instantaneous machine luminosity. Given a process with cross-section σ the events delivered by the LHC in Δt days are $N_{\Delta t} = \sigma L_{\Delta t}$, where $L_{\Delta t}$ is the instantaneous luminosity integrated over the time interval Δt.

The instantaneous luminosity, for a circular machine with approximately Gaussian bunches with dimensions σ_x, σ_z can be written as

$$L = \frac{fN^2}{4\pi\sigma_x\sigma_z} \,, \tag{4.1.1}$$

where N is the number of particle per bunch and f its revolution frequency. The design peak luminosity for LHC is 10^{34} cm^{-2} s^{-1}. In 2012 it reached $7.7 \cdot 10^{33}$cm^{-2} s^{-1}. The instantaneous luminosity is not constant over a physics run. Beam-beam or beam-gas interactions can degrade it, but the main reason for its constant dropping is the beam intensity lost in collisions. So we can parametrize the delivered luminosity as

$$L(t) = L_{\text{peak}}e^{-t/\tau}, \quad \tau^{-1} = \tau^{-1}_{\text{collisions}} + \tau^{-1}_{\text{beam}-\text{beam}} + \tau^{-1}_{\text{beam}-\text{gas}}\,. \tag{4.1.2}$$

This quantity is measured by the experiments at every bunch crossing using detectors located at small angles with respect to the beam pipe. This function in CMS is performed by the quartz-fibre calorimeter located at 11.2 m from the interaction point. However the real measurement, needed for physics analyses is given in CMS with the pixel detector, which is not read out at every bunch crossing, but has a reference cross section that is more stable with the running conditions and can be measured from a Van der Meer scan [131]. The integrated luminosity delivered to CMS in the
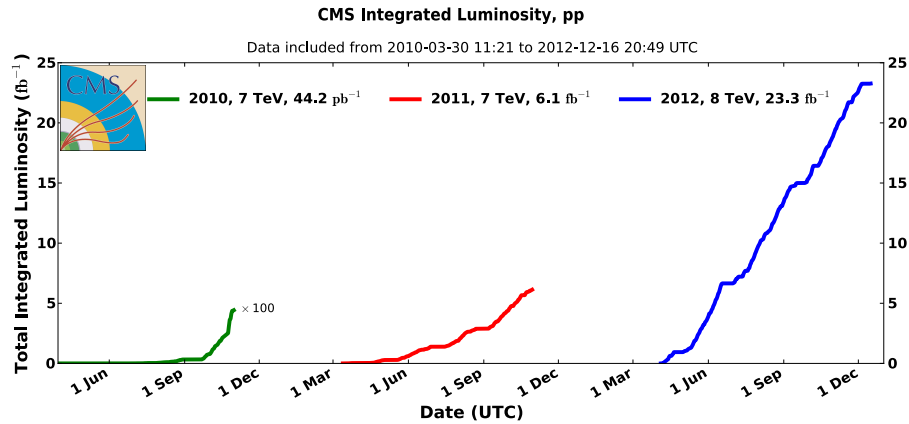
Figure 4.3: Cumulative luminosity versus day, delivered to CMS during the 2010 (green, multiplied by a factor of 100), 2011 (red) and 2012 (blue) data-taking periods [132].

past three years is shown in figure 4.3 reflecting the continuous improvement of the performances of the machine.

4.2   The Compact Muon Solenoid experiment

The Compact Muon Solenoid (CMS) detector, is located at the 5th crossing point of the LHC tunnel in the vicinity of the town of Cessy, in France. It was designed to withstand the LHC running conditions and at the same time to fulfill a rich physics program detailed in [7]. The main features of the detector, needed to operate in the LHC environment, are: radiation hardness, good time resolution and fast triggering capabilities. These requirements are imposed by the large proton-proton total cross section, the high beam intensity and the high frequency of the collisions. A further necessity is an high granularity, both to reconstruct single particles with high efficiency, in view of the physics goals, and to be able to operate with a high number of Pile-Up (PU) interactions[1] (in the 2012 run they already peak at ≈ 20 per bunch-crossing and we have not yet reached the nominal luminosity).

CMS was designed with these requirements in mind. It owes its name to a superconducting solenoid of 6 m of internal diameter that contains, within the field volume, the silicon tracking detector (pixel+strips), the $PbWO_4$ crystals electromagnetic calorimeter (ECAL) an the brass/scintillator hadron calorimeter (HCAL). Muon drift chambers (DT), cathode strip chambers (CSC) and resistive plate chambers (RPC) are embedded in the steel return yoke of the magnet. The magnetic field reaches up to 4 T.

---

[1]In a *pp* collision selected by the experiments at the LHC, other than the vertex where the hard scattering took place, several softer interactions occur. The contributions to the event from this additional interactions are generically denoted as pile-up.
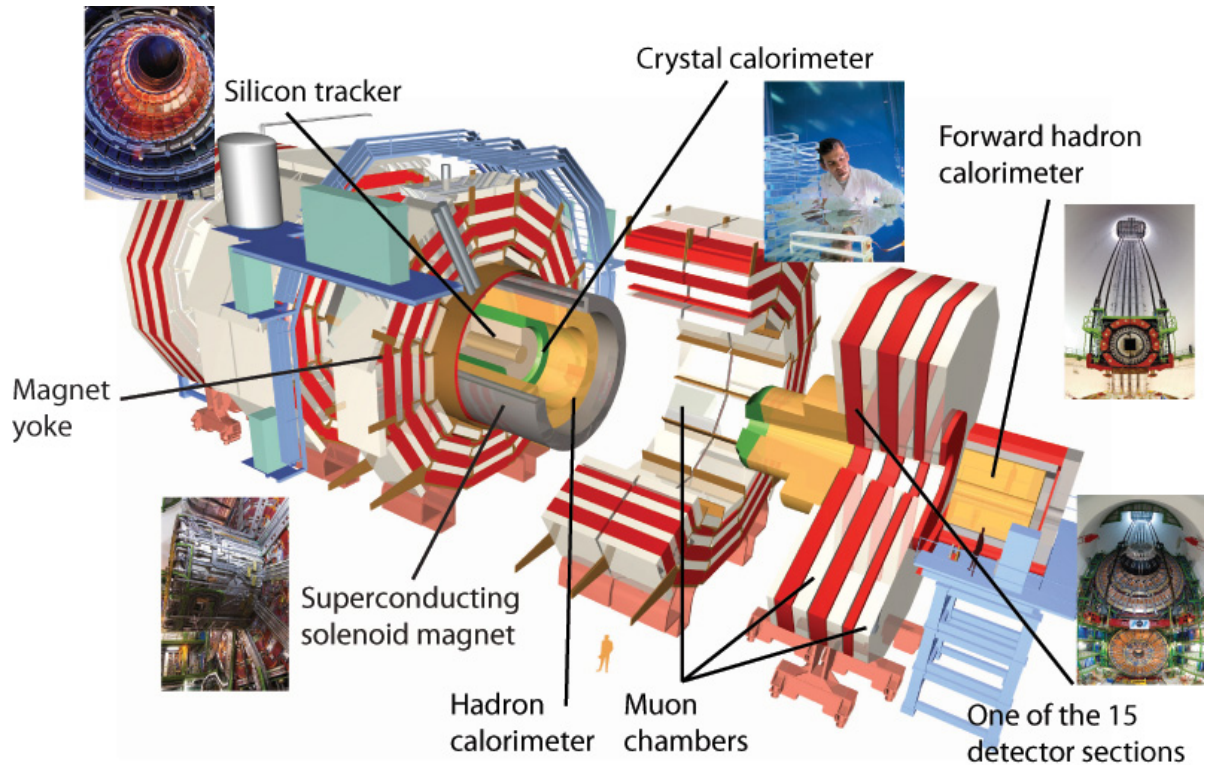
Figure 4.4: View of the CMS detector and its main components.

The apparatus is divided in a barrel, covering the central region, and two endcaps allowing almost a full coverage of the solid angle. A detailed description can be found in [129] and a global view of the detector is presented in figure 4.4

The main characteristics of this apparatus are the great electron and photon energy resolution (the dielectron and diphoton mass resolution is $\approx 1\%$ at 100 GeV), the high muon momentum resolution (also $\approx 1\%$ at 100 GeV), the efficient muon charge discrimination up to momenta of $\mathcal{O}\,(1\text{ TeV})$ and the good missing transverse energy (ME_T) and dijet mass resolution, provided by the fine segmentation of the calorimeters[2] (in particular the ECAL granularity) and their coverage up to $|\eta| < 5$. The inner pixel detector also allows efficient τ and b-jets tagging both offline and at the triggering level.

For later convenience we report that CMS uses a right-handed coordinate system, with the origin at the nominal interaction point, the x-axis pointing to the centre of the LHC, the y-axis pointing up (perpendicular to the LHC plane), and the z-axis along the anticlockwise beam direction. The polar angle, θ, is measured from the positive z-axis and the azimuthal angle, ϕ, is

---

[2]The granularity of the electromagnetic calorimeter allowed to implement the Particle Flow reconstruction algorithm that is the main reason for CMS good energy resolution. The algorithm is described in section 4.2.6.

measured in the x-y plane. The pseudorapidity is defined as $\eta = -\log\tan(\theta/2)$.

Other than the detector itself a crucial ingredient for the CMS physics program is the triggering and data acquisition infrastructure. With $\approx 10^9$ interactions/s at design luminosity it is impossible to record all LHC events. To comply with the current storage limits and speed of recording data, the trigger system has to achieve a rejection of $\approx 10^6$, ideally without missing any interesting physics. The CMS trigger and data acquisition system consists of 4 parts: the detector electronics, the Level-1 trigger processors , the readout network, and an online event filter system that executes the software for the High-Level Triggers (HLT). We discuss it in more detail in section 4.2.5, after describing, in the following subsections, the components of the CMS detector.

4.2.1   The inner tracker

The CMS inner tracker operates in the LHC environment outlined above, corresponding to roughly 700 charged particles, every 50 ns. So to insure both a fast response, radiation-hardness and high granularity, the tracker was built using 200 m^2 of silicon that cover the $|\eta| < 2.5$ region. Closest to the interaction point is the pixel detector, composed of 66 million pixels with an area of 100×150 μm^2 in the $r - \phi$ and z directions. This insures an average occupancy of $\approx 10^{-4}$. The pixels are organized in three concentric barrel layers with two endcap disks on each side of them. The 3 barrel layers are located at mean radii of 4.4 cm, 7.3 cm and 10.2 cm, and have a length of 53 cm. The two endcap disks go from 6 to 15 cm in radius and are divided in blades rotated by $20°$ around their central radial axis [133]. This was done to exploit the effect of the large magnetic field on the drift of the charges that can induce charge-sharing between neighboring pixels and produce a cluster of pixels with a signal.

Going further from the interaction point the flux is considerably reduced and in the intermediate region of the tracker ($20 < r < 55$ cm) silicon microstrips with cells of a much larger surface are installed: 10 cm $\times 80\mu$m. This still insures an occupancy of $\approx 2 - 3\%$. In the outermost region the granularity can be further reduced going to 25 cm $\times 180\mu$m, maintaining an even lower occupancy. The strip sensors are divided into a Tracker Inner Barrel (TIB) made of four layers going up to $|z| < 65$ cm, a Tracker Outer Barrell (TOB) with six layers of half-length $|z| < 110$ cm and into two endcap detectors, the Tracker End Cap (TEC) comprising 9 disks in the region 120 cm $< |z| < 280$ cm and three small disks filling the gap between the TIB and the TEC, labelled Tracker Inner Disks (TID). The modules in the first two layers of TIB and TID, the first two rings of TOB and rings 1, 2, and 5 of the TECs carry a second micro-strip detector module which is mounted back-to-back with a stereo angle of 100 mrad. A schematic view is shown in figure 4.5.

This setting insures a spatial resolution of 10 μm $\times$ 20 μm in the pixel detector and of $23 - 34$ μm $\times$ 230 μm in the silicon detector. Other than occupancy and spatial resolution, another aspect of the detector is crucial for physics. Ideally the tracker should leave a particle transversing its layers almost unaffected, not depriving it of any observable fraction of its energy. This would allow the calorimeters that follow it to operate in optimal conditions. The active material in the tracker is close to fulfill this requirement, however the silicon is supported by a
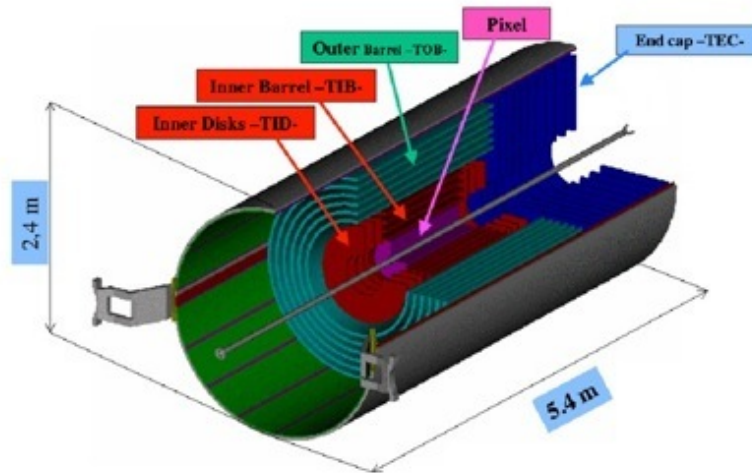
Figure 4.5: Layout of the CMS inner tracking system.

rather massive apparatus providing cooling and power. The complete material budget was measured with an accuracy higher than 10% [134] yielding the map in figure 4.6. We can see that the thickness of the tracker varies between 0.4 radiation lengths in the inner region up to 1.8 at $|\eta| \approx 1.4$. Therefore photon conversions and electron radiation must be taken into account while reconstructing electromagnetic objects.

The technical specifications described so far are reflected in great physics performances of the tracker system. In figure 4.7 we show the momentum resolution and reconstruction efficiency for muon tracks. The latter is very close to one in the whole η range while the momentum relative error is around 1% for 100 GeV muons in the central region and remains below 7% for any η. Another important feature of the tracking system is the high vertex reconstruction efficiency (that goes to one for $N_{\text{tracks}} > 4$) and the good track impact parameter resolution (well below 100 μm already for $p_T^{\text{track}} > 3$ GeV) [136], that are crucial for b-jet identification as we will better specify in the following chapter.

4.2.2   The electromagnetic calorimeter

The CMS electromagnetic calorimeter is composed of PbWO$_4$ crystals arranged in a barrel section (EB) and an endcap section (EE). The former covers the azimuthal coordinate up to $|\eta| < 1.479$, while the latter extends from there to $|\eta| < 3.0$. Crystals have a truncated pyramidal shape. They are oriented towards the interaction point, forming a quasi-projective geometry, with a slight tilt of 3° with respect to the line joining the vertex with the center of their square face. In the barrel they have the cross section facing the interaction point of 22×22 mm^2 in $\Delta\phi \times \Delta\eta$ and a length of 230 mm. In the endcap the crystals have a cross-section of 28.6×28.6 mm^2 and length 220
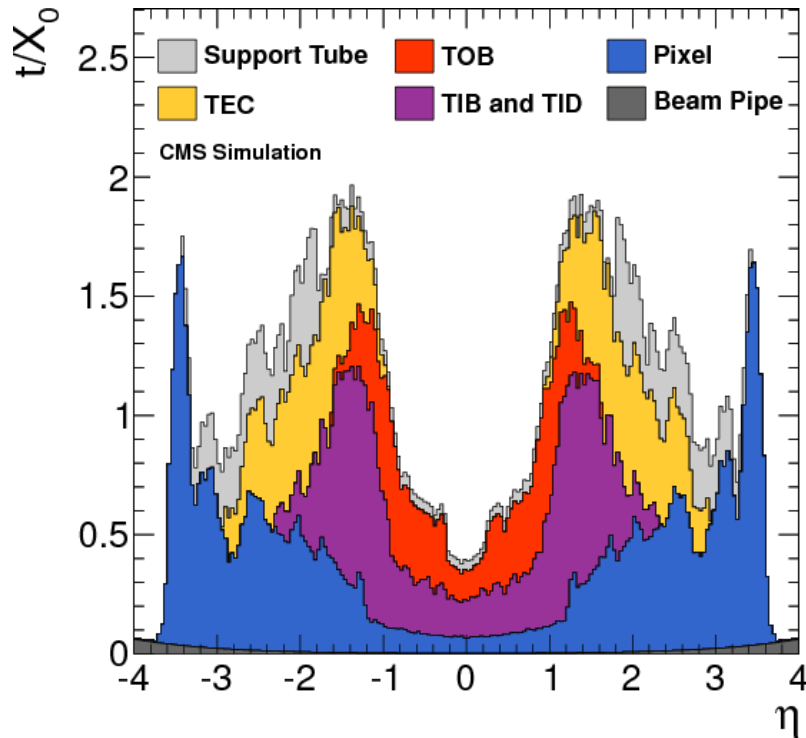
Figure 4.6: Map of the CMS tracker material budget expressed in radiation lengths, as a function of the azimuthal coordinate η [135].

mm.

The barrel detector has an inner radius of 1.29 m and contains 61200 crystals. The light readout is performed by a pair of Avalanche Photo Diodes (APDs), each with an active area of 5×5 mm^2, operated at gain 50, at a temperature of 18° C and read out in parallel. Their gain stability directly affects the ECAL energy resolution. The endcap detector is located at a distance of 3.15 m from the nominal interaction point along the beam axis. Each crystal is read out by one Vacuum Photo Triode (VPT) with a diameter of 25 mm and an active area of ≈ 280mm^2. These VPTs have an anode of very fine copper mesh (with a 10μm pitch) allowing them to operate in the CMS magnetic field.

In the region $1.653 < |\eta| < 2.5$ the crystal calorimeter is integrated by a sampling calorimeter made by lead radiators and silicon sensors (ES). This preshower detector improves the separation between prompt photons and products of π^0 decays. Two pairs of silicon sensor planes (sampling the x and y shower profile) follow two lead radiators with a depth of two and one radiation-lengths respectively.

The material of which the crystals are composed was chosen by virtue of its short radiation length $X_0 \approx 0.89$ cm, small Moliére radius ≈ 2.2 cm and fast response (80% of the light is emitted
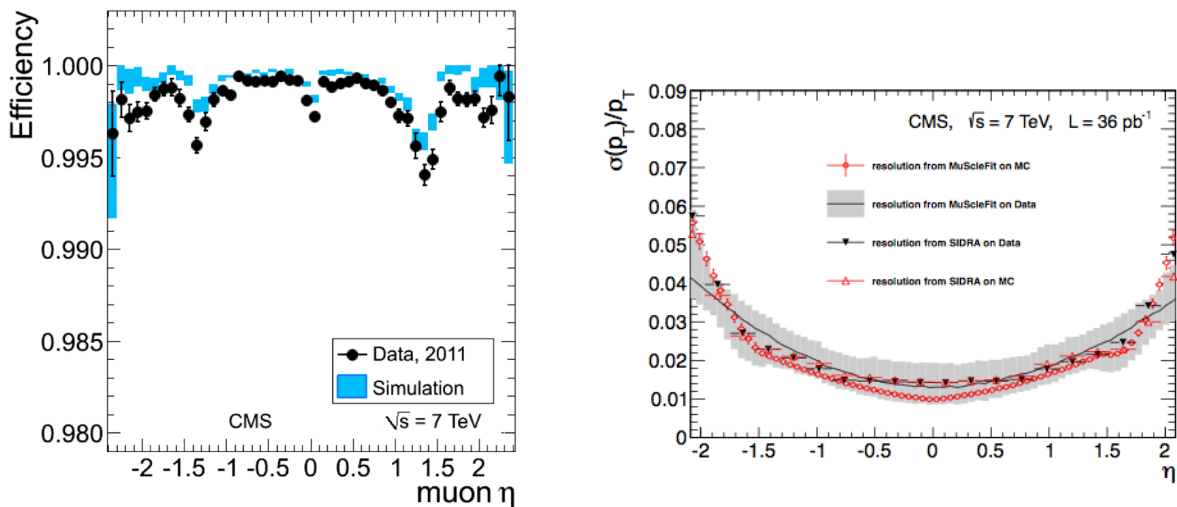
Figure 4.7: Left: Global track reconstruction efficiency for muons versus η. Right: Relative transverse momentum resolution as a function of η, in data and MC simulation measured by applying the MuScleFit and SIDRA methods [137] to muons produced in the decays of Z bosons.

within the first 25 ns). Furthermore the radiation tolerance of the crystals is sufficiently high to ensure good performances in the LHC environment. Radiation has no effect on the scintillation mechanisms, but it creates color centers in the crystal lattice. This process has been observed to be reversible if the crystals are left in a radiation-free environment. However it affects energy resolution and to have a reliable measurement CMS constantly calibrates the crystals with a laser source.

The performance of the detector was studied in electron test beams [129] and also in-situ using cosmic ray events [138] and was then finalized using collision events [139]. Here we show only results pertaining to its energy resolution that can be parametrized as

$$\left(\frac{\sigma(E)}{E}\right)^2 = \left(\frac{S}{\sqrt{E}}\right)^2 + \left(\frac{N}{E}\right)^2 + C^2 \,, \tag{4.2.1}$$

where S is the intrinsic stochastic term, N the noise and C the constant term. For test beam electrons with energies between 20 and 250 GeV the parameters were found to be $S = 2.8\%$, $N = 124$ MeV and $C = 0.3\%$. As shown in figure 4.8, for $E \sim 100$ GeV the constant term is already dominant.

4.2.3   The hadronic calorimeter

The barrel section of the hadronic calorimeter (HB) is installed between the ECAL and the super-conducting solenoid, leaving room for a total radial width of 1.18 m. Therefore space constraints
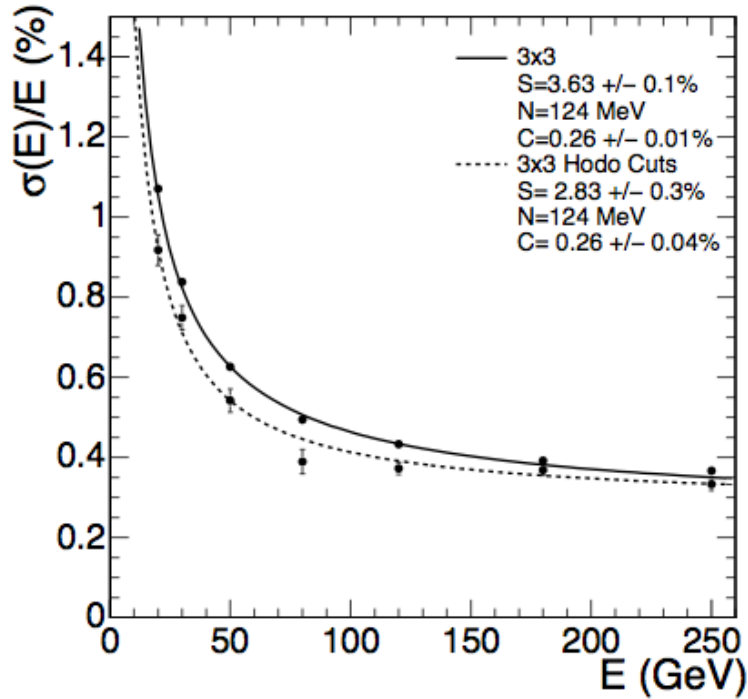
Figure 4.8: ECAL supermodule (an array of 3×3 crystals) energy resolution as a function of electron energy, measured from a test beam. The upper series of points correspond to events taken with a 20×20 mm^2 trigger. The lower series of points correspond to events selected to fall within a 4×4 mm^2 region. The energy was measured with electrons impacting the central crystal. For more details on the conditions of the measurement we refer to [140].

partially oriented the design of this subdetector that is complemented by the HO, a component placed outside of the solenoid to catch the tails of the hadronic showers. The magnet itself is used as an additional absorber layer of $1.4/\sin\theta$ interaction lengths for HO.

The key requirements for the HCAL were good containment, geometric hermeticity for ME_T measurements and minimization of the non-Gaussian tails in the energy resolution. For these reasons the HCAL design maximizes the material inside the solenoid. The barrel detector covers the central region up to $|\eta| < 1.3$, the endcap part (HE) extends to $|\eta| < 3$. The hermeticity is provided by the forward calorimeter (HF) that covers the region $3 < |\eta| < 5$. HB is organized in 36 identical azimuthal wedges. Each wedge is segmented into 16 azimuthal plates, bolted together in a way that does not leave any projective dead material.

HCAL is a sampling calorimeter, where brass is used as the absorber, except for the first and last layers, made of stainless steel for structural reasons. The active material consists of plastic scintillator tiles read out with embedded wavelength-shifting fibers. HF, to withstand the higher radiation output at low angles, is made of steel and quartz fibers.
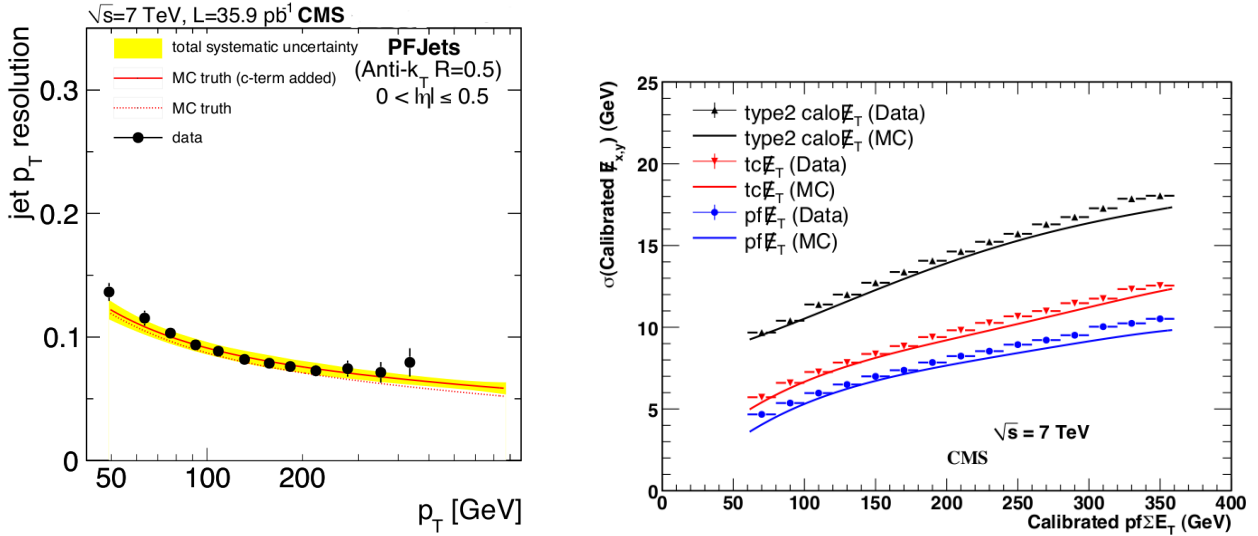
Figure 4.9: Left: PF jets p_T resolution in data versus MC truth before (dashed red line) and after (solid red line) correction for the measured discrepancy between data and simulation [144]. Right: Calibrated ME_T resolution versus calibrated Particle Flow $\sum E_T$ for different ME_T reconstruction algorithms (In blue PF technique) [143].

The granularity of HB and HE is a multiple of that of the ECAL. Up to $|\eta| < 1.6$ the towers have size $\Delta\phi \times \Delta\eta = 0.087 \times 0.087$ that increases to 0.17×0.17 for higher $|\eta|$.

Combining ECAL and HCAL the system is undercompensating, giving a larger response for electrons than for hadrons of the same energy [141]. Correcting for this effect a response linear to 1.3% to hadrons momenta between 5 and 350 GeV was achieved [141]. The jets and ME_T energy resolution was measured on $\sqrt{s} = 7$ TeV [142, 143, 144] collision data. The best performances were obtained using the Particle Flow (PF) algorithm, described in section 4.2.6. Jet p_T resolutions between 10% and 5% were achieved up to $|\eta| < 2.4$ (see the left panel of figure 4.9 for $0 < |\eta| \leq 0.5$). Similar values were obtained on the ME_T resolution, as can be seen in the right panel of figure 4.9. A more complete treatment of jets inside CMS is given in chapter 5.

4.2.4   The muon system

The muon detectors are contained in the magnet return yokes of CMS and are divided in a central part (barrel $|\eta| < 1.2$) and a forward detector (endcap $1.2 < |\eta| < 2.4$). In figure 4.10 we show pictures of the installation that allow to appreciate the geometric layout of the detector.

The barrel detector consists of 4 concentric stations of 250 chambers, divided into 5 wheels. The wheels contain 12 sectors, each covering a 30° azimuthal angle. The 2 innermost stations, consist of a DT chamber placed between 2 RPCs. The 2 outermost stations contain packages of a
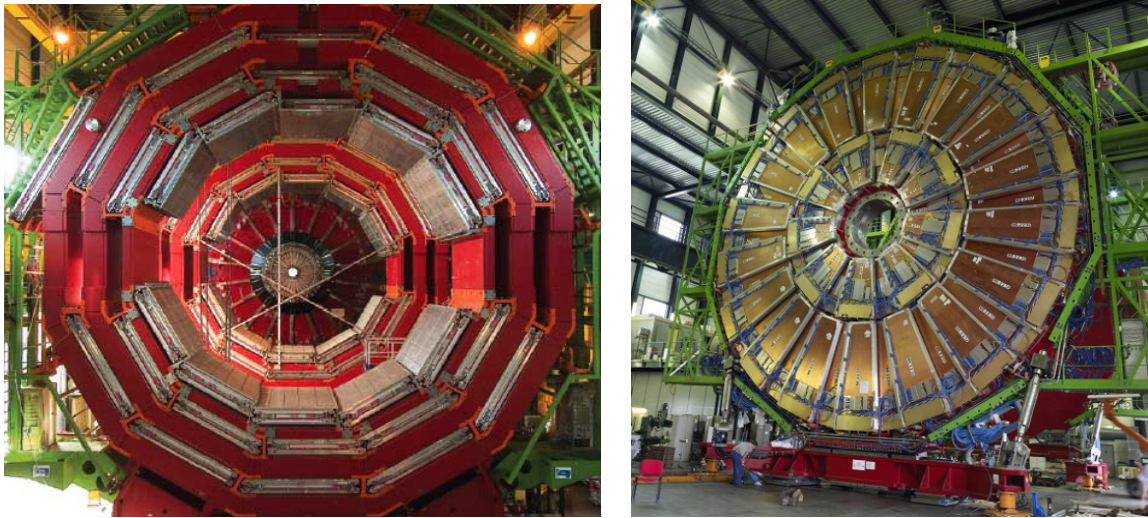
Figure 4.10: Left: View of one of the 5 wheels of the CMS muon barrel detector during installation. The steel return yoke is red, gray DT superlayers are interlaid. Right: CMS muon endcap. The copper-colored petals are cathode strip chambers.

DT chamber coupled to a layer made of 1, 2, or 4 RPCs, depending on the sector and station. Each RPC detector consists of a double-gap bakelite chamber, operating in avalanche mode to provide a very fast response, ideal for triggering, but poor spatial resolution. Position measurements are performed by the DT chambers, in each station 12 layers of drift tubes are divided into 3 groups of 4 consecutive layers (SuperLayers). Two SuperLayers measure the $r - \phi$ coordinate in the bending plane (they have wires parallel to the beam line), and the third measures the z coordinate running parallel to the beam. The first $r - \phi$ SuperLayer is separated from the other two, this gives a lever arm of about 28 cm for the measurement of the track direction.

There are two muon endcaps at the opposite sides of the barrel, each one is divided into 4 stations made of CSCs. The CSCs are trapezoidal in shape and consist of 6 gas gaps, each gap having a plane of radial cathode strips and a plane of anode wires running almost perpendicularly to the strips. The gas ionization and electron avalanche caused by a charged particle produces a charge on the anode wire and an image charge on a group of cathode strips.

The different choices between barrel and endcap are determined by the fact that in the central region the magnetic field is lower and uniform and the muon flux is less important with respect to the higher η region.

The momentum resolution has been measured using cosmic rays traversing the full detector. Comparing the momentum measurement in the upper and lower part of the spectrometer, the momentum resolution was found to vary between 1% and 10% going from $p_T^\mu \approx 10$ GeV to 1 TeV [145]. These results were later confirmed by measurements on collision data [137]. Note that the good momentum resolution of the tracker plays an important role in this measurement. This
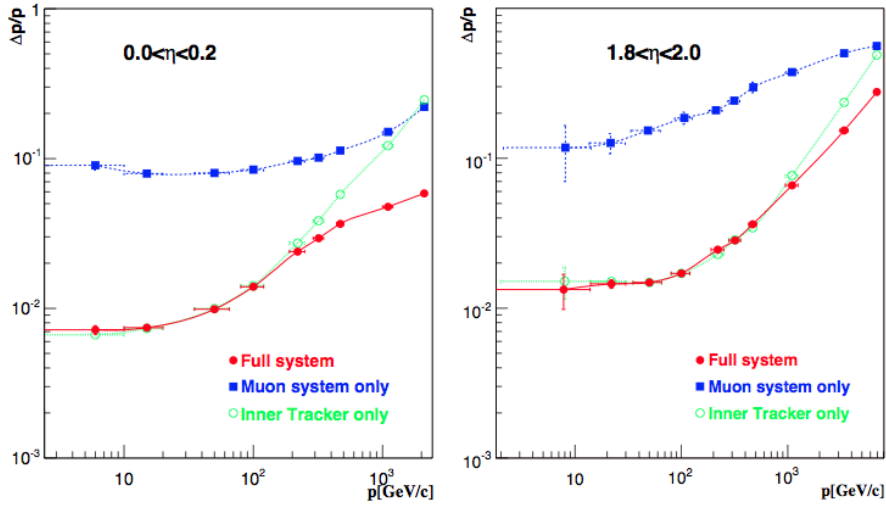
Figure 4.11: Muon p resolution for $0.0 < |\eta| < 0.2$ (left) and $1.8 < |\eta| < 2.0$ (right). The green points are for the silicon tracker only, the blue ones for the muon system only while the red ones combine all the detector information [140]. The results in figure 4.7 are more recent and show that for $|\eta| > 1.0$ these Technical Design Report estimates are slightly optimistic, but still more than adequate to show the tracker and muon system performances.

emerges from figure 4.11 from which it is clear that at low momentum the tracker dominates the resolution, while for $p \gtrsim 200$ GeV (in the central region) the contribution of the muon system becomes important.

A great dimuon mass resolution is another of the strengths of the system as illustrated by the plot of the known resonances going from the ω to the Z in figure 4.12.

4.2.5   Trigger and data acquisition

The trigger and data acquisition infrastructure is the system responsible for reducing the massive LHC data output, reading it from the detector and storing it for offline processing and analysis. To perform these functions both programmable hardware and higher level software implemented on standard processors are needed.

The CMS trigger system is divided into two levels, the level one (L1) trigger and the high level trigger (HLT).

The first step is made of the detector front-end electronics and custom (and semi-custom) programmable electronics located in a cavern physically separated from the detector. This imposes a minimum transit time for the signals to go from the detector front-end electronics to the trigger cave and back to the detector. The total time available, including the decision making, is 3.2 μs. During this time the detector data is held in buffers. The information used by the L1 trigger
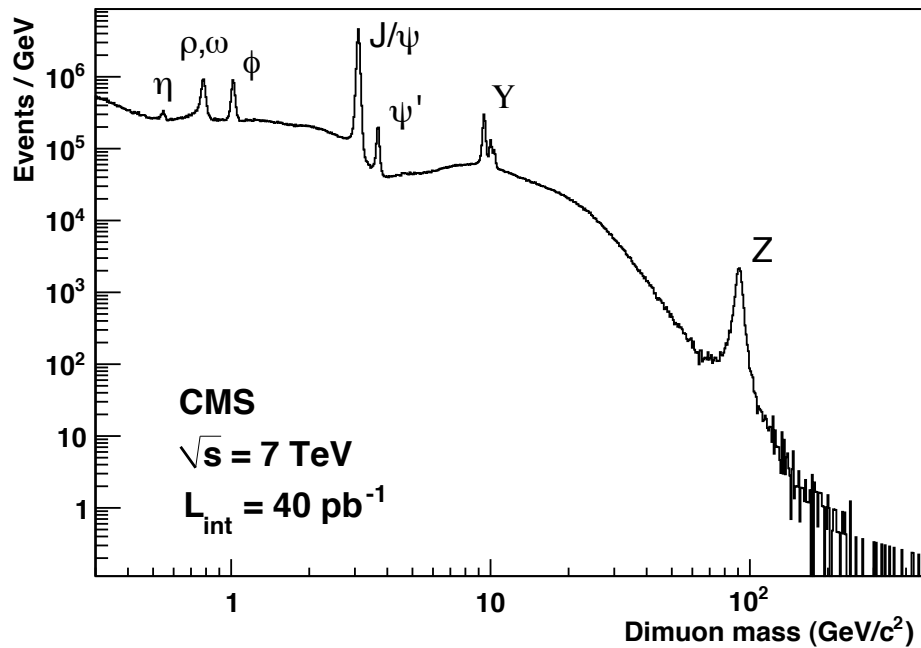
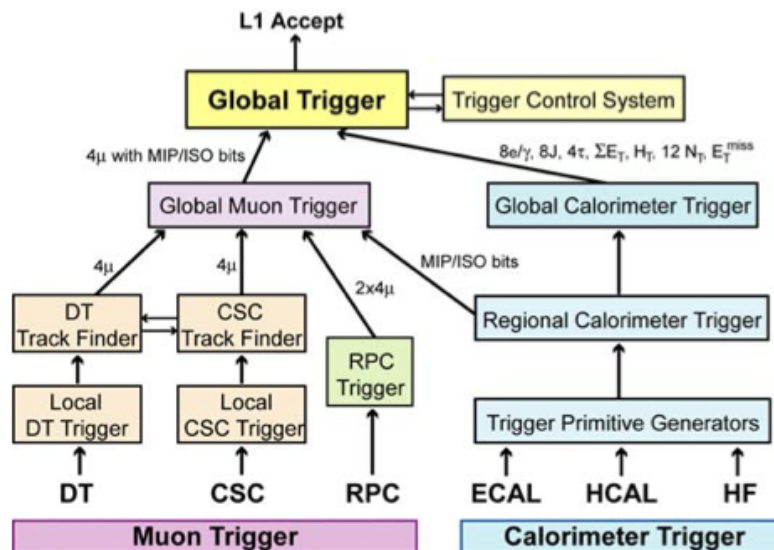Figure 4.12: Dimuon invariant mass measured with the CMS detector [146].

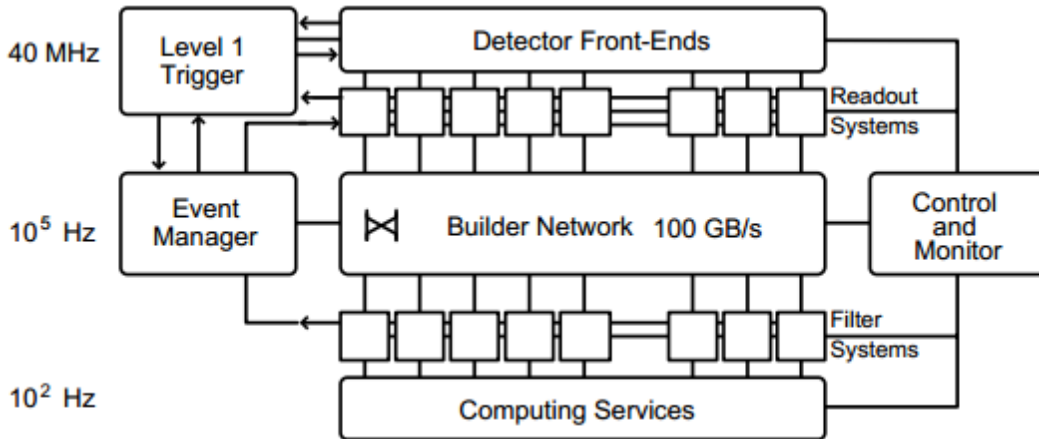Figure 4.13: Architecture of the CMS L1 trigger [129].

Figure 4.14: Schematic view of the CMS Data Acquisition infrastructure.

comes only from the calorimeters and the muon system and it is not the full event contained in the buffers, but a coarser version (resolution and granularity are reduced) based on energy deposits in calorimeter trigger towers and track segments or hit patterns in muon chambers. The logical structure of the trigger (depicted in figure 4.13) is the following: first we have Local Triggers or Trigger Primitive Generators (TPG), based on local deposits in the calorimeters and hits/segments in the muon chambers. These are followed by Regional Triggers, that combine their information and use pattern logic to determine ranked and sorted trigger objects such as electron or muon candidates in limited spatial regions. Energy or momentum and quality of the objects determine their rank. The Global Calorimeter (GCT) and Global Muon (GMT) Triggers select the highest-rank calorimeter and muon objects across the entire experiment and transfer them to the Global Trigger (GT), the highest level entity of the Level-1 hierarchy. This unit is responsible for the final decision, based on algorithmic calculations and on the readiness of the sub-detectors and the Data AcQuisition (DAQ), which is determined by the Trigger Control System (TCS). The Level-1 Accept (L1A) decision is communicated to the sub-detectors through the Timing, Trigger and Control (TTC) system. A more complete description can be found in [147].

Following the L1 decision, the HLT has access to the complete read-out data and can therefore perform complex calculations similar to those made in the offline analyses. The HLT software is hosted on a processor farm, containing $\mathcal{O}(10^3)$ processors. This choice was made both to benefit from the continuous advances in computing technology and to have the maximum possible flexibility in the design of the selection algorithms. The general concept of the triggering algorithms is constrained by speed needs. Decisions are made in the order of milliseconds. Therefore rather than reconstructing all possible objects in an event, whenever possible only those objects and regions of the detector that are actually needed for the trigger decision are reconstructed. This leads to the idea of partial reconstruction and to the notion of many virtual trigger levels. Calorimeter

and muon information are used, followed by use of the tracker pixel data and finally the use of the full event information (including full tracking).

The HLT decision is just the final step in the DAQ process shown schematically in figure 4.14. First detector front-ends are read out by "Readout Columns", each of which contains a number of Front-End Drivers and one Readout Unit which is responsible for buffering the event data and for interfacing to the switch. Then the data reach the Filtering System (FS) passing through the Builder Network (a large switching fabric, capable of supplying 800Gb/s sustained throughput to the Filtering Systems). The FS performs the HLT step of the process, then data are transmitted to the online and offline Computing Services. These data include events selected by the HLT for physics analyses and calibration, some fraction of events rejected by the triggers, collected calibration information, and data for online monitoring. Part of this output will be processed online and another fraction will be transmitted to offline systems. The whole flow of data through the DAQ system is controlled by the Event Manager. More details on the CMS DAQ system can be found in [148] and a schematic representation is shown in figure 4.14.

At the end of the DAQ flow data must be reconstructed and stored. The rate is high ≈ 230 MB/s and the collaboration is spread worldwide. This led to adopt a distributed computing model. The system is based upon Grid middleware, with the common Grid services at centers defined and managed through the Worldwide LHC Computing Grid (WLCG) project, that sees the LHC, the computing centers and their hosting institutions, as well as the middleware providers collaborating in the effort [149]. The infrastructure is organized in Tiers of decreasing size.

The data passing the HLT are divided into Primary Datasets (PD), defined in terms of basic physics objects (for instance we have a `SingleMu` PD, a ME_T PD, etc.) with a minimal overlap (no more than 10% of events are shared between two PDs). The data thus organized are received by the Tier-0 center at CERN in RAW format (the full information from the detector plus trigger decisions). The Tier-0 stores the data and reconstructs them, applying detector-specific filtering and corrections, cluster and track finding and primary and secondary vertex reconstruction. The reconstructed events contain high level physics objects and a record of the hits and clusters used in their production. After this step the data are sent to the Tier-1 centers (≈ 6) for mass storage and re-processing. At the low end of the chain are the Tier-2's (≈ 50) where the analyses are performed, they receive the data from the Tier-1 sites and are used also for Monte Carlo event generation. This concludes the flow of centrally reconstructed data, however there are also several Tier-3's that are mainly used by analysts to store data further processed with custom designed code.

4.2.6   The particle flow algorithm

One aspect of the offline reconstruction and analysis software of CMS has become more and more important to CMS physics analyses and constitutes a key ingredient of the search described in the following chapters. It is the Particle Flow reconstruction algorithm [150] that aims at reconstructing and identifying all stable particles in the event. Once a list of individual particles is produced it is used to build jets, compute the ME_T, reconstruct τ's from their decay products

and quantify charged leptons isolation.

The PF success in CMS is due to the fact that charged hadron momenta are very well measured in the tracker, the photon energy is precisely measured in the ECAL and the neutral hadrons are, on average, only 10% of the total jet constituents. A good calorimeter granularity is an important detector requirement to implement the PF algorithm, since it is needed to subtract charged hadrons and photons deposits and measure the neutral hadron energy fraction.

The ECAL granularity and the large uniform magnetic field are crucial as they allow photons to be separated from charged-particle energy deposits even in jets with a p_T of several hundreds of GeVs. Furthermore the combined resolution of ECAL and HCAL (of $\mathcal{O}(10\%)$ at 100 GeV) allows to detect neutral hadrons on top of the charged hadrons energy deposits, whose momentum is precisely measured in the tracker. One of the reasons behind the success of the PF algorithm is precisely the possibility of measuring the charged fraction of the energy of a jet using the tracker. Since most stable particles have a relatively low p_T, even in an event with high hadronic activity (an average of 10 GeV for a 500 GeV jet), the improvement in resolution is dramatic, also considering that the charged component of a jet is roughly 2/3 of the total.

The first step in the particle flow reconstruction takes into account the fact that a single particle leaves several traces in different sub-detectors: calorimeter clusters, possibly a track in the silicon detector and hits in the muon chambers. To identify the different particles all the information must be employed. The link algorithm is the first step of the PF reconstruction. It defines a distance between any two of these elements in the event. The algorithm then produces blocks of elements linked directly or indirectly. The granularity of the CMS subdetectors insures that blocks typically contain only one, two or at most three elements. Then reconstruction and identification of particles from each block is performed by the PF algorithm itself. First each `Global Muon`[3] becomes a PF muon if its momentum is within 3σ of that measured only by the tracker. In this case its track is removed from the block. Then electrons are reconstructed. Pre-identified electron tracks are refitted to follow their trajectories to the ECAL. Then, based on position compatibility between the track and the ECAL deposit and several others calorimeter and tracker-oriented variables, a PF electron is identified [150]. The track and ECAL clusters are then removed from the block.

At this point additional quality criteria are applied to the remaining tracks [150], for instance the relative uncertainty on the measured p_T must be smaller than the relative calorimetric energy resolution expected for charged hadrons. Several tracks can be linked to the same HCAL cluster, in which case the sum of their momenta is compared to the calibrated calorimetric energy. On the other hand, if a track is linked to several HCAL clusters, only the link to the closest cluster is kept for the comparison, the same is done for the ECAL. It is worth to notice that since the HCAL response to hadrons is nonlinear and the ECAL response to hadrons is different from the response to photons, the ECAL and HCAL cluster energies need to be recalibrated to have the procedure above working properly. However this affects mostly neutral hadrons that typically

---

[3]Muon reconstructed using information both from the tracker and the muon system. The selection procedure is described in more detail in section 6.3.2.

constitute 10% of the total energy in the event.

All tracks remaining in the block become PF charged hadrons. Their momentum and energy are taken directly from the track momentum, under the charged pion mass hypothesis. If the calibrated calorimetric energy is compatible with the track momentum within the uncertainty, the charged-hadron momenta are redefined by a fit of the measurements in the tracker and the calorimeters. This redefinition is relevant only at very high energies and/or pseudorapidities, where the tracker resolution is not optimal.

If the calibrated calorimetric energy is in excess with respect to the tracks momenta and the excess is larger than the expected calorimeter energy resolution (including also the uncertainty due to the presence of muons in the block) a PF photon and possibly PF neutral hadrons are identified. If the excess is larger than the total ECAL energy a photon is created with the ECAL deposit and a neutral hadron is associated to the remaining part of the excess. Otherwise only a photon is created. This is justified by the fact that 25% of the energy in a jet is carried by photons and only 3% of the ECAL deposit comes from neutral hadrons.

The most relevant aspect of the PF algorithm, for this work, is jet reconstruction that we discuss in more detail in the next chapter. For a more detailed account of its performances on other physics objects we refer to [151] and references therein. A comparison of ME_T resolutions was shown already in figure 4.9 and gives an idea of the improvement over traditional calorimeter clustering techniques.

4.3   Conclusion

In this chapter we have given an introductory description of the LHC and CMS experimental apparatuses. The ideas developed here constitute the basic building blocks of any measurement performed with the CMS detector. In the next chapter we elaborate further on two physics objects: jets and b-tagged jets, crucial to the new physics search to which these two chapters constitute the necessary introduction.

Chapter 5

Jet energy measurement and b-jet identification with the CMS detector

Measuring jets and b-jets properties is one of the main tasks of the LHC experiments. The high production cross-section facilitates studies of new kinematical regimes that can probe SM and BSM predictions. The analysis presented in this thesis explores one of these new areas of phase space, focussing on the tails of the jets and b-jets multiplicities. For this reason we present here the main ingredients needed to reconstruct and correctly measure the properties of jets with the CMS detector and the characteristics and performances of b-tagging algorithms. The results in this chapter are not original and were produced with the joint effort of several people inside the CMS collaboration, where possible we cited the relevant public document, but most of the tables and figures are present only in internal notes.

5.1 Jet reconstruction

In CMS four different types of jets are reconstructed: calorimeter (Calo) jets, Jet-Plus-Track (JPT) jets, Particle-Flow (PF) jets and track jets. We discuss jets clustered using the anti-k_T algorithm [152] with cone parameter $R = 0.5$. In the following, for comparison, we use also generator (Gen) jets reconstructed from all stable particles generated in the Monte Carlo (MC) simulation. The four "flavors" of CMS jets on data are

- **Calo jets**. They are clustered from energy deposits in the calorimeters (ECAL and HCAL). The basic building block is a calorimeter tower. In the barrel ($|\eta| < 1.4$) a tower corresponds to one HCAL cell and the underlying 5×5 crystal array in ECAL. In the endcap the geometric matching varies depending on the different regions. Towers with $E_T < 0.3$ GeV are not included in the reconstruction to suppress the contribution from pile-up events. Detector-dependent thresholds, listed in table 5.1, are imposed to reduce readout electronics noise.

- **JPT jets**. The information provided by the tracker is used to improve the p_T resolution and response of the calorimetric jets [153]. As a first step Calo jets are reconstructed following the procedure described above. Then tracks are associated to a jet using the spatial separation in (η, ϕ) between the track momentum measured at the vertex and the jet axis. The tracks momenta are then added to the jet. For tracks falling inside the jet cone an average energy deposit is subtracted from the calorimeter response. The algorithm then corrects the Calo jets axes taking into account both in-cone tracks and tracks bended outside of the calorimetric cone by the CMS magnetic field.

- **PF jets**. As discussed in the previous section the Particle Flow algorithm integrates information from different subdetectors to reconstruct a list of particles in the event. Jets are then clustered from single particles. The procedure makes use of tracking information and the excellent granularity of the ECAL that allow to separate the calorimetric contributions of charged hadrons, neutral hadrons and photons inside jets. This procedure Improves momentum and spatial resolution with respect to calorimetric jets. As discussed in section 5.3.1 only tracks compatible with the primary vertex are retained and the calorimetric deposits of charged hadrons originating from additional pile-up interactions are subtracted.

- **Track jets**. Only the information from the inner tracking system is used. Jets are reconstructed from well measured tracks, selected based on the association to the primary vertex and their quality [154]. Its independence from the calorimetric information makes this algorithm useful for cross-checks.

In the analysis and while discussing properties of b-tagging algorithms we always consider PF jets with $R = 0.5$. This reconstruction technique is known to give the best performances on the data and has become the standard for most CMS physics analyses.

5.2 Samples

The jet energy corrections discussed in the next sections were obtained from the first 1.6 fb^{-1} of 2012 $\sqrt{s} = 8$ TeV data. The data were collected using single jet triggers with p_T thresholds of $40, 80, 140, 200, 260$ and 320 GeV that together form the `Jet` dataset. The Monte Carlo samples used consist of QCD `PYTHIA` 6 [155] events reweighted to reproduce PU running conditions. The

Section	Threshold (GeV)
HB	0.7
HE	0.8
HO	1.1(3.5) Ring 0 (Ring 1,2)
HF (long)	0.5
HF (short)	0.85
EB	0.07 (per crystal)
EE	0.3 (per crystal)
EB Sum	0.2
EE Sum	0.4

Table 5.1: Offline cell thresholds used in Calo and JPT jets reconstruction in different sections of the calorimeters. Independent thresholds are placed in different sections (rings) of HO, and in different readouts in HF (long and short fiber). In ECAL, in addition to energy thresholds on individual crystals, thresholds are applied also to the sum of crystal readouts corresponding to the same tower.

pile-up distribution for data is derived by using the bunch-crossing-per-luminosity section instantaneous luminosity from the Luminosity Data Base together with the total pp inelastic cross-section to generate an expected pile-up distribution, correctly weighted by the per-bx-per-lumi section integrated luminosity over the entire data-taking period.

The Z+jets data sample was collected from the first 1.6 fb^{-1} of 2012 $\sqrt{s} = 8$ TeV data using dimuon and dielectron triggers with p_T thresholds of 17(8) GeV on the leading (subleading) lepton. The Drell-Yan MC samples were generated using `MadGraph` [156] and the tau-lepton decays were handled with `TAUOLA` [157].

The γ+jets data sample was collected from the first 1.6 fb^{-1} of 2012 $\sqrt{s} = 8$ TeV data using single photon triggers with p_T thresholds going from 10 to 35 GeV. The γ+jets MC samples were generated using `PYTHIA` 6 and its Z2 tune. All MC samples are processed through a full GEANT4 simulation of the CMS detector [158].

In several cases we refer to 7 TeV documentation while discussing 8 TeV results. The reason is that in those specific cases the documentation is more extensive and the relevant information has not changed.

5.3   Jet energy calibration

The response of the CMS calorimeters is non-uniform and non-linear. Furthermore electronic noise and pile-up (PU) interactions introduce in the event additional unwanted energy deposits. For these reasons the detector response must be corrected to obtain the energy of the true particle jet. CMS adopts a factorized multi-step procedure for jet energy calibration (JEC) that consists

of three steps (offset, MC truth correction and residual data-driven corrections) common to Calo, JPT and PF jets. The offset correction eliminates energy deposits due to PU and electronic noise. The MC truth factors are the largest component and bring the detector response close to the energy of the particle level jet, by using quantities extracted from simulation. The residual data-driven corrections are divided into a relative and an absolute scale measurement. The relative correction aims at compensating for the non-uniformity in η of the calorimeters, while the absolute correction removes variations from the non-linear p_T response. The relation between corrected four momentum P_μ^C and the uncorrected one P_μ^U can be summarized as follows

$$P_\mu^C = C_{\text{offset}}\left(p_T^{\text{raw}}\right) \times C_{MC}\left(p_T',\eta\right) \times C_R\left(\eta\right) \times C_A\left(p_T''\right) \times P_\mu^U \,, \tag{5.3.1}$$

where p_T^{raw} is the transverse momentum obtained from P_μ^U, p_T' is the transverse momentum of the jet corrected for offset and p_T'' is the transverse momentum of the jet corrected for offset, MC truth factor and η dependence. The data-driven corrections are generically small and are obtained from measurements of the absolute jet energy scale in the central region (from Z+jets and γ+jets events) and of the relative scale as a function of pseudorapidity from dijet events.

For PF jets, the only ones relevant to the original part of this work, the four-momentum is computed using the charged and neutral pion masses for hadrons and a null mass for PF photons. The single four-momenta are then added to obtain the jet P_μ.

5.3.1 Offset correction

The main component of the offset correction is due to PU interactions that have become increasingly important during LHC running, changing almost on a monthly basis. Even if PU can not be directly measured, several observables are related to it. The change in running conditions can be appreciated from the distributions of primary vertices per event in 2011 and 2012, shown in figure 5.1.

PU collectively describes three types of effects that cause energy deposits in the calorimeters at different times relative to the hard scattering process. In-time (IT) pile-up refers to energy from additional pp collisions in the current bunch-crossing (BX) other than the Primary Vertex (PV). This is the largest source of pile-up energy. In addition to that, there is early out-of-time (EOOT) pile-up, from energy left in the calorimeters during previous BXs, and late out-of-time (LOOT) pile-up, pertaining to energy from later BXs that is integrated with the current event energy. The two components of OOT PU have been dramatically reduced from 2011 to 2012 with a detector based choice. The HCAL (barrel and endcap) used an integration time of 4×25 ns, that was reduced to 2×25 ns. This brought down LOOT PU from 20% of the total PU energy deposit to almost zero and also reduced EOOT PU that gave already a small $(2 - 4\%)$ contribution in 2011. The remaining PU is corrected for using one of two software based techniques, the average offset method or the hybrid jet area method.

In the average offset procedure the p_T coming from PU is estimated from a Zero-Bias data
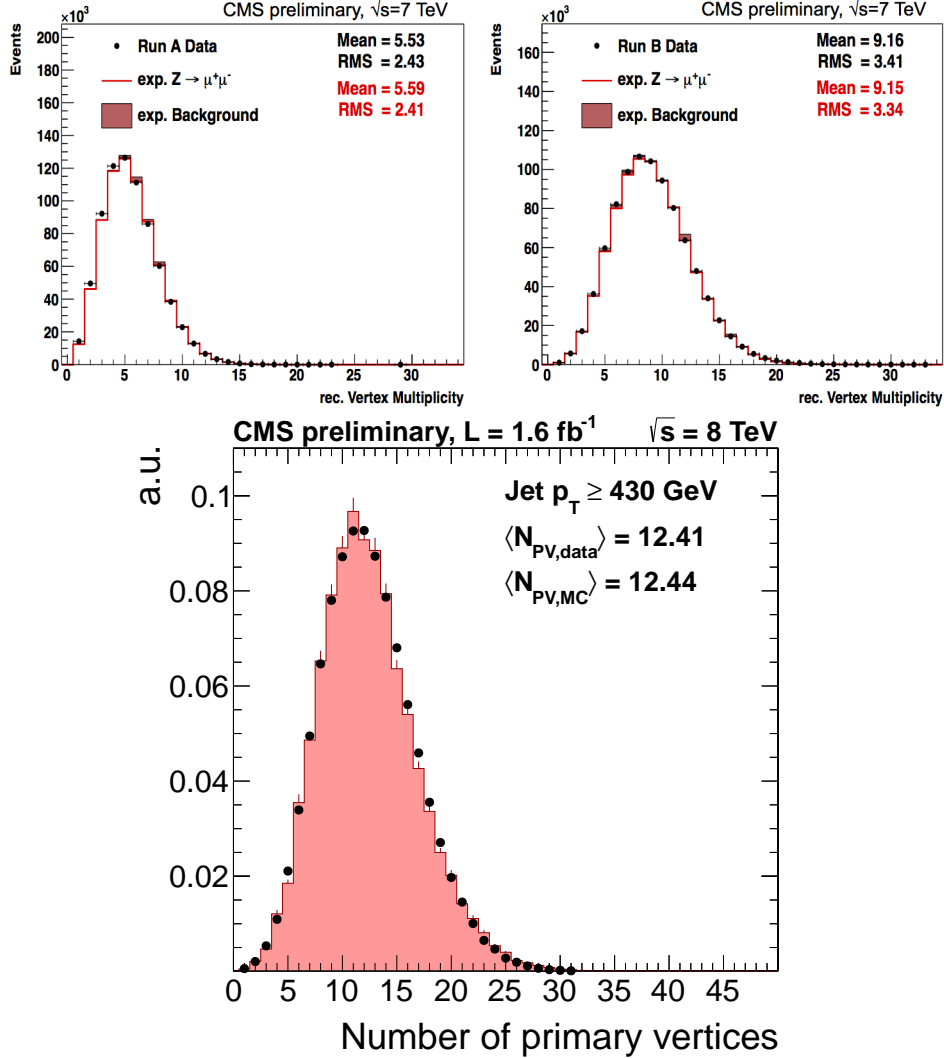
Figure 5.1: Reconstructed primary vertices per event in data and MC for the 2011 Run A period (top left), Run B period (top right) and 2012 (bottom). The $\sqrt{s} = 7$ TeV data correspond to approximately 4.6 fb^{-1} collected with dimuon triggers and further selected offline by requiring two opposite sign muons with $p_T > 20$ GeV, $|\eta| < 2.1$ and 60 GeV $< m_{\mu\mu} < 120$ GeV. The bottom plot was obtained from the jet samples described in section 5.2 after reweighting the MC.

sample [1], a Zero-Bias MC sample and a QCD MC sample. In each of the three samples the offset

---

[1]A Zero-Bias sample is collected with a beam bunch crossing-time trigger used to obtain 100% efficiency. Only active beam bunch crossings are read out to maximize the probability of obtaining events with valid collisions. The corresponding MC sample is constructed by overlaying a neutrino gun sample with Minimum-Bias events

p_T is measured event-by-event, finding the p_T deposited within the jet cone in different (η, ϕ) locations. The ϕ coordinate is chosen at random (and then the result is averaged) while η is scanned in 0.1 steps from 0 up to $|\eta| < 5$. The relevant p_T is measured from energy deposits in the case of Calo jets and from PF candidates momenta in PF jets. For each η bin the measurement is performed for different numbers of primary vertices (N_{PV}). The p_T dependence on N_{PV} can be parametrized as

$$p_T^{\text{offset}} = a + bN_{PV} + cN_{PV}^2 \,. \tag{5.3.2}$$

The coefficient a represents OOT PU (after noise is subtracted), while the other two terms are dominated by IT PU, that is almost linear in N_{PV}, $c \approx 0$. The correction is computed by averaging the offset over events and applying it as a multiplicative factor to the uncorrected p_T (p_T^U)

$$
\begin{aligned}
p_T &= p_T^U \times C_{AO}\left(\eta, N_{PV}, p_T^U\right) \,, \\
C_{AO}\left(\eta, N_{PV}, p_T^U\right) &= 1 - \frac{\langle p_T^{\text{offset}}\left(N_{PV}, \eta\right)\rangle}{p_T^U} \approx 1 - \frac{(N_{PV} - 1)\, b(\eta)}{p_T^U} \,,
\end{aligned}
\tag{5.3.3}
$$

where b is the slope of the p_T^{offset} dependence on N_{PV} in each η bin. The noise contribution (found to be < 250 MeV per jet over the entire η range) is estimated from the Zero-Bias sample, with a veto on the Minimum Bias trigger.

In this correction scheme every jet is assumed to contain the same average PU deposit. To relax this last assumption the hybrid jet area method was developed. First the area A of each jet in the event is computed [159], then the median p_T density ρ is obtained as the median of the distribution of p_T/A of the jets. The determination of ρ uses the k_T jet clustering algorithm that naturally cluster a large number of soft jets in each event [160]. Clearly the procedure would not give meaningful results in the limit in which a single jet is present in the event.

If we stopped here we would have a jet-by-jet offset correction in the form $p_T^C = p_T^U - \rho \times A$. However these first two steps are performed using the `FastJet` algorithm [161], that can not take into account the η non-uniformity of the detector. For this reason a third step is added to the algorithm where the η dependence of the offset p_T is taken from the previous average offset technique obtaining a correction factor

$$C_{HJA}\left(\rho, A, \eta, p_T^U\right) = 1 - A\frac{(\rho - \langle\rho_{UE}\rangle)\,\beta(\eta)}{p_T^U} \tag{5.3.4}$$

where $\langle\rho_{UE}\rangle$ is the average p_T density from the underlying event and electronics noise and is measured in events with exactly one reconstructed primary vertex (no pile-up). $\beta(\eta)$ is obtained from the modulation of the average p_T offset in pseudorapidity. A third technique, the Jet Area method, is equivalent to the one just described, but does not take into account the η dependence of the correction. The AO and HJA methods give a measurement of the PU energy that is in good agreement over a large range of reconstructed primary vertices, as can be seen from figure 5.2.

For PF jets there is the possibility of applying also charged hadron subtraction, which can be used in conjunction with one of the two correction methods described above. Using the tracker
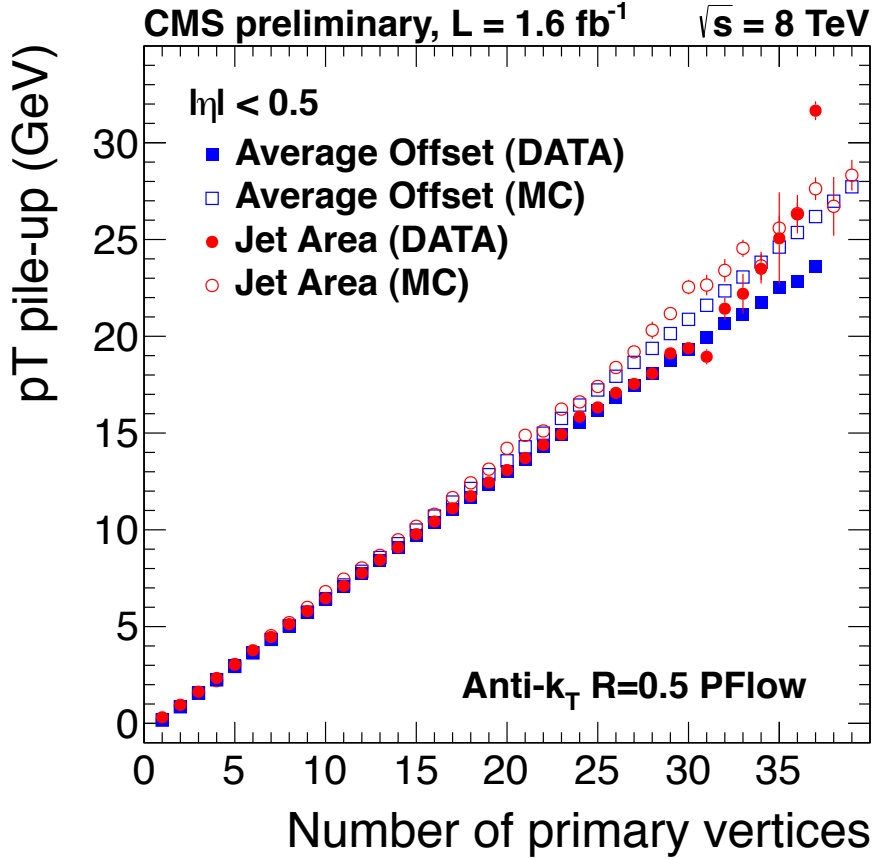
Figure 5.2: PU energy determination from the average offset and hybrid jet area methods for data and MC as a function of the number of primary vertices. Note that in the plot legend the HJA method is labelled Jet Area for brevity, but the plot was not done using the simpler Jet Area algorithm.

granularity, the subtraction is performed particle-by-particle for charge hadrons. Eliminating those that do not originate from the primary vertex. This reduces the multiplicative factors produced by one of the other two techniques and introduces the more precise particle-by-particle subtraction for a good fraction of the constituents of the jet.

The procedure described above closes nicely on data as can be seen from figure 5.3 that shows the CMS response $R = p_T^{\mathrm{corr}}/p_T^{\mathrm{gen}}$ (where p_T^{gen} is the p_T of the generator level jet) before and after PU mitigation techniques are applied for PF jets. After the corrections the response is close to 1 over two orders of magnitude in jet p_T and for $0 \leq N_{PV} \leq 30$. The residual p_T dependence is eliminated by the additional corrections described in the following sections.
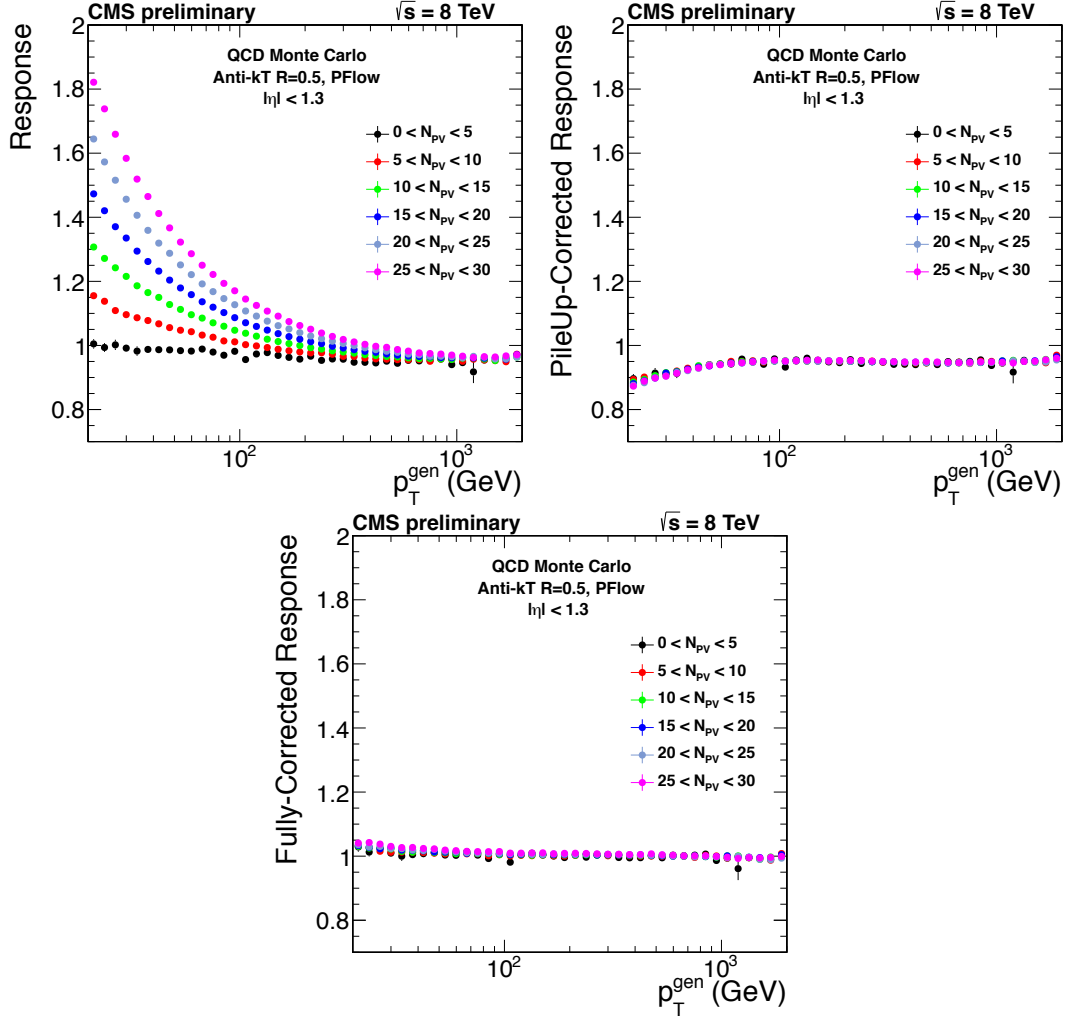
Figure 5.3: Response, $R = p_T^{\mathrm{corr}}/p_T^{\mathrm{gen}}$, versus the MC truth jet p_T for PF jets, before PU corrections are applied (top left), after PU corrections are applied (top right) and after the complete energy corrections (bottom).

5.3.2 Simulation based relative and absolute corrections

This set of corrections have been designed to take into account known effects due to the detector design that are correctly implemented in the simulation. Typical examples are the gap between barrel and endcap, the variation of the HCAL absorber thickness going as $1/\sin\theta$ and calorimetric thresholds. The simulation is sufficiently accurate not to introduce important uncertainties together with the correction factors.

The MC samples used for jet energy corrections consist of PYTHIA QCD events, further pro-

cessed through a full GEANT4 simulation of the CMS detector [158]. Jets reconstructed from the four momenta of the generated particles (GenJets) are matched in position ($\Delta R < 0.25$) to Calo, JPT and PF jets. First, comparing the response to that in the central region $|\eta| < 1.3$ (where the detector is uniform) a relative factor is extracted, then an absolute correction can be derived bringing the p_T dependence of the response to unity. The two multiplicative correction factors ($C_{a,r}$) are then applied to the four components of the momentum

$$
\begin{aligned}
P^C_\mu &= C_{MC}\left(p'_T, \eta\right) P^U_\mu\,, \\
C_{MC}\left(p'_T, \eta\right) &= C_r\left(p'_T, \eta\right) C_a\left(p'_T \times C_r\left(p'_T, \eta\right)\right)\,,
\end{aligned}
\tag{5.3.5}
$$

where p'_T is the transverse momentum of the jet corrected for noise and pile-up as discussed in the previous section. After the calibration a validation test is applied, rederiving the corrections for the already corrected jets. The agreement with unity is found to be within 2%. Total correction factors C_{MC} obtained from the samples described in section 5.2 are shown in figure 5.4 as a function of jet η for PF jets with p_T=30 GeV and with E=1 TeV. In general the shape of the correction factors reflects the calorimeter division in barrel ($|\eta| < 1.3$), endcap ($1.3 < |\eta| < 3$) and forward ($3 < |\eta| < 5$) sections. Calorimetric jets require in general larger corrections (up to 2 at low p_T), due to the non-compensating nature of the CMS calorimeters.

In the figure we show the comparison between 2012 (blue) and 2013 (red) correction factors. The small differences are due to the change in integration time in HB and HE (see section 5.3.1), the inclusion in the 2013 reconstruction of the preshower detector for $2 < |\eta| < 3$ and an update in the calibration of HF (relevant for $|\eta| > 3$).

5.3.3 Residual data-driven corrections

After MC based corrections are applied the response to a particle level jet is compared to that obtained from reference processes in data. Residual non-uniformities in η and p_T are found. To account for them an absolute scale correction is derived from Z+jets and γ+jets events in the central region $|\eta| < 1.3$, while the relative η response is determined from dijet events using a p_T balancing technique. The smallness of these additional corrections (at the few % level) justifies the application of the simulation based factors.

Relative scale

We determine variations of the response in η using dijet events. The two leading jets are required to be back-to-back in ϕ and one of them must fall into the central region. The central jet is used as the "tag" jet while the other as the probe needed to determine the relative response

$$
R_r\left(\eta^{\text{probe}}, p_T^{\text{probe}}\right) = \frac{1 + \langle A \rangle}{1 - \langle A \rangle}\,, \quad A = \frac{p_T^{\text{probe}} - p_T^{\text{tag}}}{p_T^{\text{probe}} + p_T^{\text{tag}}}\,.
\tag{5.3.6}
$$

The quantity A is averaged over events and R_r was found to be the least biased estimator of the response, as opposed to, for instance $p_T^{\text{probe}}/p_T^{\text{tag}}$ [162]. The response is determined in fine
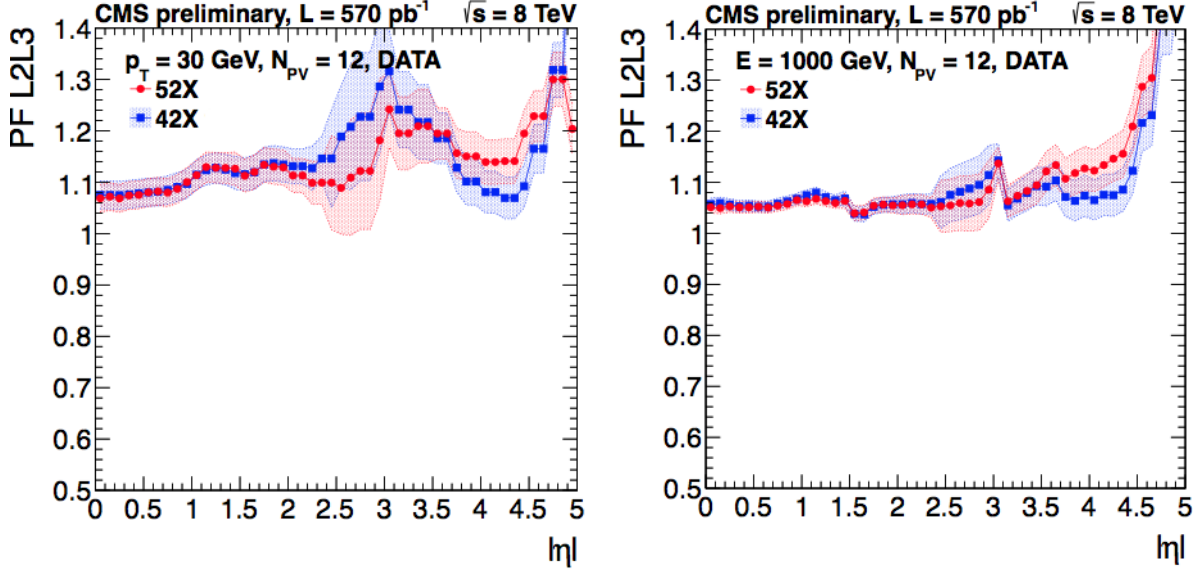
Figure 5.4: Jet energy correction factor C_{MC} derived from simulation as a function of jet η for PF jets, for $p_T = 30$ GeV (Left) and $E=1$ TeV (Right). The blue points represent corrections from 2012 while the red ones from 2013 simulation and reconstruction.

$(p_T^{\text{probe}} + p_T^{\text{tag}})/2$ $(\mathcal{O}(10 \text{ GeV}))$ and $|\eta|$ $(\mathcal{O}(0.1))$ bins. The residual correction is small, as shown in figure 5.5 for PF jets, remaining below 2.5% until $|\eta| < 2.4$ and then reflecting the transition between central and forwards calorimeters at $|\eta| = 3$. The higher relative response at larger values of $|\eta|$ is due to higher energies of forward jets compared to the central ones at fixed p_T.

Absolute scale

Z+jets and γ+jets events provide a well measured object balancing the jet assuming that we can extrapolate to zero additional event activity. The γ+jets sample is selected using single photon triggers and is known to contain a significant contamination from QCD dijet events with one jet faking a photon. A series of isolation and identification requirements are applied [162], to insure that a jet survives only in the limit in which it fluctuates to a single π^0 (with $\pi^0 \rightarrow \gamma\gamma$) surrounded by very low hadronic activity. These fakes have a scale very similar to real photons and are thus a valid reference object for our calibration purposes. The Z+jets sample is almost pure thanks to the requirement of two well identified electrons or muons.

The two methods used to determine the absolute jet response are the p_T-balance method with estimator

$$R_b = \frac{p_T^{\text{jet}}}{p_T^{\gamma,Z}} \tag{5.3.7}$$

and the missing E_T projection fraction (MPF) method that starts from the assumption that
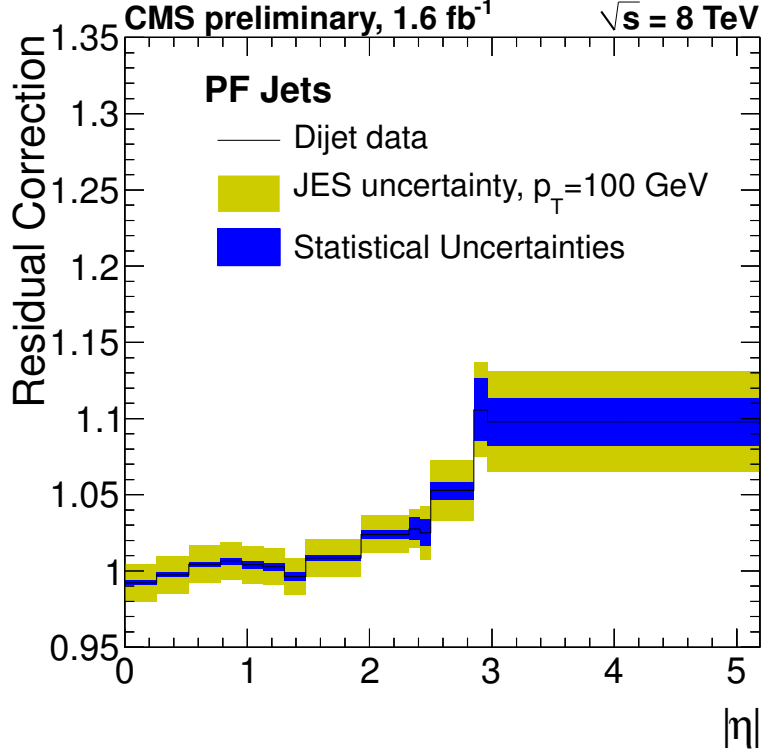
Figure 5.5: η-dependent (relative) corrections determined from $\sqrt{s} = 8$ TeV dijet data for PF jets.

γ, Z+jets events have no intrinsic ME_T. In this way any reconstructed ME_T is determined by a mismeasurement of the reconstructed objects

$$R_{\gamma,Z}\vec{p}_T^{\,\gamma,Z} + R_{\mathrm{recoil}}\vec{p}_T^{\,\mathrm{recoil}} = -ME_T \,. \tag{5.3.8}$$

Assuming Z bosons and photons to be well calibrated ($R_{\gamma,Z} = 1$) we have

$$R_{\mathrm{recoil}} = 1 + \frac{ME_T \cdot \vec{p}_T^{\,\gamma,Z}}{\left(\vec{p}_T^{\,\gamma,Z}\right)^2} \equiv R_{MPF} \,. \tag{5.3.9}$$

To obtain the single jet response we need to further assume R_{recoil} equal to the response from the leading jet. However the method is rather robust against additional hadronic activity and provides a good calibration also if particles not clustered into the leading jet have a response similar to the ones inside the jet (or are in a direction perpendicular to the photon or Z axis). The PF reconstruction clearly helps in this respect since the response to the charged hadrons and to the photons (that constitute roughly 90% of the jet energy) is identical outside and inside the jet cone, at least where tracking information is available ($|\eta| < 2.5$). However to minimize the impact of
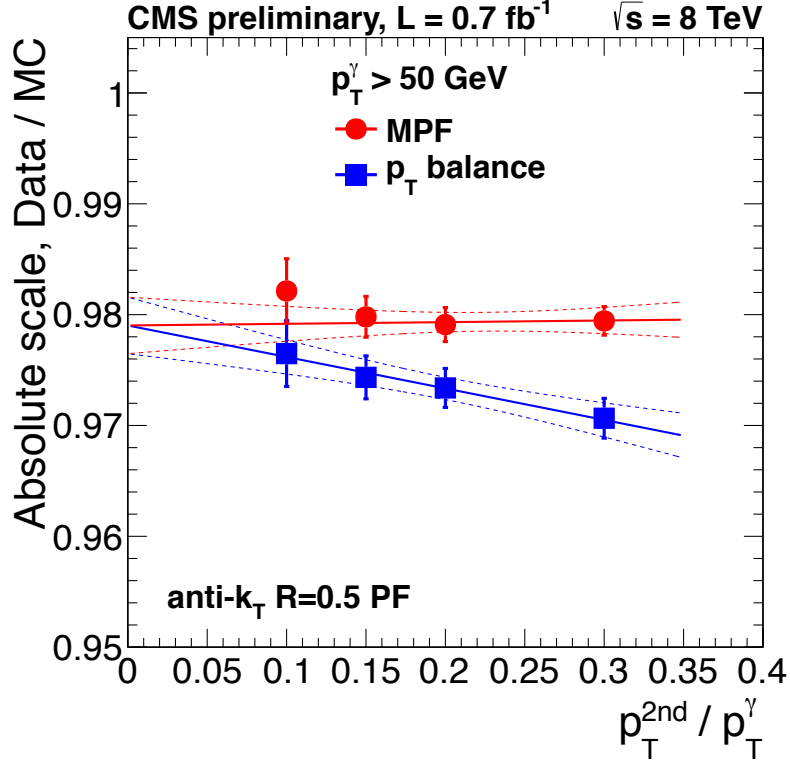
Figure 5.6: Data/MC ratio of jet responses from the MPF and p_T-balance methods, described in the text, for γ+jets events, as a function of the second jet p_T divided by the photon p_T.

additional hadronic activity both methods have a subleading jet veto described in [162] and obtain the response extrapolating to $p_T^{2\text{nd jet}}/p_T^{\gamma,Z} = 0$, as shown in figure 5.6 for PF jets. This is crucial for the p_T-balance method. The required extrapolation for the data/MC ratio depends on the MC samples used. It is rather large for Herwig++ [163] (used for cross-check studies), small for PYTHIA Z2 (γ+jets and dijet), as depicted in figure 5.6 and negligible for MadGraph+PYTHIA (used for Z+jets). The MPF method is almost insensitive to additional jet activity, but the p_T-balance technique once extrapolated to zero agrees with it.

The result is depicted in figure 5.7 for PF jets. The values from Z+jets and γ+jets samples are in good agreement and exhibit almost no p_T dependence. Overall the correction amounts to a 1.5% rescaling and suffers from systematic uncertainties due to the difference in fragmentation models in the reference MC (PYTHIA and Herwig) and to the uncertainty in the propagation of single particle response to jets. The systematics (yellow band in the figure) reintroduce a mild p_T dependence.
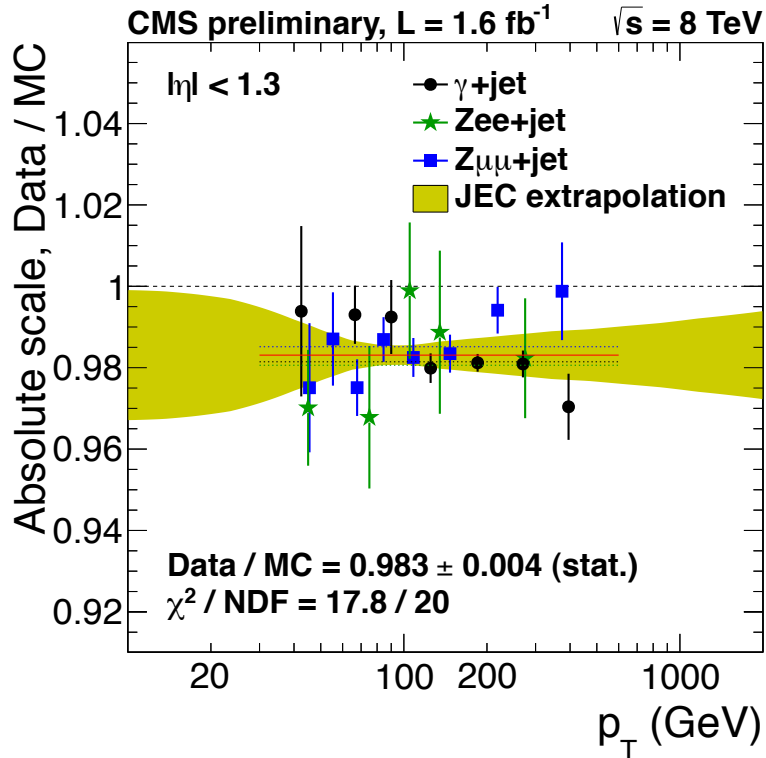
Figure 5.7: Data/MC ratio for the absolute jet scale correction after combining the MPF and p_T balance methods. The systematic uncertainties are shown as a yellow band. Data points correspond to three different samples γ+jets, $Z \rightarrow ee$+jets and $Z \rightarrow \mu\mu$+jets.

5.3.4   Jet energy scale uncertainties

The uncertainties related to the jet energy scale and its calibration play a crucial role in a number of CMS analyses and are particularly relevant to our work, since we always require at least 6 jets in the final state of our new physics search. In this paragraph we describe all sources of uncertainty, however not all of them are equally important to us since we only count the number of jets above a 30 GeV p_T threshold. Therefore we are mainly interested in the calibration around that value of jet p_T, where PU related uncertainties dominate.

The discussion of jet energy corrections shows that we have an excellent understanding of the CMS detector and of its simulation, this allows to reduce the total jet energy scale uncertainty to about 3% for a jet p_T of 30 GeV in the central region. The main sources of this error can be classified into three broad subsets

- Physics modeling in MC generators (showering, underlying event, ...).

- MC modeling of the detector (noise, zero suppression, ...).

- Biases in the processes that determine the corrections.

These three categories cover more than 16 sources of uncertainties [162]. Several of them are related and can be grouped into six coarser sets: Absolute scale, relative scale, extrapolation in p_T, PU, jet flavor and time stability. In what follows we briefly describe these six categories one by one.

The absolute scale determination in data suffers from several small systematic uncertainties:

- The energy scale of the photon and of the leptons is known to $\approx 1\%$ [164].

- The γ+jets and Z+jets samples do not cover the whole p_T range from 10 to 2×10^3 GeV. Therefore, especially in the high p_T region, it is necessary to extrapolate the result relying on the simulation. The uncertainty in the procedure is determined by the single pion response and the modeling of the jet fragmentation. For the single pion response the data is found to be in agreement with the simulation at the 3% level. The impact on the Monte Carlo truth jet energy scale is estimated by modifying it in the simulation and comparing the jet energy scale to the one with the nominal settings. This leads to an $\approx 1.5\%$ uncertainty at $p_T = 2$ TeV for PF jets. The uncertainty in the jet fragmentation modeling is estimated by using two independent models (`PYTHIA` and Herwig++), leading to an uncertainty of $\approx 4\%$ at p_T = 2 TeV again for PF jets.

- In the MPF method flavor mapping, parton correction, QCD background, secondary jets and proton fragments all contribute to the uncertainty, especially at low p_T. For a more detailed discussion we refer to [165].

The dominant uncertainties in the relative scale determination are due to the statistics and to the modeling of the resolution bias in the simulation. The latter is caused by the uncertainty on the jet p_T spectrum and the jet energy resolution in the MC. To estimate the effect, the jet p_T slope is varied by $\pm 5\%$ and the jet energy resolution by $\pm 10\%$, $\pm 20\%$ and $\pm 25\%$ for $|\eta| < 1.3$, $1.3 < |\eta| < 3$ and $|\eta| > 3$ respectively. Furthermore a systematic uncertainty is attributed to the extrapolation to zero third jet activity.

The PU uncertainty or, more precisely, the uncertainty from the offset correction, gives by far the dominant contribution for jet $p_T < 30$ GeV. It is obtained using the jet area method, varying independently ρ and $\langle \rho_{UE} \rangle$ in equation (5.3.4) and then summing in quadrature the effects from the two shifts. The event ρ uncertainty is estimated as 0.2 GeV per unit area and per PU event, while the typical value of ρ is around 0.8 GeV. This is based on the maximum slope difference between the jet area and the average offset methods (and the residual non-closure in the AO method). The $\langle \rho_{UE} \rangle$ uncertainty is estimated as 0.15 GeV per unit jet area, from the differences observed between two data samples: QCD multijet and Z+jets events.

The different response to different jet flavors becomes a relevant source of uncertainty at relatively low p_T. For PF jets is at most 3% for $|\eta| < 1.3$, as can be seen from figure 5.8, where on the y axis we have the relative variation with respect to the average response. The differences are
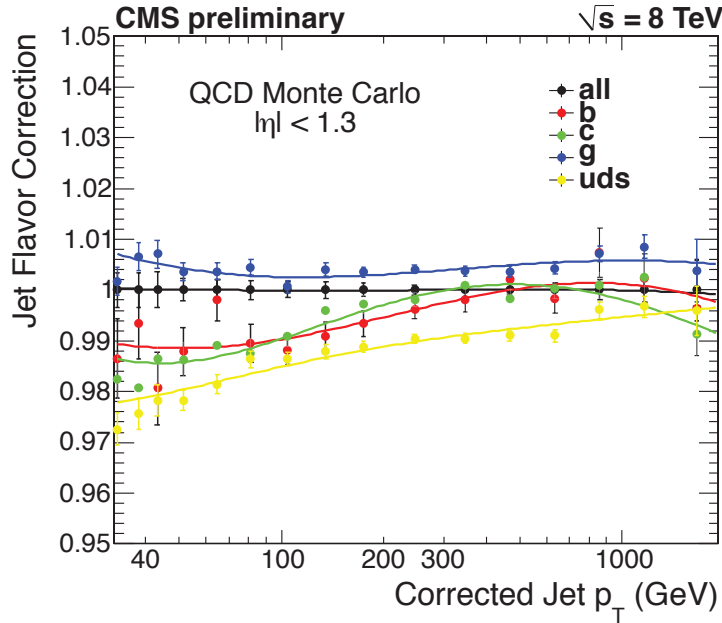
Figure 5.8: Flavor dependence of the jet energy correction in the central region ($|\eta| < 1.3$), from $\sqrt{s} = 8$ TeV data.

due to the larger gluon color charge and the larger mass of heavy quarks (b, c) that cause them to fragment to an higher number of particles, requiring a larger correction.

The "time stability" uncertainty refers to changes in the JEC over the data taking period. To account for the effect the corrections were computed separately in blocks of 4-5 runs for all the triggers, finding a variation $< 1\%$.

The full JEC uncertainty is shown in gray for PF jets, in figure 5.9 as a function of p_T in the central region and as a function of $|\eta|$ for $p_T = 100$ GeV. The single components discussed in this section are displayed separately.

5.4 Jet transverse momentum and position resolution

After the jet energy corrections presented in the previous section are applied we can measure the jet p_T and position resolutions estimating them from MC and collider data. These quantities are not as crucial to our analysis as the jet energy scale uncertainty, but are relevant to a vast class of other measurements, such as those of differential jet spectra and to searches where a precise determination of the tails of the ME_T is needed. We briefly discuss them here for completeness and refer to [142] for more details.
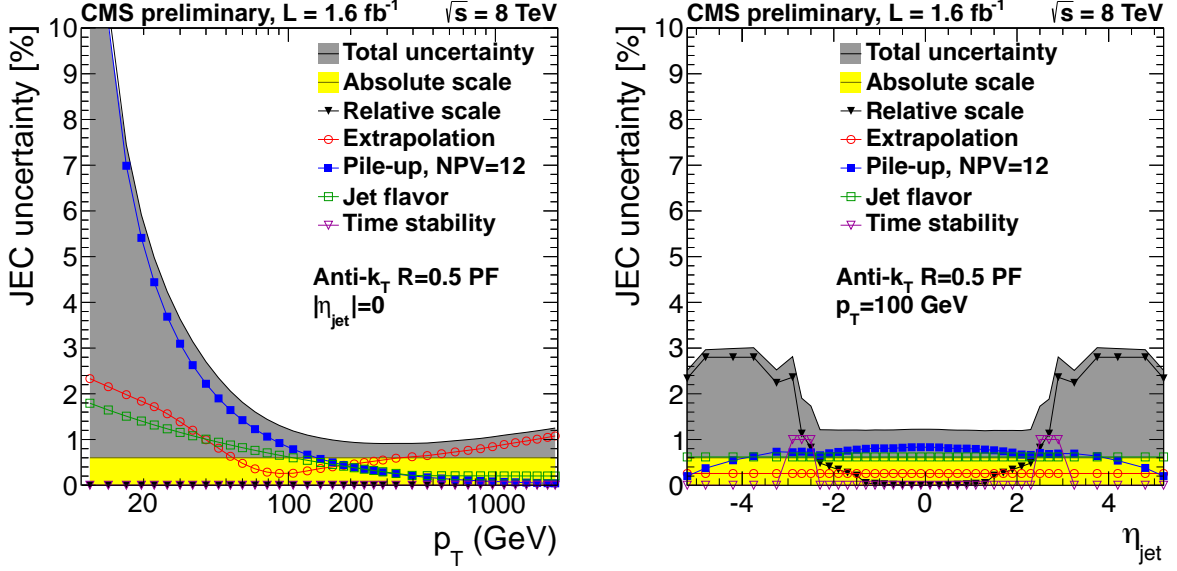
Figure 5.9: (Left) Jet energy correction uncertainty as a function of p_T for $|\eta| < 1.3$. (Right) Jet correction uncertainty as a function of $|\eta|$ for $p_T = 100$ GeV.

5.4.1   Transverse momentum resolution

Two methods are used to measure the jet transverse momentum resolution

- The dijet asymmetry method.

- The γ+jet balance method.

They both exploit momentum conservation in the transverse plane. The dijet asymmetry technique uses two descriptions of the jet resolution. The first characterizes the core of the distribution using a truncated RMS. The second fits the full distribution with a gaussian probability density function. The γ+jet balance method takes the photon as the well measured reference object, using the width of the p_T/p_T^γ distribution as a measure of the resolution, given in p_T^γ bins.

The asymmetry variable is defined as

$$A = \frac{p_T^1 - p_T^2}{p_T^1 + p_T^2} \tag{5.4.1}$$

and was already used in the measurement of the relative jet energy scale correction. Here we are interested in its variance, that we can write as

$$\sigma_A = \sqrt{\sum_{i=1}^{2} \left(\frac{\partial A}{\partial p_T^i} \right)^2 \sigma^2 \left(p_T^i \right)}. \tag{5.4.2}$$

If the two jets lie in the same η region, thanks to the balancing in the transverse plane we can write $p_T \equiv p_T^1 = p_T^2$ and $\sigma(p_T) \equiv \sigma(p_T^1) = \sigma(p_T^2)$. This gives

$$\frac{\sigma(p_T)}{p_T} = \sqrt{2}\sigma_A \,. \tag{5.4.3}$$

Clearly this is true in an ideal setting. In a real collision additional soft radiation, extra inter-actions and the underlying event spoil the balance in the transverse plane. This broadens the asymmetry distribution, producing asymmetric tails corresponding to a systematic worsening of the p_T resolution. There can also be a jet inbalance, caused by fragmentation, that can push part of the shower outside of the jet cone. For these reasons the width of the A distribution is the convolution of an intrinsic component related to the resolution and and imbalance component.

The effect of extra soft radiation is minimized by measuring σ_A in bins of p_T^3 (the p_T of the third most energetic jet in the event) and then extrapolating it to zero. The particle-level imbalance contribution to the measured jet p_T resolution is instead subtracted using the MC: the asymmetry method is applied to the generated MC particle jets, then the extrapolated particle-level resolution is subtracted in quadrature from the measurement. The p_T resolution, thus measured, is found to be well parametrized by

$$\frac{\sigma(p_T)}{p_T} = \sqrt{\text{sign}(N)\left(\frac{N}{p_T}\right)^2 + S^2 p_T^{M-1} + C^2} \,. \tag{5.4.4}$$

N, S and C are the usual "noise", "stochastic" and "constant" terms in the calorimeters resolution. The additional parameters ($\text{sign}(N)$ and M) account for the use of tracking information in the reconstruction of JPT and PF jets. The full result of the measurement was shown in figure 4.9 for PF jets and $\sqrt{s} = 7$ TeV data and lies between 15% and 5% in the p_T range $(50, 10^3)$ GeV. More details on the measurement and a complete list of systematic uncertainties (shown in the figure as a yellow band) can be found in [142].

Also in the case of γ+jets events the method requires an extrapolation to the ideal case of no additional hadronic activity. So we have an intrinsic component σ_I of the resolution and an inbalance term σ_{in} that we can parametrize as

$$\sigma_{in} = q + m\frac{p_T^2}{p_T^\gamma} \,, \tag{5.4.5}$$

where q represents the irreducible inbalance due to hadronization and photon resolution effects (among other causes) and it is obtained by fitting the MC using this functional form. p_T^2 is the p_T of the second most energetic jet in the event. To extract the intrinsic resolution σ_I, we take into account the fact that the full resolution is a convolution of the two parts and we fit both data and MC using the functional form

$$\sigma_{\text{tot}}\left(p_T^2/p_T^\gamma\right) = \sqrt{\sigma_I^2 + q^2 + 2qm\left(p_T^2/p_T^\gamma\right) + m^2\left(p_T^2/p_T^\gamma\right)^2} \,. \tag{5.4.6}$$
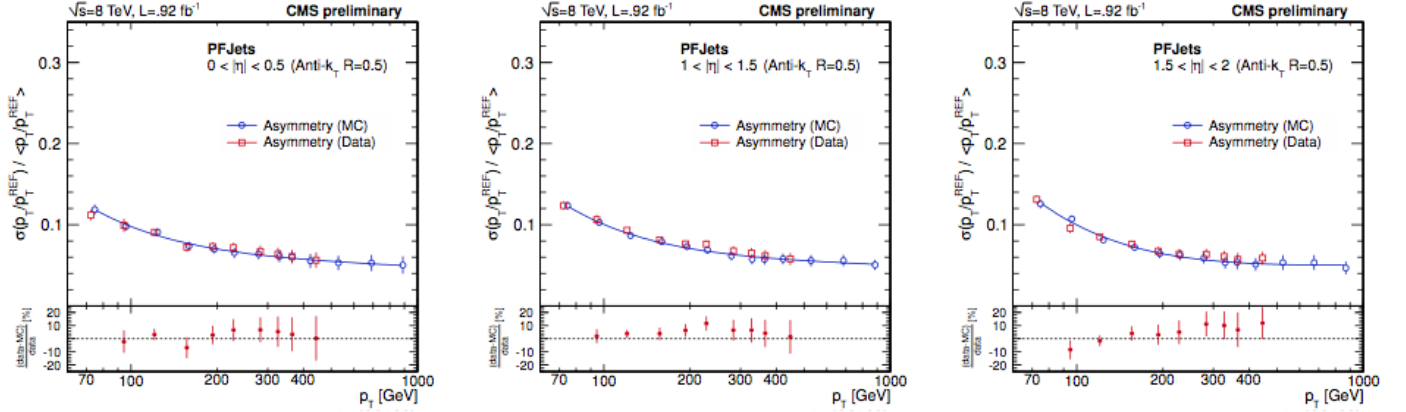
Figure 5.10: PF jet p_T resolution, as a function of the jet p_T for three different η bins. Right: $0 < |\eta| < 0.5$, Center: $1 < |\eta| < 1.5$ and Left: $1.5 < |\eta| < 2$. The blue points represent the result on the MC and the red ones on data.

As for the asymmetry method we refer to [142] for more details and a list of systematics.

The result of the asymmetry method for 8 TeV data and PF jets is shown in figure 5.10 for three different η bins ($0 < |\eta| < 0.5$, $1 < |\eta| < 1.5$ and $1.5 < |\eta| < 2$) as a function of the jet p_T, both in data and MC. The resolution is almost independent of $|\eta|$ in this region that is completely covered by the tracker.

5.4.2   Position resolution

The jet position resolution in ϕ and η is derived from simulation and a validation on data is then performed for Calo jets. We use a `PYTHIA` QCD dijet sample at $\sqrt{s} = 7$ TeV, matching Gen jets (used as a reference) with the loose requirement $\Delta R < 1.0$ for the closest match. Furthermore only the two leading jets are considered and only in events with $\Delta\phi > 2.0$ between them. These requirements are purposefully loose, in order not to introduce a bias in the resolution through the spatial matching.

The resolution is measured from the distribution of $\Delta\eta^* \equiv (\eta - \eta_{\mathrm{gen}})\,\mathrm{sign}(\eta_{\mathrm{gen}})$ and $\Delta\phi^* \equiv \phi - \phi_{\mathrm{gen}}$. Each of the two distributions is evaluated in bins of p_T and η and is composed of a Gaussian core and small exponential tails. The $\mathrm{sign}(\eta_{\mathrm{gen}})$ dependence accounts for a small asymmetric offset while binning in $|\eta_{\mathrm{gen}}|$.

The width of the Gaussian core of the distributions is taken as a measure of the resolution and the results are shown in figure 5.11 for PF jets. Particle Flow is the reconstruction algorithm that gives the best resolution and not surprisingly all the jets that include tracking information perform much better than calorimetric jets.

In order to validate the MC results we study the relative $\Delta\eta$ and $\Delta\phi$ of Calo jets with respect
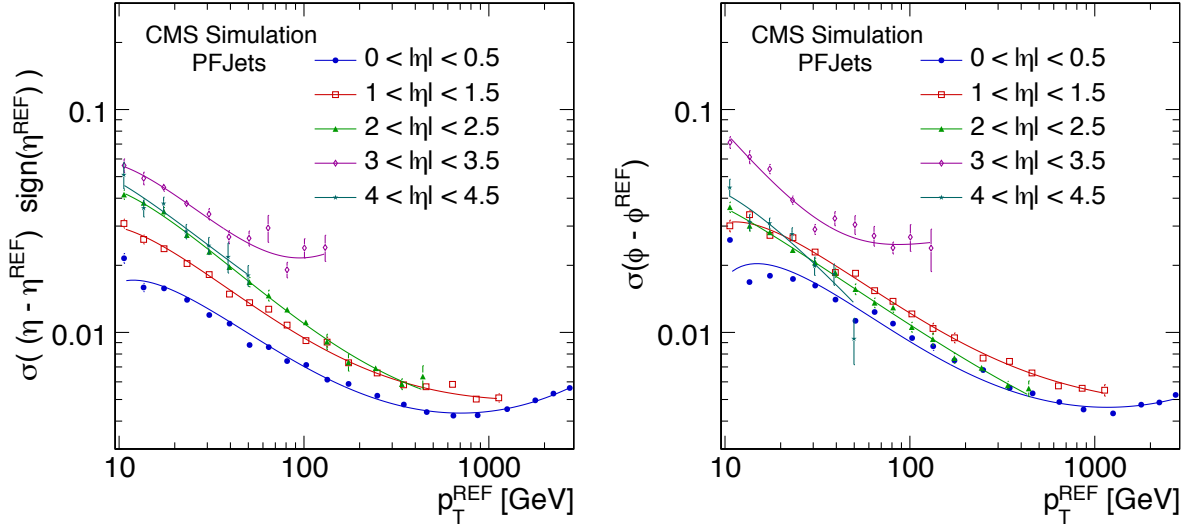
Figure 5.11: η (Left) and ϕ (Right) PF jets resolutions obtained from MC simulation as a function of generated jet p_T. Source [144]

to track and PF jets in data. We use a dijet sample collected at $\sqrt{s} = 7$ TeV in the first 8.4 nb^{-1} of data. The matching is the same described above for Gen jets, but the reference object in this case are the track and PF jets and the comparison is performed only for $|\eta| < 0.5$. PF jets are partially correlated to Calo jets, but comparing their relative position measurements supports the validation performed with track jets, since PF jets have the best position resolution. This procedure shows a good agreement with the MC based result [142]. This concludes our discussion of jet energy corrections and jet resolutions inside CMS and we can turn to the study of b-tagging techniques.

5.5 b-jet identification

The bottom quark long lifetime, large mass, abundant semileptonic decays and hard momentum spectra of daughter particles are all characteristics that enable CMS to distinguish between jets originating from a b meson and the overwhelming background from gluon and light (u, d, s and to a lesser extent c) jets. The procedure of identifying b-jets is labelled b-tagging and it is an extremely valuable tool for a number of physics analyses. In this section we review the main algorithms used by CMS for b-jet identification and their performances.

5.5.1   Samples

All the results in this part of the chapter are the latest available and were obtained using 2012 $\sqrt{s} = 8$ TeV data, excluding two illustrative plots showing the tagging performances on the MC generated at 7 TeV. The 7 TeV MC samples were generated with `PYTHIA` 6.424 using the Z2 tune. All generated events were passed through the full simulation of the CMS detector based on GEANT4. In μ-enriched QCD samples each generated event has to contain at least one generator muon with $p_T > 5$ GeV and $|\eta| < 2.5$.

The 8 TeV efficiency results from muon-jets samples are based on the first 16.7 fb^{-1} collected with CMS during the 2012 run. The triggers used to select the data are dedicated b-tag calibration triggers which require two jets with a minimum p_T and at least one muon associated to one of the jets. The jet p_T thresholds go from 20 two 300 GeV, while the muon p_T cut was kept constantly at 5 GeV. The events from these triggers are collected in the `BTag` primary dataset. The simulated events were generated in analogy with the 7 TeV samples.

The events used to measure efficiencies from $t\bar{t}$ events were collected using single lepton and dilepton triggers and correspond to the first 17 fb^{-1} of 8 TeV data. They are part of the `DoubleElectron`, `DoubleMu`, `MuEG` and `SingleMu` datasets. Single muon triggers include isolation requirements and have p_T cuts going from 17 to 24 GeV. Double letpon triggers include isolation requirements and for electrons identification requirements. They have thresholds of 17 GeV on the leading particle and 8 GeV on the subleading one. The $t\bar{t}$, $t\bar{t} + V$, W+jets and Drell-Yan+jets MC samples were generated using `MadGraph` while the single top (including tW production) samples were generated with `powheg` [166]. The tau-lepton decays were handled with `TAUOLA` (v.27.121.5) [157]. The PU reweighting of the MC events is performed in the same way described for jet energy corrections studies in section 5.2.

5.5.2   The basic physics objects

The fundamental building blocks of the b-tagging algorithms are tracks reconstructed by the CMS silicon detector. The particles trajectories are reconstructed by a standard Kalman-filter algorithm described in [167], where the tracking performance in pp collisions is also discussed. The tracks employed by the b-tagging algorithms must satisfy several purity requirements:

- $p_T > 1$ GeV.

- At least eight hits in the silicon layers should be associated with the track.

- A good fit of the trajectory is required (χ^2/d.o.f. < 5).

- At least two hits must be present in the pixel detector, since it is the one providing most of the discriminating power given the b quark lifetime.

- $d_{xy} < 0.2$ cm and $d_z < 17$ cm. The two quantities are defined as the transverse and longitudinal distances of the track to the primary vertex at the point of closest approach in
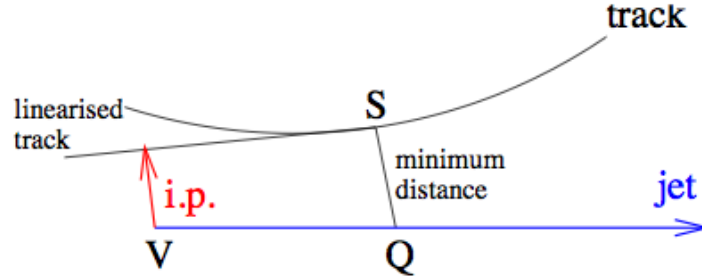
Figure 5.12: Schematic representation of the distance of closest approach of a track to the primary vertex and to the jet axis. In red is shown the impact parameter (IP) of the track.

the transverse plane. This reduces both the fraction of badly reconstructed tracks and the contamination from the decay products of long lived u, d, s mesons.

Following this selection based on intrinsic properties of the track, the matching to a jet is performed if

- The track is contained in a cone $\Delta R < 0.5$ around the jet axis.

- The distance of closest approach of the track to the axis is $< 700 \mu$m. Tracks originating from B-hadrons have a distance of order 100 μm. Large impact parameter tracks are typically fake tracks, badly measured tracks or tracks from pile-up events.

- The point of closest approach is within 5 cm of the primary vertex.

Every time we refer to a jet in this section we refer to a Particle Flow jet clustered with the anti-k_T algorithm with cone parameter $R = 0.5$ to which the energy calibration procedure described in the previous sections has been applied. The jet axis is defined by the primary vertex and the direction of the jet momentum. The point of closest approach of the track to the vertex is defined in three dimensions and so is the distance of closest approach of a track to the jet axis. They are depicted schematically in figure 5.12.

While listing the selection criteria we have relied on an intuitive notion of primary vertex (PV), but a more precise definition is necessary. PV candidates are selected by clustering reconstructed tracks using the z coordinate of their closest approach to the beam line. An adaptive vertex fit, described in [167], determines the vertices positions. A this point the PV candidate with highest $\sum \left(p_T^{\text{track}} \right)^2$ is identified as the primary vertex, where the hard interaction took place.

Another key ingredient of b-tagging techniques are secondary vertices. The procedure followed to identify them is influenced by the presence of PU interactions. For this reason we apply a second set of requirements to tracks participating in the reconstruction of secondary vertices

- The track is contained in a cone $\Delta R < 0.3$ around the jet axis.

- The track has a maximal distance to the jet axis of 0.2 cm.

- The track passes the high purity selection defined in [167]. The selection procedure combines normalized χ^2 of the track fit, the track length and impact parameter information to optimize the purity in track reconstruction.

Using this subset of tracks in the event the adaptive vertex fit algorithm [167] identifies secondary vertex candidates. Once the position is estimated a weight between 0 and 1 is assigned to each track. Tracks with weight < 0.5 are discarded and the adaptive vertex fit is performed iteratively until no new vertex candidate can be found.

The impact parameter of the tracks (IP) was not used in their selection, but is a third valuable ingredient for identifying b-quarks. It is calculated in three dimensions and its sign is determined from the scalar product of the vector pointing from the primary vertex to the point of closest approach with the jet direction. In this way tracks originating from the decay of particles traveling along the jet axis will tend to have positive IP values. Since the IP is very sensitive to the p_T and η of the track, the key tagging observable is the IP significance (the ratio between the IP and its estimated uncertainty). The IP significance is measured in three dimensions thanks to the high resolution of the pixel detector along the z coordinate. The precision in z is inferior with respect to the one in the transverse plane, but by using the 3D significance the uncertainty is not inflated as the measurement errors are correctly taken into account. The point of closest approach of the track to the primary vertex is better computed in this way, since the distance minimization is performed in full 3D space, making this method more powerful and not equivalent to separate minimization in the transverse and longitudinal planes.

We show in figure 5.13 properties of the tracks after the baseline selection (i.e. no further requirements used for the secondary vertices reconstruction are imposed) where the cut on the plotted variable is not applied. The agreement is generically good between data and MC.

The gluon splitting category is treated separately since $b\bar{b}$ pairs originating from a gluon tend to be produced with a small opening angle and can be merged by the clustering algorithm.

As mentioned above, in addition to track properties also the properties of the secondary vertex are used as an input to the tagging algorithms. In particular the flight distance and direction, based on the vector between primary and secondary vertex, the track multiplicity, the mass and the energy. In figure 5.14 we show the significance of the flight distance and the mass of the secondary vertices. Also in this case we find a good agreement between data and MC.

This concludes our description of the basic observables needed by b-tagging algorithms. However before turning to the algorithms themselves it is appropriate to notice that the tracker alignment and the PU distribution both have an impact on b-tagging. The tracker was aligned using both cosmic rays and minimum bias collisions in 2010 [168, 169]. Its movements have been constantly monitored ever since. The sensitivity of b-tagging to misalignment was studied on a simulated $t\bar{t}$ sample and found to be unaffected by deteriorations with the magnitude observed in 2011 and 2012 [170].

Turning to PU, additional interactions in the event increase the total number of tracks, but our track selection criteria are effective in rejecting tracks from extra soft scatterings. In particular
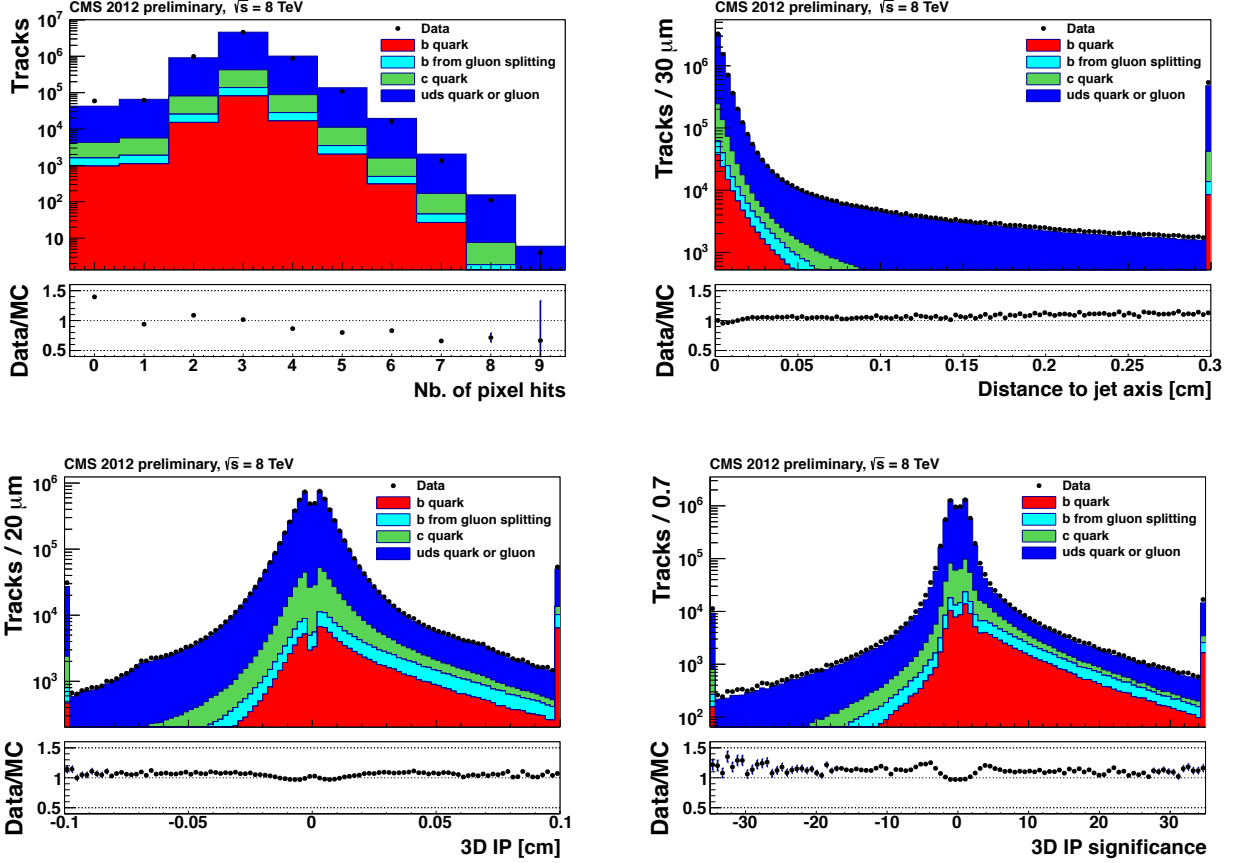
Figure 5.13: Tracks properties after the selection described in section 5.5.2 (excluding the cut on the plotted variable): (Top Left) Number of pixel hits, (Top Right) distance to the jet axis, (Bottom Left) Impact parameter and (Bottom Right) significance of the impact parameter. The overflow bin is included in all histograms and the MC distributions are normalized to the yield in data. Different colors in the histogram stacks correspond to different jet flavors identified from the MC truth information.

thanks to the requirement on the distance with respect to the jet axis. This selection criterion keeps basic tracking observables stable versus the number of reconstructed PV and insures that the b-tagging performances are only marginally affected [170].

5.5.3 Tagging algorithms

The CMS tagging algorithms can be broadly characterized as belonging to one of two classes: IP-based and secondary vertex based. In the first category we have the Track Counting (TC), Jet
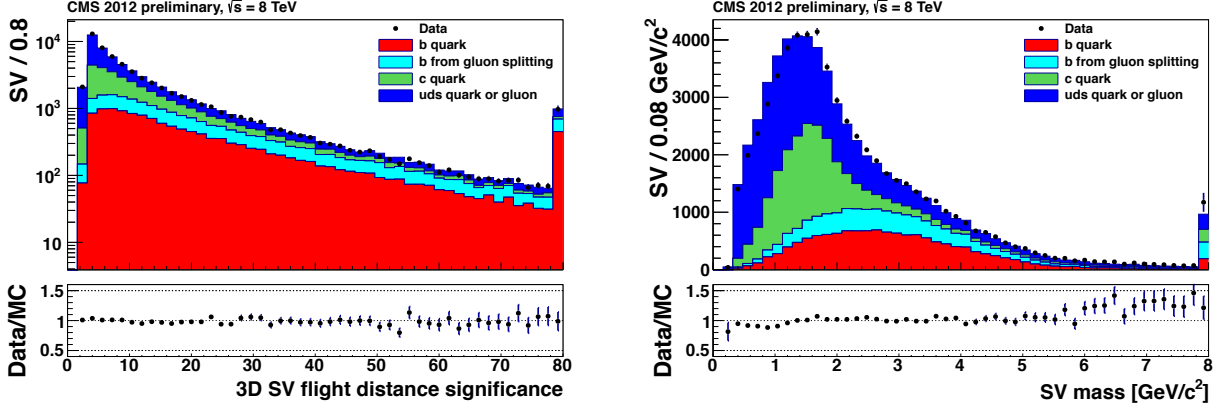
Figure 5.14: Secondary vertices properties: (Left) the significance of the flight distance and (Right) the mass. For secondary vertices passing the selection described in section 5.5.2.

Probability (JP) and Jet B Probability (JBP) algorithms. We start by describing the TC algorithm and then proceed in order of increasing complexity. In the TC procedure tracks are sorted by decreasing value of IP significance. The ranking biases the first track to have high positive values of the IP significance, but to have several tracks with this properties is rare for light flavor jets. For this reason the two variants of the algorithm Track Counting High Efficiency (TCHE) and Track Counting High Purity (TCHP) use as value of the discriminant the IP significance of the second and third track in the ranking, respectively.

The JP and JBP algorithms exploit the information from all the tracks associated to the jet, by using a likelihood of the form

$$P_{\text{jet}} = - \left[\prod_{i=1}^{N_{\text{tracks}}} \max\left(P_i, 5 \times 10^{-3}\right) \right] \sum_{n=0}^{N_{\text{tracks}}-1} \frac{\log\left(\prod_{i=1}^{N_{\text{tracks}}} \max\left(P_i, 5 \times 10^{-3}\right)\right)^n}{n!}, \qquad (5.5.1)$$

where P_i is the estimated probability of track i to originate from the PV. The P_i are constructed from the probability density functions for the IP significance of prompt tracks [171]. These functions are extracted from data for different track quality classes, using the shape of the negative part of the IP significance. The cut-off at 5×10^{-3} limits the impact of poorly reconstructed tracks.

The JP and JBP discriminators are proportional to $-\log P_{\text{jet}}$. The difference between the two algorithms resides in the fact that the JBP technique assigns an higher weight to tracks with higher IP significance, doing it for up to four tracks (the average number for b-hadron decays). The shapes of the TCHP and JP discriminators are shown in figure 5.15 and are in good agreement between data and MC.

The second class of taggers uses the presence of a secondary vertex and its properties. To en-
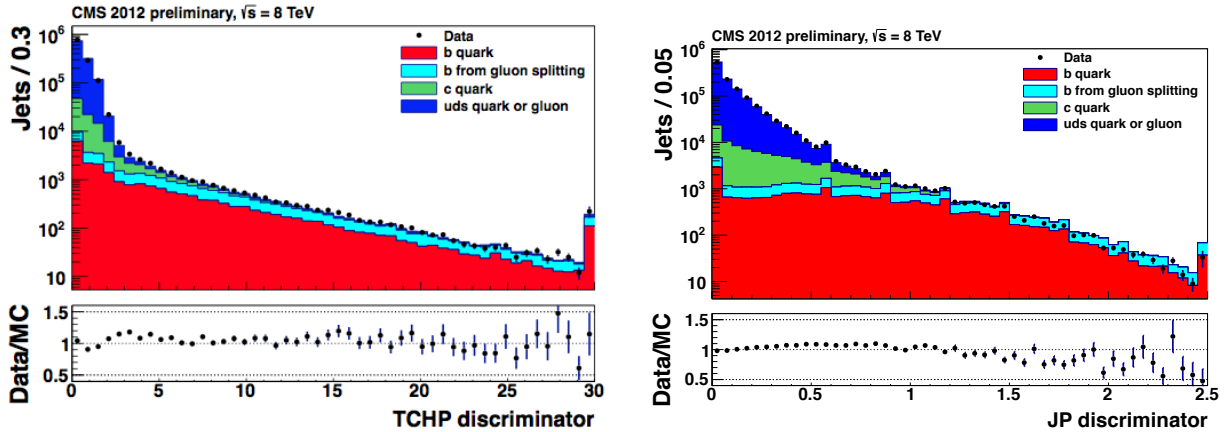
Figure 5.15: Discriminator distributions for: (Left) TCHP and (Right) JP taggers. The discontinuities in the JP discriminator are due to the 5×10^{-3} cut-off on track probabilities discussed in section 5.5.3.

hance the b purity of the sample a series of requirements is applied to secondary vertex candidates before feeding them to the algorithm

- Secondary vertices must share less than 65% of tracks with the primary vertex.

- The significance of the radial distance between PV and secondary vertex must be larger than 3σ.

- Secondary vertex candidates with a radial distance of more than 2.5 cm from the PV are rejected if their mass is compatible with the K^0 mass or it is larger than 6.5 GeV.

- The flight direction of the secondary vertex must be within a cone of $\Delta R < 0.5$ around the jet direction.

The simplest algorithm, defined on this selected sample of secondary vertices, uses the significance of the flight distance, shown in figure 5.14, as the discriminator. We denote this algorithm as the Simple Secondary Vertex (SSV) tagger. Its High Efficiency version takes into account vertices with at least two associated tracks, while the High Purity variant requires at least three tracks to be associated to the vertex.

The second tagger that relies on secondary vertex information is the Combined Secondary Vertex (CSV) tagger. It consists of two likelihood ratios built from the following variables:

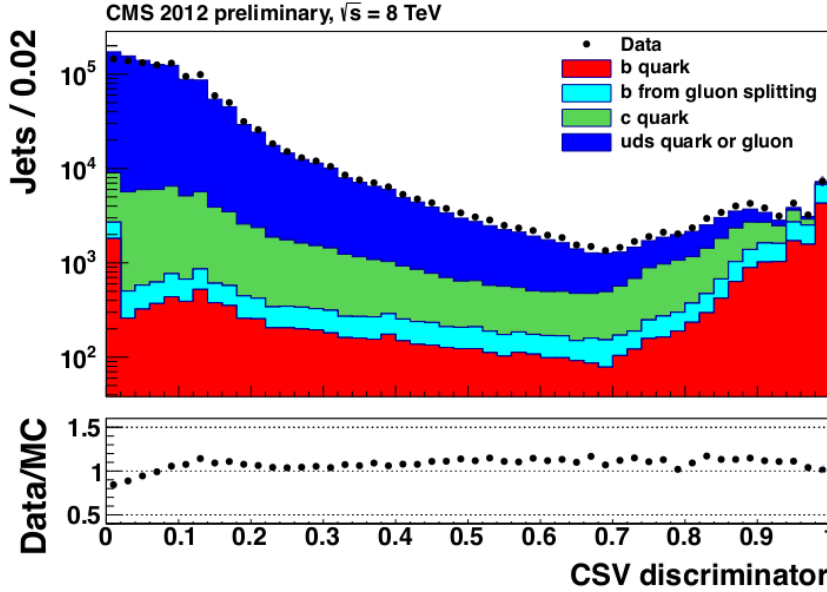- 2D flight distance significance.

- Vertex mass.

Figure 5.16: Discriminator distribution for the CSV tagger.

- Number of tracks associated to the vertex.

- η of the tracks at the vertex with respect to the jet axis.

- Ratio between the energy of the tracks at the vertex with respect to all jet's tracks.

- Number of tracks in the jet.

- 3D IP significance for each track in the jet.

- 2D IP significance of the first track that raises the vertex invariant mass above 1.5 GeV (charm threshold). The tracks are ordered by decreasing IP significance.

It also takes into account the vertex category, that depends on whether the event has a well reconstructed secondary vertex, just tracks with an IP significance > 2 that can be combined into pseudo vertices or no vertex at all. In this way the CSV algorithm is not limited by the secondary vertex reconstruction efficiency and can revert to track-based observables combined as in the JP algorithm if needed. The CSV discriminator is shown in figure 5.16.

Before concluding this section, a final remark on conventions is necessary: for each tagger three operating points are defined, Loose (L), Medium (M) and Tight (T), corresponding to mistag rates of 10%, 1% and 0.1% respectively. In the following we refer often to this definition.

5.5.4   Tagging efficiency from muon-jets events

The tagging algorithms described in the previous section make extensive use of track related physics objects, combining them in non-trivial ways. Therefore their efficiency depends crucially on running conditions, event topology, jet p_T and jet η. The relations between these "high-level" event properties, the tracking observables and ultimately the b-tagging efficiency are complex and their correct reproduction in the simulation can not be simply inferred from the good agreement shown in the previous section for "low level" observables.

Furthermore the precise determination of the b-tagging efficiency and the mistag rates (the probability of tagging a light jet as originating form a b quark) is crucial to many analyses that exploit the b content of the signal to reduce the SM backgrounds. Two examples are the searches for $h \rightarrow b\bar{b}$ and the searches for natural SUSY.

For these reasons CMS measures tagging efficiencies from data in different samples, producing Data-MC Scale Factors (SF), used by the analyses to correct the simulation efficiency. The main techniques currently used on muon-jets events are: the p_T^{rel} method, the System8 method, the IP3D method and the reference lifetime tagger method. In this section we describe the different methods for muon-jets events, in the next one we discuss the techniques used on $t\bar{t}$ events. Finally we present the results collectively in section 5.5.6. The mistag rate is evaluated separately from the negative tag information as specified in section 5.5.7.

The p_T^{rel} method

The p_T^{rel} technique takes advantage of the relatively large b quarks semileptonic branching ratio, by selecting a sample containing one jet with a muon inside the cone. The shape of the p_T of the muon relative to the jet axis is then used to discriminate between b-jets and light jets. The effectiveness of the method rests on the fact that muons originating from b-quarks tend to have a larger p_T^{rel} because of the larger b mass.

The p_T^{rel} method is applied to a data sample selected using dedicated b-tagging commissioning triggers and `PYTHIA` QCD events, enriched by requiring at least one generated muon with $p_T > 5$ GeV and $|\eta| < 2.5$, as discussed in section 5.5.1. The offline selection proceeds as follows:

- Two PF jets with $p_T > 20$ GeV and $|\eta| < 2.4$ are required.

- One `Global Muon` [172] (see also section 6.3.2) with at least one valid muon hit, more than one matching segment in the muon chambers and $\chi^2/\mathrm{ndof} < 10$ must be present.

- The muon must have $p_T > 5$ GeV and $|\eta| < 2.4$.

- The muon inner track must have > 10 tracker hits, > 0 pixel hits and $\chi^2/\mathrm{ndof} < 10$.

- The z-distance between the point of closest approach of the muon track to the selected primary vertex must be < 1 cm.

Furthermore the muon must be within $\Delta R = 0.4$ of the associated jet axis and the other jet in the event must be tagged using the medium working point of the TCHP algorithm and must have a p_T high enough not to introduce biases from the triggers.

After the selection, aimed at obtaining a relatively pure $b\bar{b}$ sample, the second step of the method consists in extracting the p_T^{rel} templates from the MC. Different flavors are distinguished by associating partons within a cone of $R = 0.3$ around the jet axis, with the priority being: first b, followed by c and eventually by light ($udsg$) jets. Only 1% of the jets remains without association. The shape of the templates and a comparison with the data p_T^{rel} distributions is shown in figure 5.17 for jets that pass and fail the JP losse working point selection (JPL). The figure shows the higher p_T^{rel} of b-jets and the good discrimination power of the JP algorithm.

The relative fractions of b and light jets in the figure are obtained with a template fit to the data distribution, performed using the `TFractionFitter` class of ROOT [173]. Two fits are performed separately for tagged and untagged[2] jets, yielding the relative fractions $f_{b,l}^T$ and $f_{b,l}^U$ respectively. Then the b-tagging efficiency is simply given by

$$\epsilon_b = \frac{f_b^T N_T}{f_b^T N_T + f_b^U N_U} \tag{5.5.2}$$

where $N_{T,U}$ are the total number of events in the two samples. The reliability of the fit was tested on pseudo experiments in 2011 [174], the true efficiency agrees with the one obtained from the fit within less than 0.1%.
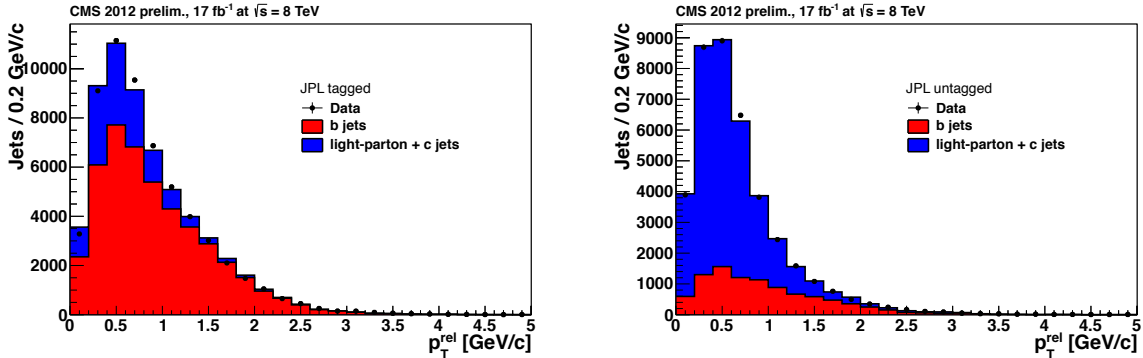
Figure 5.17: Fits to the muon p_T^{rel} with summed b and non-b templates. Left: For jets tagged with the JP algorithm (loose working point) and Right: For jets that do not pass the medium working point cut on the JP discriminator. The jet p_T is between 80 and 120 GeV and $|\eta| < 2.4$.

Other than the fit closure there are several other systematic effects that must be taken into account. First, as discussed above and shown in figure 5.17, a common template for c and light

---

[2]Here and in the following we indicate with "untagged" the jets that do not pass the cut on the tagging discriminator and not the full sample, given by the sum of tagged and untagged samples.

jets is used in the fit. To account for the uncertainty on the relative fraction of c and light jets in the MC, we vary the predicted ratio by $\pm 20\%$, repeat the fit and take the variation in the results as a systematic uncertainty. Another source of error originating from the simulation is the modeling of the fraction of gluon splitting events yielding a $b\bar{b}$ pair. This number is varied by 50% and then the fit is repeated on the modified sample, taking the deviation as a systematic error.

Also the event selection introduces biases in the efficiency measurement, that are accounted for by repeating the fit with different muon p_T thresholds (up to 9 GeV) and with different away-jet taggers (TCHEL and TCHEM instead of TCHPM).

Finally, running conditions have an impact on the b-efficiency measurement that is determined by changing the average value of PU taken from data by 10% and repeating the fit with template distributions reweighted accordingly.

The System8 method

The System8 method extracts from data eight quantities related to tagging efficiencies that are then computed by solving a system of eight linear equations. The sample used is selected in the same way as in the p_T^{rel} method, taking advantage of a muon inside a jet and an away-jet tag. Four of the eight quantities used by the System8 are properties of the muon jets:

- The number n of jets containing a muon (see the p_T^{rel} definition) in the sample, giving the overall normalization.

- The number n^{tag} of tagged muon jets.

- The number n^{ptRel} of muon jets with $p_T^{\text{rel}} > 0.8$ GeV.

- The number $n^{\text{tag;ptRel}}$ of muon jets that satisfy both criteria above.

The remaining four quantities are the equivalent numbers for the away-jets, which we label $p, p^{\text{tag}}, p^{\text{ptRel}}, p^{\text{tag;ptRel}}$. The tagging algorithm used for the away-jets is the TCHP one as in the p_T^{rel} case, but the loose working point is adopted.

The eight unknowns extracted from the eight observables listed above are the number of b and c+light jets in the samples, $n_{b,cl}$ and $p_{b,cl}$, the efficiencies of the $p_T^{\text{rel}} > 0.8$ GeV cut and the efficiencies of the tagging algorithm on b and c+light jets: $\left(\epsilon_{b,cl}^{\text{tag}}, \epsilon_{b,cl}^{\text{ptRel}}\right)$. We can relate these unknowns to the measured quantities using the eight equations

$$
\begin{aligned}
n &= n_b + n_{cl}\,, \\
p &= p_b + p_{cl}\,, \\
n^i &= \epsilon_b^i n_b + \epsilon_{cl}^i n_{cl}\,, \\
p^i &= \beta^i \epsilon_b^i p_b + \alpha^i \epsilon_{cl}^i p_{cl}\,, \\
n^{\text{tag;ptRel}} &= \beta^n \epsilon_b^{\text{tag}} \epsilon_b^{\text{ptRel}} n_b + \alpha^n \epsilon_{cl}^{\text{tag}} \epsilon_{cl}^{\text{ptRel}} n_{cl}\,, \\
p^{\text{tag;ptRel}} &= \beta^p \epsilon_b^{\text{tag}} \epsilon_b^{\text{ptRel}} p_b + \alpha^p \epsilon_{cl}^{\text{tag}} \epsilon_{cl}^{\text{ptRel}} p_{cl}\,,
\end{aligned}
\tag{5.5.3}
$$

where i = tag, ptRel and we introduced the eight factors α and β. The first four, α^i, β^i, allow for differences in efficiency between muon-jets and away-jets. The second four, $\alpha^{n,p}, \beta^{n,p}$, account for the correlation between the tagging and p_T^{rel} cuts. These factors are determined from simulation and are all found to be of $\mathcal{O}(1)$. The system of equations is solved numerically, obtaining simultaneously the tagging efficiencies and flavor compositions of the muon jets and away-jets samples.

Most of the systematics effects are the same as in the case of the p_T^{rel} method with the exception of the uncertainty on the fraction of c and light jets in the MC. Two additional sources of uncertainty must be taken into account. First the effect of the cut on the muon p_T^{rel}: it is varied to 0.5 and 1.2 GeV, the correlation factors are computed again and the system of equations is solved, taking the largest deviation as a systematic uncertainty. The second test that is performed is a closure on the MC, comparing the System8 efficiencies with the MC truth efficiencies. The disagreement is found to give a negligible systematic correction.

The IP3D method

The IP3D method closely follows the p_T^{rel} technique, substituting the template fit to the p_T^{rel} with a template fit to the impact parameter of the muon track, calculated in three dimensions. In this case b-jets tend to have larger values of the IP. This method was introduced because the p_T^{rel} separation starts to be insufficient for jet p_T larger than 120 GeV. On the contrary the IP starts providing a good separation in that regime. The variable entering the fit is $\log|IP|$ as shown in figure 5.18 for the CSVM working point. The systematic uncertainties associated to the method are the same discussed for the p_T^{rel} case. The IP distribution is strongly correlated with the distributions of the IP-based taggers, to a lesser extent this is true for all taggers and also for the p_T^{rel} distribution. However to determine the relative fraction in data of b, c and light jets it is impossible to use a variable that is completely uncorrelated to the taggers. For this reason it is always implicitly assumed that the MC well reproduces this correlation and that the shapes of b, c and light templates, taken from simulation, are reliable both before and after the cut on the tagger discriminator. This assumption is inherent to all the methods, including the System8 technique, where it is hidden in the correlation factors α and β.

The reference lifetime tagger method

Also the lifetime tagger technique falls into the category of template fits. In this case the distribution of the JP discriminator is used to determine the fraction of b, c and light jets in the data sample. The JP tagger has the advantage to provide a good discrimination between the shapes of the templates also at $p_T > 200$ GeV. Furthermore it can be calibrated using tracks with negative IP significance directly on the data [170]. Last but not least the JP discriminator is defined also for jets that have only one selected track with positive IP significance. This makes it very efficient on real b-jets, especially at high p_T.

The template fit determines the relative fractions $f_{b,c,l}$, as in the p_T^{rel} case, separately for tagged
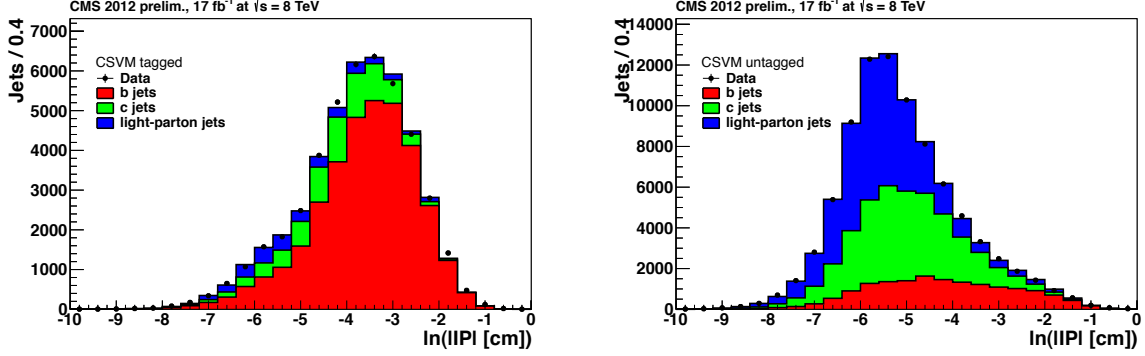
Figure 5.18: Fits to the muon track IP3D with summed b, c and light templates. Left: For jets tagged with the CSV algorithm (medium working point) and Right: For jets that do not pass the medium working point cut on the CSV discriminator. The jet p_T is between 80 and 120 GeV and $|\eta| < 2.4$

and untagged jets. This information is used to compute the tagging efficiency as

$$\epsilon_b = \frac{C_b f_b^T N_T}{f_b^U N_U + f_b^T N_T} \tag{5.5.4}$$

where C_b is the fraction of b-jets for which the JP discriminator is defined (taken from the simulation). It goes from 0.91 for $p_T = 20$ GeV to 0.98 for $p_T > 50$ GeV. We have used the usual notation where $T =$ tagged and $U =$ untagged.

The events on which the measurement is performed are selected following the $p_T^{\rm rel}$ method requirements. In this case, however, no away-jet tag is imposed for events with a muon jet and a separate sample with no requirements on the presence of a muon jet is also studied. In this inclusive sample one of the jets must be tagged with JPM to increase the b-purity.

The method has the obvious disadvantage that it can not be used to determine the efficiency of the JP and JBP taggers. However the problem is easily solved by using the CSV discriminator (also defined on $\approx 90\%$ of jets). To determine the bias thus introduced the CSV discriminator is used also to determine the efficiency of the TC algorithms, which is then compared to the JP determination. This allows to correct the JP scale factors for the bias that ranges from 0-2% to $6 - 9\%$ going from loose to tight operating points.

The systematic errors affecting the measurement consist of PU, gluon splitting and muon p_T effects already discussed for the $p_T^{\rm rel}$ method, plus three other sources of uncertainty characteristic of this technique. The fraction C_b of jets for which the JP discriminator is defined has an associated uncertainty of $\mathcal{O}(3\%)$ and computed separately for each jet p_T bin in which the fit is performed. The second effect that is accounted for as a systematic uncertainty is the difference between the SF measured in the muon jet and inclusive jet samples. If the statistical error on the inclusive jet

sample SF is larger than the difference, this statistical error is used as a systematic uncertainty. The last source of uncertainty affects only the JP and JBP scale factors and it arises from the uncertainty on the bias correction factors from the CSV fit. This error is taken to be the difference between 1 and the correction factor (computed as the ratio between the SF, for the TC algorithms, determined with the JP fit and those determined with the CSV fit).

5.5.5   Tagging efficiency from $t\bar{t}$ events

As stated before in the course of the chapter, tagging algorithms are complex objects with several moving parts in non-trivial relations with each other. They are much more sensitive to the topology of the event with respect to lepton, photon or even jet identification techniques. For this reason it is worth to measure the tagging efficiency on different data samples. The natural candidate other than muon-jets events are $t\bar{t}$ events. The reason is mainly their abundance at the LHC, which makes them both a statistically viable sample and an important background for new physics searches. A second quality of this sample is the p_T range of the b-jets that covers an interval relevant for many searches, distributed around 80 GeV.

In this section we briefly describe four techniques used in $t\bar{t}$ events to measure tagging efficiencies, while we show the results in the next section, comparing them with the muon-jets results. The techniques we discuss are: the Flavor Tag Matching (FTM), the Flavor Tag Consistency (FTC), the JP template and the bSample methods.

The events used for the measurement fall into two different categories. The lepton+jets channels, used in the bSample method, are composed of events containing one isolated muon with $p_T > 25$ GeV and $|\eta| < 2.1$ or an electron with $p_T > 32$ GeV and $|\eta| < 2.5$, at least four jets with $p_T > 40$ GeV and $|\eta| < 2.5$. The FTC method is applied to events with one isolated $p_T > 30$ GeV and $|\eta| < 2.1$ muon (additional muons and electrons are rejected), two leading jets with $p_T > 70$ GeV and 50 GeV, respectively and $ME_T > 20$ GeV. The dilepton channels, used in the FTM and JP template methods, contain events with isolated, oppositely charged leptons with $p_T > 20$ GeV and $|\eta| < 2.5$, at least two jets with $p_T > 30$ GeV and $|\eta| < 2.5$. Furthermore $ME_T > 40$ GeV is required for events with same flavor leptons. To reduce the Drell-Yan (DY) and heavy-flavor resonances background two requirements on the invariant mass of same flavor leptons are imposed: $m_{ll} > 12$ GeV and events with 76 GeV $< m_{ll} < 106$ GeV are discarded.

Without any b-tagging requirement the $e\mu$ dilepton sample contains roughly 88% of $t\bar{t}$, while the ee and $\mu\mu$ are composed at 68% of $t\bar{t}$ events. The purity of the single lepton samples is lower, around 60%.

There are systematic uncertainties common to all methods that we outline here. The uncertainty due to the MC modeling of the underlying event is estimated by comparing results between a sample generated with the PYTHIA Z2 tune to that with the D6T tune [175]. The effect due to the scale used to match clustered jets to partons is estimated by varying the p_T matching threshold by factors of 2 and 1/2. Renormalization and factorization scales uncertainties are also computed using samples with the scales varied simultaneously by a factor of 2 and 1/2. The PDF4LHC prescription [176] is followed to obtain the uncertainty on the parton distribution functions (PDF).

The last uncertainty arising from the MC simulation is related to the relative composition of simulated samples. The fractions of the different background species are varied with respect to the $t\bar{t}$ signal and each other.

There are also several effects arising from our imperfect knowledge of the detector. The jet energy scale and resolution effects have been discussed in the first part of this chapter. To a lesser extent also lepton energy scale effects enter in the error determination. The error on the trigger and lepton identification efficiencies is also taken into account. Finally to model the PU uncertainty, the average value of the distribution is varied by $\pm 10\%$.

In the following we briefly describe the FTC, FTM and bSample methods. The JP template method is identical to the reference lifetime tagger method described for μ+jets events, with small technical differences in the implementation that are not relevant for this work. The most notable one being the fact that the JP and JPB scale factors are not measured on $t\bar{t}$ events.

The flavor tag consistency method

The FTC method exploits the known dependence of the number of expected tagged jets on the tagging efficiencies

$$\mu_n = L\sigma_{t\bar{t}}\epsilon \sum_{i,j,k} F_{ijk} \hat{\sum}_{i',j',k'} \left[C_{ii'}\epsilon_b^{i'} \left(1-\epsilon_b\right)^{i-i'} C_{jj'}\epsilon_c^{j'} \left(1-\epsilon_c\right)^{j-j'} C_{kk'}\epsilon_l^{k'} \left(1-\epsilon_l\right)^{k-k'} \right] , \quad (5.5.5)$$

where L is the integrated luminosity, $\sigma_{t\bar{t}}$ is the $t\bar{t}$ production cross section and ϵ the selection efficiency of the lepton+jets sample on which the method is applied. The factors F_{ijk} are the fraction of events with i b-jets, j c-jets and k light jets, derived from simulation. The sum $\hat{\sum}$ is restricted over values of the primed indexes smaller than the corresponding non-primed index and on $i' + j' + k' = n$. Finally the factors $C_{ii'}$ are just the binomial coefficients

$$C_{ii'} = \left(\begin{array}{c} i' \\ i \end{array} \right) . \quad (5.5.6)$$

The b-tagging efficiencies are then obtained from a maximum likelihood fit to

$$\mathcal{L} = -2\log \prod_n \mathcal{P}\left(N_n^{\text{obs}}, \mu_n\right) , \quad (5.5.7)$$

where N_n^{obs} (μ_n) is the number of observed (expected) events with n b-tagged jets. The $t\bar{t}$ cross section is treated as a free parameter in the fit and the result is consistent with the CMS published values [177, 178, 179]. The c and light jet tagging efficiencies are taken from the simulation and corrected for the data/MC scale factors.

The uncertainty from the fitting procedure is determined using pseudo-experiments where the number of signal and background events are generated using Poisson statistics with mean values the number of expected events in each channel. Events are then randomly chosen in the simulated samples. The difference of the efficiency obtained from the new fit and the nominal one is taken as a systematic uncertainty. Other sources of errors are common also to the other methods and were described at the beginning of this section.

The flavor tag matching method

Also in this case an analytical estimate of the number of expected b-tagged jets is constructed,

$$\mu_n = \sum_k n_k P_{nk} \,, \tag{5.5.8}$$

where n_k is the observed number of events with k jets and the sum extends over all jets. P_{nk} is the probability to have n tags in a k jets sample. The P_{nk} are constructed as a product of tagging efficiencies and misassignement probabilities α_i that correspond to the probability that i jets from the $t\bar{t}$ decay have been reconstructed and selected. For two jets we would have

$$P_{n2} = \sum_{i=0}^{2} \alpha_i P_{n2}^i \,, \quad P_{n2}^i = \left\{ \begin{array}{l} \epsilon_l^2 \,, \ i = 0 \\ 2\epsilon_b \epsilon_l \,, \ i = 1 \\ \epsilon_b^2 \,, \ i = 2 \end{array} \right. \,, \tag{5.5.9}$$

where $\epsilon_{b(l)}$ are the tagging efficiencies for b (light=$udsgc$) jets. From the μ_n's is easy to construct a likelihood

$$\mathcal{L}(\epsilon_b) = \prod_n \mathcal{P}\left(N_n^{\text{obs}}, \mu_n\right) \prod_i \mathcal{G}\left(\alpha_i, \hat{\alpha}_i, \sigma_{\alpha_i}\right) \mathcal{G}\left(\epsilon_l, \hat{\epsilon}_l, \sigma_{\epsilon_l}\right) \,, \tag{5.5.10}$$

where $\mathcal{G}$ denotes the gaussian distribution. A maximum likelihood fit to dilepton events is then used to determine the b-tagging efficiencies.

The central values and uncertainties on the light jets tagging efficiencies are derived from simulation. The misassignement probabilities are determined from data using the tails of the invariant mass of the lepton-jet pairs that for b-quarks from $t\bar{t}$ decays have an endpoint at $\sqrt{m_t^2 - m_W^2}$. The extraction method is described in detail in [180] and is used independently in each dilepton channel and each jet-multiplicity bin. The procedure is checked and found to be unbiased with MC pseudo-experiments.

The relevant systematic uncertainties have been described at the beginning of this section. To assess them the misassignement probabilities and mistagging efficiencies are recomputed on the different MC samples (varying the matching scale for instance) and the fit is repeated. In this way all MC-based uncertainty are taken into account. The main uncertainties arise from the MC factorization scale, and to a smaller extent, the jet-parton matching threshold.

The bSample method

The measurement is performed on a b-enriched sample selected from the lepton+jets sample. First, partons are matched to the four leading jets, minimizing the χ^2

$$\chi^2 = \left(\frac{m_{bqq} - m_t}{\sigma_t}\right)^2 + \left(\frac{m_{qq} - m_W}{\sigma_W}\right)^2 \,, \tag{5.5.11}$$

where the mean masses and uncertainties are obtained from a fit to the $t\bar{t}$ simulation. In this way we have a complete description of the event topology. Subsequently a b-candidate sample is

produced by considering the jet that together with the lepton reconstructs a top candidate. In this sample there is still an high contamination from non b-jets. Therefore it is further subdivided in a b-enriched and b-depleted subsamples, based on the lepton-jet invariant mass, that in the first case is required to be 80 GeV $< m_{lj} <$ 150 GeV while in the second 150 GeV $< m_{lj} <$ 250 GeV. Finally the efficiency is determined from the discriminator distribution for the true b-jets D_b, given by the discriminators in the two subsamples

$$D_b = D_b^{\mathrm{enr}} - F \cdot D_b^{\mathrm{depl}} . \tag{5.5.12}$$

The factor F, indicating the ratio between the contamination from non-b jets in the b-enriched and b-depleted samples is computed from simulation and is found to be ≈ 1.3.

A subtlety of the method is the correlation between m_{lj} and the jet p_T that in turn introduces a correlation between the discriminator distribution and m_{lj}. To correct for it the jets are reweighted according to their p_T.

Other than the uncertainties common to all methods, an error of 0.5% is due to the choice of the boundaries of the b-depleted region. The closure test of the method on the MC gives a systematic error dominated by statistics in the samples of $\mathcal{O}(3\%)$ for the loose operating points.

5.5.6   Tagging performances

The performances in simulation of the algorithms described in the previous sections are depicted in figure 5.19. The results in the figure were obtained using $\sqrt{s} = 7$ TeV MC The typical tagging efficiency for loose working points (mistag rate = 10%) is around $80 - 85\%$. For medium working points it falls in the range of $60 - 70\%$ while for tight ones it is around $45 - 55\%$. For medium and tight selections the CSV algorithm displays the best performances and is slightly outclassed by JBP for the loose operating point. The efficiency of c-tagging is generically higher than the mistag rate *tout court* due to common properties of the c and b hadrons (relatively high mass, fragmentation functions, ...). The typical values of c-tagging probabilities are around 1/5 of the b-tagging efficiency.

The tagging performances in data are updated every year. The results remained relatively stable going from the $\sqrt{s} = 7$ TeV to the $\sqrt{s} = 8$ TeV running conditions as can be seen from tables 5.2 and 5.3 for two different p_T ranges. The SF exhibit a dependence on the jet p_T and η and have been measured in bins of these two quantities. A sample p_T dependence for $|\eta| < 2.4$ can be seen, for muon-jets events and the CSVM working point, in figure 5.20. A comparison between different taggers is instead shown in figure 5.21 for measurements performed on $t\bar{t}$ events. From the plots and tables we can conclude that the MC reproduces the data within 2% for loose operating points, 3% for medium ones and $6 - 8\%$ for tight ones, that the results of tagging efficiencies all agree within the error also across different samples and that typical uncertainties on the SF range between 2% and 5%. The combined scale factors from different methods are obtained from a weighted average that takes into account the full covariance matrix of the uncertainties following the BLUE technique [181].
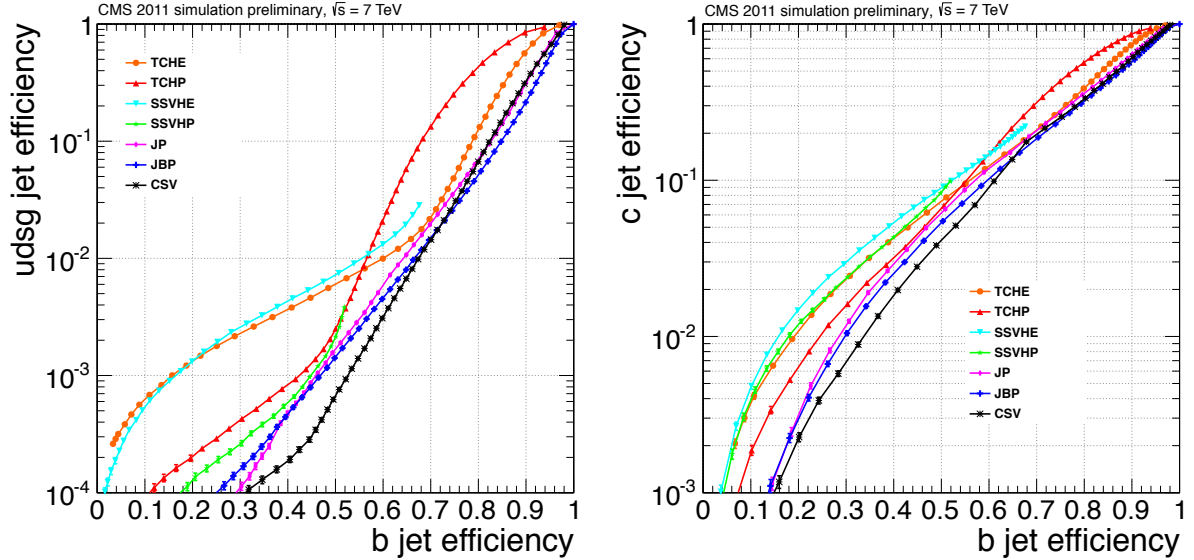
Figure 5.19: Performance curves obtained from simulation for the b-tagging algorithms described in the text. Left: mistag rate versus b-tagging efficiency. Right: c-tagging versus b-tagging efficiencies. Figures taken from [170].

Tagger	SF_b muon jets + $t\bar{t}$ (2012)	SF_b muon jets (2012)	SF_b muon jets (2011)
CSVL	0.979 ± 0.016	0.969 ± 0.022	0.985 ± 0.016
JPL	0.976 ± 0.024	0.976 ± 0.024	0.990 ± 0.026
CSVM	0.966 ± 0.025	0.961 ± 0.027	0.949 ± 0.019
JPM	0.967 ± 0.034	0.967 ± 0.034	0.923 ± 0.031
CSVT	0.931 ± 0.033	0.919 ± 0.036	0.907 ± 0.029
JPT	0.910 ± 0.044	0.910 ± 0.044	0.875 ± 0.044
TCHPT	0.944 ± 0.025	0.924 ± 0.032	0.911 ± 0.034

Table 5.2: Scale factors obtained in muon-jet and $t\bar{t}$ data in 2012, in muon-jet data alone in 2012 and in muon-jet data in 2011. The b-jet p_T range is between 80 and 120 GeV.

5.5.7   Mistag rates

The mistag rates are measured from tracks with a negative impact parameter or from secondary vertices with a negative decay length. These objects are used to define negative values of the discriminators of the tagging algorithms discussed previously. These negative taggers can be applied as ordinary b-tagging algorithms. The data sample is collected with single jet triggers.
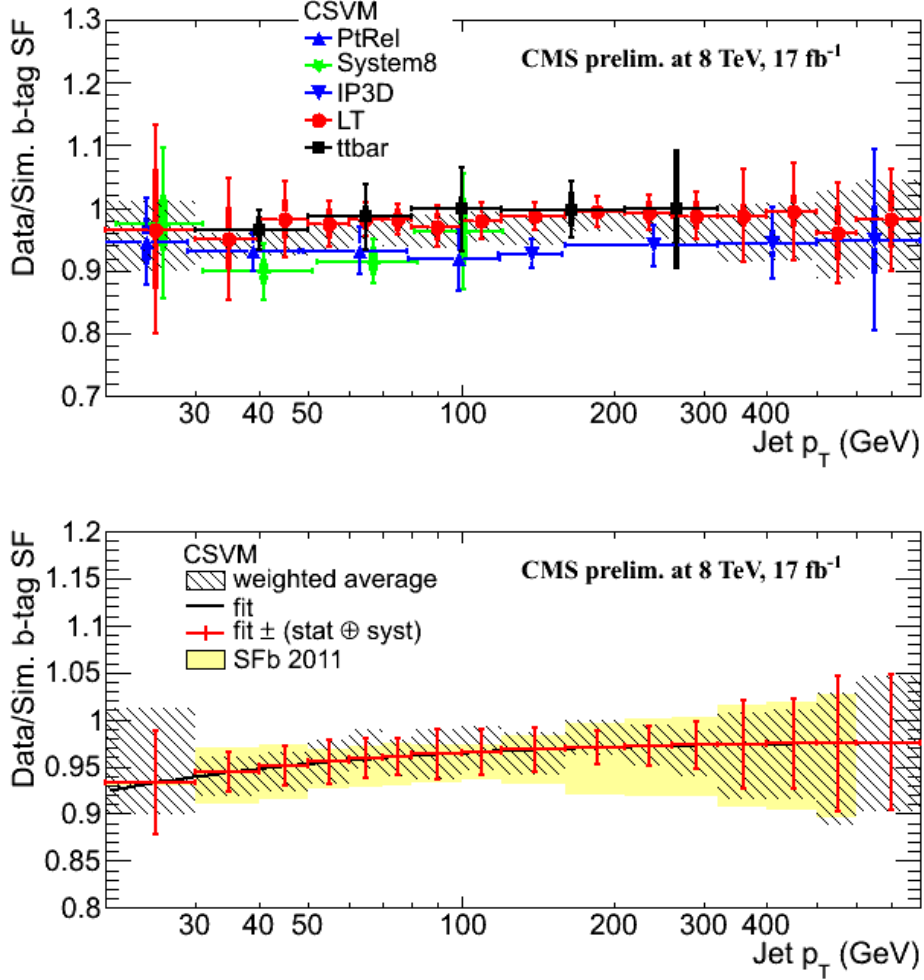
Figure 5.20: Top: data/MC SF of the b-tagging efficiency as measured with the four methods used with muon-jets events and the combined result for $t\bar{t}$ events, with statistical error and overall statistical+systematic uncertainty (thin error bar) . The combined SF_b value with its overall uncertainty is shown as a hatched area. Bottom: same combined SF_b value plus result of a polynomial fit (solid curve). The uncertainty is renormalized around the fit result (points with error bars). We show also the SF_b results from the 2011 data at 7 TeV (yellow filled area). These results are valid for the CSVM working point.

The mistag rate is then evaluated as

$$\epsilon_{\mathrm{data}}^{\mathrm{mistag}} = \epsilon_{\mathrm{data}}^{-} R_l \,, \tag{5.5.13}$$
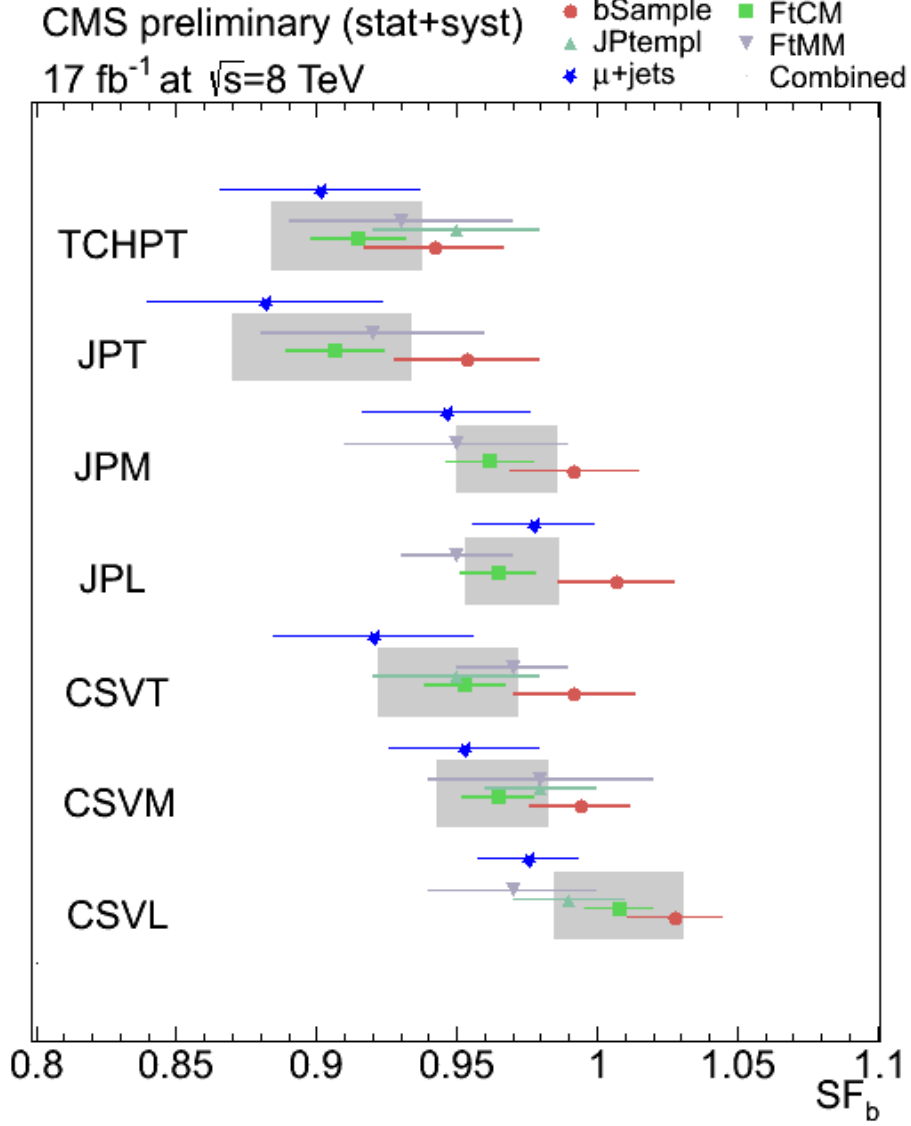
Figure 5.21: SF_b measurements in $t\bar{t}$ events averaged over the p_T range between 30 and 320 GeV. The blue points show the corresponding measurement on muon-jets events. Grey areas are given by the combination of $t\bar{t}$ scale factors.

where ϵ_{data}^- is the efficiency of the negative tagging procedure in data, while $R_l = \epsilon_{MC}^{\text{mistag}}/\epsilon_{\text{MC}}^-{}^3$. The result of the measurement is expressed in terms of a scale factor

$$SF_l = \epsilon_{\text{data}}^{\text{mistag}}/\epsilon_{MC}^{\text{mistag}}, \tag{5.5.14}$$

---
[3]It is appropriate to point out that ϵ_{MC}^- is the negative tag rate for all jets (b+c+light)

Tagger	SF_b muon jets + $t\bar{t}$ (2012)	SF_b muon jets (2012)	SF_b muon jets (2011)
CSVL	0.977 ± 0.018	0.975 ± 0.018	0.974 ± 0.026
JPL	0.976 ± 0.017	0.976 ± 0.017	0.991 ± 0.022
CSVM	0.972 ± 0.022	0.970 ± 0.025	0.957 ± 0.040
JPM	0.967 ± 0.033	0.967 ± 0.033	0.947 ± 0.036
CSVT	0.954 ± 0.043	0.947 ± 0.050	0.916 ± 0.068
JPT	0.942 ± 0.040	0.942 ± 0.040	0.909 ± 0.051

Table 5.3: Same as table 5.2 in the b-jet p_T range 160-320 GeV.

in analogy to the b-tagging efficiency measurement.

The procedure is sensitive to the fraction of b and c jets in the negatively tagged sample that tend to decrease R_l. Furthermore differences between light quarks and gluons can affect the determination of the efficiency, just as tracks from displaced decays of K_S^0 and Λ or mismeasurements in the tracker. Among others these effects are taken into account in the determination of the systematic uncertainty.

The fraction of b-jets has been measured to agree with the simulation within $\pm 20\%$ in CMS [182]. A corresponding uncertainty on R_l is derived by varying the b+c fraction in the MC by this amount. The same procedure is repeated for gluon jets, with their fraction being varied by $\pm 20\%$ to reproduce data-MC discrepancies [183]. Also the fraction of K_S^0 and Λ is not exactly reproduced by the simulation. After rescaling the MC to take this effect into account, the uncertainty on the rescaling is used to vary the correction factor and obtain new values of R_l. The difference with the nominal values gives the systematic uncertainty. Additional systematic effects include the uncertainty on the rate of secondary interactions in the pixels and of tracks not associated to a genuine charged particle. Furthermore small differences in the angle between a track and the jet axis can lead to a change of the sign of the impact parameter, changing the negative tag rate ("sign flip").

Ultimately, running conditions and event topology can also affect the measurement. The MC is reweighted to reproduce the PU distribution in data. However residual difference are estimated by splitting the sample into two according to the PV multiplicity (above and below average respectively). If the SF in the two samples differ appreciably, the difference is taken as an uncertainty.

The dominant uncertainty arises from the difference in event topology. Mistagging SF have been measured under different running conditions, for different bins of jet multiplicity and different triggers. Furthermore the SF differ between the leading and subleading jets in the event. All these effects have been taken into account collectively giving a total uncertainty of about 10%.

In figure 5.22 we show the result of the measurement for the CSVM working point. The SF change between working points and taggers, but the values of the probability $\approx 1-4\%$ and of the SF, close to unity and with an error of $\approx 10\%$, are representative of a generic medium working point.
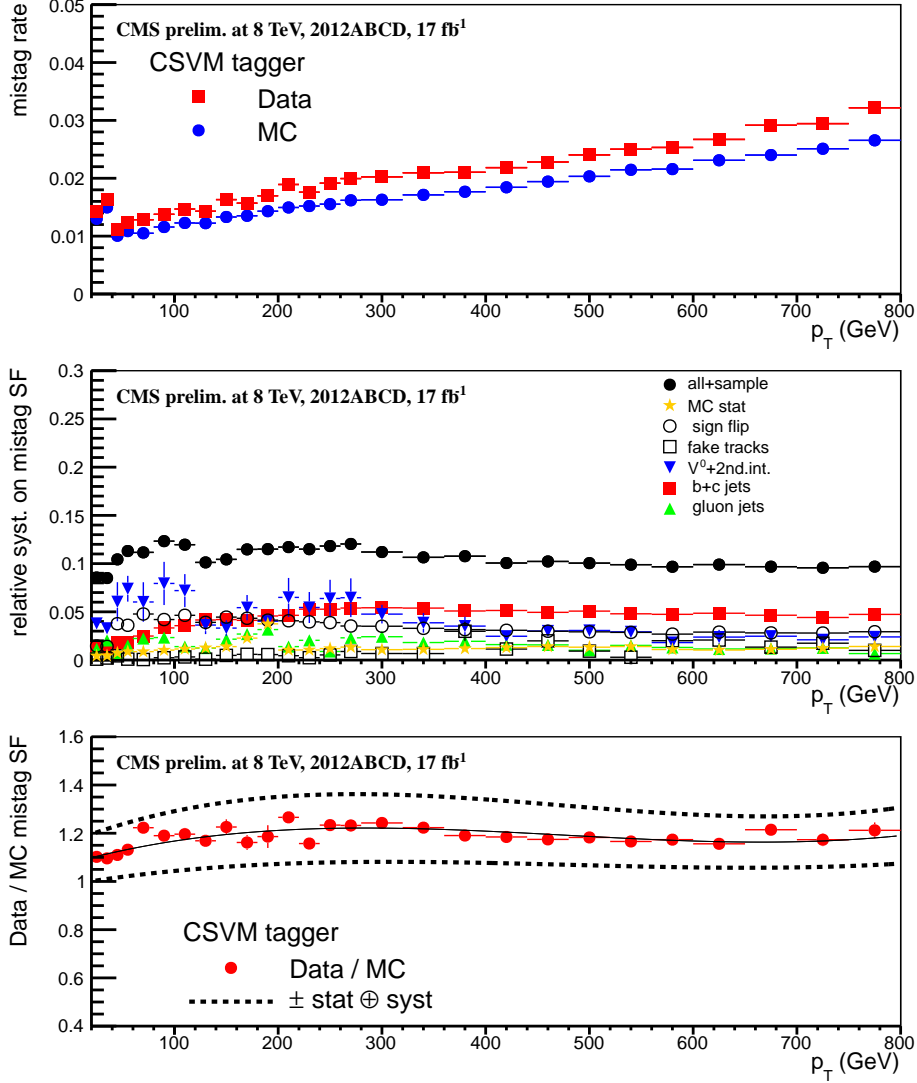
Figure 5.22: Above: Light jet misidentification probability (defined in section 5.5.7) in data (red squares) and simulation (blue dots). Center: Breakdown of the error on the mistag SF. Below: data-MC scale factors for the misidentification probability. The solid curve is given by a polynomial fit to the data. The last bin in both plots is inclusive, containing all jets with $p_T \geq 800$ GeV.

5.5.8 Residual Fast Simulation corrections

Several signal samples inside CMS are generated using a simplified version of the GEANT4 detector simulation that is known under the name of Fast Simulation (FastSim) [184]. This is particularly convenient for fine scans of SUSY masses, since it considerably reduces the processing time and

the computing resources needed. The simplification occurs mainly in the tracking part of the simulation, in particular

- Large occupancy effects are not reproduced: two hits with the same space coordinates always give two reconstructed hits.

- Edge effects are not reproduced: reconstructed hits may fall outside of a physical detector module after a smearing is applied to their position to account for resolution effects.

- Reconstructed hits on double-sided layers are reconstructed as one dimensional hits.

- There are not hits shared by different tracks.

Fast-Full simulation scale factors for tagging efficiencies have been derived by using the MC truth information on jet flavors. They have been measured only for $t\bar{t}$ MC samples. To account for the different topology we apply an additional uncertainty derived from the ratio of efficiencies in $t\bar{t}$ and SUSY Fast simulation samples, before applying them to SUSY signal samples. The overall correction is smaller than that due to data-MC SF, giving a less than 1% correction for typical SUSY signals.

5.5.9 Scale factors usage and uncertainties

In the next chapter we use the scale factor measurements presented in the previous sections to obtain the correct background prediction and signal efficiency at high b-jet multiplicities. We first measure the efficiency from the MC and then use the SFs to apply a jet-by-jet correction. Depending on the value of the SF it is possible to compute a p_T and η dependent probability that allows to decide whether the tag of a jet should be changed or not (i.e. a b-tagged jet can become untagged or vice versa). This procedure is not optimal if we are interested in distributions of some b-tag-related variables. For instance the secondary vertex mass is not well defined after our "tag switching", but this is not a problem for the search that we perform.

After scale factors have been applied their uncertainty propagates to the final efficiency. The error is computed by varying the SFs by $\pm 1\sigma$. The only subtlety associated to the procedure consists in the fact that we have only measured data-Full simulation SFs for b and light jets. The correct c-tagging efficiency is obtained by applying the scale factors measured for b-jets with twice the quoted uncertainty. Therefore while computing systematic uncertainties we treat the errors on b- and c-jets as fully correlated. We then sum the effect in quadrature with that arising from the light jets scale factor uncertainty that is largely uncorrelated.

The uncertainties across different jet p_T and η bins are also fully correlated. When computing the effect of varying the scale factors by $\pm 1\sigma$ we scale them simultaneously over the whole p_T and η ranges.

5.6   Conclusion

In this chapter we have discussed jet reconstruction and calibration with CMS and given an account of our b-tagging techniques. These are the main ingredients for the analysis presented in the following chapter that contains the truly original contributions in this part of the thesis. The great performances of jet reconstruction and b-tagging, together with the work done by the collaboration to commission MC tools and reduce the JES uncertainty allowed to explore new areas of phase space with 8 or more jets, four of which can be b-tagged. This is an extremely interesting measurement in itself, since it is probing previously unexplored regimes. From a theoretical perspective it is significant to natural supersymmetry, supersymmetry with low ME_T and generic new physics scenarios rich in top and b quarks.

Chapter 6

A new physics search on the tails of the jet and b-jet multiplicities

> A safe but sometimes chilly way of recalling the past is to force open a crammed drawer. If you are searching for anything in particular you don't find it, but something falls out at the back that is often more interesting.
>
> *James Matthew Barrie*

In this chapter we describe a new search for BSM physics performed with the CMS detector. The previous two chapters provided the necessary ingredients to introduce this analysis. The search is designed to be inclusive on final states with a large number of jets and b-jets. It is sensitive to a broad class of supersymmetric models, described at the end of chapter 3 and in general to new physics scenarios rich in top or b quarks.

6.1 Introduction

One of the many challenges that physicists must face at the LHC is the lack of a precise intuition of how physics beyond the Standard Model will manifest itself. Even if we restrict ourselves to a specific class of models, such as supersymmetric theories, a huge number of possibilities is left open in terms of experimental signatures, which, to a large extent, depend on the fine structure of the new particles spectrum. Also naturalness, used as a guiding principle, is not enough to identify a limited set of relevant final states.

For this reason we have designed an inclusive analysis, based on the event topology, that is sensitive to a wide range of theoretical models. We explore a still virgin land, focussing on

events with one lepton (either an electron or a muon) large jet multiplicities ($N_J \geq 6$) and we do not require any ME_T in the final state. The signal is extracted by performing a fit to the distribution of the number of b-tagged jets in the event with an eye to new physics scenarios rich in third generation quarks. However rather than cutting on the number of b-jets we retain all the information on the shape of the distribution. In the following we show that this allows to gain in efficiency also for signals with four b's in the final state.

We interpret the results of the search in a supersymmetric simplified model that was discussed in section 3.6 in the context of the MFV RPV MSSM. We assume the gluino to be the LSP and study its most important decay mode

$$pp \to \tilde{g}\tilde{g}, \quad \tilde{g} \to tbs\,. \tag{6.1.1}$$

The analysis was originally designed to be sensitive to a decay chain inspired by the discussion of the minimal natural R-parity conserving MSSM in section 3.5.2, containing four top quarks in the final state

$$pp \to \tilde{g}\tilde{g}, \quad \tilde{g} \to \tilde{t}_1\bar{t}, \quad \tilde{t}_1 \to t\widetilde{\chi}_0\,. \tag{6.1.2}$$

However the analysis was constructed to be inclusive and not to rely on ME_T, which makes it sensitive also to third generation RPV final states.

In the next section we describe the data and MC samples used for the analysis, then in section 6.3 we discuss the event selection. In sections 6.4 and 6.5 we present signal efficiencies and background predictions, respectively. Finally we study systematic errors in section 6.6 and show the results for the benchmark model described above in sections 6.7 and 6.8.

6.2   Samples

6.2.1   Data Sample

The data sample consists of events collected by the CMS experiment at 8 TeV center-of-mass energy during 2012. The total statistics corresponds to about 19.3 fb^{-1}. We use two sets of triggers, corresponding to two different datasets. The `SingleMu` dataset and the `SingleElectron` dataset.

Table 6.1 summarizes the list of single-muon HLT paths used and the run range for which they were kept unprescaled. In Table 6.2 the corresponding single-electron triggers are listed. Tab. 6.3 summarizes the datasets used for the analysis.

6.2.2   Monte Carlo Samples

The background studies at $\sqrt{s} = 8$ TeV are based on the following samples, centrally produced by CMS:

- 6.4×10^7 `MadGraph` W+jets events;

- 2.1×10^7 `MadGraph` $Wb\bar{b}$+jets events;

- 3.4×10^7 `MadGraph` Drell-Yan+jets events;

- 4.8×10^6 `MadGraph` inclusive $t\bar{t}$+jets events;

- 3.1×10^7 `MadGraph` fully-hadronic $t\bar{t}$+jets events;

- 2.5×10^7 `MadGraph` semi-leptonic $t\bar{t}$+jets events;

- 1.2×10^7 `MadGraph` fully-leptonic $t\bar{t}$+jets events;

- 2.0×10^5 `MadGraph` $t\bar{t}W$+jets events;

- 2.1×10^5 `MadGraph` $t\bar{t}Z$+jets events;

HLT Path	First Run	Last Run
`HLT_IsoMu24`	193834	205921
`HLT_IsoMu24_eta2p1`	190456	to the end

Table 6.1: Single muon triggers with isolation requirements used in our selection.

HLT Path	First Run	Last Run
`HLT_Ele27_WP80`	190456	to the end

Table 6.2: Single electron trigger used in the analysis.

Dataset Name	Run Range	Release
190456 - 190621	/SingleElectron/Run2012A-13Jul2012-v1/AOD	CMSSW_5_3_X
190782 - 190949	/SingleElectron/Run2012A-recover-06Aug2012-v1/AOD	CMSSW_5_3_X
193834 - 196531	/SingleElectron/Run2012B-13Jul2012-v1/AOD	CMSSW_5_3_X
197770 - 198913	/SingleElectron/Run2012C-PromptReco-v1/AOD	CMSSW_5_3_X
203003 - 203755	/SingleElectron/Run2012C-PromptReco-v2/AOD	CMSSW_5_3_X
203773 - 207469	/SingleElectron/Run2012D-PromptReco-v1/AOD	CMSSW_5_3_X
190456 - 190621	/SingleMuon/Run2012A-13Jul2012-v1/AOD	CMSSW_5_3_X
190782 - 190949	/SingleMuon/Run2012A-recover-06Aug2012-v1/AOD	CMSSW_5_3_X
193834 - 196531	/SingleMuon/Run2012B-13Jul2012-v1/AOD	CMSSW_5_3_X
197770 - 198913	/SingleMuon/Run2012C-PromptReco-v1/AOD	CMSSW_5_3_X
203003 - 203755	/SingleMuon/Run2012C-PromptReco-v2/AOD	CMSSW_5_3_X
203773 - 207469	/SingleMuon/Run2012D-PromptReco-v1/AOD	CMSSW_5_3_X

Table 6.3: Summary of the relevant single lepton 2012 datasets.

- `MadGraph` $t\bar{t}$+jets events with renormalization, factorization and matching scales shifted by the amounts specified in section 6.6

    - 5.4×10^6 events of $t\bar{t}$+jets with renormalization and factorization scales shifted up;
    - 3.6×10^6 events of $t\bar{t}$+jets with renormalization and factorization scales shifted down;
    - 5.4×10^6 events of $t\bar{t}$+jets with matching scale shifted up;
    - 3.2×10^6 events of $t\bar{t}$+jets with matching scale shifted down;

- `MadGraph` single top events divided in the following categories

    - 6.5×10^6 events of t s-channel production;
    - 1.6×10^6 events of t t-channel production;
    - 1.6×10^6 events of tW;
    - 6.5×10^6 events of $\bar{t}$ s-channel production;
    - 1.6×10^6 events of $\bar{t}$ t-channel production;
    - 1.6×10^6 events of $\bar{t}W$;

- `MadGraph` QCD events, with up to 6 partons in the final state, binned in H_T:

    - 6.5×10^6 events for 100 GeV $< H_T <$ 250 GeV;
    - 1.6×10^6 events for 250 GeV $< H_T <$ 500 GeV;
    - 1.6×10^6 events for 500 GeV $< H_T <$ 1000 GeV;
    - 1.6×10^6 events for 1000 GeV $< H_T < \infty$;

    The signal samples consist of

- `PYTHIA` events for the simplified model topology $pp \to \widetilde{g}\widetilde{g}$, $\tilde{g} \to tbs$, with the gluino mass ranging from 200 GeV to 1250 GeV.

Where not indicated otherwise `MadGraph` samples are generated with up to four partons in the final state and a matching threshold of 20 GeV for the partons.

6.3   Event Selection

After the HLT requirement described in the previous section, we apply a series of offline cuts that define our baseline selection. The events that pass the baseline selection are then used in a maximum likelihood fit of the distribution of b-tagged jets that provides the final discrimination between signal and background. Before describing the baseline selection and sketching the fitting procedure we define the relevant physics objects.

6.3.1   Primary Vertex

As discussed in section 5.5.2, PV candidates are selected by clustering reconstructed tracks using the z coordinate of their closest approach to the beam line. An adaptive vertex fit, described in [167], determines the vertices positions. After the fit the PV candidate with highest $\sum \left(p_T^{\mathrm{track}}\right)^2$ is identified as the primary vertex, where the hard interaction took place. Events without any PV candidates are discarded in our offline selection. This requirement is close to be 100% efficient on events passing the single lepton triggers listed in the previous section.

6.3.2   Muon Selection

Muon reconstruction in CMS is performed with the silicon tracker at the center of the detector and with the gas-ionization muon detectors outside of the central solenoid. In the standard algorithms for pp collisions [145, 140] tracks are first reconstructed independently in the silicon tracker and in the muon spectrometer. From these two collections of tracks a muon can be identified in two independent ways:

- `GlobalMuon`: starting from a standalone track in the muon system, a matching track is found in the tracker and a global-muon track is fitted combining hits from the tracker track and standalone-muon track.

- `TrackerMuon`: All tracker tracks with $p_T > 0.5$ GeV and $p > 2.5$ GeV are extrapolated to the muon system taking into account the expected energy loss and the uncertainty due to multiple scattering. A `TrackerMuon` is identified if at least one muon segment (i.e. a short track stub made of DT or CSC hits) matches the extrapolated track in position.

Only for 1% of collision muons a standalone track is not associated to any reconstructed track in the tracker.

Following the 2012 $h \to WW$ selection criteria [185] we identify muons using both flavors of muon reconstruction. We require the muon to be reconstructed as `GlobalMuon`, with $\chi^2/\mathrm{dof} < 10$ on the global fit, or `TrackerMuon`. In the first case we further require at least one good muon hit, and at least two matches to muon segments in different muon stations. A `TrackerMuon` must also have at least two muon segments matched at 3σ in local X and Y coordinates, with one being in the outermost muon station. Following this identification procedure a set of quality requirements is applied:

- Number of hits in the tracker > 5

- Number of pixel hits > 0

- Transverse impact parameter with respect to the primary vertex $< 0.2(0.1)$ mm for muons with p_T greater (smaller) than 20 GeV. This cut suppresses non-prompt muons, including those from decays of b and c hadrons.

- Longitudinal impact parameter of the muon with respect to the primary vertex < 1 mm

- $|\eta| < 2.1$

- Relative error on the track $p_T < 0.1$

- decay in flight with the kink finding algorithm[1]: $\chi^2/\text{dof} < 20$

- Identified as Particle-Flow (PF) Muon [186].

The total identification efficiency, not including isolation, is above 90%.

We reject events if no muon is selected with $p_T > 35$ GeV. Furthermore an isolation cut is applied. We use the PF combined isolation, that considers energy deposits of PF candidates in three different categories: charged hadrons, photons, and neutral hadrons. Pile-up subtraction is performed using an average energy density computed by `FASTJET` [161] for photons and neutral hadron candidates. Charged tracks not compatible with the primary vertex are also subtracted. A more detailed discussion of PU subtraction in CMS can be found in section 5.3.1. The variable we use is

$$\frac{\text{Iso}_{\text{PF}}}{p_T} \equiv \frac{1}{p_T} \left(\text{Iso}_{ch} + \text{Iso}_n + \text{Iso}_\gamma - \rho \times A_{eff} \right) . \tag{6.3.1}$$

Iso_{ch} is the sum of the transverse momenta of the charged candidates, Iso_n of the neutral hadrons and Iso_γ of the photons. ρ is the event-by-event energy density computed with `FASTJET` and A_{eff} an effective area computed from simulation. In the tight selection used in the signal regions the isolation cone depends on the η and p_T of the muon and the cut is performed on a BDT output described in [185]. The efficiency is comparable to that obtained with a cut of about 0.1 on $\frac{\text{Iso}_{\text{PF}}}{p_T}$ with isolation cone 0.4.

6.3.3 Electron Selection

Electrons traversing the tracker material radiate photons and the energy reaches the ECAL spread in ϕ. Integrated along the electron trajectory the effect can be very large. Thus, to obtain a measurement of the electron energy at the primary vertex and minimize the cluster containment variations, it is essential to collect bremsstrahlung photons. This is the purpose of the *supercluster*-*tering* algorithms. Therefore the basic quantity needed to reconstruct an electron in CMS is an ensemble of crystals with energy deposits that in the following we call *supercluster*. For a more complete definition, we refer to [187].

Also the electron selection follows the 2012 $h \to WW$ requirements. We adopt a selection, which roughly corresponds to an 80% efficiency on real electrons originating from an EW process. The identification procedure is based on an MVA, that takes as input kinematical variables, ECAL cluster shape and track quality information, in addition to the fraction of bremsstrahlung energy,

---

[1]A χ^2 is constructed to evaluate the compatibility of the measured track with the single track hypothesis, in order to minimize the muons from in flight decays of hadrons.

the ratio of the hadronic to the electromagnetic energy deposit and that of the energy deposited in the preshower versus that in the electron supercluster. Before cutting on the MVA, we impose two kinematical cuts: $p_T > 35$ GeV, $|\eta| < 2.5$ and

- $\sigma_{i\eta i\eta} < 0.01/0.03$ (barrel/endcap)

- $|\Delta\phi_{in}| < 0.15/0.10$

- $|\Delta\eta_{in}| < 0.007/0.009$

- $H/E < 0.12/0.10$

- $\frac{\sum_{trk} E_T}{p_T^{\text{ele}}} < 0.2$

- $\frac{\sum_{ECAL} E_T - 1}{p_T^{\text{ele}}} < 0.2$

- $\frac{\sum_{HCAL} E_T}{p_T^{\text{ele}}} < 0.2$

H and E refer to the fraction of hadronic and electromagnetic energy. The differences in angular coordinates are between the supercluster and the electron track and $\sigma_{i\eta i\eta}$ is the supercluster spread in η. For the last three variables the sum is extended to a cone of radius 0.3. After these ID requirements we compute the particle flow combined isolation as in the case of muons, defined as the scalar sum of the p_T of the particle flow candidates that satisfy some basic quality requirements. The cuts we impose for electrons are: $\frac{\text{Iso}_{\text{PF}}}{p_T} < 0.105$ for $|\eta| > 0.8$, $\frac{\text{Iso}_{\text{PF}}}{p_T} < 0.178$ for $0.8 \leq |\eta| < 1.479$ and $\frac{\text{Iso}_{\text{PF}}}{p_T} < 0.15$ for $|\eta| \geq 1.479$.

6.3.4 Jet Selection

In the analysis we consider PF jets, clustered from charged and neutral particles reconstructed by the Particle Flow algorithm [186, 188] that was described in section 4.2.6. For clustering we use the infrared-safe anti$-k_T$ algorithm [152] with cone parameter $R = 0.5$. More details on jets reconstruction in CMS can be found in chapter 5.

Jets are selected requiring that their p_T be larger than 30 GeV and $|\eta| < 2.4$. Jets within $\Delta R = 0.5$ of a selected muon or electron are not included in the jet count. We use jets for which the p_T of charged particles not compatible with the primary vertex is subtracted and so is an average energy deposit from neutral components computed with the Hybrid Jet Area method described in section 5.3.1. We apply the standard CMS jet energy corrections described in chapter 5. We also cut on an MVA-based jet identification variable that allows to reject jets from pile-up interactions. It exploits the different shape of the energy deposit in a jet cone. Pile-up jets can pass the p_T threshold only if they are overlaid (typically they are too soft), hence the deposit should be more

spread. The MVA combines the variables β^*, RMS, defined as

$$
\begin{aligned}
\beta^* &= \frac{\sum_{jetPUvtx} p_T^{track}}{\sum_{jet} p_T^{track}}, \\
RMS &= \frac{\sum_c (p_T^2)_c (\Delta R^2)_c}{(p_T^2)_c}, \quad c = \text{constituents}, \quad (6.3.2)
\end{aligned}
$$

the jet ΔR profile and the charged and neutral multiplicities.

We define b-tagged jets using the Combined Secondary Vertex (CSV) algorithm and its medium working point. Descriptions of the algorithm and of its performances were given in sections 5.5.3 and 5.5.6, respectively. To correct MC efficiencies we apply both data-MC scale factors and, when needed, also Fast-Full simulation SFs. To apply the SFs and determine the resulting systematic uncertainty we follow the procedure described in section 5.5.9.

6.3.5 Baseline selection and signal extraction

In the previous sections we have defined the physics objects relevant for the analysis. Now we can introduce the structure of the cutflow and the procedure used to extract the signal. The following set of cuts, applied in the order in which they are listed, define our baseline selection for the muon box

1. We select events with at least one muon that passes the ID and isolation requirements described above.

2. We ask for the presence of 6 or more jets in the event.

3. One of the jets in the event must be tagged as originating from a b quark.

The selection for the electron box differs only in the first requirement, where we ask for at least one electron to be present. To avoid double counting we veto events within the electron sample if they also contain an identified muon. Note that extra leptons (both muons and electrons) are not vetoed in the two boxes. There are several reasons for allowing their presence: i) it is more probable to find these extra leptons in signal rather than in background events. ii) for the main source of background ($t\bar{t}$+jets) each extra lepton (typically originating from a W) implies two jets less in the $t\bar{t}$ decay chain, hence a suppression of $\mathcal{O}(\alpha_s^2)$. iii) The only difference implied by the extra lepton (additional ME_T in the event) has no impact on our background discrimination (based on jet multiplicity and b-tagging).

After the baseline selection we identify three signal regions with $= 6$, $= 7$ and ≥ 8 jets. We then perform a fit simultaneously in the 6 exclusive boxes (6, 7, 8) jets $\times$ (electron, muon). We fit the shape of the distribution of the number of b-tagged jets, taking the normalization from data and the shape templates from the MC for both signal and background. A detailed description of the fitting procedure can be found in section 6.8.
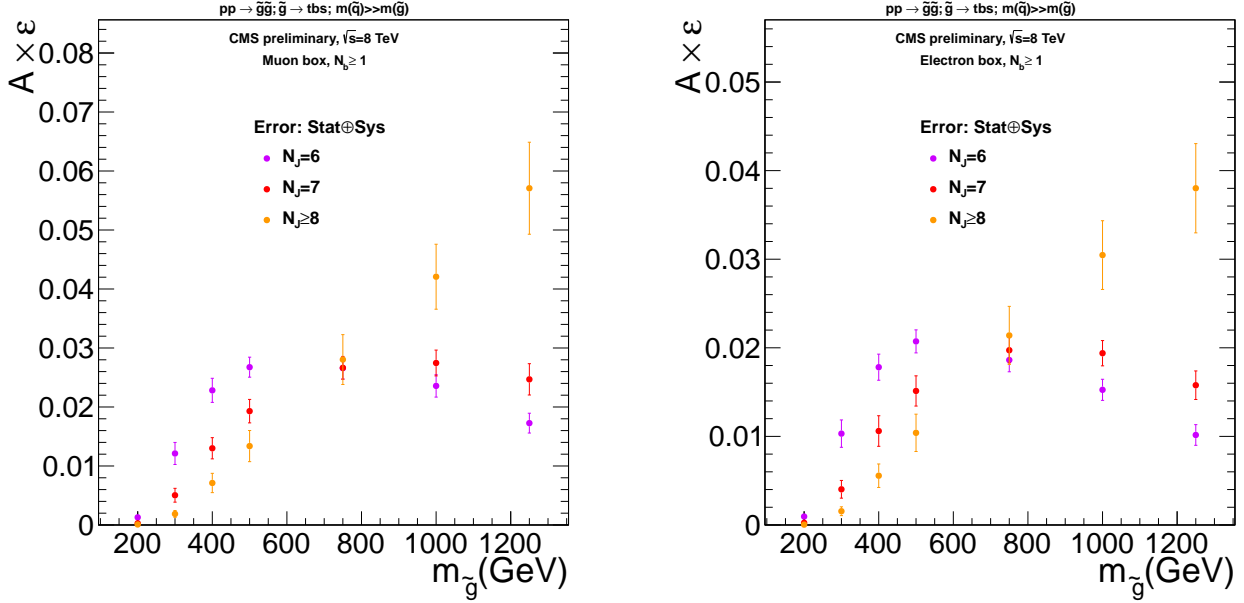
Figure 6.1: Signal efficiency as a function of the gluino mass for the $\tilde{g} \to tbs$ RPV simplified model. Left(Right): after the muon(electron) baseline selection for events with exactly 6 jets (purple), 7 jets (red) and ≥ 8 jets (orange).

In the next section we discuss the efficiency on the signal of the baseline selection and of the requirement of extra jets, which gives a feeling of which signal regions drive the sensitivity of the fit. In sections 6.5 and A we show that the shape of the b-jets distribution of the background is well reproduced by the MC simulation.

6.4 Signal efficiency

In figure 6.1 the efficiency of the full selection for the three signal regions, including the trigger requirement, is presented. The difference in efficiency between electrons and muons is due to the different ID requirements. This singles out the 8 jet signal region as the most promising, being the overall efficiency comparable with respect to the 6 jets one that is plagued by a factor of 10 more in background (see figures 6.2 and 6.4). Furthermore it is worth to notice that as the gluino mass increases higher jet multiplicities get more populated. This is of course an artifact of the kinematical threshold on the jets. In principle with one lepton coming from one of the W's we expect 8 jets in the final state, but for low gluino masses one or two do not make it past even our loose $p_T > 30$ GeV cut. The reason is that the top quarks in the *tbs* final state are always required to be on-shell and this pushes the p_T of the s and b jets below threshold. To obtain these results we have corrected b-tagging efficiencies with both data-MC and Fast-Full simulation SFs. The
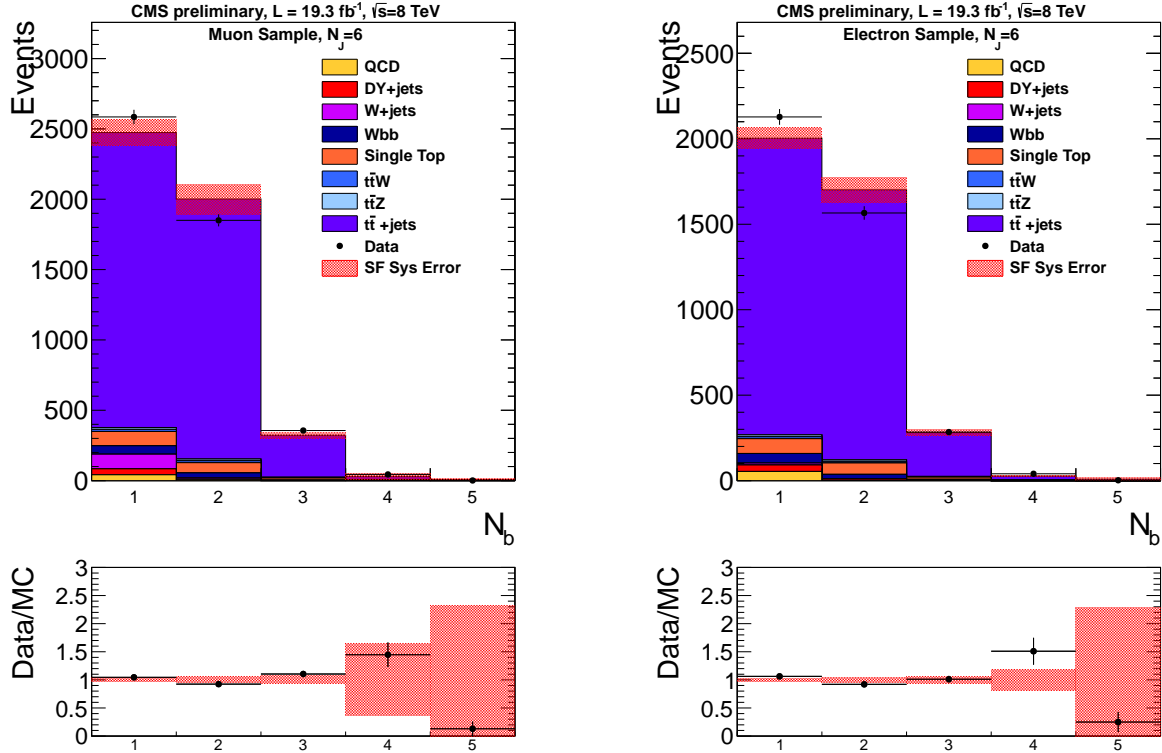
Figure 6.2: Distribution of the number of b-jets for events with one muon (left) or electron (right) and 6 jets, compared to the background prediction from simulation, corrected for the b-tagging response in data. The red band represents the uncertainty originating from the error on the b-tag correction factors.

error shown in the figures is the total statistical plus systematic one, excluding that arising from PDF uncertainties. The systematic uncertainties are discussed in detail in section 6.6. The offline selection is not fully efficient on the trigger. We take this effect into account applying weights that depend on the p_T and $|\eta|$ of the lepton.

6.5 Background Determination

As discussed above, the selected events are divided in three signal regions, according to their jet multiplicity: 6 jets, 7 jets, and ≥ 8 jets. For each signal region, the background is separated from the signal by comparing the observed b-tag multiplicity with that predicted for the SM background.

The main source of background to this search is provided by QCD production of pairs of top quarks in association with jets. Additional contributions from single top production, production of vector bosons and QCD multijet events are relevant for low b-tag multiplicities, becoming
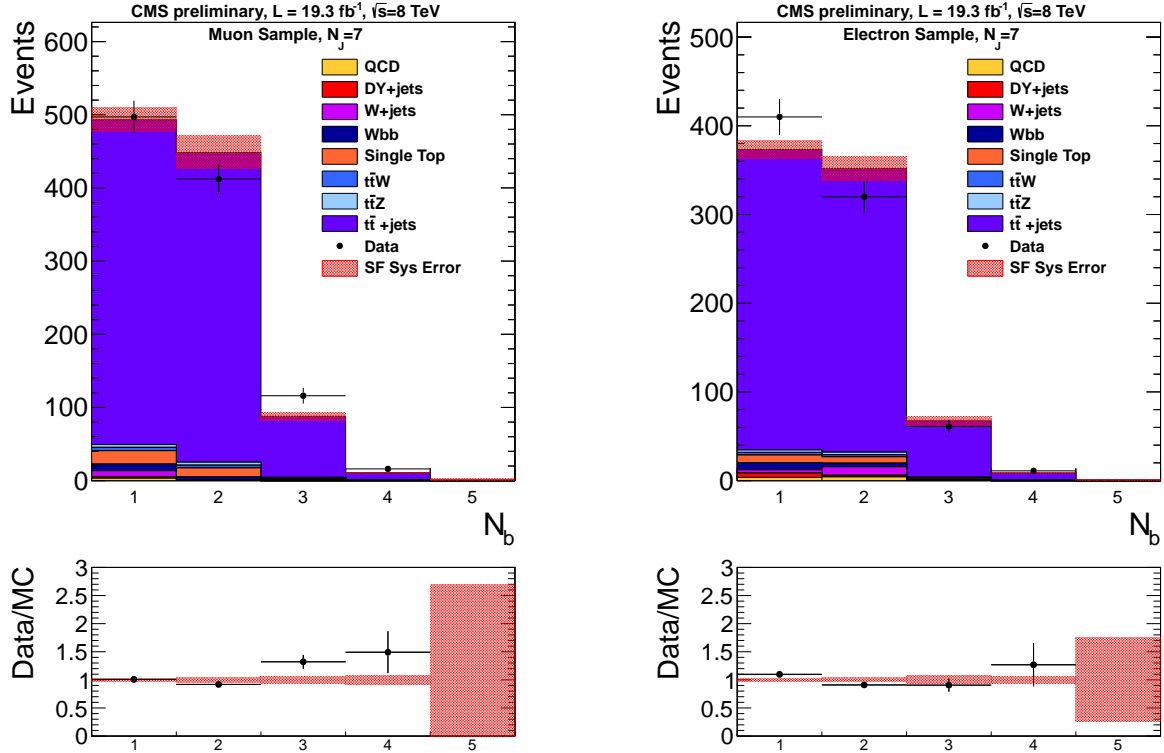
Figure 6.3: Distribution of the number of b-jets for events with one muon (left) or electron (right) and 7 jets (center), compared to the background prediction from simulation, corrected for the b-tagging response in data. The red band represents the uncertainty originating from the error on the b-tag correction factors.

negligible for events with at least three b-tags. The high b-tag multiplicities have also a small contamination, typically below 1%, from $t\bar{t} + V$ events (where $V = W$ or Z). The background from four-top production in the SM and $t\bar{t}H$ production is negligible, due to the low expected cross section.

We study the b-tag multiplicity of the backgrounds using Monte Carlo (MC) simulation. Events are generated with MADGRAPH [189] and showered in PYTHIA [155]. The matching between the matrix element and the parton shower is performed using the MLM algorithm [190]. The generated events are then processed by a simulation of the CMS detector, based on GEANT [158]. Events are corrected for the different response of the b-tagging algorithm in simulation and data. A weight is applied to the response of the b-tagging algorithm for each jet which is matched to a b quark. The weight is determined from data control samples of $t\bar{t}$ and μ+jets events, as a function of the kinematic properties of the jet, as seen in chapter 5. A similar procedure is applied to model the mis-tag probability for jets originating from light quarks (u,d,s), c quarks, and gluons. The scale factors (SF), from which these weights are computed, were measured at lower jet multiplicities
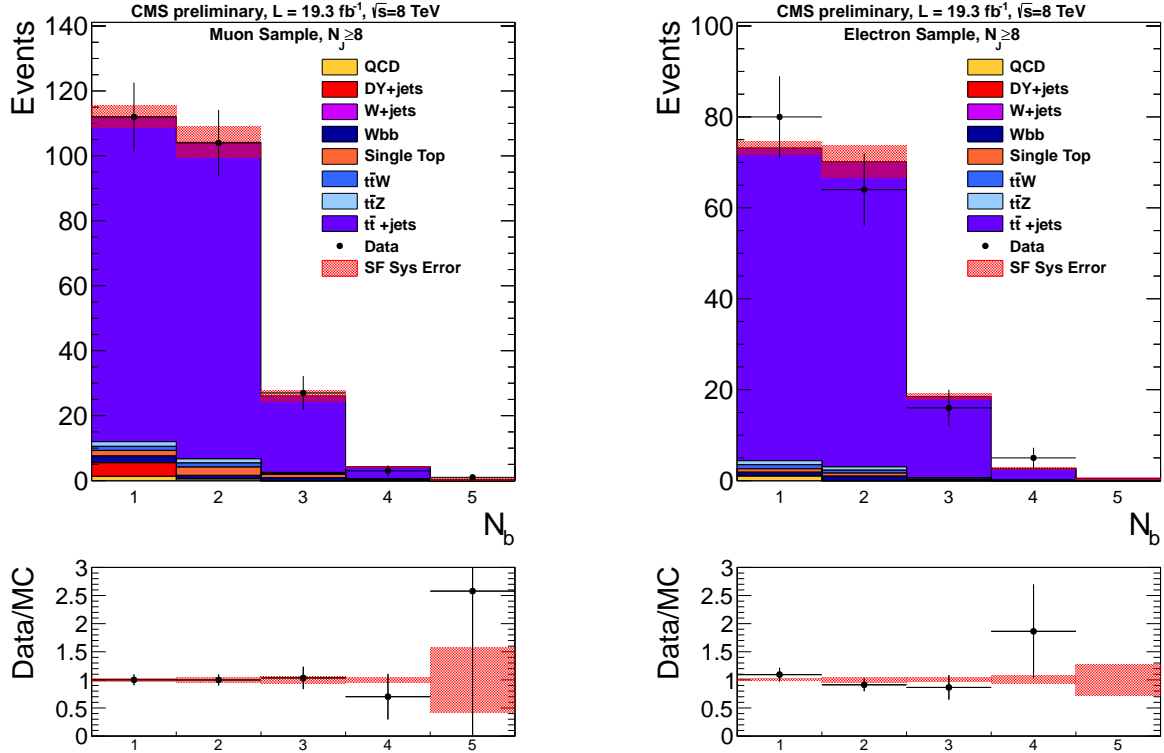
Figure 6.4: Distribution of the number of b-jets for events with one muon (left) or electron (right) and ≥ 8 jets, compared to the background prediction from simulation, corrected for the b-tagging response in data. The red band represents the uncertainty originating from the error on the b-tag correction factors.

and then validated for the higher multiplicities studied in the analysis, the validation procedure is described in appendix A. We verified that the b-tagging efficiency and the mis-tag rate vary negligibly in semileptonic $t\bar{t}$ events going from 4 to 9 jets, always remaining within their error. Furthermore we compared data and MC in control regions with one or two leptons and four or five jets and obtained good agreement within the errors on the b-tagging correction factors alone. Residual small discrepancies were accounted for allowing for a MC mismodeling of SM events with four b quarks, as discussed in more detail in section 6.6.

The corrected b-tag multiplicity provides the prediction for the SM background, which is compared to data in order to check for the presence of a signal. The final signal extraction fit obtains the background normalization from data using an extended likelihood. Therefore only the shape of the tagged jets multiplicity distribution is taken from simulation. This considerably reduces the total error on the background, since this shape is very mildly dependent on the jet energy scale and on the choices of matching and renormalization scales.

Figures 6.2, 6.3 and 6.4 show the b-tag multiplicity for the 6 jets, 7 jets, and ≥ 8 jets signal

regions, for events with at least one well identified muon and for events with at least one well identified electron. The error band represents the uncertainty coming from the error on the b-tagging correction factor.

6.6 Systematics

6.6.1 Background

The background shape is affected by the jet energy scale (JES) uncertainty, the b-tagging scale factors uncertainty, the variation of renormalization, factorization and matching scales and the finite MC statistics. Furthermore we include a systematic effect parametrized as a mismodeling of the fraction of events with four b quarks in the MC.

The evaluation of JES, matching, renormalization and factorization scale effects consists in repeating the selection procedure on samples with the scales shifted up or down. The JES shift is p_T and η dependent, amounting to a 3% variation for jets with $p_T = 30$ GeV and $|\eta| < 1.3$. The shift in matching, renormalization and factorization scales is fixed to be a factor of 2 and 1/2 with respect to the nominal values used in the CMS samples. Renormalization and factorization scales are always varied simultaneously. These effects are extremely small since we are taking the yields at fixed jet multiplicities from the data and extracting just the shape of the b-tagging distribution from the MC, more details can be found in appendix C.

The error from the b-tagging SF is computed by comparing b-tagged jets distributions obtained correcting tagging efficiencies with SF shifted by ± 1 standard deviation. The errors on the b-jets and c-jets corrections are taken to be correlated and the corresponding scale factors are varied simultaneously.

The parametrization of the mismodeling of four b quark events is unique to this analysis and not as straightforward as the computation of the other uncertainties. While the data-corrected MC distribution is expected to account for events with multiple b-tags originating from mis-tags, the contribution from $b\bar{b}$ splitting of the gluon and of SM four b quark events in general, is sensitive to the details of the MC modeling. We constrain this contribution by studying the agreement between data and MC in a dileptonic sample of events with one identified electron, one identified muon and associated jets. We consider separately events with four or five jets. Furthermore we use single lepton control regions selecting events with one electron or one muon and four or five jets. These control regions provide a high-purity sample of $t\bar{t}$+jets events, for which the signal contamination is expected to be negligible. Figure 6.5 shows that the largest difference between the prediction used in the analysis and the observed yield in the dileptonic control sample is a less than one standard deviation excess in the = 3 b-tag bin for the = 4 jets sample. Also the single lepton control regions show similar small discrepancies for $N_b \geq 3$. These are the b-tag bins most sensitive to the signal so we parametrize this effect and include it in the analysis as a systematic uncertainty.

Using the data yields from these control samples in different b-tag bins it is easy to construct
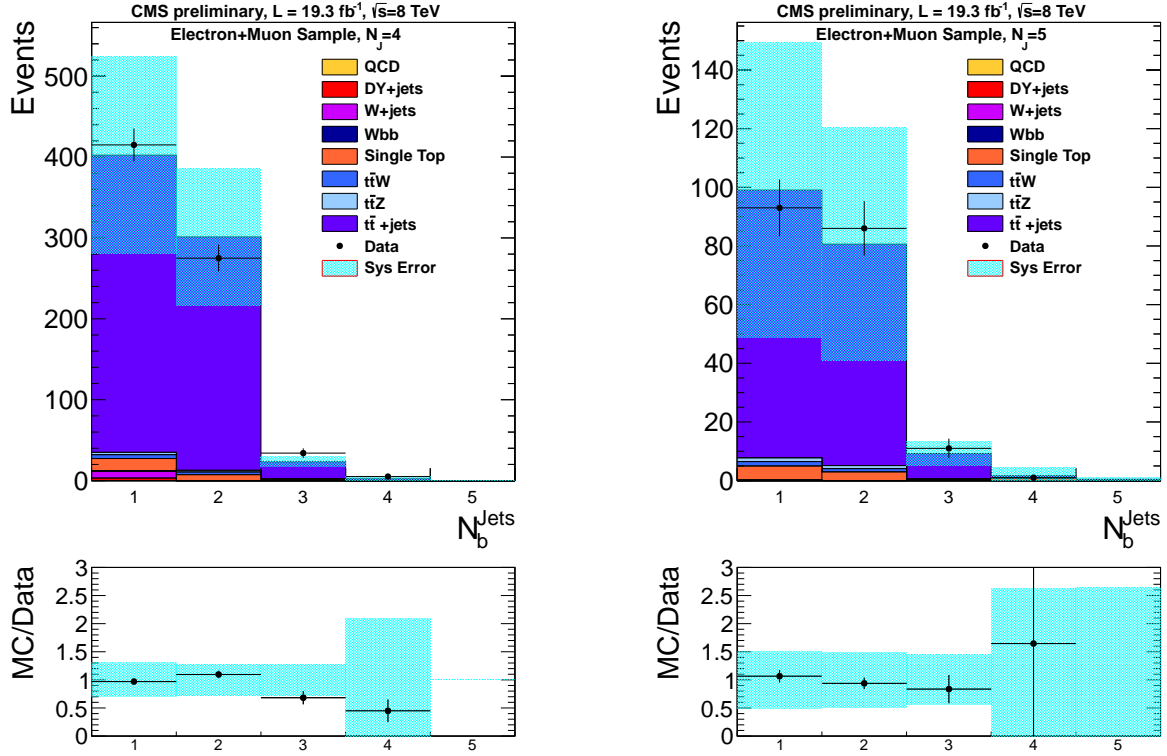
Figure 6.5: Distribution of the number of b-jets for events with one electron, one muon, and $N_{\text{jets}} = 4$ (left) or $N_{\text{jets}} = 5$ (right) in data, compared to the background prediction from simulation corrected for the b-tagging response. The cerulean band represents the total uncertainty on the background yield.

a system of three equations and three unknowns for each control region. We take the unknowns to be the average tagging efficiency, the average mis-tag rate and the difference in the fraction of events with four b quarks between data and MC (f_{4b}). We solve numerically the system of equations, neglecting terms quadratic in the mis-tag rate. After having solved the system we use the values of the average tagging efficiency and the average mis-tag rate determined in each control region to construct a global χ^2

$$\chi^2\left(f_{4b}\right) = \sum_{j \in \text{C.R.}} \sum_{i=1}^{N_b} \frac{\left(N_{\text{obs}}^{ij} - N_{MC}^{ij} - N_{4b}(\epsilon_b^j, \epsilon_l^j, f_{4b})\right)^2}{\sigma_{ij}^2}, \tag{6.6.1}$$

where the sum over j spans the different control regions and the one over i the single b-tag multiplicity bins. Minimizing the χ^2 we obtain an improved determination of f_{4b} from the data in all control regions. Since f_{4b} accounts for the difference between data and MC it can take both positive and negative values. It is positive if the MC predicts less four b quarks events than observed in the data and negative if it overpredicts the fraction of these events.

We associate a systematic error with the shape of the background, by determining f_{4b} with the information from both the dilepton and single lepton control regions, obtaining $f_{4b} = -0.011 \pm 0.049$. We use $f_{4b} + 1\sigma$ and $f_{4b} - 1\sigma$ to construct two new background shapes in the 6 jets, 7 jets, and ≥ 8 jets signal regions. The choice of combining the two control regions is justified by the fact that fitting them separately we obtain compatible results[2]. Nonetheless the determination of the systematic error depends on the values of the efficiencies used in the fit, on their error and on the choice of control regions. For this reason we compute the limit on the signal cross section for several different choices of control regions [3] and tagging and mis-tag efficiencies. The observed variations are below 10^{-3} of the cross section value obtained with $f_{4b} = -0.011 \pm 0.049$ from the combined fit.

6.6.2 Signal

The errors on signal efficiency and signal shape include the JES uncertainty, the b-tagging SF uncertainty, the error on the parton density functions (PDF), the error on the collected luminosity, the uncertainty on trigger and identification efficiencies for leptons and the uncertainty on the MC modeling of ISR and FSR. Combining all the signal uncertainties gives a total error of $\sim 10 - 20\%$ on the single b-tag multiplicity bins. At high gluino masses ($m_{\tilde{g}} \geq 1$ TeV) the error is dominated by the PDF uncertainty, while for lower masses the JES error constitutes the most important source of uncertainty, followed in magnitude by the ISR/FSR error. A breakdown of the error on the efficiency can be found in figures 6.6 and 6.7.

The JES and SF errors are computed in the same way described for the background. However, since the signal samples are processed through a fast rather than full detector simulation, we take into account also the uncertainty from b-tagging SF correcting the fast simulation efficiencies to the full simulation ones. The error on the collected luminosity was measured to be 2.6% [191]. The uncertainty on the knowledge of the parton density functions is obtained applying the prescription of the PDF4LHC working group [192] on three different PDF sets. The errors on the reconstruction and trigger efficiencies of muons and electrons are estimated from $Z \to \ell\ell$ events in bins of η and p_T of the lepton, both are found to be always below 1%. The nominal efficiency from MC is also corrected in order to reflect the lepton efficiency measured in data. Finally the ISR/FSR error was obtained from the discrepancies between data and simulation observed in the p_T distributions of Z+jets, dibosons+jets and $t\bar{t}$+jets events as a function of the p_T of the recoiling system and is discussed in more detail in appendix C.

In the next section we present the final results and the limit setting procedure.

---

[2]Dilepton control region: $f_{4b} = 0.022 \pm 0.11$, Single lepton control region: $f_{4b} = -0.015 \pm 0.042$.

[3]For instance we take $f_{4b} + 1\sigma$ from the dilepton control region and $f_{4b} - 1\sigma$ from the single lepton control region to compute a background systematic error.
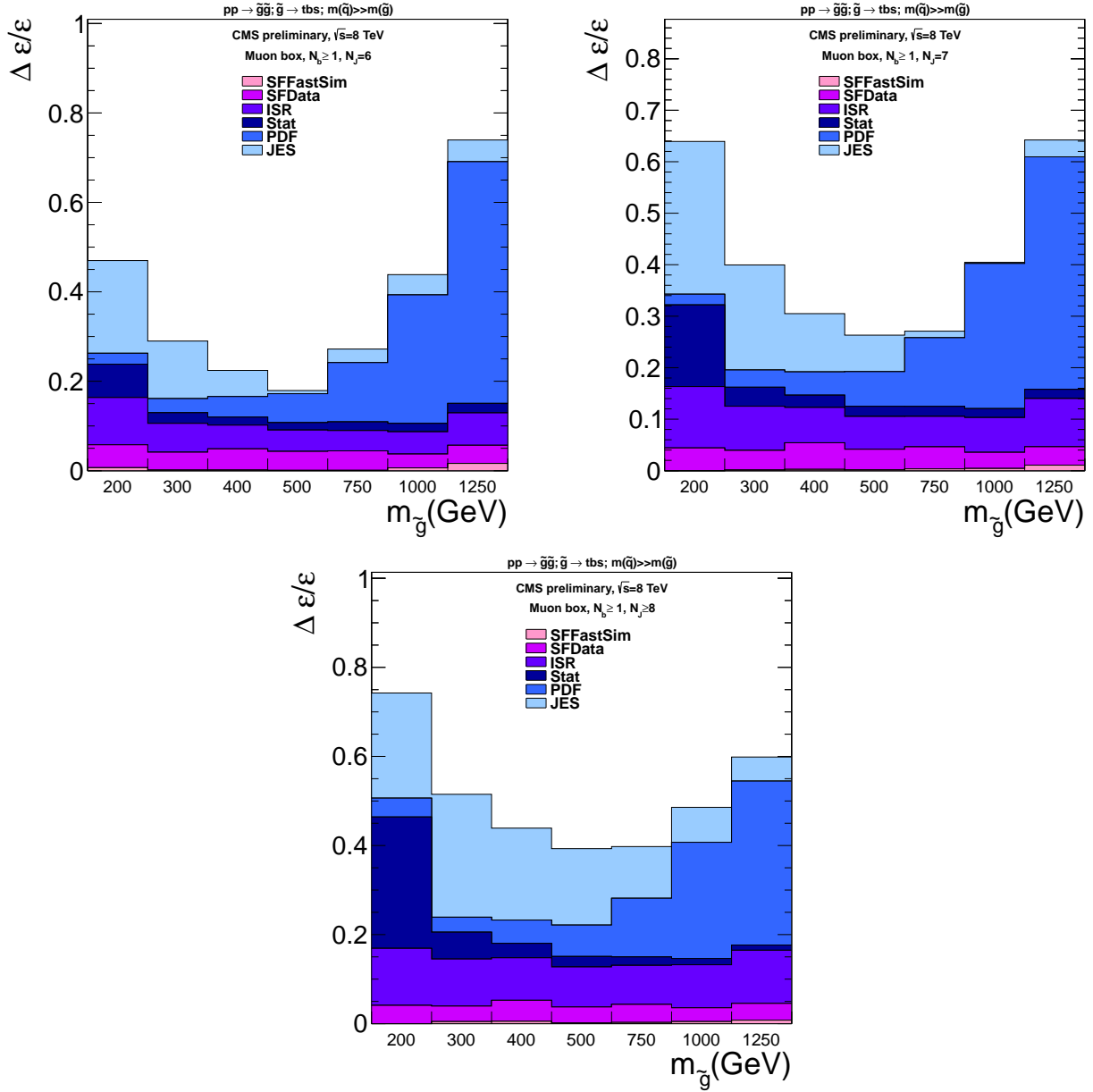
Figure 6.6: Breakdown of the relative error on the signal efficiency, as a function of the gluino mass in the muon box, for events with exactly 6 jets (left), 7 jets (right) and ≥8 jets (bottom).

6.7   Results

We summarize in Tab. 6.4 and Tab. 6.5 the expected background, the expected signal for $m_{\tilde{g}} = 1$ TeV and the observed yield in each signal region considered. The error on the background prediction
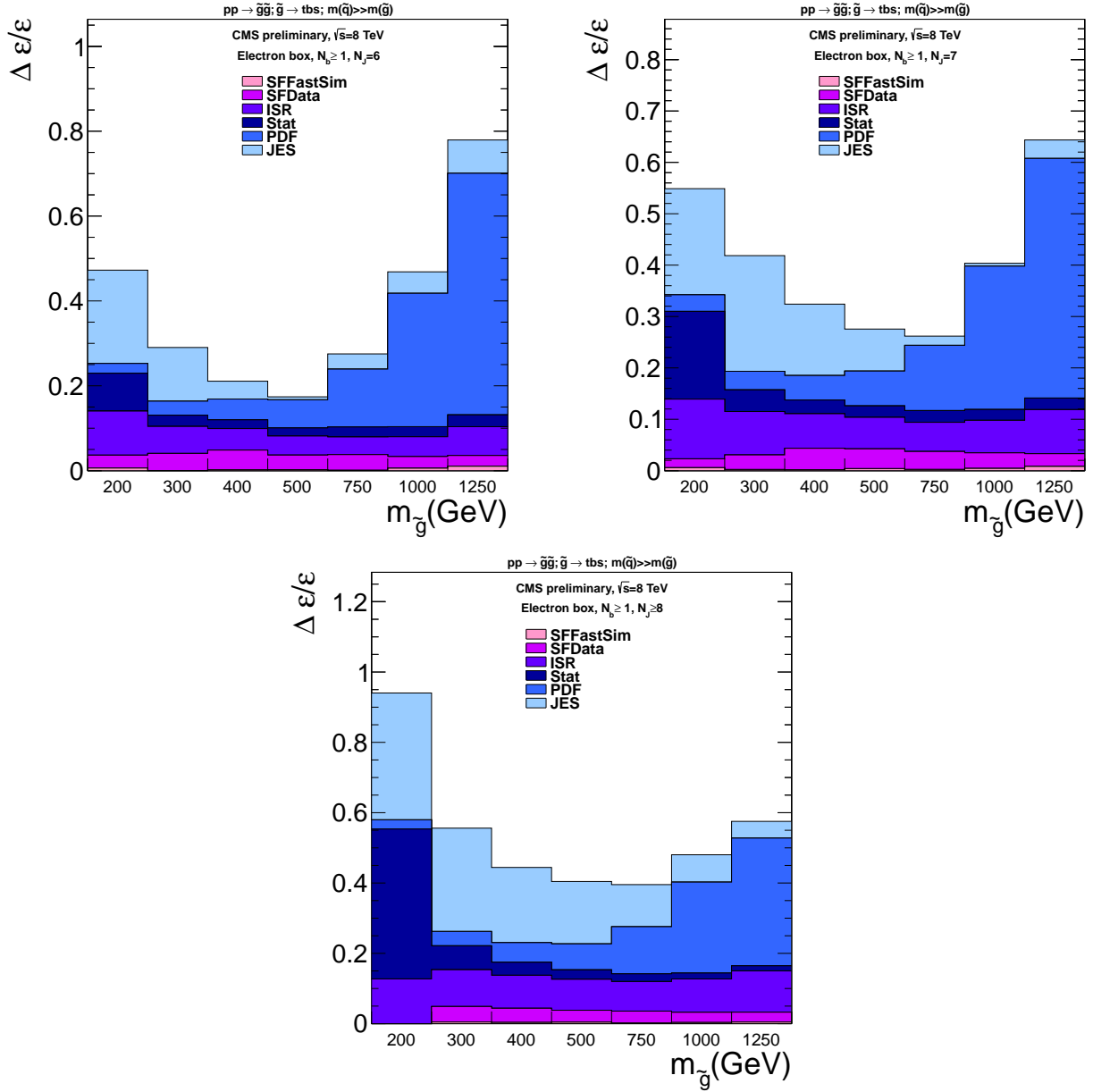
Figure 6.7: Breakdown of the relative error on the signal efficiency, as a function of the gluino mass in the electron box, for events with exactly 6 jets (left), 7 jets (right) and ≥ 8 jets (bottom).

(first line of the tables) includes the yield error and can be used for counting experiment reinterpretations. In the bins with ≤ 2 b-tags the dominant sources of uncertainty come from JES, renormalization and factorization scales. For higher b-tag multiplicities the error on the tagging SF and the mismodeling of four b quark events become the main sources of uncertainty. The

post-fit uncertainties on the background, shown in the fourth line of the tables, are considerably reduced with respect to the errors on the prediction. The fit, extracting the background normalization from data, reduces the total error to an error on the shape of the b-tagged jets distribution. Therefore uncertainties coming from JES, matching scale and renormalization and factorization scales that affect mostly the total yield, become almost negligible. The electron and muon samples, although presented separately to facilitate reinterpretations, are fitted simultaneously. A more detailed description of the fit is included in section 6.8.

In the second line of the tables we report the signal prediction for $m_{\tilde{g}} = 1$ TeV. As discussed in the previous section for lower gluino masses the JES error dominates, while at higher masses ($m_{\tilde{g}} \geq 1$ TeV) the error on the PDFs constitutes the main uncertainty.

No sizable deviation from the expected yields is observed. We interpret the absence of an excess as an upper bound on the cross section for SUSY models predicting final states with one lepton and multiple b-tagged jets. These bounds are then converted to a mass bound, assuming a gluino pair production cross section calculated at Next-to-Leading order (NLO) in α_s and Next-to-Leading logs (NLL), under the assumption of decoupling for the other sparticles [**?**]. The cross section limit is obtained with a maximum likelihood fit to the shape of the tagged jets distribution, described in the next section.

Mu + 6 jets	1 b-tag	2 b-tags	3 b-tags	4 b-tags	5 b-tags
Background prediction	2474±977	2002±801	322±152	30±29	7.7±6.5
Signal ($m_{\tilde{g}} = 1$ TeV)	3.04±0.49	4.58±0.73	2.83±0.43	0.63±0.11	0.043±0.026
Data	2585	1850	356	44	1
Background Post-Fit	2425±60	1985±49	340±11	43.0±3.5	3.1±1.1
Mu + 7 jets	1 b-tag	2 b-tags	3 b-tags	4 b-tags	5 b-tags
Background prediction	493±203	448±180	88±39	10.7±7.2	0.9±2.8
Signal ($m_{\tilde{g}} = 1$ TeV)	2.96±0.46	4.91±0.74	3.88±0.58	1.13±0.19	0.093±0.043
Data	497	412	116	16	0
Background Post-Fit	506±15	462±13	95.9±3.0	14.81±0.99	1.03±0.18
Mu + 8 jets	1 b-tag	2 b-tags	3 b-tags	4 b-tags	5 b-tags
Background prediction	112±47	104±46	26±12	4.3±2.1	0.39±0.75
Signal ($m_{\tilde{g}} = 1$ TeV)	3.69±0.60	7.0±1.0	6.38±0.92	2.45±0.39	0.328±0.064
Data	112	104	27	3	1
Background Post-Fit	119.7±4.3	110.7±3.6	29.0±1.0	5.63±0.34	0.54±0.072

Table 6.4: Summary of expected background, expected signal for $m_{\tilde{g}} = 1$ TeV, observed yields and total background after the (background only) fit for the muon samples considered in the analysis. We report the total uncertainty on the predicted yield.

Ele + 6 jets	1 b-tag	2 b-tags	3 b-tags	4 b-tags	5 b-tags
Background prediction	2003±827	1701±762	281±130	27±17	8.0±6.8
Signal ($m_{\tilde{g}}$ = 1 TeV)	1.85±0.32	2.94±0.51	1.89±0.32	0.411±0.097	0.025±0.013
Data	2128	1566	284	40	2
Background Post-Fit	1967±54	1636±53	296.1±9.5	33.6±3.0	1.9±1.2
Ele + 7 jets	1 b-tag	2 b-tags	3 b-tags	4 b-tags	5 b-tags
Background prediction	373±200	352±199	67±39	8.7±6.3	1.1±1.1
Signal ($m_{\tilde{g}}$ = 1 TeV)	1.99±0.30	3.38±0.51	2.71±0.43	0.86±0.15	0.068±0.023
Data	410	320	61	11	0
Background Post-Fit	368±13	347±12	70.6±2.8	10.38±0.65	0.70±0.12
Ele + 8 jets	1 b-tag	2 b-tags	3 b-tags	4 b-tags	5 b-tags
Background prediction	73±51	70±49	18±15	2.7±2.1	0.47±0.38
Signal ($m_{\tilde{g}}$ = 1 TeV)	2.44±0.37	4.88±0.77	4.67±0.71	1.95±0.28	0.232±0.041
Data	80	64	16	5	0
Background Post-Fit	74.9±3.1	71.0±3.1	18.94±0.93	3.40±0.20	0.440±0.032

Table 6.5: Summary of expected background, expected signal for $m_{\tilde{g}}$ = 1 TeV, observed yields and total background after the (background only) fit for the electron samples considered in the analysis. We report the total uncertainty on the predicted yield.

6.8 Limit Extraction

In absence of an excess of events, we set a limit on new physics considering the $\tilde{g} \to tbs$ simplified model as the benchmark model.

To this end we use the the fully frequentist LHC CL$_s$, computed by `RooStats` [193]. The reference likelihood L_R is written as a Poisson function for n observed events, given an expected yield of $\epsilon\mathcal{L}\sigma + b$:

$$L_R = \frac{e^{-(\epsilon\mathcal{L}\sigma+b)}}{n!}(\epsilon\mathcal{L}\sigma + b)^n \ . \tag{6.8.1}$$

Here b is the expected background yield, ϵ is the signal efficiency, $\mathcal{L}$ is the dataset luminosity and σ is the cross section on which we want to set the limit. The likelihood is modified to include the systematic error associated to the signal and the background prediction. These uncertainties are modeled as log-normal functions (similarly to what is done with the prior functions in Bayesian models). The likelihood is then written as:

$$L = \frac{e^{-(\epsilon\mathcal{L}\sigma+b)}}{n!}(\epsilon\mathcal{L}\sigma + b)^n P_{ln}(\bar{\epsilon}|\epsilon, \delta\epsilon) P_{ln}(\bar{\mathcal{L}}|\mathcal{L}, \delta\mathcal{L}) P_{ln}(\bar{b}|b, \delta b) \tag{6.8.2}$$

where $P_{ln}(\bar{x}|x, \delta x)$ is a log-normal function of the measured value x with an expected value $\bar{x}$ (the same parameter appearing in the real likelihood) and a parameter δx (representing the associated uncertainty).
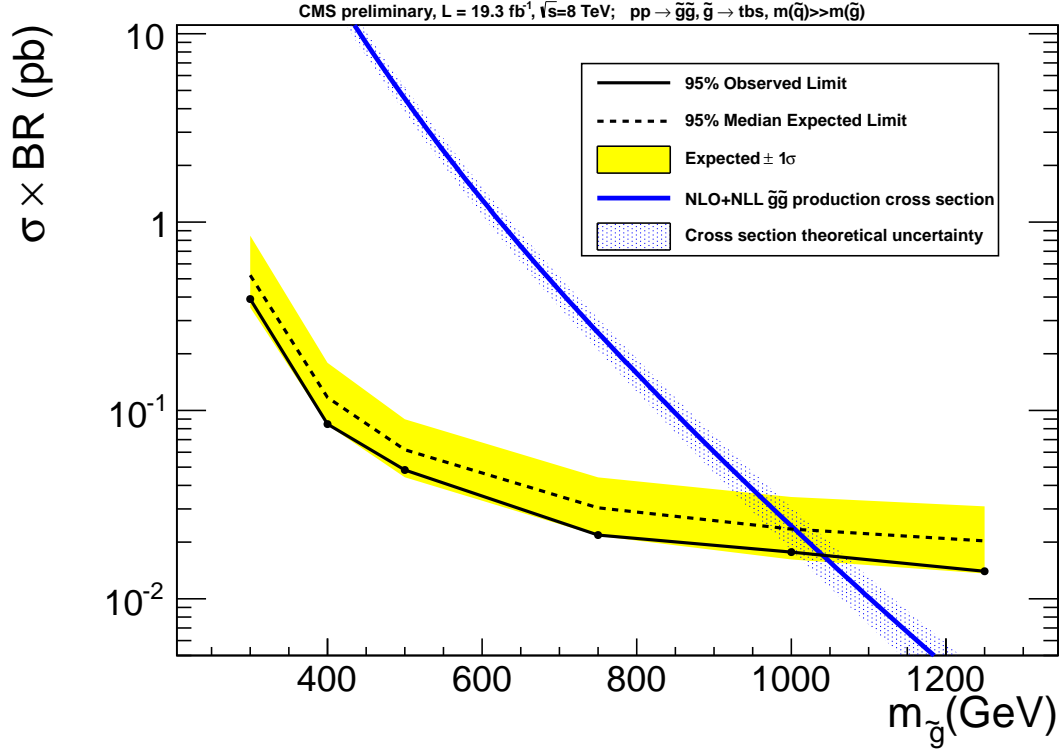
Figure 6.8: 95% C.L. limit on gluino pair production cross section computed following the LHC CLs prescriptions. The signal considered is $pp \to \tilde{g}\tilde{g}$, followed by the decay $\tilde{g} \to tbs$.

This likelihood describes the signal+background hypothesis under test, against the alternative hypothesis (background only). The likelihood of the background-only hypothesis is obtained fixing $\sigma = 0$.

For each value of σ the likelihood is profiled with respect to the nuisance parameters ($\mathcal{L}$, ϵ, and b). The CL$_s$ is computed for a set of toy Monte Carlo samples in each point of the gluino mass scan and the excluded (at 95% CL) cross section is compared to the value predicted by SUSY. We use the combination tool currently adopted by the Higgs group to perform the profiling and to compute the value of σ corresponding to CL$_s$=0.95. We take as input the shape of the distributions of b-tagged jets in the different signal regions. The combination tool performs a binned fit computing the likelihood described above bin by bin. In order to construct the nuisances distributions, for each systematic the corresponding distribution with, for instance, the JES scaled up by 1σ is also given to the tool for a total of $2 \times N_{sys}$ histograms.

The different signal regions are all fitted simultaneously, taking into account the correlation introduced by the systematics. The results of this procedure is shown in figure 6.8. With the current statistics we can exclude at 95% C.L. a gluino of mass $m_{\tilde{g}} < 1036$ GeV decaying to tbs with unitary branching ratio.

Part III

Naturalness and the Higgs boson

Introduction

In chapter 2 we have discussed the observation of a new state by the LHC experiments. All evidence is in favor of a spin-0 field with properties very similar to those of the SM Higgs boson. We use this as a working hypothesis in the following chapters, allowing for deviations in its couplings with respect to a purely SM Higgs.

Clearly this is a finding of crucial importance for BSM physics. The measured value of the mass of the new boson and of its couplings can not be ignored when formulating an extension of the SM. Furthermore these measurements can shed light on the question of the naturalness of the Fermi scale. Until now we have addressed it from the point of view of direct searches for new particles. In this part of the thesis we attack the problem from a different angle, studying indirect constraints from Higgs measurements.

Naively, if the Higgs couples to new particles that stabilize the quantum corrections to its mass, we expect that these particles also influence Higgs couplings, in particular those arising at one-loop in the SM. In the next two chapters we make this statement more quantitative, formulating sharp predictions, both in complete theories and simplified models that can lead to understand whether current and future measurements point to a natural or an unnatural theory at the TeV scale.

In chapter 7 we identify the relevant subset of parameters determining the Higgs couplings in natural supersymmetry, considering both the MSSM and some of its D-term and F-term extensions. We show that definite predictions can be made also in complete models and we test these predictions against LHC data.

In chapter 8 we identify some simple observations that can immediately rule out generic unnatural theories, defined as those theories that, below a certain scale, can be described as the SM plus extra fermionic fields only.

The work presented in this third part of the thesis was previously published in [8, 9, 10].

Chapter 7

The Higgs in natural Supersymmetry

Without culture, and the
relative freedom it implies,
society, even when perfect, is
but a jungle.

Albert Camus,
The Myth of Sisyphus.

7.1   Introduction

Current LHC data have provided no evidence for beyond the Standard Model physics, in particular, supersymmetry. Instead, as discussed in section 3.5, lower bounds were set on weak-scale SUSY, especially on the masses of the gluino and first two generation squarks [194, 195]. It is not inconceivable that, with time, we will learn that the weak scale is tuned [89].

Nevertheless, the game is not over for naturalness as we have argued in section 3.5 and was shown in [105] using older LHC results. The exclusions on stops and sbottoms are getting stronger, but are model dependent, and it is still easy to find regions in the squark-neutralino-chargino parameter space where these bounds cease to apply, with no need to invoke tuned degeneracies [105, 196, 197, 198, 199, 200]. On the theory side, rather than excluding naturalness, it is a consistent approach to take the experimental constraints as guidelines for model building of natural soft SUSY breaking.

In light of this debate between paradigms, the recent hint of a 125-126 GeV Higgs that we discussed in section 2.7 is exciting. In the MSSM, this Higgs mass would imply fine-tuning at the few parts per thousand or so [201, 202]. Therefore if SUSY is to be natural, it cannot be minimal, namely, new interactions beyond the MSSM must deform the Higgs sector.

Even if natural SUSY exists, given its evasive nature so far there is no guarantee that we shall see direct signatures of new physics any time soon. Also abandoning the traditional ME_T

signatures, we have shown in chapter 6 yet another null result. However, data have already begun to accumulate for one particular new set of measurements, the production cross sections and decay rates of the Higgs boson. This data set is rich: a 125 GeV SM-like Higgs supports $\mathcal{O}(10)$ experimentally independent production and decay channels, including e.g. gluon fusion (GF) and vector boson fusion (VBF) production and decays such as $h \to \gamma\gamma$, WW, ZZ, $b\bar{b}$, $\tau\bar{\tau}$. This information provides promising means to probe indirectly the existence and details of natural SUSY. Given that the experimental uncertainties for each individual channel are rather large, the degree by which one can draw information from this new set of data depends crucially on the degree of predictive power provided by the theory. This sets the scope for the current chapter.

In the MSSM, the third-generation sfermion, higgsino, gaugino, and Higgs sectors contain many free soft SUSY breaking parameters that can affect the Higgs couplings. The question arises what definite predictions can be made if naturalness (together with experimental constraints) is used as a guiding principle. The question gains depth given that a non-minimal Higgs sector would plausibly introduce additional free parameters in the scalar potential.

In this chapter we address this question. Our working assumptions are:

1. An $m_h \approx 125$ GeV Higgs exists[1], and is embedded in a natural (and therefore non-minimal) supersymmetric model;

2. We neglect beyond-MSSM physics in loops, assuming that the leading loop corrections to the Higgs-SM couplings involve MSSM fields only.

With these assumptions we obtain a predictive framework and show that it can be definitively tested against Higgs data. One may worry that satisfying assumption 1 simultaneously with 2 may be difficult in concrete models. However, modifying the fragile MSSM Higgs quartic potential is quite easy even with only heavy new physics. In sections7.3.2-7.3.3 we review gauge and singlet extensions of the MSSM that fulfill both assumptions.

In general, we study the modifications to the Higgs couplings to SM particles, denoted by

$$r_i \equiv \frac{g_{hii}}{g_{hii}^{\text{SM}}}, \qquad (7.1.1)$$

with $i = t, V, G, \gamma, b, \tau$ standing for top, massive vector gauge boson, gluon, photon, bottom and tau respectively[2]. Our main task is to organize existing computations into concrete predictions, distinguishing relevant from irrelevant contributions in our framework. We anticipate a list of relevant effects in table 7.1.

In the following we adopt the request of a moderate fine-tuning (10% for concreteness) to identify the main deviations of these couplings expected in natural supersymmetry. We comment on the prospects of falsifying natural supersymmetry through their measurement at the LHC and

---

[1]Recent experimental results point to a value for its mass closer to 126 GeV [53, 54], but the theoretical discussion in this chapter is completely unaltered by a shift of 1 GeV (which is also compatible with the experimental uncertainty).

[2]While this may not be strictly necessitated by data, we make the further assumption that $r_W = r_Z = r_V$.

Particles	Parameters	Observables
$\widetilde{t}_{1,2}$	$m_{\widetilde{Q}_3}, m_{\widetilde{u}_3}, A_t, \mu, \tan\beta$	r_G, r_γ
$\widetilde{\chi}^{\pm}_{1,2}$	$M_2, \mu, \tan\beta$	r_γ
H_u, H_d, S	α, β, ϕ	r_b, r_τ, r_t, r_V

Table 7.1: Summary of relevant (above 5%) contributions to Higgs couplings deviations in natural supersymmetry. The first column contains the name of the particles responsible for the effect, the second lists the relevant Lagrangian parameters (or in the case of tree-level effects the independent angles, where we have indicated with S a possible extra singlet and with ϕ the mixing angle that it introduces in the theory) and the third displays the observables affected. We have omitted extra degrees of freedom from D-term extensions of the Higgs sector that leave the two Higgs doublet model structure of the Higgs potential unaltered, but we discuss them in detail in the following.

compare the reach of precision coupling measurements with direct searches for supersymmetric particles.

7.2   The Higgs mass and fine-tuning

The most widely studied radiative correction associated with stops is the increase in the Higgs mass. A well known, simple, analytic one-loop estimate that nevertheless includes the most relevant two-loop correction is given by [203]

$$m_h^2 \approx m_Z^2 c_{2\beta}^2 + \frac{3G_F}{\sqrt{2}\pi^2} \left[m_t^4(Q_1) \log\left(\frac{M_s^2}{m_t^2}\right) + m_t^4(Q_2)\frac{X_t^2}{M_s^2}\left(1 - \frac{X_t^2}{12M_s^2}\right) \right]. \tag{7.2.1}$$

Here $M_s^2 = m_{\widetilde{t}_1} m_{\widetilde{t}_2}$, $Q_1 = \sqrt{m_t M_s}$, $Q_2 = M_s$, and $m_t(Q)$ is the running top mass taken at scale Q,

$$m_t(Q) = M_t \left(1 - \frac{4\alpha_s(M_t)}{3\pi}\right) \left(\frac{\alpha_s(Q)}{\alpha_s(M_t)}\right)^{12/23} \tag{7.2.2}$$

with M_t being the top pole mass, that we fix at 172.5 GeV. The stop mixing parameter X_t is defined by equation 3.4.31.

Equation (7.2.1) overestimates the Higgs mass, at a level of ~ 2 GeV, compared to the numerical two-loop package FeynHiggs [204]. Here in part of the analysis we use equation (7.2.1) as a tight but robust upper bound to the Higgs mass in the MSSM, while in other parts we prefer the full FeynHiggs calculation, advising the reader accordingly.

The correction to the Higgs quartic coupling, leading to equation (7.2.1), is accompanied by a shift to the Higgs self-energy that must be balanced by the bare mass in order not to destabilize the electroweak scale. Using the fine-tuning measure, Δ, defined in section 3.5.1, we recall that

the approximate stop contribution to it is

$$\left(\Delta^{-1}\right)_{\tilde{t}} = \left|\frac{2\delta m_{H_u}^2}{m_h^2}\right|, \qquad \delta m_{H_u}^2|_{stop} = -\frac{3}{8\pi^2}y_t^2\left(m_{\tilde{Q}_3}^2 + m_{\tilde{u}3}^2 + A_t^2\right)\log\left(\frac{\Lambda}{\text{TeV}}\right). \qquad (7.2.3)$$

In what follows we assume conservatively a low SUSY breaking mediation scale $\Lambda = 20$ TeV.

Equations (7.2.1) and (7.2.3) imply that a Higgs mass of 125 GeV would be highly fine-tuned in the MSSM [201, 202]. Including quantum corrections, the natural Higgs mass prediction in the MSSM does not exceed approximately 115 GeV (see figure 7.9). Unless we let go of natural SUSY, some physics beyond the MSSM must deform the scalar Higgs sector. Under this assumption, equation (7.2.1) does not directly constrain the stop sector. However, equation (7.2.3) continues to provide a reasonable guide to the fine-tuning associated with stops. Before turning to its relevance and to stop effects on Higgs couplings we discuss the deviations expected at tree-level. First studying a generic two Higgs Doublet Model (2HDM) and then discussing more concrete examples, such as the NMSSM and D-term extensions of the MSSM.

7.3   Tree-level deviations from Higgs mixing

As seen in the previous section a Higgs at 125 GeV is not compatible with a natural MSSM. The MSSM quartic couplings in the scalar potential need corrections at the $\sim 50\%$ level from new physics beyond the MSSM in order to accommodate it. These corrections can modify the Higgs-fermion and Higgs-vector couplings from their MSSM values at a similar level, in a model dependent manner, through Higgs mixing. In this section we derive these Higgs coupling modifications. We start from a general 2HDM framework. We then discuss the implications for specific model examples.

We do not consider here the possibility of additional light fields mixing with $H_{u,d}$, as could occur e.g. if the MSSM is augmented with a light singlet, treating this case in section 7.6.2. In addition, we assume that non-renormalizable interactions in the effective 2HDM can be neglected. Then above the weak scale but below (at least most of) the superpartners, the supersymmetric Higgs sector is described by an approximately type-II 2HDM [205, 206],

$$\begin{aligned}
-\mathcal{L} &= H_1^\dagger\mathcal{D}^2H_1 + H_2^\dagger\mathcal{D}^2H_2 + m_1^2|H_1|^2 + m_2^2|H_2|^2 \\
&+ \frac{\lambda_1}{2}|H_1|^4 + \frac{\lambda_2}{2}|H_2|^4 + \lambda_3|H_1|^2|H_2|^2 + \lambda_4|H_1\sigma_2H_2|^2 \\
&+ \left\{\frac{\lambda_5}{2}(H_1^\dagger H_2)^2 + (H_1^\dagger H_2)\left(m_{12}^2 + \lambda_6|H_1|^2 + \lambda_7|H_2|^2\right)\right. \\
&+ \left. Y_t H_2\epsilon\bar{t}_R Q_{L3} + \left(Y_b H_1^\dagger - Y_b\Delta_b H_2^\dagger\right)\bar{b}_R Q_{L3} + \left(Y_\tau H_1^\dagger - Y_\tau\Delta_\tau H_2^\dagger\right)\bar{\tau}_R L_3 + h.c.\right\},
\end{aligned}$$
$$(7.3.1)$$

where $H_{1,2} \sim (1,2)_{+1/2}$ and we identify $H_2 = H_u$, $H_1 = i\sigma_2 H_d^*$. In equation (7.3.1) we include "wrong" Higgs couplings for bottom and tau fermions with coefficients $\Delta_{b,\tau}$, that come about

from integrating out third generation squarks, higgsinos and gauginos at one-loop. We omit first and second generation fermions. As discussed in the next section, in the MSSM, at tree-level, $\lambda_5 = \lambda_6 = \lambda_7 = \Delta_b = \Delta_\tau = 0$.

As we anticipated in section 3.4.1, traditionally, the analysis of Higgs couplings is achieved by diagonalizing the Higgs mass matrix and expressing the couplings in terms of the rotation angle α, connecting the interaction basis of equation (7.3.1) to the mass basis, and the ratio

$$\tan\beta = \frac{\langle H_u \rangle}{\langle H_d \rangle}. \tag{7.3.2}$$

Omitting for the moment $\Delta_{b,\tau}$, we have $r_b = r_\tau$, and

$$r_b = \frac{v g_{hb\bar{b}}}{m_b} = -\frac{\sin\alpha}{\cos\beta}, \quad r_t = \frac{v g_{ht\bar{t}}}{m_t} = \frac{\cos\alpha}{\sin\beta}, \quad r_V = \frac{v g_{hVV}}{2 m_V^2} = \sin(\beta - \alpha), \tag{7.3.3}$$

implying the inequalities

$$r_b^2 \le \tan^2\beta + 1, \quad r_t^2 \le \frac{1}{\tan^2\beta} + 1, \quad r_V^2 \le 1. \tag{7.3.4}$$

We are free to choose two independent parameters to describe r_b, r_t and r_V. We choose these parameters to be $\tan\beta$ and r_b. With this choice we can write

$$r_t = \sqrt{1 - \frac{r_b^2 - 1}{\tan^2\beta}}, \quad r_V = \frac{\tan\beta}{1 + \tan^2\beta}\left(\frac{r_b}{\tan\beta} + \sqrt{1 + \tan^2\beta - r_b^2}\right), \tag{7.3.5}$$

valid for all $\tan\beta$. We assumed that $r_t \ge 0$, taking the positive root.

We now comment on the validity of neglecting $\Delta_{b,\tau}$ in equation (7.3.5). They enter the Higgs couplings $\tan\beta$-enhanced and only become quantitatively relevant at large $\tan\beta$. However, if $(r_b/\tan\beta)^2 \ll 1$, then deviations in r_t, r_V are suppressed compared to deviations in r_b. As we discuss below in more detail, this results in the fact that whenever the values of r_t or r_V are non-negligible phenomenologically, then equation (7.3.5) applies to high accuracy even when finite $\Delta_{b,\tau}$ are introduced. This conclusion is useful: it means that for arbitrary new physics deformations of the MSSM Higgs potential – just as long as the basic 2HDM structure is maintained – only two variables, r_b and $\tan\beta$, are required to describe Higgs mixing effects on the lightest Higgs effective couplings.

Note, finally, that similar diagrams to those that produce $\Delta_{b,\tau}$, also produce finite $\lambda_{6,7}$. As the latter couplings are vanishing in the MSSM, this can lead to non-negligible modification to Higgs couplings [207, 208]. However, these corrections are fully accounted for in equations (7.3.3-7.3.5), by assuming renormalized couplings in the potential (7.3.1).

For the purpose of understanding the phenomenology of specific models it is useful to express r_b in terms of the parameters in equation (7.3.1). As a simple but interesting scenario, consider $\tan\beta \ge 3$, where we can use $(1/\tan\beta)$ as an expansion parameter [207, 208]. We assume some

hierarchy between the masses of the two doublets, expand r_b also in v/m_A and set $\Delta_b = 0$, obtaining

$$
\begin{aligned}
r_b &= 1 + \frac{m_h^2 - \lambda_{35}v^2 - \lambda_7 v^2 \tan\beta}{m_A^2} + \mathcal{O}\left(\frac{v^4}{m_A^4}, \frac{1}{\tan\beta}\right), \\
r_V, r_t &= 1 + \mathcal{O}\left(\frac{1}{\tan^2\beta}\right).
\end{aligned}
\tag{7.3.6}
$$

The approximation in equation (7.3.6) is useful because it allows us to make generic predictions for a rather wide range of models [207, 208]. We show in the next section that it is also fairly accurate. The couplings λ_5, λ_7 (and λ_6) correspond to hard breaking of a $U(1)_{PQ}$ symmetry under which $(H_u H_d)$ is charged. Many phenomenologically relevant models (e.g. the MSSM) break $U(1)_{PQ}$ only softly and/or only at loop-level, and thus $\lambda_{5,7}$ are suppressed while λ_3 can be $\mathcal{O}(1)$. Hence in many cases, λ_{35} controls the deviation of r_b from unity and its sign determines whether r_b is increased or decreased. This, in absence of hard PQ breaking, is true at order $1/\tan^2\beta$, but to all orders in v/m_A [207]. Some generic classes of SUSY models predict fixed signs of λ_{35} and thus the direction of the shift in r_b.

In the next subsections we apply equations (7.3.5) and (7.3.6) to SUSY models, starting from the MSSM and then considering natural extensions that can accommodate $m_h = 125$ GeV. We show that even though $\mathcal{O}(1)$ variations in r_b can easily occur in such models, nevertheless significant predictive power is maintained, particularly in the approximate PQ limit.

7.3.1   MSSM analysis

The tree-level MSSM quartic Higgs potential is given by $G \equiv SU(2)_W \times U(1)_Y$ D-terms,

$$
V_D = \sum_G \frac{g_G^2}{2}\left(H_u^\dagger T_G^a H_u + H_d^\dagger T_G^a H_d\right)^2 = \frac{g^2 + g'^2}{8}\left(\left|h_u^0\right|^2 - \left|h_d^0\right|^2\right)^2 + \cdots,
$$

where the dots represent the charged Higgs potential. g and g' are the $SU(2)_W$ and the $U(1)_Y$ gauge couplings. Mapping onto the 2HDM, we have at tree level

$$
\lambda_1 = \lambda_2 = -\lambda_{35} = \frac{g^2 + g'^2}{4} \approx 0.14, \quad \lambda_5 = \lambda_6 = \lambda_7 = 0, \quad \Delta_b = \Delta_\tau = 0.
\tag{7.3.7}
$$

The coupling λ_{35} is negative, and so equation (7.3.6) tells us that the value of r_b is enhanced in the MSSM: $r_b \approx 1 + (m_Z^2 + m_h^2)/m_A^2 \approx 1 + 0.25\,(m_A/300\,\text{GeV})^{-2}$.

Finite $\Delta_{b,\tau}$ and $\lambda_{5,6,7}$ arise at loop order; using the results of [209, 210] we have, parametrically[3]

$$
\lambda_7 \sim -10^{-2}\left(\frac{A_t\mu}{m_{\tilde t}^2}\right), \quad \Delta_b \sim 3\times 10^{-3}\left[\left(\frac{A_t\mu}{m_{\tilde t}^2}\right) + 4\left(\frac{m_{\tilde g}\mu}{m_{\tilde b}^2}\right)\right], \quad \Delta_\tau \sim 10^{-4}\left(\frac{m_{\tilde B}\mu}{m_{\tilde\tau}^2}\right).
\tag{7.3.8}
$$

---

[3]A contribution to λ_7, coming from stau loops, may become comparable to the stop contribution if one allows very large $(A_\tau\mu/m_{\tilde\tau}^2)$.

We can now get back to estimate the validity of some of our previous approximations. First, while equation (7.3.5) automatically accounts for finite $\lambda_{5,6,7}$ (either radiatively generated or otherwise), it does not encode finite Δ_b and we should verify its applicability. Note that Δ_b enters Higgs effective couplings multiplied by $\tan\beta$. However, from equation (7.3.8) we expect that equation (7.3.5) should apply to reasonable accuracy even for $\tan\beta \sim 10$, in which case, because of the relative $\tan^2\beta$ suppression, deviations in r_t, r_V are already at most marginally relevant experimentally. In figure 7.1 we verify this point directly by comparing equation (7.3.5) with the full one-loop results from FeynHiggs. We find that for moderate $\tan\beta = 3$ the agreement is excellent, while for $\tan\beta = 10$ the agreement is better than 10%. However it should be kept in mind that the deviation from unity of r_t and r_V is so small in this regime to be completely negligible phenomenologically, making these discrepancies even less relevant.
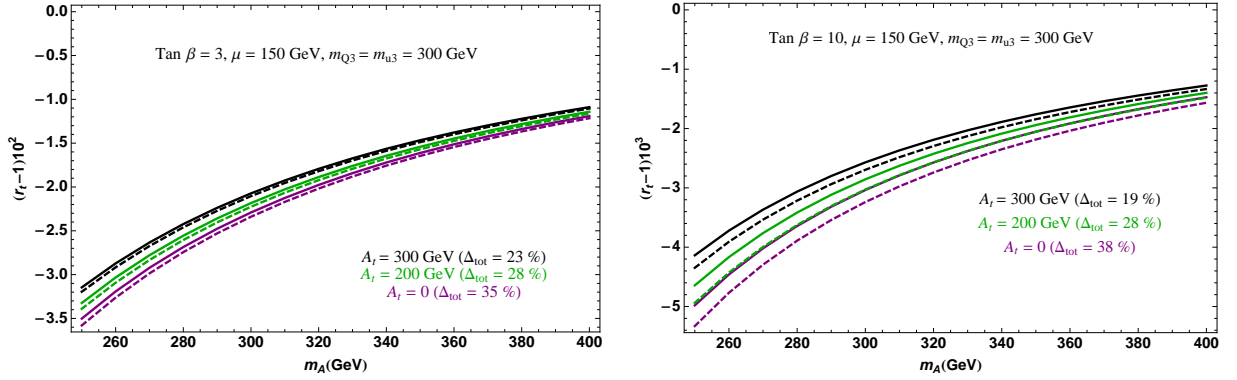
Figure 7.1: $(r_t - 1)$ as a function of m_A for $\tan\beta = 3$ (left) and $\tan\beta = 10$ (right). In addition to the stop-higgsino loop with parameters A_t and μ as shown, a sbottom-gluino contribution is also included with $m_{d_3} = 300$ GeV, $m_{\widetilde{g}} = 800$ GeV. The solid curves are derived by using the value of r_t in our formula (7.3.5). The dashed curves are derived using FeynHiggs. Similar results are found for r_V.

Next, we consider the $1/\tan\beta$ expansion of r_b [207], whose leading order in v/m_A is in equation (7.3.6). As we argued in section 2, naturalness favors $A_t \lesssim 300$ GeV. Thus unless $\tan\beta$ is very large, the contributions from λ_7 (and Δ_b, Δ_τ) are subdominant. In figure 7.2 we study the accuracy the $1/\tan\beta$ expansion for r_b using the tree-level couplings (7.3.7) and comparing to the numerical results from FeynHiggs. We find that the expansion[4] captures the correct result to 5% accuracy for intermediate $\tan\beta = 10$, still to 10% for low $\tan\beta = 3$, where the $1/\tan\beta$ expansion ceases to be valid, and to better than 20% accuracy for large $\tan\beta = 40$, where $\tan\beta$-enhanced loop corrections are in effect.

Last, we question the approximation $r_b \approx r_\tau$, that is violated by $\Delta_b \neq \Delta_\tau$. Again, the non-

---

[4]The expansion in [207], valid to $\mathcal{O}(1/\tan^2\beta)$ of which we showed the leading term in equation (7.3.6).
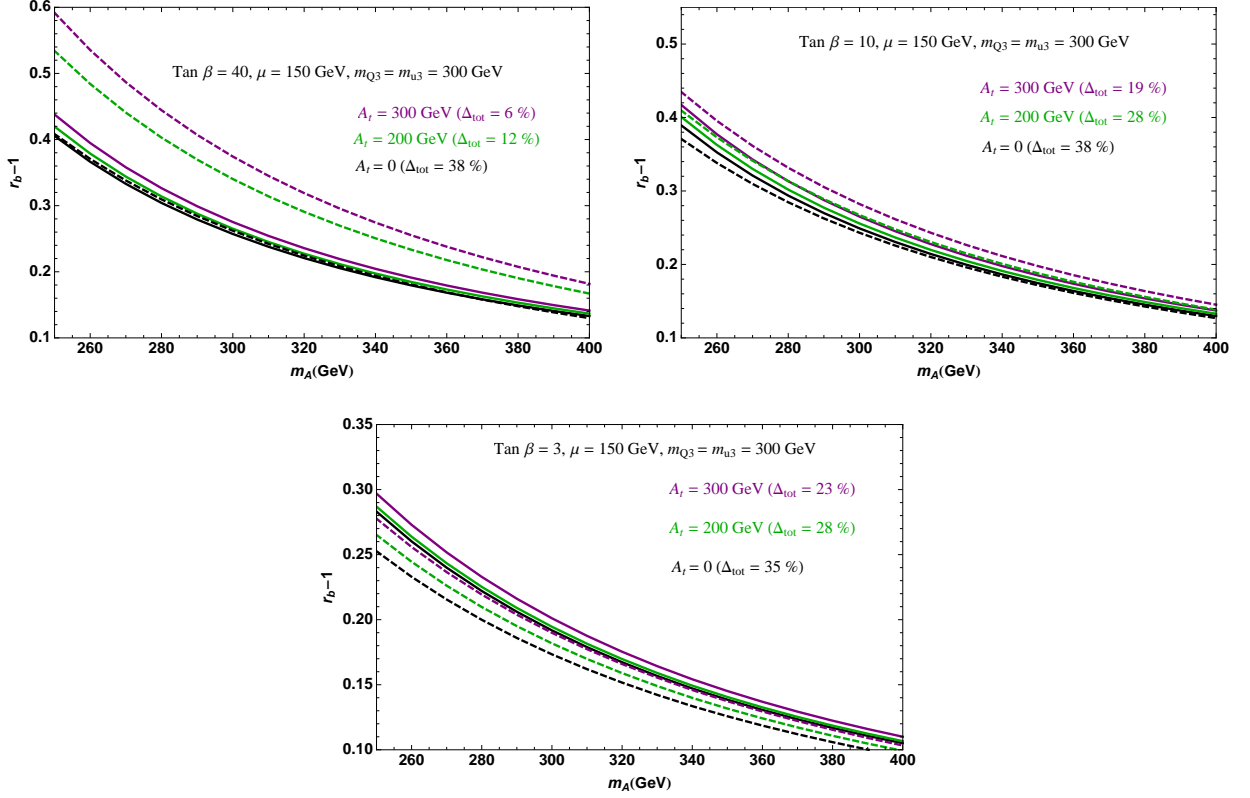
Figure 7.2: $r_b - 1$ as a function of m_A for $\tan\beta = 40$ (top left), $\tan\beta = 10$ (top right), $\tan\beta = 3$ (bottom). The solid curves are tree-level leading results in the large $\tan\beta$ approximation with Δ_b and λ_7 set to zero. The dashed curves are the full results computed with FeynHiggs. We decouple the right-handed sbottom in the computation.

holomorphic corrections are small unless $\tan\beta$ is large. We have

$$\frac{r_b}{r_\tau} \approx \frac{r_{b0} + (1 - r_{b0})\Delta_b \tan\beta}{r_{b0} + (1 - r_{b0})\Delta_\tau \tan\beta}, \tag{7.3.9}$$

with $r_{b0} = r_{\tau 0}$ denoting the result for $\Delta_b = \Delta_\tau = 0$. We conclude that $r_b \approx r_\tau$ is a reasonable approximation as long as $r_b, r_\tau = \mathcal{O}(1)$. The approximation can fail if the $hb\bar{b}$ and $h\tau\bar{\tau}$ couplings are strongly suppressed compared to the SM prediction; however this possibility is already disfavored by data, as seen in chapter 2.

7.3.2 Non-decoupling D-term models

In this section we study theories with new gauge interactions, in which D-terms contribute the leading effect in raising the Higgs mass. Examples in the literature include [211, 212, 213]. We

focus here on models in which the Higgs fields transform in a vector representation (H_u, H_d) under the new gauge group, so that a μ term, $\mu H_u H_d$, is allowed in the superpotential. We show that these models generically predict an enhancement in the $hb\bar{b}$ and $h\tau\bar{\tau}$ couplings. Models that go beyond the vectorial charge assignment for the Higgs fields must gauge the $U(1)_{PQ}$ symmetry and tend to consist a hybrid of D-term and F-term extensions [214, 215] that we discuss in the following section.

Consider two-site Moose models with a product gauge group $SU(N)_A \times SU(N)_B$ and gauge couplings g_A and g_B (for example, $SU(N) = SU(2)$ in [211]), depicted in figure 7.3. The product group is broken to the diagonal, identified as the SM electroweak gauge group G. This can be
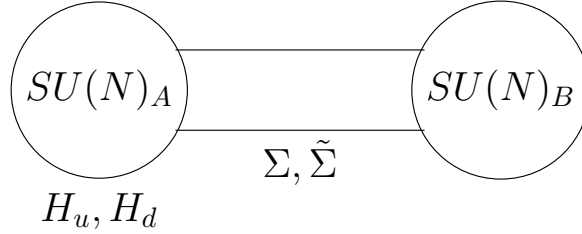
Figure 7.3: The fundamental building block in vector-like D-term models.

done, for instance, by introducing bi-fundamental link fields $(\Sigma, \tilde{\Sigma})$, developing VEVs $\langle\Sigma\rangle = \langle\tilde{\Sigma}\rangle$ through a superpotential $W = \lambda(\det\Sigma + \det\tilde{\Sigma}) + f\,\mathrm{Tr}\Sigma\tilde{\Sigma}$. The broken generator vector multiplets acquire a mass M_V. To arrange for a non-decoupling effect, a large soft SUSY breaking mass M_s can be introduced for the link fields. Then, the low energy effective potential of these models takes the same form as the MSSM D-term potential with rescaled coefficients:

$$
\begin{aligned}
V_D &= \sum_G \frac{g_G^2}{2}\left(1 + \frac{g_A^2}{g_B^2}\frac{M_s^2}{M_V^2 + M_s^2}\right)\left(H_u^\dagger T_G^a H_u + H_d^\dagger T_G^a H_d\right)^2 \supset \\
&\supset \frac{g^2(1+\Delta) + g'^2(1+\Delta')}{8}\left(\left|h_u^0\right|^2 - \left|h_d^0\right|^2\right)^2 .
\end{aligned}
\tag{7.3.10}
$$

This low energy effective potential can be derived following [216]. As stated above, we take the link fields $(\Sigma, \tilde{\Sigma})$ to be bi-fundamentals under the product gauge group with a canonical Kähler potential

$$
K \supset \mathrm{Tr}\,e^{g_A V_A}\Sigma e^{-g_B V_B}\Sigma^\dagger + \mathrm{Tr}\,e^{g_B V_B}\tilde{\Sigma}e^{-g_A V_A}\tilde{\Sigma}^\dagger,
\tag{7.3.11}
$$

where $g_{A,B}$ are the gauge couplings of gauge group A and B and $V_{A,B}$ are the corresponding vector multiplets. After Σ, $\tilde{\Sigma}$ develop a VEV, f, the product gauge group is broken down to the diagonal group, which is identified as the SM electroweak gauge group G with a massless vector multiplet

$$
V_G = \frac{g_A V_B + g_B V_A}{\sqrt{g_A^2 + g_B^2}} .
\tag{7.3.12}
$$

The SM gauge coupling is given by $g_G^{-2} = g_A^{-2} + g_B^{-2}$. The orthogonal combination,

$$V_H = \frac{-g_A V_A + g_B V_B}{\sqrt{g_A^2 + g_B^2}}, \tag{7.3.13}$$

is massive, with a mass term in the Kahler potential

$$K_V = M_V^2 V_H^2 + \cdots, \tag{7.3.14}$$

where $M_V = (g_A^2 + g_B^2)f^2$. Both MSSM Higgs fields are only charged under $SU(N)_A$ with an initially canonical Kahler potential

$$K_H = \sum_{i=u,d} H_i^\dagger e^{g_A V_A} H_i = \sum_{i=u,d} \left(H_i^\dagger e^{g_G V_G} H_i - \frac{g_{SM} g_A}{g_B} H_i^\dagger V_H H_i \right), \tag{7.3.15}$$

where we expand to the leading order in V_H. After integrating out V_H through its equation of motion, we have

$$K_H^{eff} = \sum_{i=u,d} H_i^\dagger e^{g_G V_G} H_i - \sum_G \frac{g_G^2 g_A^2}{g_B^2 M_V^2} \left| \sum_{i=u,d} H_i^\dagger T_G^a H_i \right|^2, \tag{7.3.16}$$

whose contributions to the Higgs quartic couplings are of order μ^2/M_V^2. Electroweak precision tests require that $M_V > 3$ TeV [217]. Given the naturalness condition $\mu < 300$ GeV, these supersymmetric corrections are thus too small to explain a Higgs mass at 125 GeV.

Introducing SUSY breaking effects via a universal soft mass, m_s, to the link fields, modifies the Kahler potential of the heavy vector multiplet,

$$K_V = (M_V^2 + \theta^4 m_s^2) V_H^2 + \cdots. \tag{7.3.17}$$

Again after integrating out V_H, we have

$$K_H^{eff} = \sum_{i=u,d} H_i^\dagger e^{g_G V_G} H_i - \sum_G \frac{g_G^2 g_A^2}{g_B^2} \left(\frac{1}{M_V^2} - \frac{\theta^4 m_s^2}{M_V^2 + m_s^2} \right) \left| \sum_{i=u,d} H_i^\dagger T_G^a H_i \right|^2, \tag{7.3.18}$$

which gives rise to the low-energy potential in equation (7.3.10).

Consider two limits of the modified Higgs couplings in equation (7.3.10):

- $M_V \gg m_s$, corresponding to a nearly supersymmetric heavy threshold, with

$$\Delta(\Delta') = \frac{g_A^2}{g_B^2} \frac{m_s^2}{M_V^2} \ll \frac{g_A^2}{g_B^2}$$

- $m_s \gg M_V$, corresponding to hard SUSY breaking in the low energy potential, with

$$\Delta(\Delta') = \frac{g_A^2}{g_B^2}.$$

Given that $g_G^{-2} = g_A^{-2} + g_B^{-2}$, we cannot take g_B very small at the weak scale. Assuming $g_A/g_B = \mathcal{O}(1)$, we learn that D-term models need a SUSY breaking mass m_s at least comparable to the supersymmetric scale M_V. These models are thus unlikely to be well described by the nearly supersymmetric effective field theory of [216].

Finally we comment on the fine-tuning in these models. The new non-supersymmetric contribution to the Higgs quartic couplings leads to a quadratic divergence in the Higgs mass squared, cut off by m_s. If we require this additional fine-tuning to be no worse than 10%,

$$\frac{g_G^2 \Delta}{16\pi^2} \frac{m_s^2}{m_h^2} < 10, \tag{7.3.19}$$

we obtain a conservative upper bound, $m_s \lesssim 10$ TeV. Taking into account the electroweak constraint, $M_V > 3$ TeV, and the requirement $M_V < m_s$ coming from equation (7.3.21), we find that m_s is approximately limited to the range 3 – 10 TeV.
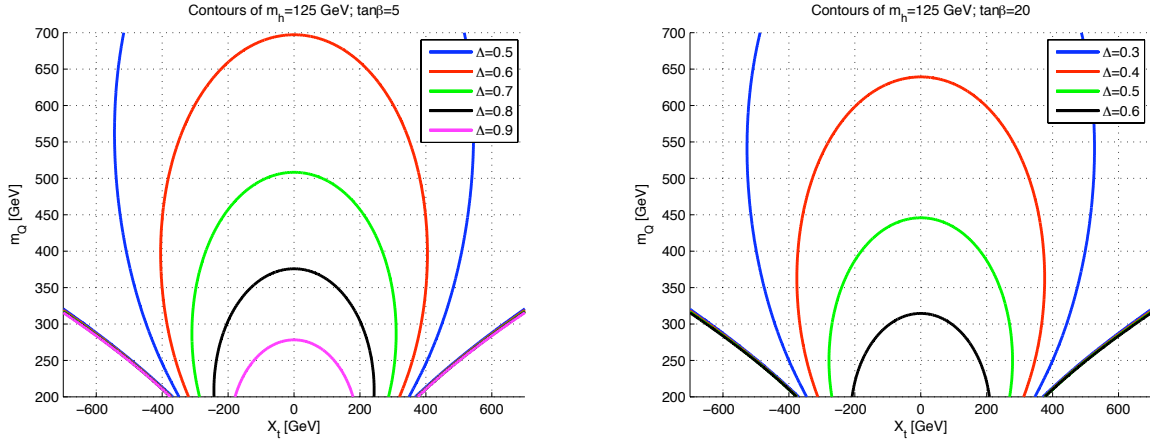

Figure 7.4: Contours of $m_h = 125$ GeV in the (X_t, m_{Q_3}) plane, for different values of the D-term correction parameter Δ. Left: $\tan\beta = 5$; Right: $\tan\beta = 20$. We have set $\Delta = \Delta'$ for simplicity, but the results are not sensitive to this choice.

The effect of this kind of D-term models on the Higgs quartic potential is simply:

$$-\lambda_1 = -\lambda_2 = \lambda_{35} = \lambda_{35}^{\text{MSSM}} \left(1 + \frac{g^2\Delta + g'^2\Delta'}{g^2 + g'^2} \right). \tag{7.3.20}$$

More specifically, accepting $m_h = 125$ GeV, we can compute the size of the required Δ. In figure 7.4 we set $\Delta = \Delta'$ and plot contours of $m_h = 125$ GeV for different values of Δ in the stop soft mass-mixing plane, using equation (7.2.1) modified by the D-term correction. Requiring light stops with fine-tuning no worse than 1:10, we find:

$$\Delta \gtrsim 0.5, \tag{7.3.21}$$

As we have seen above, equation (7.3.21) implies that D-term models that address $m_h = 125$ GeV should indeed be close to the non-decoupling regime.

7.3.3   Non-decoupling F-term models

Here we consider models that raise the Higgs mass through new non-gauge interactions in the superpotential. The classic example includes a SM singlet[5], interacting with the Higgs doublets via

$$\delta\mathcal{W} = \lambda S H_u H_d. \tag{7.3.22}$$

If S is given a large soft SUSY breaking mass, $m_s^2 \gg m_H^2, M_s^2$, with m_H being the mass of the heavier MSSM Higgs doublet and M_s a possible supersymmetric mass for S, then the effective potential below m_s is modified with a non-decoupling correction,

$$V = V^{\mathrm{MSSM}} + |\lambda|^2 |H_u H_d|^2. \tag{7.3.23}$$

This gives, using the notation in (7.3.1),

$$\lambda_4 = \lambda_4^{\mathrm{MSSM}} - |\lambda|^2, \quad \lambda_{35} = \lambda_{35}^{\mathrm{MSSM}} + |\lambda|^2. \tag{7.3.24}$$

By equation (7.3.6), these models tend to decrease r_b. To estimate the size of the effect, note that the correction to the Higgs mass, still neglecting mixing, is

$$\delta m_h^2 = m_Z^2 \left(\frac{2|\lambda|^2}{g^2 + g'^2} \right) \sin^2 2\beta. \tag{7.3.25}$$

In figure 7.5 we plot the value of λ required for $m_h = 125$ GeV, by adding equation (7.3.25) to equation (7.2.1). Mixing with the heavy singlet S reduces the lightest Higgs mass due to level splitting [202]; as a result, for fixed m_h, the value of λ in figure 7.5 serves only as a lower bound. We conclude that λ_{35} is always positive in this model and much larger than its gauge-coupling value in the MSSM. This reduces the $hb\bar{b}$ coupling below its SM value.

    As pointed out in [202], the non-decoupling limit discussed above has limited applicability because naturalness constrains $m_s \lesssim$ TeV. In contrast with D-term models, however, where electroweak precision tests constrain the SUSY scale, the singlet F-term example is phenomenologically viable also in the SUSY limit. In analogy with the D-term example, adding a supersymmetric

---

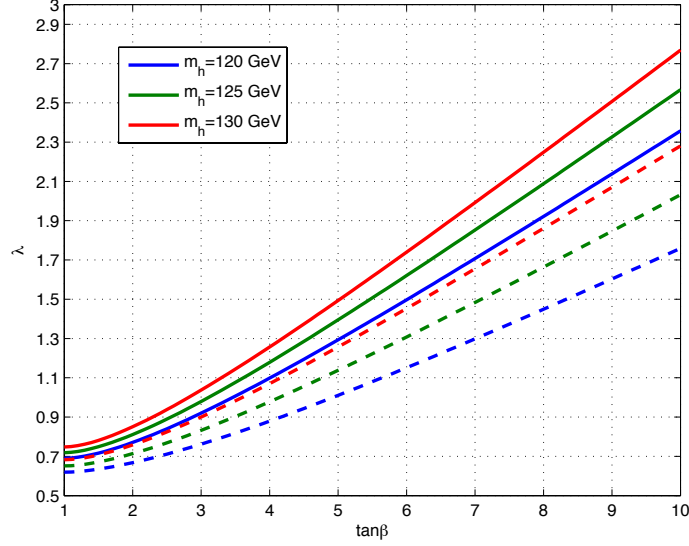[5]We would get the same results by making S a hypercharge-neutral SU(2) triplet.

Figure 7.5: Contours of $m_h = 120, 125, 130$ GeV, in the $(\tan\beta, \lambda)$ plane. Smooth lines: tree level; dashed lines: including stop correction with $X_t = 0$, $m_{\tilde{t}_1} = m_{\tilde{t}_2} = 380$ GeV.

mass term, $\delta\mathcal{W} \supset (M_s/2)S^2$, the shift in λ_{35} is suppressed by factors of (m_s/M_s); however, a supersymmetric correction $\lambda_7 = -(\lambda^2\mu^*/M_s)$ is generated. The λ_7 term modifies the Higgs mass by $\delta m_h^2 \propto -(\lambda_7 v^2/\tan\beta)$. With $|M_s| = 700$ GeV, $|\mu| = 200$ GeV, $\tan\beta = 2$ and $|\lambda| = 0.7$, the Higgs mass could be raised to 125 GeV [216, 218] with just a little help from $\sim$300 GeV stops. From equation (7.3.6), the small negative λ_7 will also act to decrease r_b.

We should stress, however, that it is not difficult to construct F-term models that do not decrease r_b. In particular, models that attempt to produce the μ term dynamically via a weak-scale singlet vacuum expectation value, tend to predict a light singlet, in which case the 2HDM analysis ceases to apply. An example is the Z3-NMSSM,

$$\mathcal{W} = \lambda S H_u H_d + \frac{\kappa}{3}S^3. \tag{7.3.26}$$

Parametric scans of this model show that the shift in r_b does not have a definite direction once S is allowed to be light [219, 220]. To understand how this can happen, consider equation (7.3.26) with the following hierarchy of masses: $m_H^2 \approx m_{H_d}^2 > |m_s|^2 > |m_{H_u}|^2$, where $m_s^2 < 0$. Integrating out first H_d and then S, and expanding to leading order in $(1/\tan\beta)$, we have

$$r_b \approx 1 - \frac{|\lambda|^2 v^2}{|m_s^2|} + \frac{v^2}{m_H^2 - m_h^2}\left(\frac{g^2 + g'^2}{4} + \frac{|\lambda|^4}{2|\kappa|^2}\right). \tag{7.3.27}$$

Notice that there is no longer a correction scaling as $|\lambda|^2 v^2/m_H^2$, instead there are two opposite-sign contributions that could be parametrically comparable.

Another example that increases the Higgs mass with no definite effect in the $h b \bar{b}$ coupling is found by adding an SU(2) triplet chiral superfield, $\Delta_- \sim (1,3)_{-1}$, with super potential $\delta \mathcal{W} = \lambda \Delta_- H_u H_u$. With a large SUSY breaking mass m_{s-}, integrating out the field Δ_- inserts a hard SUSY-breaking correction $\lambda_2 \to \lambda_2 + |\lambda|^2$ without modifying any of the other quartics in equation (7.3.1), lifting the Higgs mass with no further effect on the Higgs-fermion couplings.

Our main conclusions from the discussion in sections 7.3.2 and 7.3.3 are the following: (i) $\mathcal{O}(1)$ modifications to $r_{b,\tau}$ are plausible through Higgs mixing in concrete extensions of the MSSM, that give the correct Higgs mass; (ii) measuring a deviation in r_b will have strong implications for generic classes of models, in particular, non-decoupling D-term and F-term models, that predict opposite sign effects. The value of $(r_b - 1)$ will provide very suggestive hints for the masses, quantum numbers and couplings of new particles beyond the MSSM.

7.4   Loop effects

In this section we discuss the implications of light superpartners for Higgs production and decay channels at hadron colliders. The quantities that are most affected are the light Higgs couplings to gluons and photons and for this reason we recall the definition of r_G and r_γ given by the ratios

$$r_i \equiv \frac{g_{hii}}{g_{hii}^{\rm SM}}, \quad i = G, \gamma \,. \tag{7.4.1}$$

After this reminder, we begin the discussion by summarizing the results. The effects we consider include loop contributions from the charged Higgs, higgsinos, gauginos, stops, sbottoms, and staus. Of these, the only quantitatively relevant effects (potentially larger than $\sim 5\%$) involve stops and charginos that affect the Higgs couplings to photons and gluons. The stop contribution to the Higgs-gluon coupling, $r_G^{\tilde{t}}$, is directly related and opposite in sign to the stop contribution to the Higgs photon coupling, $r_\gamma^{\tilde{t}}$. The chargino contribution to r_γ decouples for $\tan \beta \gtrsim 5$, as the chargino-Higgs coupling scales linearly with $(1/\tan \beta)$.

The stop and chargino effects are constrained by direct searches for these particles and, to some extent, by naturalness. Imposing collider limits together with demanding fine tuning no worse than 10%, we check the possible size of these effects by varying the relevant theory parameters.

The results are plotted in figure 7.6, where the lines show the maximal and minimal values of r_γ obtained within natural SUSY. The possible stop contribution to r_G is plotted in figure 7.7.

The ranges of the different contributions to r_G and r_γ in natural SUSY are summarized in table 7.2, for $\tan \beta \geq 2$. We also report upper limit estimates on the subdominant contribution of staus and sbottoms. In the following subsections we provide more details of the calculations.

In this chapter we have very generously allowed the lightest stop to go as low as 100 GeV (close to the LEP bound). This is hard to accommodate in a realistic model after LHC results and also in tension with ElectroWeak Precision Tests. However the only consequence is to have less sharp statements on r_G and r_γ that can vary in a broader range, thus making our conclusions more conservative. We comment on their allowed interval in more detail in section 7.4.1, specifying when
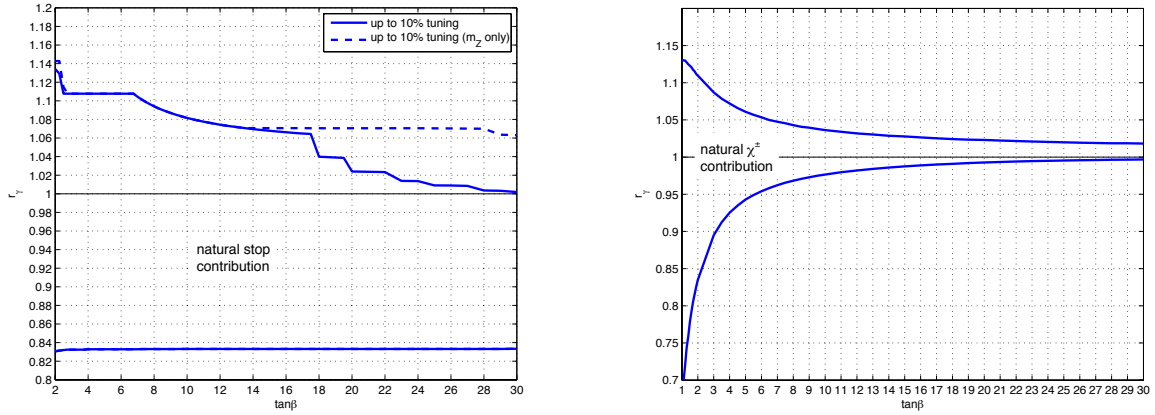
Figure 7.6: The range in r_γ as a function of $\tan\beta$, compatible with fine-tuning no worse than 1:10 (details in sections 7.4.1 and 7.4.2). Left: stop contribution. Right: chargino contribution. In the left panel, solid curves correspond to total fine-tuning, defined in equation (7.4.11), while dashed curves correspond to tuning with respect to the Z boson mass alone, defined in equation (7.2.3). Note that the stop contribution to r_γ (left panel) is inversely related to r_G, see equation (7.4.6).
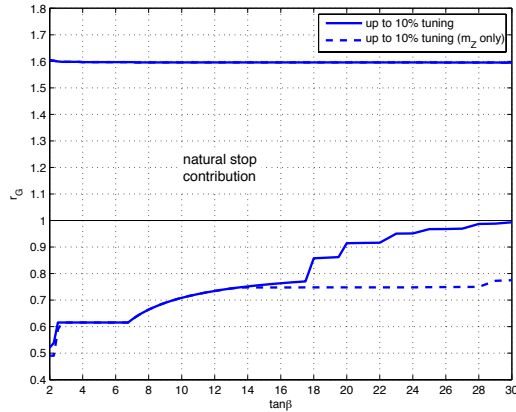
Figure 7.7: Natural range in r_G as a function of $\tan\beta$ (details in section 7.4.1). Solid curves correspond to total fine-tuning, defined in equation (7.4.11), while dashed curves correspond to tuning with respect to the Z boson mass alone, defined in equation (7.2.3). Note that the stop contribution to r_G is inversely related to r_γ, see equation (7.4.6).

the lower bounds from direct searches are relevant and providing numbers also for $m_{\tilde{t}_1} > 400$ GeV. Furthermore this choice does not affect at all the results of the fit to Higgs couplings presented in

	r_G	r_γ
$\tilde{t}$	$1^{+0.6}_{-0.4}$	$1^{+0.11}_{-0.16}$
$\tilde{t}\ (m_{\tilde{t}_1} > 400\ \text{GeV})$	$1^{+0.1}_{-0}$	$1^{+0}_{-0.03}$
$\tilde{\chi}^{\pm}$	1	$1^{+0.1}_{-0.16}$
$\tilde{b}$	$1^{+0}_{-0.01}$	$1^{+0.01}_{-0}$
$\tilde{\tau}$	1	$1^{+0.03}_{-0}$

Table 7.2: Ranges of r_G and r_γ in natural SUSY from different contributions, for $\tan\beta \geq 2$. The stop contributions to r_G and r_γ are anti-correlated, see equation (7.4.6). For stops we show two ranges corresponding to the LEP limit on the lightest stop mass and to $m_{\tilde{t}_1} > 400$ GeV. All the other entries are also given for the superpartner mass just above the LEP limit ($m_{\tilde{b}_1}, m_{\tilde{\tau}_1} > 100$ GeV, $m_{\tilde{\chi}_1^\pm} > 94$ GeV). As discussed in the following the only relevant contributions in natural SUSY arise from stops and charginos.

section 7.6.

7.4.1   Stops

Higgs couplings to gluons and photons

The Higgs low energy theorem tells us that in the presence of heavy colored multiplets whose masses depend on the Higgs vacuum expectation value, e.g., the top-stop multiplet, the leading log Higgs-gluon-gluon coupling at the one-loop level is given by [49, 50]

$$\mathcal{L}_{hgg} = \frac{\alpha_s}{12\pi} \frac{h}{v} \left(2 \sum_F t_F \frac{\partial \log \det m_F(v)}{\partial \log v} + \frac{1}{2} \sum_S t_S \frac{\partial \log \det m_S(v)}{\partial \log v} \right) G^a_{\mu\nu} G^{a\mu\nu}, \qquad (7.4.2)$$

where F and S denote respectively colored fermion and scalar with Dynkin index t_X (= 1/2 for the fundamental representation) and mass matrices $m(v)$. Applying equation (7.4.2) to the top-stop multiplet, we have [221]

$$r_G^{\tilde{t}} - 1 \approx \frac{1}{4} \left(\frac{m_t^2}{m_{\tilde{t}_1}^2} + \frac{m_t^2}{m_{\tilde{t}_2}^2} - \frac{m_t^2 X_t^2}{m_{\tilde{t}_1}^2 m_{\tilde{t}_2}^2} \right), \quad \text{stop contribution}, \qquad (7.4.3)$$

where we neglect D-terms. We took out an overall correction factor r_t, defined via equation (7.1.1), that comes about by Higgs mixing. The total hGG vertex correction reads

$$r_G = r_t\, r_G^{\tilde{t}}. \qquad (7.4.4)$$

Equation (7.4.3) compares well with results from FeynHiggs. Nevertheless, in numerical computations we use the complete expression including D-term contributions. The leading log approximation can be checked by comparing the full fermion and scalar loop function ratio evaluated at

m_t and $m_{\tilde{t}}, \left[\mathcal{F}_0 \left(m_h^2 / 4m_{\tilde{t}}^2 \right) / \mathcal{F}_{1/2} \left(m_h^2 / 4m_t^2 \right) \right]$, to the asymptotic value (1/4) of this ratio at $m_h \to 0$. Varying $m_{\tilde{t}}$ between 150-1000 GeV, we find that the leading log approximation is good to about 6%.

For reasonably light stops, equation (7.4.3) leads to a substantial effect, e.g. with $m_{\tilde{t}_1} = m_{\tilde{t}_2} = 250$ GeV, $r_G = 1.24$, implying a 53% increase in GF production[6]. As long as stop mixing is small, the hGG coupling is enhanced compared to the SM and consequently the GF rate is enhanced. So what limits the enhancement are direct searches. As commented in the previous section our lower limit of $m_{\tilde{t}_1} > 100$ GeV is generous in view of recent LHC results. Taking, for instance, $m_{\tilde{t}_1} = m_{\tilde{t}_2} = 400$ GeV, would reduce the effect to $r_G \approx 1.1$ implying a GF production increased by 20%.

As discussed in [50], large X_t could in principle reduce the hGG coupling. However, naturalness, together with the direct bounds on $m_{\tilde{t}_1}$, limit this possibility: large X_t adds to the weak-scale fine tuning both directly, through equation (7.2.3), and indirectly because it requires a larger diagonal soft mass to start with. In the next section we show further constraints on such large X_t that arise from rare B decays at large $\tan \beta$. Imposing $m_{\tilde{t}_1} > 400$ GeV, limits $r_G \geq 1$, while for $m_{\tilde{t}_1} > 100$ GeV we can still get $r_G \approx 0.6$.

There is an inverse correlation between the top/stop contributions to the Higgs effective coupling to photons and to gluons, the negative sign coming because of the dominant W diagram that contributes to $h\gamma\gamma$ with opposite sign from the matter loops. To see this, let us denote the W and top loop contributions to the $h\gamma\gamma$ amplitude by $\mathcal{A}_W^\gamma$ and $\mathcal{A}_t^\gamma$, respectively, and the stop contribution by $\mathcal{A}_{\tilde{t}}^\gamma$. Let us further define the hGG top and stop-induced amplitudes by $\mathcal{A}_t^G$ and $\mathcal{A}_{\tilde{t}}^G$, and note that

$$\frac{\mathcal{A}_{\tilde{t}}^\gamma}{\mathcal{A}_t^\gamma} = \frac{\mathcal{A}_{\tilde{t}}^G}{\mathcal{A}_t^G} = r_G^{\tilde{t}} - 1, \tag{7.4.5}$$

to leading order in α_s. This gives

$$r_\gamma = \frac{\mathcal{A}_W^\gamma + \mathcal{A}_t^\gamma + \mathcal{A}_{\tilde{t}}^\gamma}{\left(\mathcal{A}_W^\gamma + \mathcal{A}_t^\gamma \right)^{\text{SM}}} \approx 1.28 r_V - 0.28 r_G, \quad W, \text{ top, and stop contributions}, \tag{7.4.6}$$

using $\mathcal{A}_W^\gamma \approx 8.33$ and $\mathcal{A}_t^\gamma \approx -1.84$ in the SM, valid for $m_h = 125$ GeV.

Equations (7.4.4) and (7.4.6) do not include loop contributions of additional particles, notably bottom and tau fermions, charginos and scalars. The bottom and tau fermion contributions remain below about five percent of the top even for $r_{b,\tau} \sim 10$. The chargino, sbottom and stau contributions can in principle become relevant in some corners of the MSSM parameter space, resulting in some loss of predictivity by disturbing the $r_\gamma - r_G$ correlation of equation (7.4.6). Below we examine these terms in more detail, concluding that in natural SUSY, the sbottom and stau contributions can be neglected while charginos may lead to marginally observable effects. First, however, we comment about an additional source of fine-tuning that can further limit the allowed values of X_t.

---

[6]Already extremely hard to reconcile with experimental results and only at the price of tuning down Higgs couplings to other SM particles (in particular ZZ, WW and $\gamma\gamma$).

Large stop mixing vs. fine-tuning in $BR(B \to X_s \gamma)$

Light, mixed stops are constrained by rare B decays. The branching fraction for the rare decay $B \to X_s \gamma$ has been measured experimentally to a precision of better than ten percent [222],

$$BR(B \to X_s \gamma)^{\text{exp}} = (3.52 \pm 0.25) \times 10^{-4}. \tag{7.4.7}$$

The theoretical SM NNLO calculation has reached a similar accuracy [223][7],

$$BR(B \to X_s \gamma)^{\text{SM}} = (2.98 \pm 0.26) \times 10^{-4}. \tag{7.4.8}$$

The theoretical NNLO SM prediction is fully determined by observable quantities, namely the masses of the top quark and of the W boson and gauge couplings. Therefore, the agreement (within $\sim 1.5\sigma$) between equations (7.4.7) and (7.4.8) allows us to define an observable quantity, $\mathcal{O}_{bs\gamma}$, that we can compare against models of new physics,

$$\mathcal{O}_{bs\gamma} = \frac{BR(B \to X_s \gamma)^{\text{exp}}}{BR(B \to X_s \gamma)^{\text{SM}}} - 1 = 0.18 \pm 0.13. \tag{7.4.9}$$

Equation (7.4.9) means that new physics is now only allowed to contribute to $B \to X_s \gamma$ at about thirty percent of the SM contribution. Since the it begins at one-loop, new physics models such as SUSY can easily produce larger contributions. Exploiting the possibility of accidental cancellations, typical SUSY Higgs analyses in the literature either ignore $B \to X_s \gamma$ or focus on parameter regions where these cancellations occur. Here, given our interest in natural models, we use equation (7.4.9) to estimate the level of fine-tuning involved in the latter approach [225].

Given a model input parameter P (e.g., A_t) that contributes to $BR(B \to X_s \gamma)$, we assess the degree of fine-tuning $\Delta_{\mathcal{O}_{bs\gamma}}$ associated with it in a similar way to the fine-tuning measure commonly associated with the Z boson mass. The only slight modification we apply here is to account for the uncertainty in the experimental determination of $\mathcal{O}_{bs\gamma}$:

$$\left[\Delta_{\mathcal{O}_{bs\gamma}}^{(P)}\right]^{-1} = \left| \frac{\mathcal{O}_{bs\gamma}}{\sigma_{\mathcal{O}_{bs\gamma}}} \frac{\partial \log \mathcal{O}_{bs\gamma}}{\partial \log P} \right| = \left| \frac{P}{0.3} \frac{\partial \mathcal{O}_{bs\gamma}}{\partial P} \right|, \tag{7.4.10}$$

where we chose to combine linearly the central value and the uncertainty on the right hand side of equation (7.4.9), setting $\sigma_{\mathcal{O}_{bs\gamma}} = 0.3$. Then we choose to adopt the total fine tuning measure

$$\Delta_{tot}^{-1} = \sqrt{\Delta^{-2} + \Delta_{\mathcal{O}_{bs\gamma}}^{-2}}, \tag{7.4.11}$$

where Δ is the usual tuning of the Fermi scale defined in section 3.5.1. To get a rough estimate of the importance of equation (7.4.10), consider minimally flavor violating new physics contributions to the Wilson coefficients $C_{7,8}$ of the electromagnetic and chromomagnetic dipole operators $\mathcal{O}_{7,8}$,

$$\mathcal{O}_7 = \frac{e}{16\pi^2} m_b \left(\bar{s}_L \sigma_{\mu\nu} b_R \right) F^{\mu\nu}, \quad \mathcal{O}_8 = \frac{g}{16\pi^2} m_b \left(\bar{s}_L \sigma_{\mu\nu} T^a b_R \right) G^{a\mu\nu}. \tag{7.4.12}$$

---

[7]Ref. [224] found the theoretical result $BR(B \to X_s \gamma)^{\text{SM}} = (3.15 \pm 0.25) \times 10^{-4}$. As it becomes clear in the following we have chosen the value that gives us the most conservative results.

Taking $C_{7,8}$ to be input at the top mass scale, the contribution to $\mathcal{O}_{bs\gamma}$ can be approximated by [226]

$$\mathcal{O}_{bs\gamma} = a_{77}|C_7|^2 + a_{88}|C_8|^2 + \Re\{a_7 C_7 + a_8 C_8 + a_{78}C_7 C_8^*\}, \qquad (7.4.13)$$

with $a_7 = -2.41 + 0.21i$, $a_8 = -0.75 - 0.19i$, $a_{77} = 1.59$, $a_{88} = 0.26$, $a_{78} = 0.82 - 0.30i$. The MSSM with light mixed stops and light higgsinos gives a $\tan\beta$-enhanced contribution to the Wilson coefficients, of the form

$$C_{7,8} \approx \frac{m_t^2 A_t \mu}{m_{\tilde{t}}^4} \mathcal{F}_{7,8}\left(\frac{m_{\tilde{t}_1}^2}{|\mu|^2}, \frac{m_{\tilde{t}_2}^2}{|\mu|^2}\right) \tan\beta, \qquad (7.4.14)$$

where $\mathcal{F}_{7,8}(x,y)$ are loop functions that take $\mathcal{O}(1)$ values for $x \sim y = \mathcal{O}(1)$. Using equations (7.4.14), (7.4.13) and (7.4.10) we see that if we wish to avoid accidental cancellations to a level of one part per ten, then we must have $(A_t \mu \tan\beta/m_{\tilde{t}}^2) < \text{few}$.

In our numerical calculations, we sum in quadrature the contributions to $\Delta_{\mathcal{O}_{bs\gamma}}^{-1}$ coming from the parameters A_t, μ, and $m_{\tilde{g}}$ (the gluino mass): $\Delta_{\mathcal{O}_{bs\gamma}}^{-2} = \sum_P \left[\Delta_{\mathcal{O}_{bs\gamma}}^{(P)}\right]^{-2}$. We compute the derivatives $(\partial\mathcal{O}_{bs\gamma}/\partial P)$ numerically, including the full one-loop results, and holding all other parameters fixed. In taking the derivative we fix also dependent vacuum parameters such as $\tan\beta$ and m_Z. This is not strictly consistent when one considers the vacuum configuration as the output of a certain combination of soft SUSY-breaking parameters. Nevertheless, this is a good enough treatment for our purposes, (a) given our underlying assumption of extra dynamics, beyond the MSSM, affecting the Higgs potential, and (b) given our limited choice of varied parameters $P = \{A_t, \mu, m_{\tilde{g}}\}$.

Summary of stop effects

In figures 7.6 (left) and 7.7 we study the range of values for $r_\gamma^{\tilde{t}}$ and $r_G^{\tilde{t}}$ that can be naturally expected due to light stops. There we plot the extremal (upper and lower) values of $r_\gamma^{\tilde{t}}$ and $r_G^{\tilde{t}}$ that can be achieved by varying $A_t, \mu, m_{\widetilde{Q}_3}, m_{\widetilde{u}_3}$ for different values of $\tan\beta$, while imposing $\Delta_{tot} \lesssim 10\%$, or tuning no worse than one part per ten. We also, very conservatively, demand that $m_{\tilde{t}_1} > 100$ GeV. The extra fine-tuning incurred by large A_t, as seen by equations (7.2.3) and (7.4.14), suggests that stop mixing should not be large, and more so for larger $\tan\beta$. As a result, the lower bound on $r_G^{\tilde{t}}$ (upper bound on $r_\gamma^{\tilde{t}}$) is set by naturalness.

We learn that $r_G^{\tilde{t}} < 0.6$ does not arise within natural SUSY, while a rather significant increase of $r_G^{\tilde{t}}$ is obtained with light, unmixed stops. The upper bound $r_G^{\tilde{t}} < 1.6$ is obtained when stops are un-mixed and as light as we let them, close to the top mass. Ignoring the possibility of additional SUSY contributions, this ultra-light region is in strong tension with electroweak precision tests (EWPTs). For example, setting $X_t = 0$, $m_{\widetilde{Q}_3} = m_{\widetilde{u}_3} = 100$ GeV ($m_{\tilde{t}_{1,2}} \approx 200$ GeV) and neglecting sbottom mixing we find $(\Delta\rho/\rho) \approx 3.5 \times 10^{-3}$, more than an 8σ deviation. However, it is not inconceivable that contributions from the Higgs and gaugino sectors could ameliorate this tension.

While such cancellation would certainly be fine-tuned, the level of tuning does not quite make it to the 1:10 level except at this very low mass end. Instead of complicating the analysis by folding in EWPTs into our naturalness criterion, we simply report that if we impose that the stop-sbottom contribution to $(\Delta\rho/\rho)$ remains within the 4σ range, we obtain stronger limits on the Higgs-gluon and Higgs-photon vertices, $0.9 < r_G^{\tilde{t}} < 1.3$ and $0.9 < r_\gamma^{\tilde{t}} < 1.03$. We can also require the lightest stop to be heavier in view of LHC searches that here we do not discuss in detail. Imposing a stronger bound on the lightest stop mass $m_{\tilde{t}_1} > 400$ GeV[8] leads to $1 \le r_G^{\tilde{t}} < 1.1$ and $0.97 < r_\gamma^{\tilde{t}} \le 1$.

Finally, while our philosophy in this work is that additional physics beyond the MSSM must affect the Higgs sector to account for the Higgs mass, it is nevertheless interesting to show the implications of naturalness for the stop contribution to m_h. In figure 7.8 we plot the maximal value of m_h obtained by varying the SUSY parameters as above. We use the analytical estimate for m_h and so this plot provides an upper bound. The plot shows how tuning for $B \to X_s\gamma$ makes a large stop contribution to m_h less plausible for large $\tan\beta$. figure 7.9 shows contours of the MSSM Higgs mass (computed now using FeynHiggs), the total fine tuning defined in equation (7.4.11) and $\left(r_G^{\tilde{t}}\right)^2$ in equation (7.4.3), for two values of $\tan\beta = 10, 30$. At large $\tan\beta$, tuning for $B \to X_s\gamma$ disfavors the high mixing region, causing the maximal value of m_h to drop substantially.
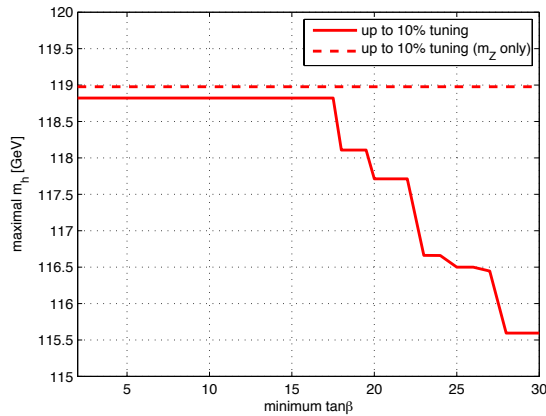

Figure 7.8: Upper limit on m_h in the MSSM, as a function of $\tan\beta$. The solid line corresponds to scenarios with up to 10% total fine-tuning (defined in equation (7.4.11)), while the dashed line corresponds to Z boson mass tuning alone (equation (7.2.3)).

---

[8]Imposing at the same time a similar constraint on the sbottom mass would not alter our predictions for Higgs couplings and would automatically satisfy the $(\Delta\rho/\rho)$ bound. Note also that we are not implicitly stating that the LHC is excluding everything below 400 GeV and that anything above is consistent with their bounds. We are just choosing a representative scenario with heavier stops.
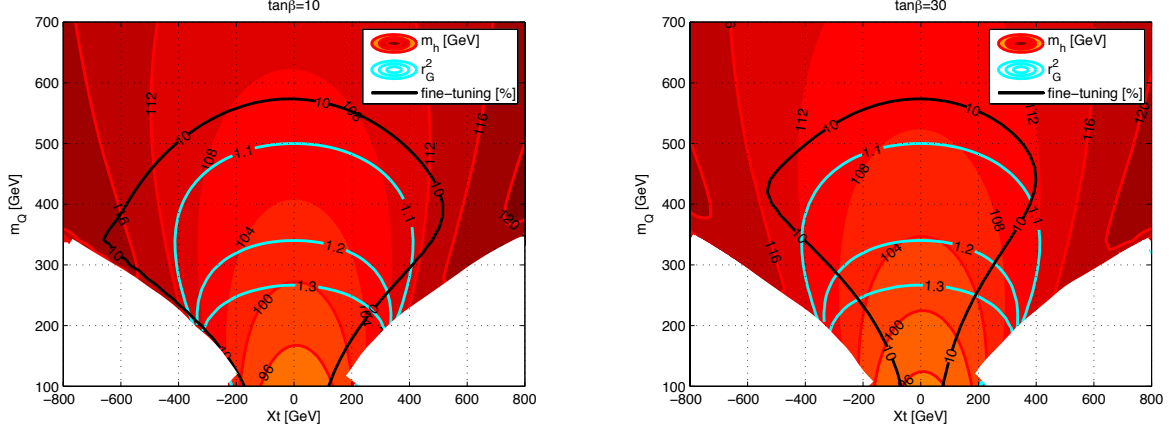
Figure 7.9: Contours of the Higgs mass, the total fine tuning and r_G^2 in the (m_{Q_3}, X_t) plane. We set $\mu = 150$ GeV, $m_{\widetilde{Q}_3} = m_{\widetilde{u}_3} \equiv m_Q$ and $X_t = A_t - \mu/\tan\beta$.

7.4.2   Charginos

Naturalness dictates that at least one chargino must be light, $m_{\tilde\chi^\pm} \lesssim 200$ GeV. Hence, the chargino contribution to r_γ may be expected to become relevant [227, 228, 229]. What limits the effect to be modest is the direct LEP bound: $m_{\tilde\chi^\pm} > 94$ GeV [230]. Imposing this constraint, we compute the chargino contribution to r_γ, varying the relevant parameters in the range $-300 < \mu/\text{GeV} < 300$, $0 < M_2/\text{GeV} < 1000$, $1 < \tan\beta < 40$. The result is shown in the right panel of figure 7.6. We conclude that:

- A sizable effect is possible only for low $\tan\beta < 3$, mostly limited to a reduction in r_γ. The effect is larger for $\tan\beta = 1$, where we find $0.7 < r_\gamma^{\tilde\chi^\pm} < 1.13$. If we restrict to $\tan\beta \geq 2$, we have: $0.8 < r_\gamma^{\tilde\chi^\pm} < 1.1$. The sign of $(r_\gamma^{\tilde\chi^\pm} - 1)$ depends on the sign of (μM_2).

- Restricting to $\tan\beta > 3$ ($\tan\beta > 5$) diminishes the effect, as the chargino-Higgs coupling $\propto \sin 2\beta$ is reduced. Here we find $|r_\gamma^{\tilde\chi^\pm} - 1| < 10\%(6\%)$, where saturating the upper limit requires two very light charginos with $m_{\tilde\chi_1^\pm} \sim m_{\tilde\chi_2^\pm} \sim 100$ GeV.

The upper bound of approximately $+10\%$ for the chargino enhancement to the Higgs-photon coupling can be understood as follows. Taking $\tan\beta = 1$ one obtains, at leading log,

$$r_\gamma^{\tilde\chi^\pm} \approx \frac{-6.49 - \frac{8}{3}\frac{m_W^2}{M_2\mu - m_W^2}}{-6.49} \leq 1 + \frac{8}{3 \times 6.49}\frac{m_W^2}{m_{\tilde\chi_1^\pm}^2}\left(1 + \frac{2m_W}{m_{\tilde\chi_1^\pm}}\right)^{-1}, \qquad (7.4.15)$$

where we took $M_2\mu > m_W^2$ in order to obtain positive interference with the W-dominated SM amplitude $\mathcal{A}_{SM} \approx -6.49$. Imposing the bound $m_{\tilde\chi_1^\pm} > 94$ GeV, we obtain $r_\gamma^{\tilde\chi^\pm} - 1 \lesssim 10\%$, in good agreement with the full one-loop computation.

The bottom line is that a chargino contribution to the $h\gamma\gamma$ vertex, with a sign that is theoretically unconstrained, can disturb the correlation between r_γ and r_G that we have found, accounting for the stop contribution alone. As a result we will be forced to assess r_G and r_γ independently when we come to predict Higgs observables. Nevertheless, it will still be useful to describe the modified $h\gamma\gamma$ and hGG in terms of $r_G^{\tilde{t}}$ and $r_\gamma^{\tilde{\chi}^\pm}$. This separation becomes practical for $\tan\beta \gtrsim 3$, when the chargino correction decouples, with ramifications to Higgs mixing effects.

7.4.3   Charged Higgs

A charged Higgs loop diagram contributes to r_γ, with [207]

$$r_\gamma \approx 1 - 0.007 \left(\frac{\lambda_{hH^+H^-}}{\lambda_{hH^+H^-}^{MSSM}} \right) \left(\frac{m_{H^\pm}}{250\,\text{GeV}} \right)^{-2}, \tag{7.4.16}$$

where $\lambda_{hH^+H^-}^{MSSM}/v = (g^2 - g'^2)/4 \approx 0.07$ is the MSSM coupling. The contribution is negligible unless the charged Higgs is very light, in strong tension with $B \to X_s\gamma$ [224][9], or the coupling $\lambda_{hH^+H^-}$ receives very large corrections from an extended Higgs sector. We note that in F-term models where singlet chiral superfields are added, a numerically large correction to some Higgs quartic couplings is conceivable; however, the coupling $\lambda_{hH^+H^-}$ remains unaffected.

7.4.4   Staus and sbottoms

The possibility that light scalar τ's could boost the $h\gamma\gamma$ coupling was entertained in [231, 232]. This possibility is, however, outside of the scope of natural SUSY. Naturalness limits this effect as follows. The stau mass eigenvalues are

$$m_{\tilde{\tau}_{1,2}}^2 \cong \frac{m_{\tilde{L}}^2 + m_{\tilde{e}}^2 + \frac{m_Z^2 c_{2\beta}}{2}}{2} \pm \sqrt{\frac{\left(m_{\tilde{L}}^2 - m_{\tilde{e}}^2 + 2m_Z^2 s_W^2 c_{2\beta} \right)^2}{4} + m_\tau^2 X_{\tilde{\tau}}^2}, \tag{7.4.17}$$

with $X_{\tilde{\tau}} = A_{\tilde{\tau}} - \mu\tan\beta$. Let us neglect D-terms in the following discussion, for clarity, including them numerically later to verify our conclusions. The leading log contribution to r_γ can then be estimated as

$$r_\gamma - 1 \approx \frac{1}{6\mathcal{A}_{SM}} \frac{\partial \log\left(m_{\tilde{\tau}_1}^2 m_{\tilde{\tau}_2}^2 \right)}{\partial \log v} = 1 - \frac{r_\tau}{3\mathcal{A}_{SM}} \frac{m_\tau^2 X_{\tilde{\tau}}^2}{m_{\tilde{\tau}_1}^2 m_{\tilde{\tau}_2}^2}, \quad \text{stau contribution}, \tag{7.4.18}$$

where $\mathcal{A}_{SM} \approx -6.49$ is the SM (W and t loop) amplitude, evaluated at $m_h = 125$ GeV. Using the fact that $m_{\tilde{\tau}_2}^2 \geq m_{\tilde{\tau}_1}^2 + 2m_\tau |X_{\tilde{\tau}}|$, we obtain

$$0 < r_\gamma - 1 \lesssim 4r_\tau \times 10^{-4} \left(\frac{|X_{\tilde{\tau}}|}{100\,\text{GeV}} \right) \left(\frac{m_{\tilde{\tau}_1}}{100\,\text{GeV}} \right)^{-2}, \quad \text{stau contribution}. \tag{7.4.19}$$

---

[9]The tension with $B \to X_s\gamma$ may be ameliorated if the charged state is taken from an additional inert Higgs multiplet.

Imposing conservatively $m_{\tilde{\tau}_1} > 100$ GeV and demanding fine-tuning no worse than 10% ($|\mu| \lesssim 300$ GeV), we find that in natural SUSY the effect is not larger than 3% for $\tan\beta < 50$ and $r_\tau \sim 1$.

The sbottom contribution to r_γ is estimated to be even smaller because of the smaller electric charge,

$$0 < r_\gamma - 1 \lesssim r_b \times 10^{-4} \left(\frac{|X_{\tilde{b}}|}{100\,\text{GeV}} \right) \left(\frac{m_{\tilde{b}_1}}{100\,\text{GeV}} \right)^{-2}, \quad \text{sbottom contribution.} \tag{7.4.20}$$

The contribution to the hGG vertex is given by

$$r_G - 1 \approx -\frac{(r_b/r_t)}{4} \frac{m_b^2 X_{\tilde{b}}^2}{m_{\tilde{b}_1}^2 m_{\tilde{b}_2}^2}, \quad \text{sbottom contribution} \tag{7.4.21}$$

and we can bound it by

$$0 > r_G - 1 \gtrsim -0.01(r_b/r_t) \left(\frac{|X_{\tilde{b}}|}{100\,\text{GeV}} \right) \left(\frac{m_{\tilde{b}_1}}{100\,\text{GeV}} \right)^{-2}, \quad \text{sbottom contribution.} \tag{7.4.22}$$

To make the stau or sbottom contributions to r_γ or r_G larger than a few percent, large values of r_τ, r_b, arising from Higgs mixing, would be required. As we show in the next sections, (i) one expects $r_b \sim r_\tau$; (ii) large r_b would increase the total Higgs width, implying a suppression to the $h \to \gamma\gamma$ rate that would more than compensate for the loop correction and that is not seen in the data; and (iii) $r_b \gtrsim 3$ does not arise naturally in the MSSM or any extension we are aware of for lifting the Higgs mass. We conclude that the sbottom and stau contributions to r_γ and r_G can be safely neglected in assessing the predictions of natural SUSY to a few percent accuracy.

7.5   Summary and predictions

We have seen that in the natural MSSM and its D-term extensions, Higgs couplings can be expressed in terms of only two parameters at tree-level, as in a general type-II 2HDM. Adding a singlet chiral superfield, as for example in the NMSSM, in general increases the number of parameters to three, if we assume all couplings to be CP conserving. The additional degree of freedom parameterizes the mixing between the new CP even state and the lightest scalar Higgs: $c_\phi \equiv \langle S|h \rangle$. We had disregarded the possibility in the previous sections, but we find it an economical generalization that allows to capture a vast class of models. Therefore we keep it in mind while comparing the predictions with LHC data.

We have seen that naturalness also prefers stops and charginos to be fairly light, and for this reason we considered their loop contributions to the Higgs to digluon/diphoton partial widths, introducing two new parameters. They can be chosen as $\delta r_G^{\tilde{t}}$, characterizing the stop contribution to the dimension-5 Higgs-gluon-gluon coupling and $\delta r_\gamma^{\tilde{\chi}^\pm}$, characterizing the chargino contribution to the dimension-5 Higgs-photon-photon-coupling. While fitting the data, in the next section, r_G

and r_γ are treated as independent parameters. Thus we capture any loop effect on these vertexes, possibly arising also from the small stau, sbottom and charged Higgs effects.

In the previous sections we have not only identified a small set of relevant parameters, but we have also found limited numerical ranges for them. This allows us to make some sharp statements even before fitting the LHC data. Consider now the following six processes, with GF, VBF and VH standing for gluon fusion, vector boson fusion and associated production, respectively:

$$\mu_{\gamma\gamma;GF} = \frac{r_G^2 r_\gamma^2}{\mu_{\text{tot}}}, \tag{7.5.1}$$

$$\mu_{\gamma\gamma;VBF} = \frac{r_V^2 r_\gamma^2}{\mu_{\text{tot}}}, \tag{7.5.2}$$

$$\mu_{ZZ,WW;GF} = \frac{r_G^2 r_V^2}{\mu_{\text{tot}}}, \tag{7.5.3}$$

$$\mu_{bb,\tau\tau;VH} = \frac{r_V^2 r_b^2}{\mu_{\text{tot}}}. \tag{7.5.4}$$

Some relevant questions, motivated in part by the current experimental situation (summarized in section 7.6.1), are the following:

1. **What is the maximal enhancement for $h \to \gamma\gamma$ in GF production?** The bound is obtained with large positive stop corrections, suppressed $h b\bar{b}$ coupling $r_b \ll 1$ and SM-like $r_t \approx r_V \approx 1$. We find

$$\mu_{\gamma\gamma;GF} \lesssim 3.4 \text{ to } 6.2, \tag{7.5.5}$$

   where we allow stops to provide $r_G^{\tilde{t}} = 1.1$ to 1.5, respectively. $\mu_{\gamma\gamma;GF} \sim 2$ is easy to achieve in beyond-MSSM SUSY by a suppressed $h b\bar{b}$ coupling, together with a little help from natural stops. Note that our upper limits on the chargino loop contribution implies that if the diphoton rate is increased by more than $\sim 20\%$, then the ZZ, WW rates should also be enhanced (see bullet (3) below).

2. **What is the maximal enhancement for $h \to b\bar{b}$ in VH?** This question is partially motivated by the hint for a factor ~ 2 enhancement in $h \to b\bar{b}$ associated production, reported by the Tevatron experiments (but not confirmed by LHC results). A constraint comes simply from 2HDM trigonometry,

$$\mu_{bb;VH} = \frac{r_V^2 r_b^2}{\mu_{\text{tot}}} \leq 1.5. \tag{7.5.6}$$

   We obtain the upper bound of 1.5 by examining $0.1 \leq \tan\beta \leq 40$, $0 \leq r_b \leq 10$, and varying $r_G^{\tilde{t}}$ in the range $[0.6, 1.6]$. The upper limit is essentially unaltered by taking $r_G^{\tilde{t}}$ in the range $[1, 1.1]$ (i.e. $m_{\tilde{t}_1} > 400$ GeV). The maximal value is obtained for $\tan\beta \gtrsim 30$ and $r_b \gtrsim 3.5$. This shows that an enhancement of 50% is extremely hard to accommodate if all other rates are broadly consistent with the SM. Experimentally establishing a nontrivial lower bound on $\mu_{bb;VH}$ would have profound implications for natural SUSY. For instance, establishing

$\mu_{bb;VH} \geq 1.4$ would provide the lower bounds $\tan\beta > 8$, $r_b > 2$, ruling out F-term models like λSUSY, while making a strong case for D-term models that enhance $hb\bar{b}$. Provided that a concrete model giving all other Higgs rates consistent with the measurements can be constructed also for $r_b > 2$.

3. **What is the maximal ratio of $h \to \gamma\gamma$ vs. ZZ, WW in the GF production channel?** ATLAS reports $\mu_{\gamma\gamma;GF} \gtrsim 2 \times \mu_{WW;GF}$, and a low WW rate is also found at the Tevatron. The ratio and the answer are given by

$$\frac{\mu_{\gamma\gamma;GF}}{\mu_{WW,ZZ;GF}} = \frac{r_\gamma^2}{r_V^2} = \left| 1.28 - 0.28(r_G^{\tilde{t}} r_t/r_V) + (\delta r_\gamma^{\tilde{\chi}^\pm}/r_V) \right|^2 < 1.4, \qquad (7.5.7)$$

where $\delta r_\gamma^{\tilde{\chi}^\pm} \equiv r_\gamma^{\tilde{\chi}^\pm} - 1$. The numerical value of 1.4 answers a slightly modified question: "**what is the maximal value of equation (7.5.7), assuming that $h \to \gamma\gamma$ is not suppressed**, i.e. assuming $\mu_{\gamma\gamma;GF} \geq 0.75$?" This is more relevant, because to truly maximize equation (7.5.7) one would need to take r_V small, which would diminish the actual observed $\gamma\gamma$ rate. Imposing $\mu_{\gamma\gamma;GF} \geq 0.75$ and varying $r_b, \tan\beta, r_G^{\tilde{t}}, r_\gamma^{\tilde{\chi}^\pm}$, we find the numerical bound in equation (7.5.7). Restricting to $m_{\tilde{t}_1} > 400$ GeV and $r_G \leq 1.1$ brings down the upper bound to 1.3.

4. **What is the maximal ratio of $h \to \gamma\gamma$ in the VBF vs. the GF channels?** Again, we further impose $\mu_{\gamma\gamma;GF} \geq 0.75$, this time in order to avoid irrelevant solutions with $r_t \ll 1$ and vanishing GF production. The upper bound we obtain is:

$$\frac{\mu_{\gamma\gamma;VBF}}{\mu_{\gamma\gamma;GF}} = \frac{r_V^2}{r_G^2} < 2.8. \qquad (7.5.8)$$

Note that this last result, in contrast to the previous three items, is directly sensitive to our specific criterion for naturalness, because the bound (7.5.8) comes about by using stops to decrease the Higgs-gluon coupling, an effect that requires large stop mixing. For example, restricting to 20% tuning instead of 10%, would change the bound in equation (7.5.8) to 1.5 instead of 2.8. Taking $m_{\tilde{t}_1} > 400$ GeV and consequently $r_G^{\tilde{t}} \geq 1$, leads to an upper bound of 1.

The sample questions above give a sense to the level of predictive power in natural SUSY. However, the usefulness of reducing the number of free parameters to just a few comes also in interpreting a larger set of independent measurements. In what follows we demonstrate this point by fitting the relevant parameters to current data and interpreting the results.

7.6   Natural SUSY predictions and LHC data

The LHC experiments have released Higgs coupling measurements in several channels that we have described in section 2.7. Here we compare natural SUSY predictions with the data performing simple χ^2 fits.

In the next section we describe the data used and the fitting procedure. We then show the results of fits to deviations induced by tree-level mixing and those of a complete five dimensional fit that parametrizes a generic natural SUSY theory, including also loop-effects.

7.6.1   Data and fitting procedure

In order to constrain the supersymmetric parameters, we take into account all the available Higgs channel rates. We use the latest LHC data published in occasion of the *Recontres de Moriond* in March 2013 and shortly after. The rates depend on the product of the overall production cross-section and branching ratio for the particular channel. The results are typically reported as a confidence interval on the event rate relative to the SM prediction, denoted by $\hat{\mu}$. We take the CMS $\hat{\mu}$'s at the best fit value for the mass, $m_h = 125.7$ GeV, from [233]. ATLAS results are taken from the public notes of the individual analyses ([234, 235, 236, 237, 238, 239]) that for $\gamma\gamma$, WW and ZZ contain the results of a fit separating GF production from VBF production. The mass for which we take the rate varies channel by channel and can be found in the individual references, but is always within 1 GeV of 126 GeV. For the Tevatron $h \to b\bar{b}$ rate we take the value of $\hat{\mu}$ at $m_h = 126$ GeV.

In table 7.6.1 we list the measurements relevant for our fit, regrouped by channel, and the corresponding values of the $\hat{\mu}$'s. Most of these measurements were performed on the full available dataset and it is reasonable to assume that they will not change considerably until the LHC restarts its operations in two years. Nonetheless regularly updated mass determinations and rates can be found in the documents linked from the public pages of the ATLAS and CMS collaborations [53, 54].

In any given model, the signal strengths are determined by the r_i's. For the LHC, the four relevant production modes and their respective theoretical dependance are

- Gluon fusion ($gg \to h$): $\sigma_{GF}/\sigma_{GF}^{\mathrm{SM}} = |r_G|^2$,

- Vector boson fusion ($qq \to hqq$): $\sigma_{VBF}/\sigma_{VBF}^{\mathrm{SM}} = |r_V|^2$,

- Vector boson associated production ($q\bar{q} \to hV$): $\sigma_{VH}/\sigma_{VH}^{\mathrm{SM}} = |r_V|^2$,

- Top associated production ($gg \to ht\bar{t}$): $\sigma_{ht\bar{t}}/\sigma_{ht\bar{t}}^{\mathrm{SM}} = |r_t|^2$.

In some cases, a channel can include events from several production modes; for instance, the dijet tagged signature in table 7.6.1 is dominantly produced via vector boson fusion, but contains a non-negligible contribution from gluon fusion. The collaborations have made public the numbers needed to assess the composition in terms of the physical production modes in the references listed above. In the fit we use the fractions provided channel by channel, but we find a good uniformity between different final states inside CMS, giving roughly $75 - 80\%$ of VBF and $20 - 25\%$ of GF in the dijet tagged categories. The only exception is the ZZ dijet tagged category that is dominated by GF.

ATLAS' numbers for WW, ZZ and $\gamma\gamma$ are to be considered as pure VBF in the dijet tagged category and pure GF in the untagged one, since they were provided by the collaboration from a maximum likelihood fit used to separate them, which is described in the references listed above. In all other cases, the relative fractions of the untagged mode are close to be the relative cross-section fractions of the different channels. Therefore, where efficiencies are not publicly available, we use the ratio between cross-sections to determine the composition of the sample. The VH and ttH categories can be considered pure.

The fits to the data are performed minimizing the χ^2

$$\chi^2 = \sum_{i=\text{channels}} \frac{(\mu_i(r_j) - \hat{\mu}_i)^2}{\sigma_i^2} \tag{7.6.1}$$

where $\mu_i(r_j)$ are predicted rates and σ_i's are two-sided errors (depending on the sign of $\mu_i - \hat{\mu}_i$). By performing the χ^2 test we are assuming that the likelihood functions for $\hat{\mu}$ follow an approximate two-sided gaussian distribution and the correlations can be neglected, both of which have been shown to be valid approximations [240, 241]. Furthermore we have compared our results with the two dimensional fits released by the collaborations, obtaining a good agreement. In the plots shown in the following sections we always normalize the χ^2 to the number of degrees of freedom and subtract the value at the minimum.

In the following we refer to "preferred" and "allowed" regions. Preferred regions are obtained by varying an N-parameters subset of the r_i's, while fixing the other parameters to their SM-values. Strictly speaking, allowed regions are found including all the r_i's, the possibility of flavor non-universality (for instance $r_b \neq r_\tau$), vertex structures different from the SM and the presence of an invisible width. At this stage, with limited precision in the measurements, we find the theoretically inspired five dimensional fit a reasonable approximation of the most generic setting. In this framework we obtain lower dimensional confidence intervals by profiling the likelihood with respect to the remaining independent parameters (given a lower dimensional point the other parameters are varied to give the best possible fit).

7.6.2   Fits to tree-level effects

If the superpartners are relatively heavy, i.e. $m_{\tilde{t}_1} \gtrsim 400$ GeV and $m_{\chi_1^\pm} \gtrsim 200$ GeV, loop corrections to Higgs couplings are at most of the order of 10% in a broad region of parameter space, provided that the stop mixing is limited by naturalness, as we have seen in the previous sections. Therefore it is easy to decouple these effects without incurring excessive fine-tuning and without the need to single out narrow corners of parameter space. With this in mind, we begin by fitting the tree-level corrections in the MSSM and its extensions.

Without loss of generality, we can take $\tan\beta > 0$ [242], with equation (7.6.8) implying $\sin\alpha < 0$. We require that the top Yukawa does not blow up above the electroweak scale, which imposes the lower bound $\tan\beta \geq 1$ [66]. As discussed in section 7.3, demanding loop corrections to the type-II 2HDM structure to be negligible provides the additional constraint $\tan\beta \leq 40$ (that can be relaxed or made stronger depending on the level of fine-tuning that we allow in the theory).

ATLAS	untagged	dijet tagged	VH	ttH
$h \to \gamma\gamma$	$1.60^{+0.41}_{-0.36}$	$1.70^{+0.94}_{-0.89}$	$1.8^{+1.5}_{-1.3}$	$\times$
$h \to WW$	0.82 ± 0.36	1.66 ± 0.79	$\times$	$\times$
$h \to ZZ$	$1.80^{+0.80}_{-0.50}$	$1.2^{+3.8}_{-1.4}$	$\times$	$\times$
$h \to \tau\tau$	0.8 ± 0.7	$0.69^{+0.71}_{-0.69}$	$\times$	$\times$
$h \to b\bar{b}$	$\times$	$\times$	-0.4 ± 1.0	$\times$
CMS	untagged	dijet tagged	VH	ttH
$h \to \gamma\gamma$	$0.70^{+0.33}_{-0.29}$	$1.01^{+0.63}_{-0.54}$	$\times$	$\times$
$h \to WW$	$0.73^{+0.22}_{-0.20}$	$-0.047^{+0.75}_{-0.56}$	$0.51^{+1.3}_{-0.94}$	$\times$
$h \to ZZ$	$0.86^{+0.32}_{-0.26}$	$1.24^{+0.85}_{-0.58}$	$\times$	$\times$
$h \to \tau\tau$	$0.77^{+0.58}_{-0.55}$	$1.42^{+0.70}_{-0.64}$	$1.0^{+1.7}_{-1.5}$	$\times$
$h \to b\bar{b}$	$\times$	$\times$	$1.31^{+0.68}_{-0.61}$	$-0.2^{+2.8}_{-2.9}$
CDF+D0	untagged	dijet tagged	VH	ttH
$h \to b\bar{b}$	$\times$	$\times$	$1.61^{+0.74}_{-0.75}$	$\times$

Table 7.3: Rates relative to their SM value with the respective 68% confidence interval, as measured by the ATLAS (top), CMS (middle) and CDF+D0 (bottom) experimental collaborations.

Since the measured rates broadly agree with the SM, the results of the fit, which are shown in figure 7.10, point to the decoupling limit of the Higgs sector, $\xi \equiv \alpha - \beta + \pi/2 \approx 0$ with a slight preference for negative values of ξ that work to decrease the diboson rates

$$r_b = 1 - \xi \tan\beta + \mathcal{O}(\xi^2), \quad r_t = 1 + \xi/\tan\beta + \mathcal{O}(\xi^2), \quad r_V = 1 - \frac{\xi^2}{2} + \mathcal{O}(\xi^4). \qquad (7.6.2)$$

What is more significant is the vicinity to the decoupling limit that can be quantified as $-0.11 \leq \xi \leq 0.06$ at 95% C.L.

Other than looking at the angles α and β, we can also express the fit constraints in the (m_A, $\tan\beta$) plane and compare our results with direct searches. To do so, the requirement of naturalness needs to be abandoned in the MSSM to allow for the stops' radiative corrections to raise the Higgs mass to 125 GeV. Considering only the leading loop contribution only the $H_u - H_u$ element of the CP even mass matrix receives a correction. The usual tree-level relations are shifted to [243]

$$\begin{aligned} \frac{\tan 2\alpha}{\tan 2\beta} &= \frac{m_A^2 + m_Z^2}{m_A^2 - m_Z^2 + \delta m^2 / \cos 2\beta}, \\ m_H^2 &= -m_h^2 + m_A^2 + m_Z^2 + \delta m^2, \end{aligned} \qquad (7.6.3)$$

where δm^2 can be approximated by the leading stop correction

$$\delta m^2 \approx \frac{3m_t^4}{2\pi^2 v^2 \sin^2\beta} \left[\log \frac{M_{\tilde{t}}^2}{m_t^2} + \frac{X_t^2}{2M_{\tilde{t}}^2} \left(1 - \frac{X_t^2}{6M_{\tilde{t}}^2} \right) \right], \quad M_{\tilde{t}} = \frac{1}{2} \left(m_{\tilde{t}_1} + m_{\tilde{t}_2} \right), \qquad (7.6.4)$$
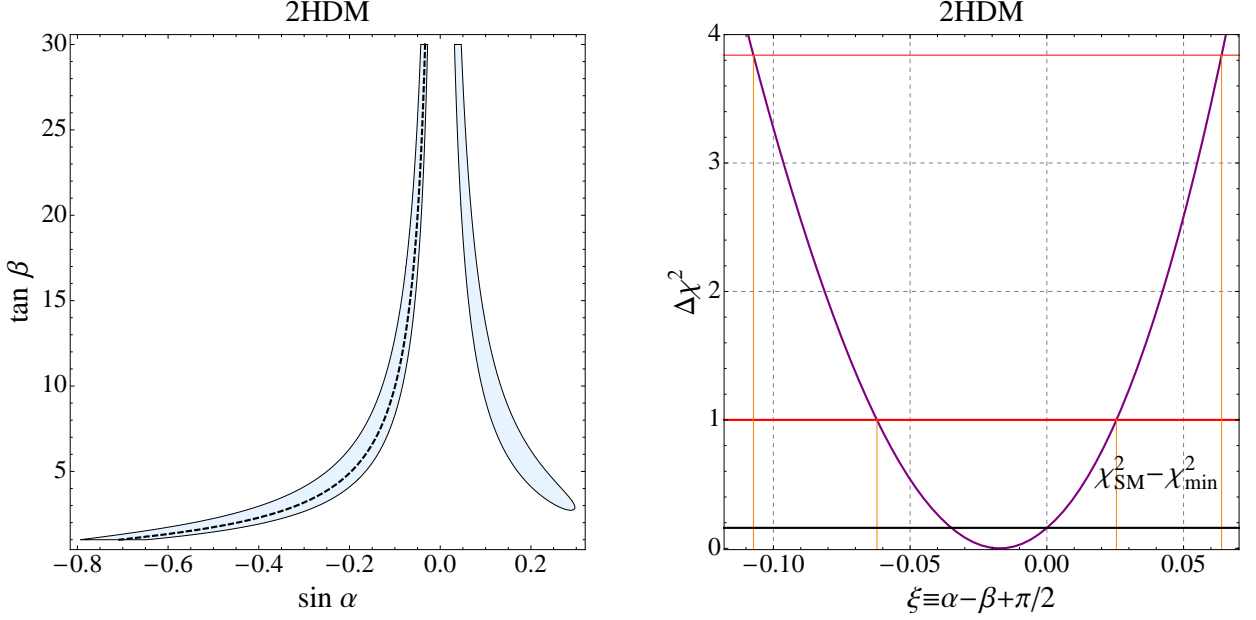
Figure 7.10: Left: χ^2 contours corresponding to the 95% confidence level in the $(\sin\alpha, \tan\beta)$ plane (for a type-II 2HDM). Note that in the MSSM $\sin\alpha < 0$. The black dashed line corresponds to the decoupling limit of the MSSM $\alpha = \beta - \pi/2$. Right: $\Delta\chi^2$ vs. $\xi(\equiv \alpha - \beta + \pi/2)$. The red lines mark the 68% and 95% confidence levels heights of the $\Delta\chi^2$. In black the offset between the SM value of the χ^2 and the 2HDM value at the minimum.

but in the following we always fix it to the m_A and $\tan\beta$ dependent value giving the correct Higgs mass

$$\delta m^2|_{m_A,\tan\beta} = \frac{m_h^2(m_A^2 - m_h^2 + m_Z^2) - m_A^2 m_Z^2 \cos^2 2\beta}{m_Z^2 \cos^2\beta + m_A^2 \sin^2\beta - m_h^2} \,. \tag{7.6.5}$$

Before describing the results of the fit we review current LHC searches for MSSM Higgses. Direct searches for the neutral MSSM Higgses are currently performed in the $\phi \to \tau^+\tau^-$ [244, 247], $b\bar{b}\phi \to b\bar{b}\mu\mu$ [248] and $b\bar{b}\phi \to b\bar{b}b\bar{b}$ [249] channels. The strongest bound is set by the CMS measurement [244] with 17 fb^{-1} of combined 7 TeV and 8 TeV data. It ranges from $m_H \gtrsim 250$ GeV for $\tan\beta = 5$ to $m_H \gtrsim 700$ GeV for $\tan\beta = 40$. The sensitivity vanishes below $\tan\beta = 5$. These searches benefit from large $\tan\beta$, both thanks to new production mechanisms that become important (b and $b\bar{b}$ associated production for instance) and from the increase in the branching ratio to $\tau^+\tau^-$. We also include the LEP bound [245] in our comparison with Higgs rates, but we do not consider the implications of searches for the charged Higgs that are currently not as sensitive as the $\phi \to \tau^+\tau^-$ one plus the LEP constraint. The experimental collaborations use the $m_h^{\max}$ scenario [246] to set their limits, and varying the soft supersymmetry breaking parameters
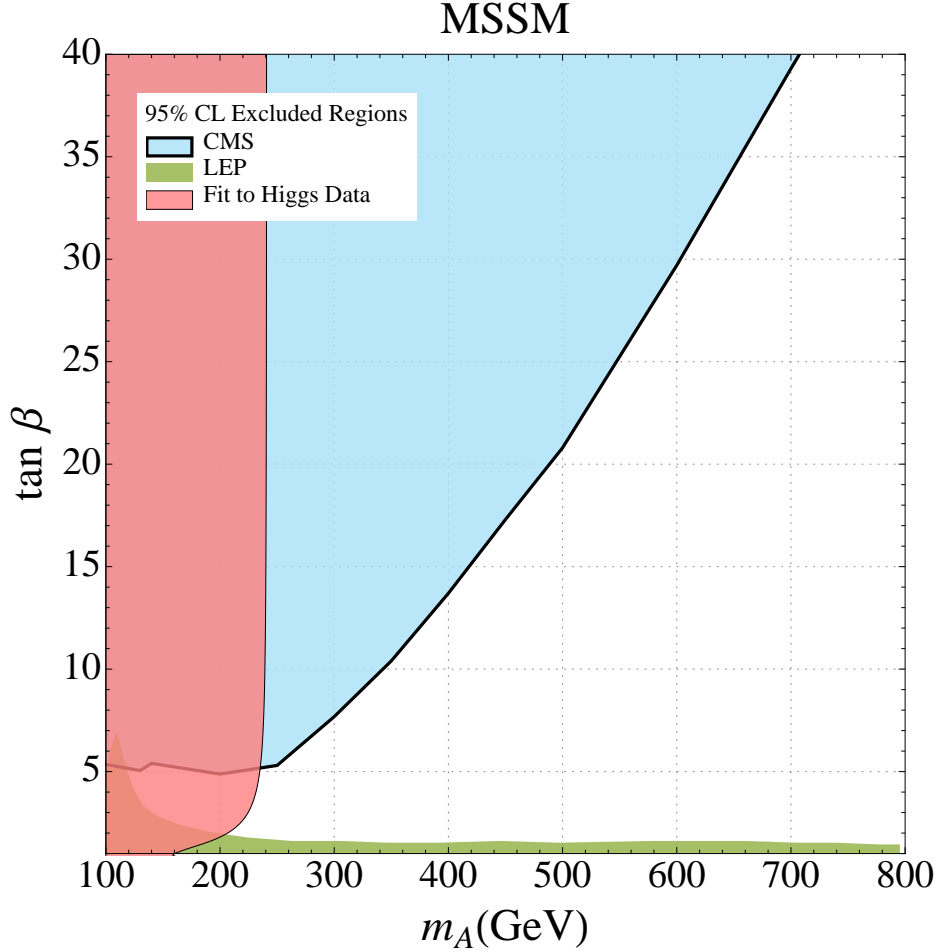
Figure 7.11: Comparison between the fit exclusion in the $(m_A, \tan\beta)$ plane and the direct exclusions from CMS [244] and LEP [245]. The excluded region was obtained profiling the full five dimensional χ^2. Note that the experimental collaborations use the $m_h^{\max}$ scenario [246] to set their limits, without imposing $m_h \approx 125$ GeV.

might lead to modifications of the observed bounds [250]. The effects are stronger for large $\tan\beta$ mainly due to loop corrections to y_b and can not produce any significant gain in sensitivity in the region $3 \lesssim \tan\beta \lesssim 12$, where production cross sections become too small and our analysis starts to be competitive. Additionally, the collaborations do not impose $m_h \approx 125$ GeV. Ideally, the bounds from [244] should be reinterpreted as a bound on $\sigma(pp \to \phi)Br(\phi \to \tau^+\tau^-)$, but it is beyond the scope of this work.

Figure 7.11 shows the overlay of these bounds with the results of the fit to the Higgs data. In the slice $2 \lesssim \tan\beta \lesssim 5$ Higgs rates are probing regions of the parameter space not directly accessible to CMS and LEP. The fit results in figure 7.11 are an anticipation of the five dimensional

fit discussed in section 7.6.3 since the excluded region was obtained profiling the five dimensional χ^2, treating r_γ and r_G as nuisances. This is reflected in the fact that for low $\tan\beta$ the bound becomes less stringent. In that region the relevant tree-level deviations are on r_t which in a five parameters fit, where r_G can vary freely, is essentially unconstrained. Fixing r_G to 1 would result in a slightly stronger bound at low $\tan\beta$ than at large $\tan\beta$, where we have $m_A \gtrsim 240$ GeV. The difference between this bound and the one in [251] is due to the fact that we are profiling a five dimensional likelihood rather than turning on only tree-level effects. Therefore the 95% interval for r_b is broader and, as stated above, r_t is almost unconstrained.

Singlet Mixing

Finally, we consider the effects of the singlet mixing with the two Higgs doublets. We take the superpotential (7.3.22) and do not specify the detailed form of the soft supersymmetry breaking terms or extra superpotential interactions. For simplicity we take all new couplings to be CP conserving and assume the SM-like Higgs to be CP even and the lightest Higgs state in the theory. With these assumptions we do not need to consider exotic decays that could be triggered by approximate $U(1)$'s, including the $U(1)_R$, generating light pseudo-goldstone bosons in the Higgs sector. This considerably simplifies the problem, leaving the relevant parameters to be contained in the 3×3 mixing matrix for the scalar CP even states,

$$
\begin{pmatrix} H_2 \\ H_1 \\ h \end{pmatrix} = \begin{pmatrix} s_\phi c_\chi & -c_\alpha s_\chi + s_\alpha c_\phi c_\chi & -s_\alpha s_\chi - c_\alpha c_\phi c_\chi \\ s_\phi s_\chi & c_\alpha c_\chi + s_\alpha c_\phi s_\chi & s_\alpha c_\chi - c_\alpha c_\phi s_\chi \\ c_\phi & -s_\phi s_\alpha & s_\phi c_\alpha \end{pmatrix} \begin{pmatrix} S \\ H_d \\ H_u \end{pmatrix}, \qquad (7.6.6)
$$

where $c_x = \cos x, s_x = \sin x$. In this notation, the tree-level Higgs couplings depend on (α, ϕ, β), and equation (7.6.7) is modified to

$$
r_b = -\sin\phi \frac{\sin\alpha}{\cos\beta}, \quad r_t = \sin\phi \frac{\cos\alpha}{\sin\beta}, \quad r_V = \sin\phi \sin(\beta - \alpha), \qquad (7.6.7)
$$

where $\cos\phi \equiv \langle S|h \rangle$ measures the amount of singlet in the lightest Higgs. The relations

$$
\frac{\sin 2\alpha}{\sin 2\beta} = -\frac{m_H^2 + m_h^2}{m_H^2 - m_h^2}, \qquad \frac{\tan 2\alpha}{\tan 2\beta} = \frac{m_A^2 + m_Z^2}{m_A^2 - m_Z^2}. \qquad (7.6.8)
$$

are only valid in the MSSM, so that m_A is no longer determined solely (at tree level) from the mixing parameters α and β. Thus, we do not impose any constraint on α and ϕ, but still restrict to $\tan\beta \geq 1$. In figure 7.12, we plot $\Delta\chi^2$ vs $\cos^2\phi$. We fix $\xi \equiv \alpha - \beta + \pi/2$ [10] to zero and obtain the constraint $|\cos\phi| \lesssim 0.45$ at 95% C.L. in agreement with [251].

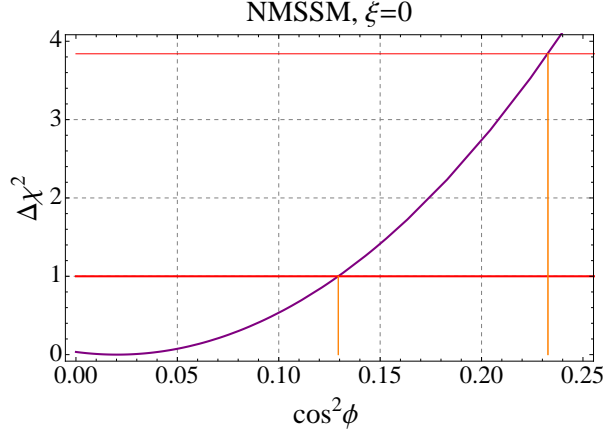[10]Where α is the new angle defined in this section different with respect to the MSSM α.

Figure 7.12: $\Delta\chi^2$ as a function of the singlet mixing parameter $\cos^2\phi$ for $\xi \equiv \alpha - \beta + \pi/2 = 0$. The 68% and 95% confidence levels are marked in red.

7.6.3   Five parameters fit

In the previous sections we fit the data to simplified scenarios in which all the Higgs rates could be expressed in terms of one or two tree-level parameters. This gave an idea of the level of agreement between the data and some physically motivated corners of the parameter space of natural supersymmetry. In spite of the fact that only three channels per experiments have errors below the 50% level (namely $\gamma\gamma$, ZZ and WW untagged) we still find it interesting to explore the more general case in which r_γ, r_G, r_b, r_t and r_V all play a role. This is a small modification of the four parameter natural MSSM, inspired by the possibility of adding a new singlet, and comes closer to approximating a fit with all couplings left to float. The only difference with respect to a four parameter fit resides in the fact that r_t is virtually unconstrained and not artificially limited by its relation with r_V. The results of the fit can be applied also outside of the framework of natural supersymmetry and to facilitate possible attempts we show profiles of the χ^2 for the five couplings in Appendix D. In table 7.6.3 we show the corresponding one dimensional 95% C.L. intervals.

The errors on the single couplings vary from 30% to 100%, which alone is not enough to lose all hope of constraining the parameter space of natural supersymmetry. Not all sensitivity is lost on tree-level modifications of Higgs couplings. We have already shown that the $(m_A, \tan\beta)$ exclusion is competitive with direct searches. Furthermore the statements about singlet mixing and the decoupling limit are still meaningful. Repeating the exercise in section 7.6.2, but profiling the full five dimensional χ^2 we obtain $|\cos\phi| \lesssim 0.7$ at 95% C.L. Both the tree-level fit and the five dimensional one are dominated by the lower bound on r_V that for $\alpha \sim \beta - \pi/2$ [11] becomes $r_V \approx \sin\phi$. The bound on $\cos\phi$ becomes much stronger away from the decoupling limit as can be

---

[11]Note that this is the α defined in equation 7.6.6.

	95% C.L. **(5D)**
r_b	$1.06^{+0.50}_{-0.47}$
r_V	$0.99^{+0.22}_{-0.26}$
r_G	$0.97^{+0.25}_{-0.23}$
r_γ	$1.12^{+0.36}_{-0.32}$
r_t	< 2.43

Table 7.4: Confidence intervals for the five parameters that encode natural SUSY predictions for Higgs rates. All down-type couplings scale with r_b and all up-type ones with r_t. All other couplings not present in the table are fixed to their SM value.
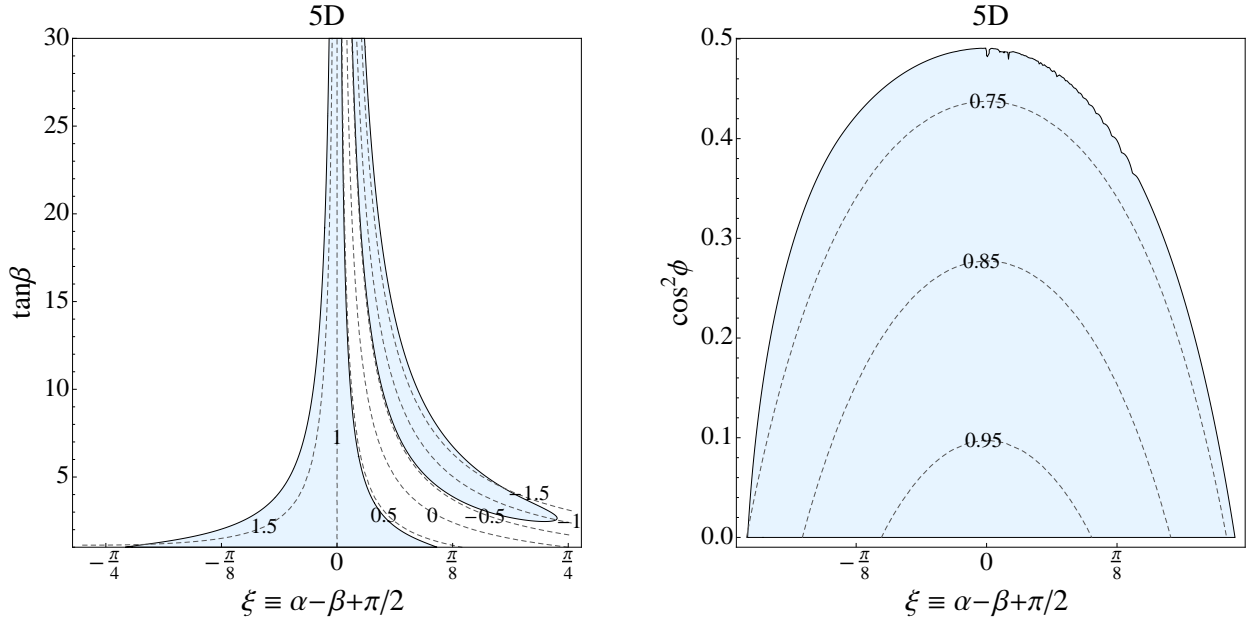
Figure 7.13: Left: The 95% C.L. region in the $(\xi, \tan\beta)$ plane, obtained profiling the full five dimensional χ^2. The dashed contours indicate r_b for $\cos^2\phi = 0$. Right: The 95% C.L. region in the $(\xi, \cos^2\phi)$ plane, obtained profiling the full five dimensional χ^2. The dashed contours correspond to different values of r_V.

seen in the right panel of figure 7.13.

We can also extract information on the level of decoupling of the Higgs sector as a function of $\tan\beta$. In figure 7.13 the 95% C.L. contour is plotted in the $(\xi, \tan\beta)$ plane. The key message is that large $\tan\beta$ is allowed only for values of ξ close to decoupling, where corrections to $r_b \approx 1 - \xi\tan\beta$ are small. This is reflected in the $(m_A, \tan\beta)$ exclusion discussed in section 7.6.2 that is even

competitive with direct searches. Many of these bounds apply to a vast class of complete theories and indicate that in the MSSM and many of its motivated extensions, tree-level effects in the Higgs sector are already strongly constrained, mainly by the measurements of the $h \to WW$ and $h \to ZZ$ rates that in our setting are always below their SM value unless $\xi = 0$ and $\cos \phi = 0$.

7.7   Direct searches in the Higgs sector

We have seen that naturalness leads to consider extensions of the supersymmetric Higgs sector and that Higgs coupling measurements can already constrain some of them. A question that is worthwhile to ask is whether we can distinguish between different extensions through direct searches and between an extension and the vanilla MSSM. The answer is largely model dependent and would require a detailed study. However it is possible to identify some general features of the phenomenology of the extended models.

First and foremost we expect the lightest Higgs to be present in the decay chains of the new particles. This points to final states with two or more b-quarks. Taking this argument further, we can consider cases in which the new particles couple almost exclusively to the Higgs sector of the theory and might decay predominantly to hh. This is a rather general feature in F-terms extensions of the MSSM that does not require to dwell in tuned corners of the parameter space. A typical example is a nearly pure NMSSM singlet as the second lightest Higgs. This case was studied in [251] where a branching ratio of the heaviest Higgs to hh was found to reach up to 90% and the GF production cross section to be still in the $1 - 0.1$ pb range. A CMS search for $b\bar{b}h \to b\bar{b}b\bar{b}$ [249] is already in place, but it is not optimized for double Higgs production. From this point of view also ATLAS' search for $H \to 4\gamma$ [252] is interesting and at 14 TeV it would be worth to expand the searches to mixed signatures ($2b2\gamma$). Richer final states can also be obtained, through the production of heavier Higgses that would decay predominantly to lighter Higgses, leading potentially to signals with 8 b-quarks. With some gymnastics double-higgs signatures can be obtained also in the MSSM. So finding other SUSY particles close to the TeV scale would be important, constituting a strong hint that the underlying theory is natural, thus giving an indirect indication that the MSSM is extended.

Decay chains rich in Higgs bosons can be obtained also in D-terms extensions of the MSSM. However their characteristic feature is the prediction of new gauge bosons that in general live above 3 TeV to be consistent with LEP EWPTs. This can lead to boosted topologies. In particular it would be interesting to study $Z' \to hh$ and $W'^{\pm} \to H^{\pm}h$, both with the Higgses' decay products merging in a single fat jet ($\Delta R \sim 1$) and in the more extreme case in which the two Higgses form a single boosted object. Fat jets with W-tagging are already studied in CMS [253] and it would be a simple exercise to extend these techniques to Higgs-tagging. This would not be relevant only for SUSY searches, but also for mesons of composite sectors decaying to Higgs and gauge bosons. It is also worth to point out that the new gauge bosons can be extremely hard to detect, since nothing prohibits them to be coupled only to the Higgs sector of the MSSM and an extra scalar sector with heavy ($>$ TeV) bosons.

In all these scenarios $H \to t\bar{t}$ is another final state worth exploring. It can hardly discriminate between different realizations of natural SUSY, but would be another indicator of a non-SM Higgs sector.

Direct searches focussed on natural SUSY Higgses are challenging due to the low production cross sections of particles coupling predominantly to the Higgs boson[12] and to the high QCD background for the 4 b-quarks final states that are likely to be produced. Summarizing, multi-Higgs production would be a smoking gun for non-minimal Higgs sectors and boosted final states would point to D-terms extensions of the MSSM.

7.8   Conclusion

In this chapter we have used naturalness to limit the number of parameters entering Higgs rates in complete supersymmetric theories. The number of relevant parameters is small (4 or 5 depending on the nature of the supersymmetric Higgs sector) and more important than that we were able to predict limited numerical ranges for them.

This led to the predictions listed in section 7.5 that mainly rule out the possibility of a natural supersymmetric explanation for large deviations (more than $\approx 100\%$) in Higgs couplings relatively to their SM values. Current LHC measurements only marginally differ from the SM, but the situation might change in the future giving new relevance to these statements. Other than formulating these predictions we have compared the LHC data with our theoretical framework.

Fitting the data in a generic five parameter setting we found that interesting conclusions on tree-level mixings in the Higgs sector can be drawn. First we observed that the data tend to prefer the decoupling limit of the Higgs sector in the MSSM. However there is a strong correlation between the size of $\tan\beta$ and the vicinity of the theory to the decoupling limit. This was translated into an exclusion in the $(m_A, \tan\beta)$ plane of the MSSM, that is competitive with direct searches. These bounds hold in a large class of complete theories, where loop corrections to the Yukawa couplings are small. Then we obtained an upper bound on singlet mixing, $|\cos\phi| \lesssim 0.7$ at 95% C.L.

Furthermore we briefly commented upon direct searches for new particles in the supersymmetric Higgs sector. The relevant final states are expected to be rich in b-quarks and in the case of D-term models to be characterized by boosted topologies.

In conclusion we have shown that Higgs coupling measurements are an interesting probe of natural supersymmetry and that definite statements can be made also in complete theories. This opens a line of research complementary to direct searches that can be especially useful if supersymmetry is hiding in final states difficult to probe by the LHC.

---

[12]We have not elaborated on this point here. We refer to early 2HDM papers that pointed to the study of Higgs couplings to detect extra MSSM Higgses [207, 208]

Chapter 8

The Higgs in unnatural theories

> The unnatural, that too is
> natural.
>
> *Johann Wolfgang Von Goethe*

8.1 Introduction

We have seen that complete natural supersymmetric theories can be meaningfully tested against the data. In this chapter we show that there is at least one measurement, already performed at the LHC, that can rule out a large class of unnatural theories.

Currently $\sigma \times BR(h \to ZZ^*)$ and $\sigma \times BR(h \to WW^*)$ seem compatible with the SM, but there appears to be an enhancement in the diphoton channel $\sigma \times BR(h \to \gamma\gamma)$:

$$\mu_{\gamma\gamma} \;\; = \;\; \frac{\sigma \times BR(h \to \gamma\gamma)}{\sigma \times BR(h \to \gamma\gamma)_{SM}} \sim 1.5, \qquad (8.1.1)$$

$$\mu_{VV} \;\; = \;\; \frac{\sigma \times BR(h \to VV)}{\sigma \times BR(h \to VV)_{SM}} \sim 1. \qquad (8.1.2)$$

Of course the most likely possibility is that this modest excess will not survive further scrutiny since it is already diminishing now that CMS has released results on the full 2012 dataset. It is nonetheless interesting to contemplate the sorts of new physics that could be responsible for such a deviation in $\sigma \times BR(h \to \gamma\gamma)$ while leaving $\sigma \times Br(h \to ZZ^*, WW^*)$ essentially unaltered.

While it is possible, in principle, to satisfy equations (8.1.1-8.1.2) by only adjusting the tree-level couplings of the Higgs to SM particles, we find this possibility rather unlikely for the following simple reason. Assuming that the only modification is via the SM tree-level couplings, then for $m_h = 125$ GeV we have $\mu_{\gamma\gamma}^{(\text{tree})} \approx \left(1.28 - 0.28 \frac{r_t}{r_V} \right)^2 \times \mu_{VV}^{(\text{tree})}$, where r_t, r_V are the ratio of the couplings of the higgs to the top and the W/Z relative to the SM couplings. Now in order to

obtain, for instance, $\mu_{\gamma\gamma} = 1.5 \, \mu_{VV}$, there are two solutions: i. $(r_t/r_V) \approx 0.2$, or ii. $(r_t/r_V) \approx 9$.[1]
Both of these solutions are highly implausible: allowing an order of magnitude modification to the couplings, it is unlikely that the $\sim$126 GeV resonance found at the LHC should have production and decay rates that are all-in-all broadly consistent with the SM Higgs boson.

We conclude that equations (8.1.1-8.1.2) most likely require a loop contribution from new particles, enhancing $h \to \gamma\gamma$. Indeed, a large number of groups have explored this possibility, with additional scalars, vector-like fermions and gauge bosons of various types [254, 255]. Our purpose in this chapter is not to rehash these arguments, but to point out that such a large $\mu_{\gamma\gamma}$ has a profound implication for the deepest question that confronts us at the TeV scale and that inspired all the work in this thesis: Is electroweak symmetry breaking natural?

Natural theories of electroweak symmetry breaking are expected to have a plethora of new particles at the weak scale, associated with a solution to the hierarchy problem. Some of these particles could be responsible for the observed diphoton enhancement, though this does not automatically occur in the most minimal models. For instance among the minimal supersymmetric SM (MSSM) superparticles, a non-negligible effect can only naturally arise from very light charginos, but even pushing the relevant parameters to their limits one finds $\mu_{\gamma\gamma} \lesssim 1.25$ and, more typically, $\mu_{\gamma\gamma} < 1.1$ as seen in the previous chapter. Combining tree-level Higgs mixing with loop corrections from charginos and stops can boost $\mu_{\gamma\gamma} > 1.5$, but still keeps $(\mu_{\gamma\gamma}/\mu_{VV}) \lesssim 1.4$. Other possibilities, like e.g. light staus with extreme left-right mixing, can be realized [231, 232] but come at the cost of fine-tuning.

As is well-known, the concept of naturalness has been under some pressure from a variety of directions, and in the past decade new possibilities for physics beyond the SM have been explored. The idea is that the Higgs is fine-tuned to be light, as a less-dramatic counterpart to Weinberg's anthropic explanation of the smallness of the cosmological constant [6].

These models tend to be more constrained and predictive in their structure than many natural theories. The main reason is that arbitrary fine-tunings are not allowed; any fine-tuning should have a clear "environmental" purpose. If we consider a completely generic theory with many interacting scalars, fermions and gauge fields, a separate fine-tuning is needed for every light scalar. But additional scalars beyond the Higgs serve no "environmental" purpose. Thus in this framework we don't expect any new light scalars beyond the Higgs. Additional gauge fields would have to be higgsed by fine-tuned scalars[2], so we don't expect new gauge bosons either. Thus, this restricted class of fine-tuned theories can only include new fermions, with no new scalars or gauge fields, up to some scale $\Lambda_{UV} \gg$ TeV. As an example, in "minimally split" SUSY [94], we expect a loop factor splitting between scalars and gauginos. Here the cut-off of the effective theory Λ_{UV} is the mass of the heavy scalars, with 10 TeV $< \Lambda_{UV} < 10^3$ TeV.

Consider the diphoton enhancement in these theories. With the Higgs as the only new scalar, we cannot even entertain the possibility of tree-level modifications giving $r_V \neq 1$: this route is

---

[1]It is worth recalling that $r_V > 1$ can only be realized in models with doubly-charged scalars [254].

[2]We do not consider the possibility that additional gauge groups are broken by technicolor-like interactions while the SM gauge symmetry is broken by a fine-tuned Higgs.

not only implausible, but impossible. We could, in principle, modify r_t through fermion mixing. However, with $r_t \approx 0.2$ there would be no Higgs signal at all, whereas $r_t \approx 9$ would not be perturbative. Thus we can only rely on loop effects from new fermions with Yukawa couplings to the Higgs.

We can certainly imagine extra fermions near the TeV scale; a collection of fermions can have their masses protected by a common chiral symmetry and set by the same scale.

In what follows we show that restricting to unnatural models with only new fermions immediately leads us to a very narrow set-up with sharp theoretical and experimental implications: (1) new, vector-like, un-colored fermions with electroweak quantum numbers must exist and be very light, within the range $100 - 150$ GeV; (2) the cut-off scale of the theory where additional bosonic degrees of freedom must kick in, cannot be high and is in fact bounded by $\Lambda_{UV} \lesssim 1 - 10$ TeV. The cut-off can be somewhat increased but only at the expanse of significant model-building gymnastics, which further destroys any hope of perturbative gauge coupling unification.

8.2   The diphoton rate

A fermionic loop contribution enhancing the Higgs-diphoton coupling requires vector-like representations and large Yukawa couplings to the Higgs boson. This has important ramifications for the consistency of the theory at high scale. To see this, note that in the presence of a new fermion f with electric charge Q, the $h \to \gamma\gamma$ partial width reads[3]

$$\frac{\Gamma(h \to \gamma\gamma)}{\Gamma(h \to \gamma\gamma)_{SM}} \approx \left| 1 + \frac{1}{\mathcal{A}_{SM}^{\gamma}} Q^2 \frac{4}{3} \left(\frac{\partial \log m_f}{\partial \log v} \right) \left(1 + \frac{7\, m_h^2}{120\, m_f^2} \right) \right|^2, \qquad (8.2.1)$$

with $\Gamma(h \to \gamma\gamma)_{SM} = \left(\frac{G_F \alpha^2 m_h^3}{128\sqrt{2}\pi^3} \right) |\mathcal{A}_{SM}^{\gamma}|^2$ and $\mathcal{A}_{SM}^{\gamma} \approx -6.49$, as seen in the previous chapter. Constructive interference between the SM and the new fermion amplitude requires electroweak symmetry breaking to contribute negatively to the mass of the new fermion. Thus f must be part of a vector-like representation with an electroweak-conserving source of mass.

The basic building block is then the charged vector-like fermion mass matrix,

$$\mathcal{L}_M = - \left(\psi^{+Q}\ \chi^{+Q} \right) \begin{pmatrix} m_\psi & \frac{yv}{\sqrt{2}} \\ \frac{y^c v}{\sqrt{2}} & m_\chi \end{pmatrix} \begin{pmatrix} \psi^{-Q} \\ \chi^{-Q} \end{pmatrix} + \text{h.c.}, \qquad (8.2.2)$$

with the Higgs VEV given by $\langle H \rangle = v/\sqrt{2} = 174$ GeV. Equation (8.2.2) contains one physical phase, $\phi = \arg\left(m_\psi^* m_\chi^* y y^c \right)$, that cannot be rotated away by field redefinitions. It is straightforward to show that $\phi = 0$ maximizes the effect we are after, making $\phi \neq 0$ an un-illuminating complication for our current purpose. Hence for simplicity we assume $\phi = 0$ in what follows. We

---

[3]At leading-log plus leading finite-mass correction; see e.g. [255] for a recent discussion.

are then allowed to take all of the parameters in equation (8.2.2) to be real and positive. The two Dirac mass eigenvalues are split by an amount

$$m_2 = m_1 \left(1 + \sqrt{\Delta_v^2 + \Delta_y^2 + \Delta_m^2} \right), \quad \Delta_v^2 = \frac{2yy^c v^2}{m_1^2}, \quad \Delta_y^2 = \frac{(y - y^c)^2 v^2}{2m_1^2}, \quad \Delta_m^2 = \frac{(m_\psi - m_\chi)^2}{m_1^2} \quad (8.2.3)$$

Using equation (8.2.1) and assuming that the diphoton rate enhancement comes from changing the partial width $\Gamma(h \to \gamma\gamma)$, with no change to the gluon fusion production cross section, we have[4]

$$\mu_{\gamma\gamma} = \frac{\Gamma(h \to \gamma\gamma)}{\Gamma(h \to \gamma\gamma)_{SM}} \approx \left| 1 + 0.1 \, \mathcal{N} \, Q^2 \Delta_v^2 \left(1 + \sqrt{\Delta_v^2 + \Delta_y^2 + \Delta_m^2} \right)^{-1} \right|^2, \qquad (8.2.4)$$

where we generalized to $\mathcal{N}$ copies of (8.2.2). Noting the LEPII constraint $m_1 \gtrsim 100$ GeV, we immediately see that large Yukawa couplings are required in order to achieve a noticeable effect, at least for common charge assignments $Q^2 \leq 1$. Even if we maximize the effect by tuning $\Delta_m = \Delta_y = 0$ (via $m_\psi = m_\chi$, $y = y^c$), an enhancement of $\mu_{\gamma\gamma} \geq 1.5$ still requires $yy^c \geq \left(\frac{0.86}{\mathcal{N} Q^2} \frac{m_1}{100 \text{ GeV}} \right)^2$.

Before pursuing further the implications of equation (8.2.4), we pause to point out that we find it implausible for colored particles (either fermions or bosons, for that matter) to deliver the effect we are after. For colored fermions, the gluon fusion rate is approximately given by an equation similar to (8.2.1), but replacing $(4N_c Q^2/3\mathcal{A}_{SM}^\gamma) \to 2t_c$, where t_c and N_c are the Dynkin index and dimension. A diphoton width enhancement, $\Gamma(h \to \gamma\gamma)/\Gamma(h \to \gamma\gamma)_{SM} = |1 + \delta|^2$, would lead to a digluon effect $\mu_{GG} \approx |1 - 9.7(t_c/N_c Q^2)\delta|^2$, going through to the ZZ, WW channels as $\mu_{VV} \approx \mu_{GG}$. For scalars (vector bosons), we would simply rescale δ by a factor of $4 \left(-\frac{4}{21} \right)$, arriving at the same result. For example, $Q = 2/3$ particles in the **3** of color would give $\mu_{GG} \approx |1 - 3.6\,\delta|^2$. We have seen this already in the previous chapters while discussing stop corrections to the Higgs couplings.

To accommodate both of equations (8.1.1-8.1.2) in this case, one would need – similar to our discussion of tree-level solutions – to accept large distortions of the SM couplings that conspire to leave a moderately small net observable effect. In figure 8.1 we illustrate this point, by plotting $\mu_{\gamma\gamma}$ and μ_{GG} as a function of the diphoton amplitude modification δ, for $Q = 2/3$ particles. For uncolored particles (smooth) we have $\mu_{GG} = \mu_{VV} = 1$ and $\mu_{\gamma\gamma} = |1 + \delta|^2$, while for particles in the **3** of color (dashed) we have $\mu_{GG} = \mu_{VV} = |1 - 3.6\,\delta|^2$ and $\mu_{\gamma\gamma} = |1 + \delta|^2 |1 - 3.6\,\delta|^2$. It is obvious from the plot that substantial tuning is required for the colored solution to roughly satisfy equations (8.1.1-8.1.2). Note that while there are two separate colored solutions to $\mu_{\gamma\gamma} \sim 1.5 - 2$, one with $\delta \approx +0.5$ and one with $\delta \approx -0.15$, the former would imply some ZZ suppression, $\mu_{VV} \sim 0.6 - 0.8$, while the latter would greatly overshoot the SM value $\mu_{VV} \sim 2 - 3$. We therefore discard the possibility of colored particles for addressing the diphoton rate enhancement, at least for electric charge assignments $Q^2 \leq 1$.

We now turn our attention to equation (8.2.4) and to the large Yukawa couplings that it requires (given some reasonable assumptions about the sorts of multiplets we allow), in order to

---

[4]In equation (8.2.4), for clarity, we neglected sub-leading finite-mass terms that amount to $< 10\%$ correction for $m_f > 100$ GeV. However, we keep these terms in our plots.
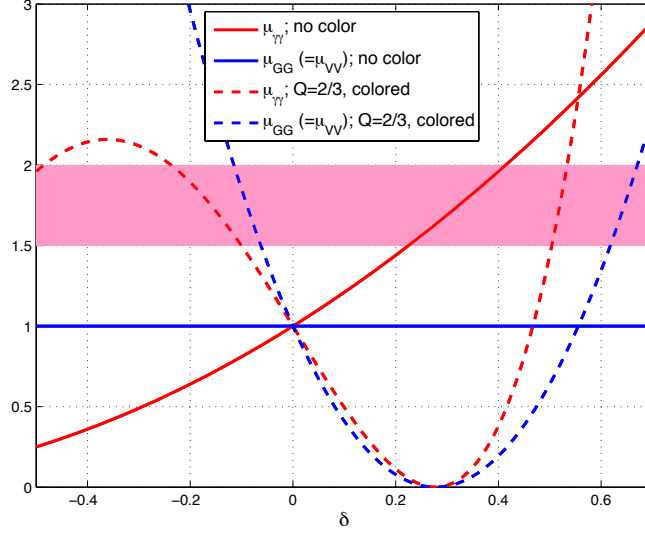
Figure 8.1: Uncolored (smooth lines) and colored (dashed lines) particles effects on $h \to \gamma\gamma$ and $h \to gg$ rates.

give an enhancement of $\mu_{\gamma\gamma} \sim 1.5 - 2$. In fact, the needed Yukawa couplings are so large that, unless the new particles are extremely light, the Higgs quartic coupling λ is rapidly driven negative at high scales. IIf we assume only fermions to be present up to an high scale, the addition of any other fermions only drives the quartic even more negative. Thus vacuum stability becomes an important constraint. At some scale Λ_{UV}, λ gets so negative that the tunneling rate through false vacuum bubbles of size Λ_{UV}^{-1} becomes less than the age of the universe. We define Λ_{UV} as the cut-off scale of the (unnatural) theory: here, new bosonic fields must kick in to cure the instability.

To substantiate these statements we consider two concrete examples. Our Higgs field transforms as $H \sim (1,2)_{\frac{1}{2}}$. It remains to assign $SU(2)$ representations to the fermions in equation (8.2.2).

Vector doublets + singlets ("vector-like lepton"): $\psi, \psi^c \sim (1,2)_{\pm\frac{1}{2}}$, $\chi, \chi^c \sim (1,1)_{\mp 1}$. The Lagrangian leading to (8.2.2) is

$$-\mathcal{L} = m_\psi \psi\psi^c + m_\chi \chi\chi^c + yH\psi\chi + y^c H^\dagger \psi^c \chi^c + \text{h.c.} . \qquad (8.2.5)$$

There are two charged Dirac fermions $L_{1,2}$ with masses $m_{L_{1,2}}$ ($m_{L_1} < m_{L_2}$), separated as in equation (8.2.3), and one neutral Dirac fermion N with mass m_ψ. Given $m_{L_{1,2}}$, we can compute both $\mu_{\gamma\gamma}$ and the coupling product (yy^c). Using y, y^c as initial conditions, we run the theory up in energy. The renormalization group equations (RGEs) are given in appendix E. In the left panel of

figure 8.2, we plot bands of constant $\mu_{\gamma\gamma}$ (pink) in the (m_{L_1}, m_{L_2}) plane. The width of the bands is obtained by varying Δ_m (see equation (8.2.3)) from zero to one. We also plot bands of Λ_{UV} in gray. In dark gray we tune $y = y^c$ and in pale gray we set $y = 2y^c$ (the same result is obtained for $y^c = 2y$).

Only a very small window of masses, 100 GeV$< m_{L_1} <$115 GeV and $m_{L_2} \gtrsim$ 430 GeV, is compatible with $\mu_{\gamma\gamma} > 1.5$ and $\Lambda_{UV} > 10$ TeV. Even allowing for $\Lambda_{UV} = 1$ TeV, the maximal lighter state mass compatible with $\mu_{\gamma\gamma} > 1.5$ is bounded by $m_{L_1} \lesssim 140$ GeV. The maximum possible value of $\mu_{\gamma\gamma}$ compatible with $\Lambda_{UV} > 1$ TeV is ≈ 1.8.

One can repeat the same exercise for larger $\mathcal{N}$. For instance, for $\mathcal{N} = 4$, we find that allowing for $\Lambda_{UV} = 10$ TeV, the maximal lighter state mass compatible with $\mu_{\gamma\gamma} > 1.5$ is bounded by $m_{L_1} \lesssim 200$ GeV.

Vector doublets + triplet ("wino-higgsino"): $\psi, \psi^c \sim (1, 2)_{\pm\frac{1}{2}}$, $\chi \sim (1, 3)_0$. We identify χ and χ^c; the Lagrangian leading to (8.2.2) is

$$-\mathcal{L} = m_\psi \psi\psi^c + \frac{1}{2}m_\chi \chi\chi + \sqrt{2}yH\psi\chi + \sqrt{2}y^c H^\dagger \psi^c \chi + \text{h.c.} . \qquad (8.2.6)$$

As in the "vector-like lepton" model, there are two charged Dirac fermions with masses m_l, m_h ($m_l < m_h$). Again, the relevant RGEs are given in appendix E. The results are depicted in the right panel of figure 8.2. The bounds on $\mu_{\gamma\gamma}$ are somewhat more severe than for the previous example, with $\Lambda_{UV} \geq 10$ TeV and $\mu_{\gamma\gamma} \geq 1.5$ only possible for $m_l < 105$ GeV. Allowing for $\Lambda_{UV} = 1$ TeV, the maximal lighter state mass compatible with $\mu_{\gamma\gamma} > 1.5$ is bounded by $m_l \lesssim 130$ GeV. The maximum possible value of $\mu_{\gamma\gamma}$ compatible with $\Lambda_{UV} > 1$ TeV is ≈ 1.75.

The "wino-higgsino" example also coincides with SUSY, where χ and ψ, ψ^c play the role of the wino and higgsinos. We show the SUSY result by green dashed lines (achieved by varying μ, M_2) in the right panel of figure 8.2. In this case y, y^c are limited by the gauge couplings $g\sin\beta, g\cos\beta \lesssim 0.5$, so the diphoton effect is modest, $\mu_{\gamma\gamma} \lesssim 1.2$.

The choice $y = y^c$ maximizes the value of Λ_{UV} for a fixed $\mu_{\gamma\gamma}$. This amounts to some fine-tuning of parameters: given $\mu_{\gamma\gamma}$, the product (yy^c) is essentially fixed and so the cut-off scale is very sensitive to mismatch $y \neq y^c$, as the Higgs quartic runs with $(d\lambda/dt) \propto y^4 + y^{c4}$. This result is clear in figure 8.2, where, already for mild splitting $y = 2y^c$, the pale gray band of $\Lambda_{UV} = 10$ TeV excludes $\mu_{\gamma\gamma} \gtrsim 1.4$.

Admitting large charge $Q^2 > 1$ would ameliorate the instability problem. For example, vector-like leptons with $Q = 2$, $\psi, \psi^c \sim (1, 2)_{\pm\frac{3}{2}}$, $\chi, \chi^c \sim (1, 1)_{\mp 2}$, can be tuned to provide $\mu_{\gamma\gamma} = 1.5$ with $\Lambda_{UV} = 10$ TeV and the lightest doubly-charged state at 300 GeV. Similarly, considering multiple copies of fermions, $\mathcal{N} > 1$, would increase the cut-off Λ_{UV} for a fixed $\mu_{\gamma\gamma}$ and fermion mass. The fact that Λ_{UV} rises with $\mathcal{N}$ can be understood as follows. If we rescale $\mathcal{N}$ at fixed $\mu_{\gamma\gamma}$ and mass m_{L_1}, the weak-scale initial condition for the Yukawa RGE changes roughly as $y_0^2 \to (y_0^2/\mathcal{N})$. Keeping only the y terms in the Yukawa RGEs we have $d(\mathcal{N}y^2)/dt \propto (\mathcal{N}y^2)^2$; hence the running

coupling ($\mathcal{N}y^2$) is approximately invariant under $\mathcal{N}$ rescaling. Including only the y^4 contribution in the running of the Higgs quartic λ, we now have $d\lambda/dt \propto (\mathcal{N}y^2)^2/\mathcal{N}$. As a result, the cut-off scale shifts roughly as $\Lambda_{UV} \rightarrow \Lambda_{UV}^{\mathcal{N}}$. In figure 8.3 we repeat our exercise of figure 8.2 with $\mathcal{N} = 2$ identical copies of vector like fermions. The maximal lightest fermion mass compatible with $\mu_{\gamma\gamma} = 1.5$ is somewhat larger than for $\mathcal{N} = 1$, but still not larger than ~ 150 GeV for $\Lambda_{UV} \gtrsim 10$ TeV.

Instead of doubling our basic "vector-like lepton" model, it is arguably more economical to add only vector-like $SU(2)$ singlets, or doublets, but not both. It is straightforward to show, however, that the vacuum stability constraint in this case is more severe than for $\mathcal{N} = 2$ copies of the full set-up. The reason is that the Yukawa and Higgs quartic RGEs in the two possibilities are the same, up to an un-important difference in the SM gauge beta functions, while the diphoton enhancement from the three resulting charged Dirac eigenstates cannot exceed that from the four eigenstates of $\mathcal{N} = 2$. A similar conclusion applies if we extend the "wino-higgsino" model by adding either extra triplets or extra doublets but not both.

Finally we return briefly to the possibility, explored in figure 8.1 and the corresponding discussion, that the diphoton enhancement is produced by colored particles. There, we argued in general that the colored solution inevitably involves fine tuning, regardless of the spin of the particle. For colored fermions, this possibility is also strongly constrained by vacuum stability, as it requires very large Yukawa couplings. Indeed, calculating the RGEs for a generation of vector-like up-type quarks[5], we find that imposing $\Lambda_{UV} > 1$ TeV implies $\mu_{\gamma\gamma} < 1$.

To conclude, a diphoton enhancement $\mu_{\gamma\gamma} = 1.5$ through a single vector-like set of fermions requires a light charged state with mass below 115 GeV, even when we allow a very low cut-off scale $\Lambda_{UV} = 10$ TeV for the theory and judiciously tune the parameters to maximize the effect by setting[6] $\phi = 0$, $\Delta_m = 0$, and $y = y^c$. Relaxing the parameter tuning slightly brings us down to the LEPII bound, excluding the model or, at best, implying that the numerical value of the mass is tuned. Extending the set-up to $\mathcal{N} = 2$ identical copies of vector-like fermions allows for slightly less precise parameter tuning (though the number of tuned parameters is doubled), but the lightest fermions must still lie below ~ 150 GeV for $\Lambda_{UV} \gtrsim 10$ TeV. Even allowing $\mathcal{N} = 4$ identical copies of vector-like fermions, the upper bound of the lightest fermions' masses only slightly increases to ~ 200 GeV for $\Lambda_{UV} \gtrsim 10$ TeV.

8.3   Collider signals and electroweak constraints

The light charged fermions discussed in the previous section are produced through electroweak processes with appreciable rates at hadron colliders. In this section we consider constraints and detection prospects from current and upcoming searches, assessing characteristic detection channels and providing rough estimates of the experimental sensitivity. We stress that our analysis is

---

[5]The field content we consider is $\psi \sim (3,2)_{\frac{1}{6}}$, $\psi^c \sim (\bar{3},2)_{-\frac{1}{6}}$, $\chi \sim (\bar{3},1)_{-\frac{2}{3}}$, $\chi^c \sim (3,1)_{\frac{2}{3}}$. See [256, 257, 258] for electroweak precision constraints on this field content, in the context of modified Higgs couplings.

[6]See equations (8.2.2-8.2.3) and the discussion between them for the definition of y, y^c, Δ_m and ϕ.
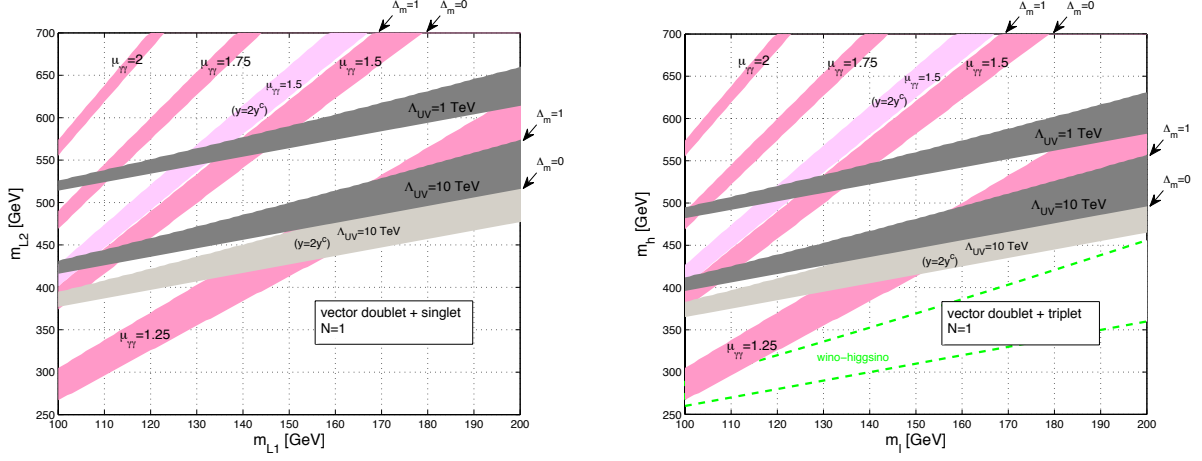
Figure 8.2: Left: "vector-like lepton" model. Right: "wino-higgsino" model. The horizontal and vertical axes correspond to the light and heavy mass eigenvalues, respectively. Pink bands denote the diphoton enhancement $\mu_{\gamma\gamma}$. Gray bands denote the vacuum instability cut-off Λ_{UV}. Dark is for $y = y^c$; pale is for $y = 2y^c$. The width of the bands (for both $\mu_{\gamma\gamma}$ and Λ_{UV}) correspond to varying the electroweak-conserving mass splitting term Δ_m (see equation (8.2.3)) from zero to one. Green dashed band, on the right, denotes the SUSY wino-higgsino scenario.
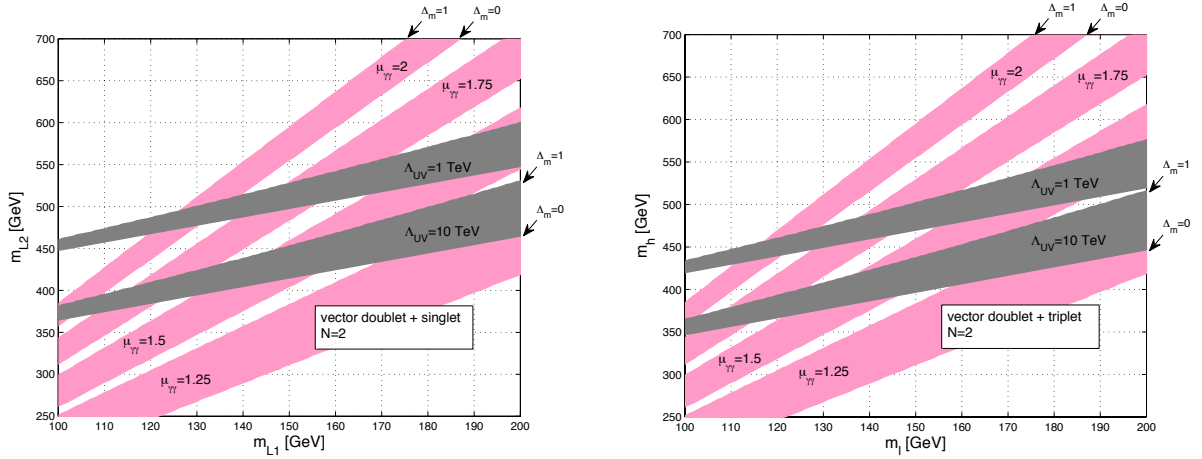
Figure 8.3: Same as figure 8.2, but for $\mathcal{N} = 2$ copies of vector like fermions.

simplistic, and can by no means replace a full-fledged collider study. Nevertheless, our estimates provide solid motivation and concrete guidelines for a more dedicated study in the future, should the diphoton enhancement be confirmed by upcoming data. We limit the discussion to a single set of vector-like fermions. We use the notation of our "vector-like lepton" example, for simplicity,

but most of the discussion also applies to the "wino-higgsino" model.

The most important production mode for $\mathcal{N} = 1$ is $pp \to L_1^+ L_1^-$. To calculate the production cross sections we use the FeynRules package [259] interfaced with MadGraph 5 [156]. In the left panel of figure 8.4 we plot $\sigma(pp \to L_1^+ L_1^-)$, in the "vector-like lepton" model, as a function of the lightest charged state mass, setting $y = y^c$ and $\Delta_m = 0$. Other cross sections are generically smaller, because of the mass gap that is required to enhance the Higgs diphoton coupling. For example, for $m_{L_1} = 100$ GeV, obtaining $\mu_{\gamma\gamma} = 1.5$ requires $m_{L_2} \geq 368$ GeV and $m_N \geq 234$ GeV, with $\sigma(pp \to L_1^\pm N) \approx 70$ fb, $\sigma(pp \to NN) \approx 29$ fb and $\sigma(pp \to L_1 L_2) \approx 5$ fb at the LHC with $\sqrt{s} =$ 7 TeV.

In the right panel of figure 8.4 we plot the cross section of the lightest charged state pair production in the "wino-higgsino" model. The cross section is much larger compared to the "vector-like lepton" case. The reason is that in the $y = y^c$, $\Delta_m = 0$ limit, where the singlet and doublet components are maximally mixed, the lightest charged state coupling to the Z boson is accidentally suppressed by a small factor $(4 \sin \theta_W^2 - 1) \approx 0.08$. Thus $pp(\bar{p}) \to L_1^+ L_1^-$ mainly goes through a photon. The cross section grows away from the $y = y^c$, $\Delta_m = 0$ limit, where the doublet component of the lightest state can be increased (at the cost of reducing the Higgs diphoton coupling), and the suppression is absent in the "wino-higgsino" model. Thus the left panel of figure 8.4 gives the rock bottom lower limit for the cross section expected in our scenario, while the right panel gives a rough upper limit.
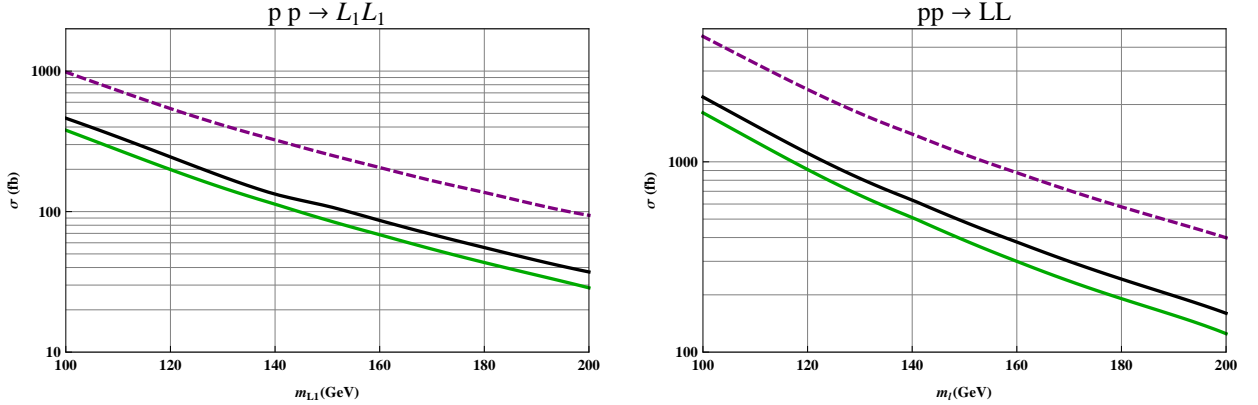

Figure 8.4: Left: $\sigma(pp \to L_1^+ L_1^-)$ as a function of the lightest charged state mass in the "vector-like lepton" model at the LHC7 (green, bottom), LHC8 (black, middle) and LHC14 (purple, top). Right: same, for the "wino-higgsino" model.

In our models, taken as they are, the lightest charged fermion is stable. For the masses of interest, however, this possibility is already excluded by searches for heavy stable charged particles (HSCPs) [260, 261]. It is easy to reach this conclusion by looking at the excluded cross section in the direct stau production case. The rather model independent cuts on the heavy particle p_T, time of flight and energy loss by ionization should retain a comparable efficiency on our signal.

We therefore consider two modifications of the minimal set-up:

(A)   It is always possible to add one or more extra SM singlets n ("sterile neutrino" or "bino" in the "vector-like lepton" and "wino-higgsino" models, respectively), with Yukawa couplings $\mathcal{L} = -y_n H^\dagger \psi n - y_n^c H \psi^c n + \text{h.c.}$ and mass term $\frac{1}{2} m_n nn$. Mixing with the $SU(2)$ component, N, makes room for a neutral state, n_1, with mass below that of the charged L_1. This opens up the decay mode $L_1 \to W^{(*)} n_1$, where the W boson can be on- or off-shell depending on the mass splitting between L_1 and n_1.

(B)   Alternatively, a small mass mixing with the SM leptons would induce decays such as $L_1 \to Zl(\tau)$ and $L_1 \to W\nu$, where $l \equiv e, \mu$ and $\nu \equiv \nu_e, \nu_\mu, \nu_\tau$. Constraints on the flavor changing processes $\mu \to e\gamma$ and $\tau \to e\gamma$ limit the mixing angles to $|U_{eL} U_{\mu L}| < 10^{-4}$ and $|U_{eL} U_{\tau L}| < 10^{-2}$ [230]. Additional constraints arise from LEP measurements of the Z widths to leptons [230], that are roughly known to ~ 1 part in 10^4 for each of the three generations. We thus require conservatively $|U_{iL}| \lesssim 10^{-2}$ for $i = e, \mu, \tau$. Note that as long as a mixing angle is bigger than $\sim 10^{-4}$, the decay is prompt[7].

In case **(A)**, the main signature is the pair production of two charged particles decaying to $W^{(*)} W^{(*)} + ME_T$, depicted in the left panel of figure 8.5. The closest result we have from the LHC is a 7 TeV ATLAS analysis targeting final states with two leptons and ME_T [268]. After the full selection in [268], in the m_{T2} signal region an efficiency ranging between 1% and 7% is observed for a signal consisting of chargino pair production, while the measured range for slepton pair production is lower. We take the same efficiency on our signal as that measured in the chargino case. Note that this is only an order of magnitude estimate, as the decay chains are not identical.

The limit on the cross section (that takes into account the WW leptonic branching ratio) from the ATLAS m_{T2} signal region (all flavor combined channel) is 42 fb. This should be compared with the cross sections in figure 8.4 multiplied by the efficiency assumed above. We find that in the "vector-like lepton" case there is not enough sensitivity to probe cross sections comparable to ours, while for large enough mass splittings between L_1 and n_1 (efficiency $\sim 7\%$) we can already exclude the interesting mass range in the "wino-higgsino" model ($m_l \lesssim 140$ GeV) and it is likely that the LHC will be sensitive to the "vector-like lepton" model by the end of the year ($\sigma \times \epsilon \approx 31(7)$fb for $m_{L_1} = 100(140)$ GeV).

Note that the minimum mass splitting between chargino and LSP considered in the analysis above is always greater than 75 GeV. In our case, decreasing the splitting between m_{L_1} and m_{n_1}, ME_T and m_{T2} cuts quickly loose efficiency and eventually even final state leptons become too soft to be triggered. The only experimental handles in this case are monojet and monophoton $+ ME_T$ searches [269, 270, 271, 272, 273, 274, 275], that can also detect the pair production of the lightest

---

[7]Searches for displaced vertices and long lived particles decaying inside the detector are currently ongoing at the LHC (see for example [262]) and were performed at the Tevatron [263, 264, 265, 266, 267], but there is still no systematic coverage of all the possible lifetimes and final states. We will ignore this possibility in what follows, even though experimentally it is intriguing and could be the subject of a dedicated study.

neutral state. Current searches are beginning to probe colored particle production cross sections for masses in the few hundred GeV range, not having yet sensitivity to electroweak production. Translating current limits on new signals is a non-trivial task in the monojet case, due to the large uncertainties on the simulation of ISR [276] and it is even harder to make predictions for the near future. However it was estimated that the discovery reach of the 14 TeV LHC is about 200 GeV for a gaugino LSP and that masses around 120 GeV can be probed already with 10 fb^{-1} if systematic uncertainties are kept under control [277, 278, 279]. Monojet estimates must be taken with caution, for the reasons mentioned above, but it was also shown that at the LHC an ISR jet has often a companion in the event. Therefore the results from a second channel with two jets and ME_T can be combined with the monojet searches to further increase the sensitivity. Attempts in this direction have already been made and the CMS "razor" analysis [280] was shown to have a comparable sensitivity to dark matter production to that of monojet searches [276, 281].

In case **(B)**, several different processes lead to multi-lepton final states with little hadronic activity. This scenario is depicted in the middle panel of figure 8.5. The CMS multilepton search [282] is currently the most sensitive to final states with low ME_T, and can already exclude a large fraction of the relevant parameter space. Here, for simplicity, we consider a few decay modes in single exclusive channels. If we take, for example, BR($L_1 \rightarrow Z + l$) $\approx$ 100%, and assume a flat 70% efficiency times acceptance for each of the four leptons[8], then we find that our two models are excluded in the relevant parameter space ($m_{L_1} \lesssim$ 200 GeV). This estimate was made using a standard CL$_s$ technique described in appendix F from a single channel $4l$ with S_T < 300 GeV and a Drell-Yan lepton pair from a Z decay. The limits are weaker for $L_1 \rightarrow Z + \tau$. In this case we are sensitive to the "vector-like lepton" model only up to $m_{L_1} \approx$ 104 GeV, while we are sensitive to masses up to $\approx$ 155 GeV in the "wino-higgsino" one. Again this estimate was obtained by looking at a single channel: $3l + 1\tau_h$[9] with S_T < 300 GeV and a Drell-Yan lepton pair from a Z decay. It is clear that the rest of the relevant parameter space can easily be covered by the end of the year and that, combining different channels and possibly results from the two experiments, the sensitivity would be increased, covering also more generic scenarios in which the branching ratio to these final states is not exactly one.

In summary, for $\mathcal{N} = 1$, an L_1 decaying to SM leptons is either already ruled out or within reach of a dedicated 8 TeV search (we have never taken advantage of the combination of multiple channels). If, instead, $L_1 \rightarrow W^* n_1(\nu)$ dominates, the relevant final state is $WW+ ME_T$ from $L_1 L_1$ production, which is still unconstrained for the "vector-like lepton" model and for which we await an 8 TeV update that could start to probe the relevant parameter space. In the worst case, when L_1 and n_1 are nearly degenerate in mass, the monojet searches will be able to exclude the relevant parameter space at the 14 TeV LHC. In the latter case, other interesting channels,

---

[8]From [283] we get an efficiency of the kinematical cuts $\sim$ 0.87. Taking into account the finite acceptance (somewhat optimistically) we obtain the final 0.7 [284]. Notice that this is a huge simplification of the experimental set-up that does not even distinguish between electrons and muons, and is thus only intended to give an order of magnitude estimate.

[9]Assuming an hadronic tau identification efficiency, for the HPS algorithm used in the CMS paper, $\epsilon_{\tau_h} = 0.35$ [285, 286, 287, 284] and the same 0.7 efficiency as before for any extra lepton.

especially for $\mathcal{N} > 1$, would be the $WWW + ME_T$ and, to a lesser extent, $WZ + ME_T$ final states arising from the production of $L_1 N$ as depicted in the right panel of figure 8.5. Dedicated analyses, beyond the scope of this paper, would improve the current sensitivities for some of the channels[10]. For our purpose here it suffices to show that if the enhancement of the $\gamma\gamma$ rate will be confirmed and an unnatural theory is responsible for it, then we expect the new fermions involved to be detected in the next few years, or even months.
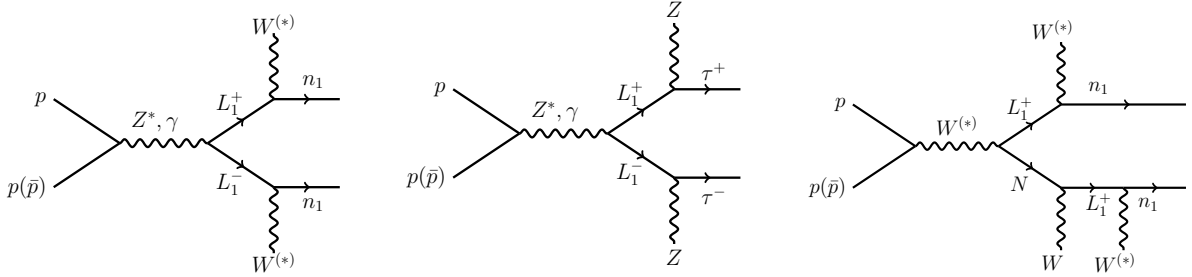
Figure 8.5: Feynman diagrams for new fermion production and decay.

Finally, in addition to direct searches, light non-singlet fermions are constrained indirectly by electroweak precision tests (EWPTs), especially so given the need for a large electroweak breaking mass to affect $\mu_{\gamma\gamma}$. Indeed, specializing to the "vector-like lepton" example[11], in the minimal field content specified by equation (8.2.5), we find that $\mu_{\gamma\gamma} > 1.5$ comes along with a sizable T parameter, whereas $\mu_{\gamma\gamma} > 1.75$ would be firmly excluded. Nevertheless, the tension with EWPTs can be tuned away by means of additional free model parameters. For instance, mixing with a neutral singlet n, as discussed earlier, produces an opposite contribution to T that can bring the model back to life even for $\mu_{\gamma\gamma} = 2$. Since this counter effect relies, again, on sizable Yukawa couplings y_n, y_n^c, it comes at the cost of lowering somewhat further the instability cut-off Λ_{UV}.

In figure 8.6 we illustrate this behavior by computing S and T, following [289] and performing the EWPT fit for $m_h = 125$ GeV [290]. In the left panel, we indicate with a green shaded area the 95%CL EWPT exclusion region in the (m_{L_2}, x_n) plane. Here, x_n is defined in analogy with equation (8.2.3) as $x_n^2 = (2y_n y_n^c v^2 / m_{n_1}^2)$, where m_{n_1} is the lighter neutral state mass, and m_{L_2} is the mass of the heavier charged state. We set $m_{L_1} = 100$ GeV, $y = y^c$, $y_n = y_n^c$ and $m_\psi = m_\chi = m_n$. Also plotted are the diphoton enhancement (pink) and values of Λ_{UV} (gray). In reading the plot, note that walking on the horizontal axis towards larger m_{L_2} is equivalent to walking up on the left edge of the left panel of figure 8.2. We see that with some neutral mixing, it is possible to tune away the tension with EWPTs, even for large $\mu_{\gamma\gamma}$. In the right panel of figure 8.6 we show on the $S - T$ ellipse three sample model points, marked correspondingly on the left.

---

[10]It is sufficient to think about possible three-lepton resonance searches or monojet searches with the additional requirement of soft leptons in the final state [279].

[11]We expect similar results to hold for the "wino-higgsino" model, as can be deduced e.g. from [288].
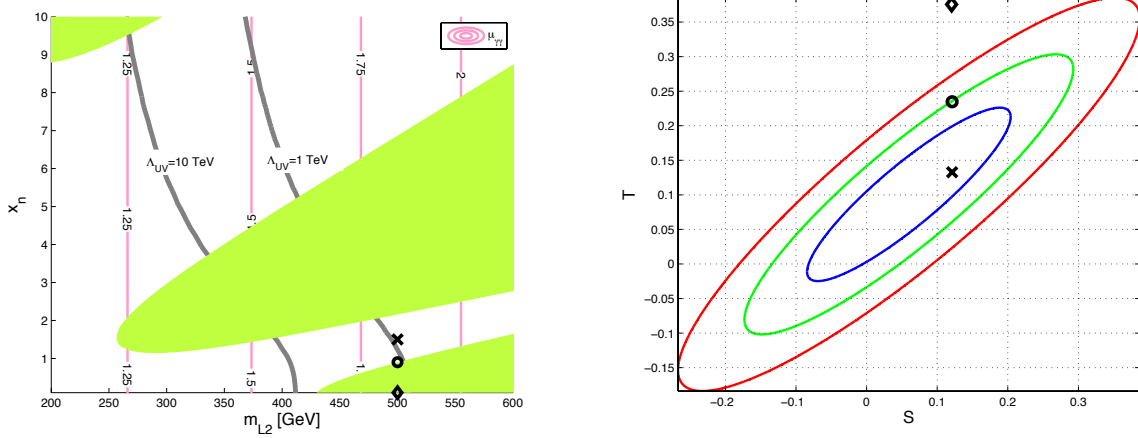
Figure 8.6: Electroweak constraints for the "vector-like lepton" model. Left: contours of $\mu_{\gamma\gamma}$ (pink) plotted in the (m_{L_2}, x_n) plane, where m_{L_2} is the heavier charged state mass and x_n is defined in analogy with equation (8.2.3) as $x_n^2 = (2y_n y_n^c v^2/m_{n_1}^2)$, with m_{n_1} the lighter neutral state mass. Gray lines denote the vacuum instability cut-off Λ_{UV}. The green filled area is excluded at 95%CL or more by EWPTs. The lighter charged fermion mass is fixed to $m_{L_1} = 100$ GeV. Right: Markers show the model position with respect to the $S - T$ error ellipse, for three sample points in the left panel. Blue, green and red lines denote the 68.27% C.L., 95% C.L. and 99.73% C.L. ranges.

8.4 Conclusion

For a single set of new vector-like fermions, with large enough Yukawa couplings to give an enhancement of $\mu_{\gamma\gamma} = 1.5$, demanding that the tunneling rate through false vacuum bubbles of size $\Lambda_{UV}^{-1} \sim (10 \text{ TeV})^{-1}$ is less than the age of the universe requires the existence of a new, un-colored, charged fermion lighter than about 115 GeV. Even with a very low cut-off scale, $\Lambda_{UV} = 1$ TeV, an enhancement of $\mu_{\gamma\gamma} = 2$ is impossible.

A larger number $\mathcal{N}$ of fermions allows us parametrically to keep a large enhancement for $\mu_{\gamma\gamma}$ while ameliorating vacuum stability. It is in principle possible, though contrived, to get $\mu_{\gamma\gamma} = 1.5$ while deferring the instability scale to $\Lambda_{UV} \sim 10$ TeV, but even for $\mathcal{N} = 2(4)$ this requires the fermions to be lighter than 150 (200) GeV.

Furthermore the cases with large $\mathcal{N}$ are in great tension with any picture of gauge coupling unification in the ultraviolet. Let us look at theories which add vector-like matter to split SUSY. One of the main motivations for split SUSY is maintaining supersymmetric gauge coupling unification, but it is easy to see that this feature is lost with a large number of multiplets. Consider the case where the new vector-like matter is in complete multiplets of $SU(5)$. The "vector-like lepton" fit inside a full generation + antigeneration; $\mathcal{N} = 1$ of these multiplets are consistent with perturbative gauge coupling unification, but $\mathcal{N} > 1$ are not. Similarly, the "wino-higgsino"

multiplet can fit in a **24** of $SU(5)$, and again only $\mathcal{N} = 1$ is (marginally) consistent with perturbative unification. We can even go as far as to consider complete multiplets of $SU(3)^3/Z_3$. The multiplet $(3,1,1) + (1,3,1) + (1,1,3)+$ conjugate contains exactly stable uncolored fractionally charged particles; these could give a diphoton enhancement but are forced to be so heavy by HSCP searches that the required Yukawa couplings are too large to be consistent with vacuum stability even for $\mathcal{N} = 1$ multiplet. The usual matter multiplet $(3,\bar{3},1) + (1,3,\bar{3}) + (\bar{3},1,3)+$ conjugate is too large even for $\mathcal{N} = 1$. Finally we can consider $(8,1,1) + (1,8,1) + (1,1,8)$; this contains both the "vector-like lepton" and "wino-higgsinos". But again gauge coupling unification restricts us to having at most one of these multiplets. We conclude that in any reasonable picture preserving perturbative gauge coupling unification, we can have either $\mathcal{N} = 1$ "vector-like lepton" or "wino-higgsino", or at most one of each.

We thus conclude that even non-minimal unnatural theories at the weak scale can not explain a large $\mu_{\gamma\gamma}$, unless they have new charged fermions lighter than about $115 - 150$ GeV. These charged fermions are so light that in most cases they should be possible to exclude or discover with the 2012 LHC data. If such light states are not discovered, and at the same time a large enhancement $\mu_{\gamma\gamma} \sim 1.5$ persists, then there must be new scalars or gauge bosons far beneath the 10 TeV scale. The CMS results is now approaching the SM value, but it is not inconceivable that the result will change in the future. In that case an enhanced diphoton rate could be the harbinger of natural electroweak symmetry breaking within reach of the LHC. Alternately, fine-tuned theories such as split SUSY or any of its variants unambiguously predict that the hint for an enhanced diphoton rate and unaffected ZZ rate in the current data must disappear.

Conclusion

Particle physics has been deeply changed by the first three years of LHC operations. The wealth of data produced can not be ignored and will dominate the field for the years to come. This is pushing the theoretical and experimental communities to collaborate more closely. However it is still extremely rare to find theorists that have hands-on experience with the data or experimentalists familiar with all the most relevant theoretical scenarios for new physics at the LHC. Nonetheless there are fundamental questions that need both a good understanding of theory and a good understanding of experiment to be answered. This work addresses one of them: Is electroweak symmetry breaking natural?

It is clear that the path towards an answer requires an effort in the two fields and this thesis is a product of experience gained in both. The two aspects are interconnected, but the thesis is organized into three parts to roughly reflect the division: introduction, experiment and theory.

In the second part we have described a direct search for natural theories. In chapter 3 we have seen that the LHC has not yet excluded natural supersymmetric models, but the reach at 14 TeV will be enough to say the final word on the MSSM with roughly 10% tuning. At the same time we have discussed some generic features of natural theories that led us to consider regions of parameter space that are still relatively unexplored. Therefore we have designed a search capable of covering natural signatures with low ME_T and described it in chapter 6. We did not find any significant excess and interpreted the result in a particular realization of RPV natural SUSY [118] obtaining a lower bound on the gluino mass: $m_{\widetilde{g}} > 1$ TeV. The bound assumes $\mathrm{BR}\,(\widetilde{g} \to tbs) = 100\%$. Clearly the search is much more general than its interpretation and should be repeated at 14 TeV to contribute to a definite answer on naturalness in supersymmetric (and to a lesser extent also non-supersymmetric) theories.

In the third part of the thesis we have adopted a different approach to the question of naturalness, studying Higgs boson couplings. In chapter 7 we have shown that sharp predictions can be made in natural supersymmetric models, in spite of the large number of free parameters. For instance $h \to b\bar{b}$ in associated production can not exceed its SM rate by more than 1.5 and a similar upper bound can be obtained for the ratio of $h \to \gamma\gamma$ and $h \to VV$ in gluon fusion production. We have found that Higgs coupling deviations can be described in terms of only five parameters with limited numerical ranges in vast classes of supersymmetric models (MSSM, MSSM+ extra D-terms, NMSSM, ...). This allowed to meaningfully test the theories against current LHC measurements. The most interesting result is a mass exclusion for heavy Higgses in

the MSSM, which at moderate $\tan \beta$ ($\lesssim 5$) is more stringent than the one emerging from direct searches. In chapter 8 we have extended the discussion to unnatural theories, identifying a simple measurement (that of the ratio between $h \to \gamma\gamma$ and $h \to VV$) that, together with direct searches, can exclude all models that add to the SM only extra fermions.

In conclusion, we have addressed the question of naturalness at the LHC by proposing new techniques that can shed light on the tuning of the Fermi scale. It is not yet possible to give a conclusive answer, but exciting times await us at the beginning of the 14 TeV run.

Acknowledgements

Appendix A

More on the reliability of the background prediction

We have seen that the MC prediction for the shape of the b-tagged jets multiplicity is in good agreement with the data, even including only the systematic error due to the b-tagging SFs. However these SFs have been derived in topologies different from our signal regions. For this reason we study in more detail the dependence of the tagging efficiency and of the shape of N_b^{jets} on the number of jets in the event. We also show that the predictions are not affected by the lepton flavor in the final state and that other observables (such as jet multiplicity, H_T and ME_T) are well reproduced by the MC in the signal regions.

A.1 Jet multiplicity and b-tagging efficiency

The N_b distributions for lower jet multiplicities ($= 4$ and $= 5$) are in figure A.1 and A.2 for muons and electrons, respectively. Note that contrary to the signal regions plots in chapter 6 the figures display the ratio of MC over data, rather than data over simulation. The $= 4$, $= 5$ jets selections provide good control regions, as can be seen from the signal efficiencies in figure A.3. The efficiencies are not completely negligible, but by comparing them to the signal regions (in figure 6.1), taking into account also the background yields, it is clear that anything that would disturb the $= 4$ and $= 5$ jets control regions would disrupt completely the data-MC shape agreement in the signal regions, showing up as a huge signal. This can also be seen *a posteriori*, from the exclusion limit in figure 6.8. For gluino masses that would give a contamination of more than a few % (i.e. $m_{\widetilde{g}} \lesssim 500$ GeV) we exclude a cross-section at least two orders of magnitude smaller than that of the signal.

The good agreement between data and SF corrected MC, together with the very mild dependence (well within the SF error) of the b-tagging efficiency on the number of jets in the event (displayed in figure A.4) support the claim that we are correctly describing the shape of N_b in our signal regions. Using the same SFs at $= 4$, $= 5$, $= 6$, $= 7$ and ≥ 8 jets we always obtain that
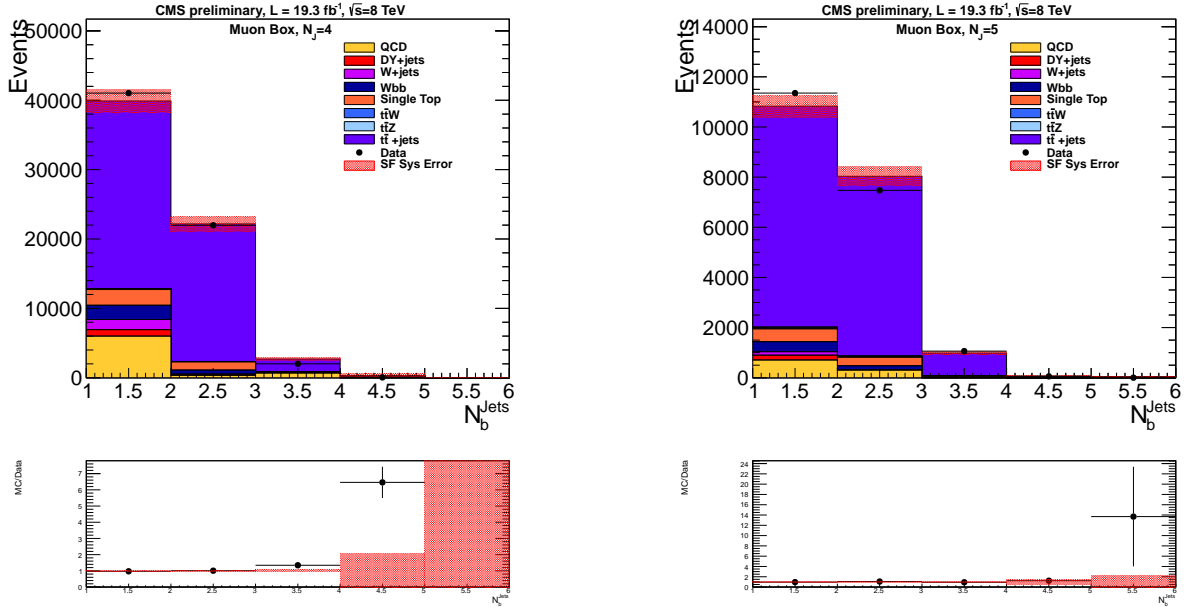
Figure A.1: Distribution of the number of b-jets , in the muon box, after applying the baseline selection (excluding the cut on the number of jets) and rescaling the Monte Carlo using the b-tagging scale factors, for = 4 (left) and = 5 jets (right). The red band in the figures corresponds to the systematic error obtained varying the scale factors by $\pm 1\sigma$.

the data are well reproduced by the MC, in general within the SF error alone (not including JES, matching, renormalization and factorization scale uncertainties). The bin with 1 and 2 b-tags in the electron 4 jets control region are an exception, but are well within the total systematic error, as can be seen from table B.5 in appendix B. The only significant discrepancy between data and MC that we find is a MC overprediction in the bins with 3 and 4 b-tags at four jets. This effect is still within the total error, but manifest itself both in the muon and electron box and, in a different way, also in the dilepton control control region presented in section 6.6. We parametrize these discrepancies as a mismodeling in the MC of the fraction of 4 b events and include it as a systematic uncertainty, as discussed in section 6.6.

A.2 Electron and muon samples

In this section we show that the shape of the N_b distribution does not depend on the lepton in the final state. This might not emerge immediately from the plots in section 6.5, but becomes clear thanks to figure A.5. There we show the ratios between the shapes of the distributions in the two channels for the three signal regions. The errors are statistical only, since systematic effects in the
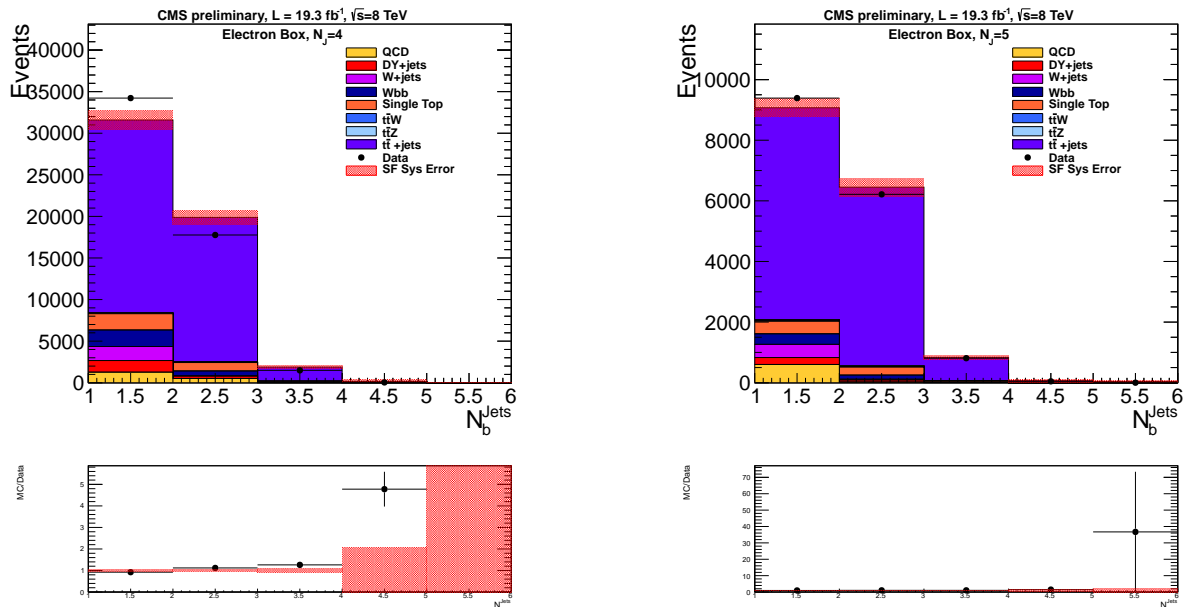
Figure A.2: Distribution of the number of b-jets, in the electron box, after applying the baseline selection (excluding the cut on the number of jets) and rescaling the Monte Carlo using the b-tagging scale factors, for = 4 (left) and = 5 jets (right). The red band in the figures corresponds to the systematic error obtained varying the scale factors by $\pm 1\sigma$.

MC cancel in the ratio. The χ^2 for the comparison of the ratios with 1 are

$$
\begin{aligned}
\chi^2/\text{ndof}\,, &\quad \text{Data}\,, &\quad 6\text{J}: 0.43 &\quad 7\text{J}: 1.3 &\quad 8\text{J}: 1.2 \\
\chi^2/\text{ndof}\,, &\quad \text{MC}\,, &\quad 6\text{J}: 0.62 &\quad 7\text{J}: 0.12 &\quad 8\text{J}: 0.54
\end{aligned}
\tag{A.2.1}
$$

This further check shows that we are not neglecting a possible additional systematic effect related to the mismodeling of the lepton efficiencies.

A.3   Additional Data-MC comparisons

In figures A.6 and A.7 we collect Data-MC comparisons plots for jet multiplicity, H_T and ME_T for events passing the baseline selections. We observe a generic good agreement within the JES error alone. The only exceptions are the high jet multiplicity bins that tend to be slightly overpredicted by the MC. This does not influence our analysis, since at a fixed jet multiplicity we take the total yield from data.
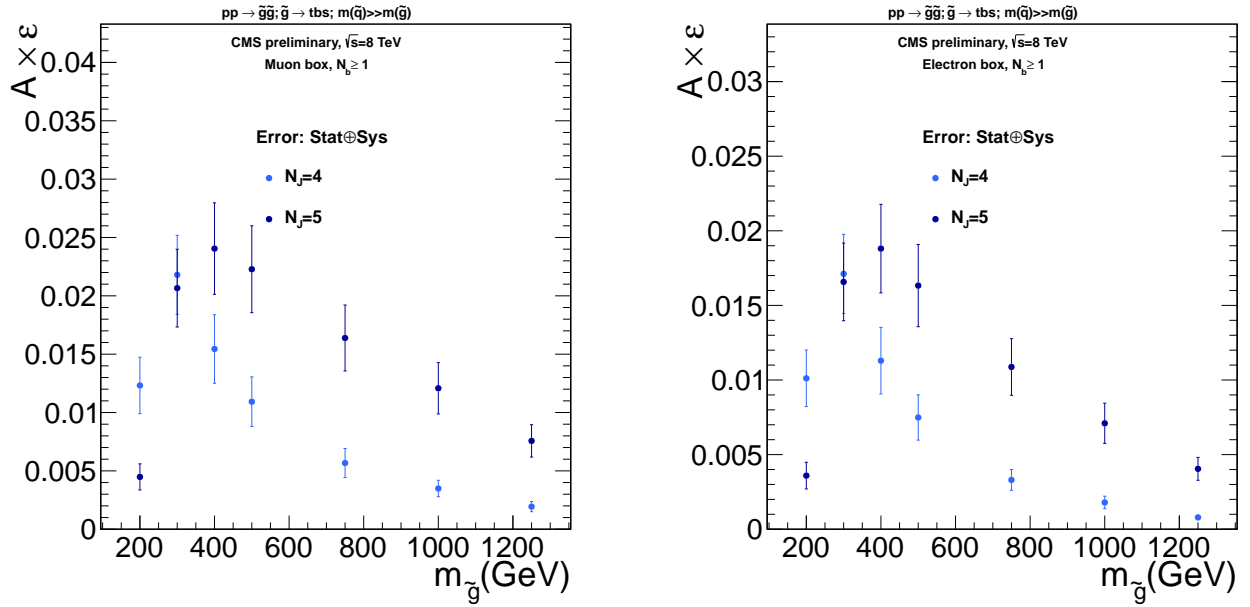
Figure A.3: Signal efficiency as a function of the gluino mass for the $\tilde{g} \to tbs$ RPV simplified model. Left(Right): after the muon(electron) baseline selection for events with exactly 4 jets (light blue), 5 jets (dark blue). The error includes both statistics and systematics, excluding the PDF uncertainty.
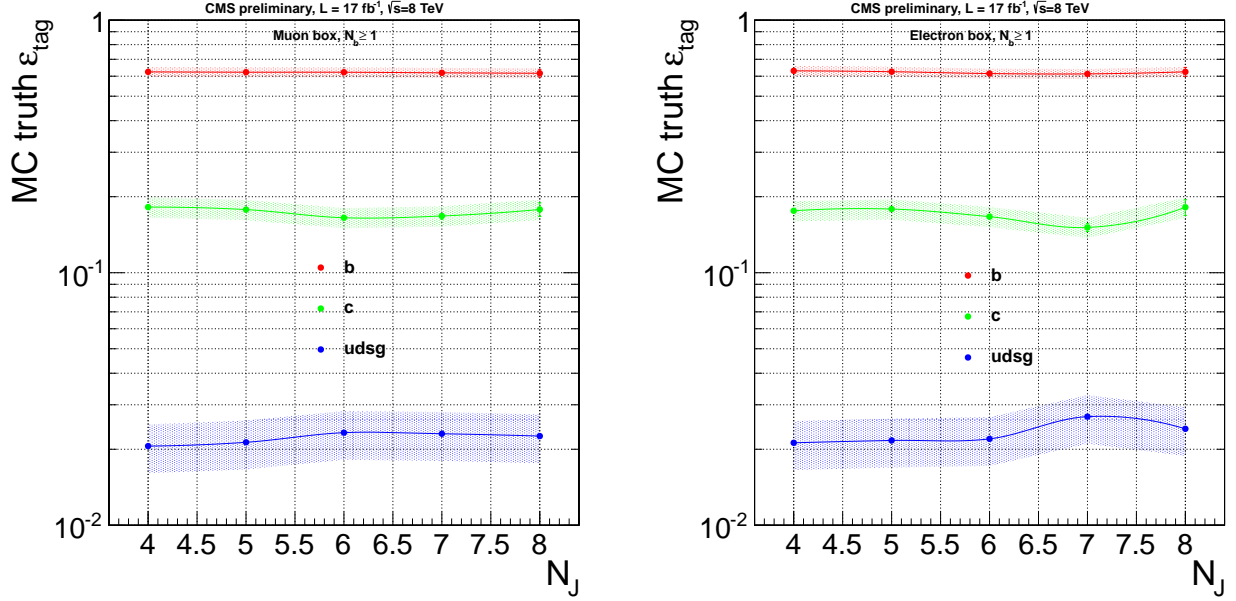
Figure A.4: Uncorrected MC truth tagging efficiency versus number of jets in the event for b (red), c (green) and *udsg* (blue) jets in the muon box (left) and electron box (right). The systematic band corresponds to a SF error obtained averaging over all p_T and η bins.
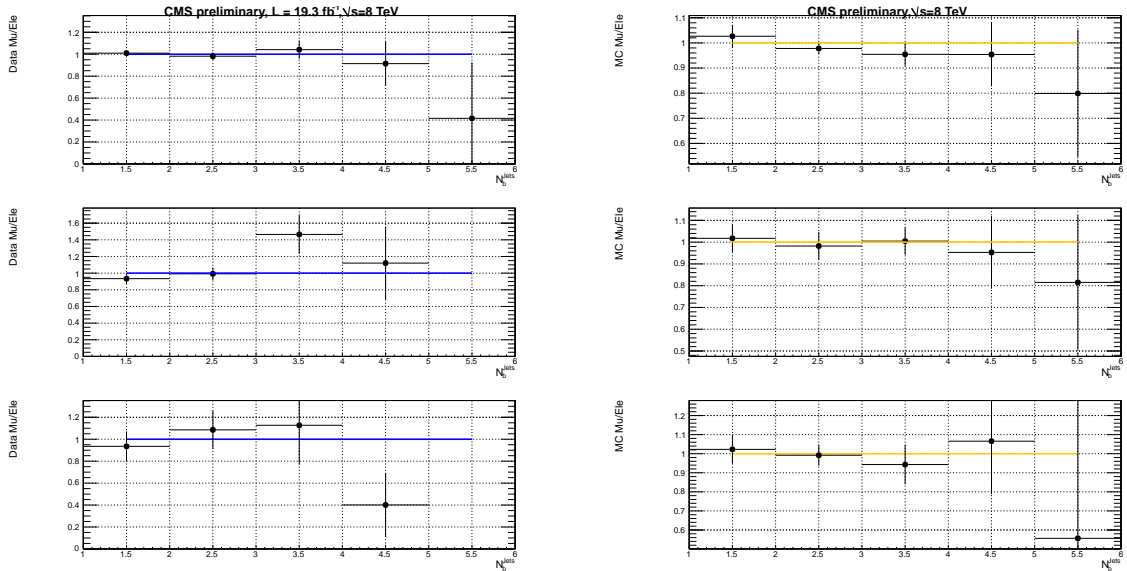

Figure A.5: Left: Ratio between the shapes of the N_b distributions in data in the muon and electron channel, for 6 (top), 7 (center) and ≥ 8 (bottom) jets in the final state. Right: Same for the MC simulation.
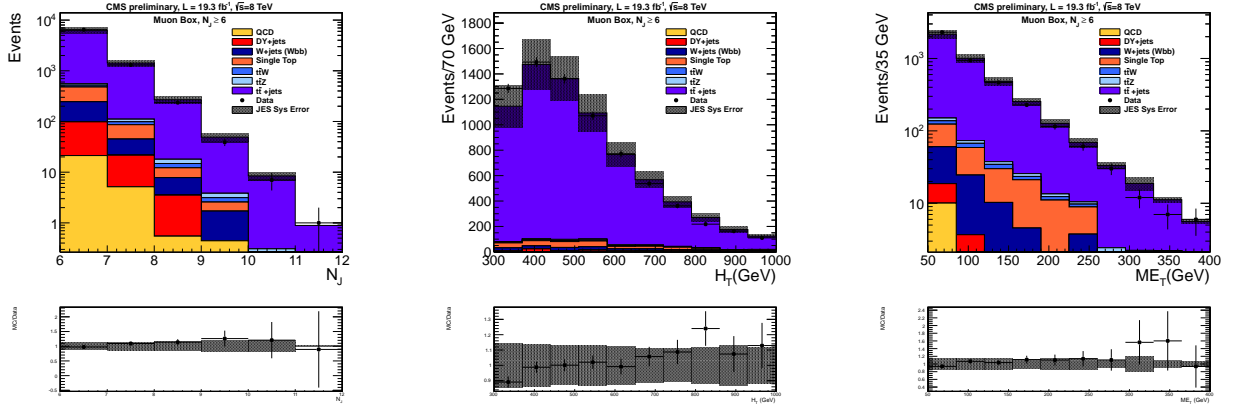
Figure A.6: Data-MC comparisons for jet multiplicity (left), H_T (middle) and ME_T (right) for events passing the muon baseline selection. The black band is the JES systematic uncertainty.
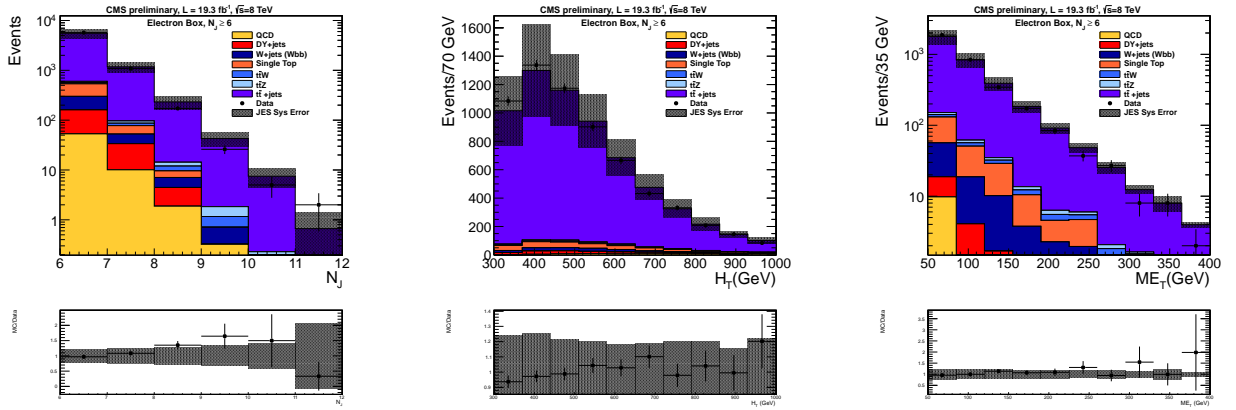

Figure A.7: Data-MC comparisons for jet multiplicity (left), H_T (middle) and ME_T (right) for events passing the electron baseline selection. The black band is the JES systematic uncertainty.

Appendix B

Control regions predicted and observed yields

In this appendix we list for completeness the predicted and observed yields in the control regions used to estimate the gluon splitting systematic for the analysis presented in chapter 6. The dilepton control regions always contain a well identified and isolated electron and a muon. The single lepton control regions contain either an electron or a muon and veto the presence of extra "tight" leptons. The yields for the dilepton control regions with 4 and 5 jets are in tables B.1 and B.2, respectively. The single muon and single electron results can be found in tables B.3 to B.6. The error does not include the gluon splitting systematic that was estimated from these control regions. The symbol ₋ in the tables stands for zero predicted events with zero systematic error and a Poisson uncertainty of $-\log(0.12) \approx 0.5$ that we round up to 1.

EleMu + 4 jets	1 bjet	2 bjet	3 bjet	4 bjet	5 bjet
$t\bar{t}$ + jets	367±173	288±81	21±15	2.2±3.5	₋
W+jets	8.4±8.4	₋	₋	₋	₋
$Wb\bar{b}$	0.85±0.52	₋	₋	₋	₋
$t\bar{t}W$	4.69±0.46	3.29±0.39	0.49±0.12	0.000±0.020	₋
$t\bar{t}Z$	2.88±0.30	2.14±0.21	0.41±0.12	0.028±0.030	₋
DY+jets	2.9±1.7	₋	₋	₋	₋
SingleTop	15.6±3.6	7.3±2.2	1.210±0.49	₋	₋
QCD	₋	₋	₋	₋	₋
Total MC	402±174	301±82	23±15	2.2±3.6	₋
Data	415	275	34	5	0

Table B.1: Predicted and observed event yield for different b-jet multiplicities and exactly 4 jets, in the ele-mu control region defined in section 6.6.

EleMu + 5 jets	1 bjet	2 bjet	3 bjet	4 bjet	5 bjet
$t\bar{t}$ + jets	91±48	75±38	8.8±3.9	0.83±0.39	0.46±0.54
W+jets	–	–	–	–	–
$Wb\bar{b}$	0.22±0.35	–	0.31±0.28	–	–
$t\bar{t}W$	1.54±0.28	1.13±0.19	0.144±0.069	0.000±0.022	–
$t\bar{t}Z$	1.24±0.21	1.09±0.15	0.170±0.072	0.067±0.085	–
DY+jets	–	–	–	0.0±1.9	–
SingleTop	4.6±2.2	2.3±1.4	–	0.73±0.35	–
QCD	–	–	–	–	–
Total MC	99±48	80±38	9.19±3.10	1.5±2.1	0.46±0.54
Data	93	86	11	1	0

Table B.2: Predicted and observed event yield for different b-jet multiplicities and exactly 5 jets, in the ele-mu control region defined in section 6.6.

Mu + 4 jets	1 bjet	2 bjet	3 bjet	4 bjet	5 bjet
$t\bar{t}$	27073±4520	19834±2861	1868±255	73±60	–
W+jets	1471±217	–	14±15	176±207	–
$Wb\bar{b}$	2045±794	603±2210	42±19	5±11	–
$t\bar{t}W$	66.5±3.7	38.6±3.1	4.01±0.49	0.198±0.077	–
$t\bar{t}Z$	48.2±2.3	33.1±2.6	5.510±0.60	0.67±0.28	–
DY+jets	937±123	154±27	6.7±7.1	28±32	–
SingleTop	2275±481	1175±224	101±27	7±12	–
Total MC	39898±7300	22174±3190	2698±514	291±316	–
Data	41032	21977	2007	45	0

Table B.3: Predicted and observed event yield for different b-jet multiplicities and exactly 4 jets, in the muon control region defined in appendix A.1.

Mu + 5 jets	1 bjet	2 bjet	3 bjet	4 bjet	5 bjet
$t\bar{t}$	8812±3241	7167±2297	917±260	58±27	12±18
W+jets	137±86	–	0.0±5.4	–	13±22
$Wb\bar{b}$	400±169	147±67	13.6±5.8	3.4±4.0	0.6±1.3
$t\bar{t}W$	40.1±3.5	27.8±2.2	3.82±0.53	0.126±0.073	0.000±0.058
$t\bar{t}Z$	31.2±3.3	24.10±3.2	5.10±0.66	0.710±0.28	0.057±0.047
DY+jets	195±26	26±10	2.09±3.10	0.00±1.10	1.5±2.8
SingleTop	512±116	342±98	39.2±8.7	3.9±6.4	0.00±0.16
QCD	700±272	298±215	3.5±3.5	–	0.000±0.051
Total MC	10829±3437	8034±2403	985±272	67±36	27±41
Data	11352	7473	1061	54	2

Table B.4: Predicted and observed event yield for different b-jet multiplicities and exactly 5 jets, in the muon control region defined in appendix A.1.

Ele + 4 jets	1 bjet	2 bjet	3 bjet	4 bjet	5 bjet
$t\bar{t}$	23194±3583	17389±2245	1701±301	86±81	–
W+jets	1688±534	–	0±39	40±147	–
$Wb\bar{b}$	1972±743	615±235	39±16	8±15	–
$t\bar{t}W$	53.1±2.9	33.68±1.10	4.092±0.610	0.34±0.29	–
$t\bar{t}Z$	41.4±1.8	29.9±1.5	5.03±0.42	0.54±0.21	–
DY+jets	1409±262	276±55	17.10±7.4	12±28	–
SingleTop	1972±434	1025±205	100±27	17±17	–
QCD	1256±703	509±303	9.10±4.9	0±14	–
Total MC	31588±5365	19879±2779	1877±361	167±251	–
Data	34225	17763	1488	35	0

Table B.5: Predicted and observed event yield for different b-jet multiplicities and exactly 4 jets, in the electron control region defined in appendix A.1.

Ele + 5 jets	1 bjet	2 bjet	3 bjet	4 bjet	5 bjet
$t\bar{t}$	6988±2464	5892±1790	772±274	61±43	16±23
W+jets	433±114	25±38	0±25	0±11	15±24
$Wb\bar{b}$	346±146	135±59	8.5±4.5	1.1±2.1	1.7±1.8
$t\bar{t}W$	29.3±3.1	22.10±2.1	3.58±0.42	0.35±0.18	0.058±0.074
$t\bar{t}Z$	25.3±1.9	19.7±1.5	4.34±0.38	0.85±0.22	0.12±0.18
DY+jets	228±58	68±19	3.0±1.9	–	0.0±2.5
SingleTop	417±119	266±58	38±11	4.8±4.4	3.2±3.4
QCD	601±289	18.86±7.10	5.5±6.7	0.26±0.25	0.7±1.5
Total MC	9070±2720	6450±1869	836±288	68±58	37±53
Data	9390	6215	809	46	1

Table B.6: Predicted and observed event yield for different b-jet multiplicities and exactly 5 jets, in the electron control region defined in appendix A.1.

Appendix C

Background and signal systematic uncertainties

C.1 JES

To evaluate the effect on the signal efficiency and the background shape of the jet energy scale, we vary it by $\pm 1\sigma$. The systematic associated to the background is small, as can be seen from figures C.1 and C.2. This is not suprising since we are taking the yields at fixed jet multiplicities from the data and extracting just the shape of the b-tagging distribution from the MC.

C.2 Renormalization, factorization and matching

The MC samples we are using are generated with a choice of renormalization and factorization scales. In addition to that also a minimum p_T is required for the partons to be matched after showering (20 GeV for the `MadGraph` samples used for $t\bar{t}$). Changing these parameters has an impact on the shape of the b-tagged jets multiplicity distribution. We compute the systematic error from these two separate sources by running our selection on $t\bar{t}$+jets samples with the matching scale shifted by a factor of 2 and 1/2 and by doing the same for renormalization and factorization scales. In the 8 jets and 7 jets signal regions the study is done requiring a MC truth lepton originating from a W rather than following the lepton selection described previously. This reduces the statistical error of the MC samples. For the same reason we use samples with at least two MC-truth leptons originating from a W to compute the systematic error in the Ele-Mu 5 jets control region.

In analogy with the JES uncertainty, the error induced on the shape is very small, as can be seen in figures C.3 and C.4 for muons and electrons, respectively. The error on the yield is clearly much larger, going up to 50%. However this does not affect the sensitivity of the analysis that takes the total yield from data.
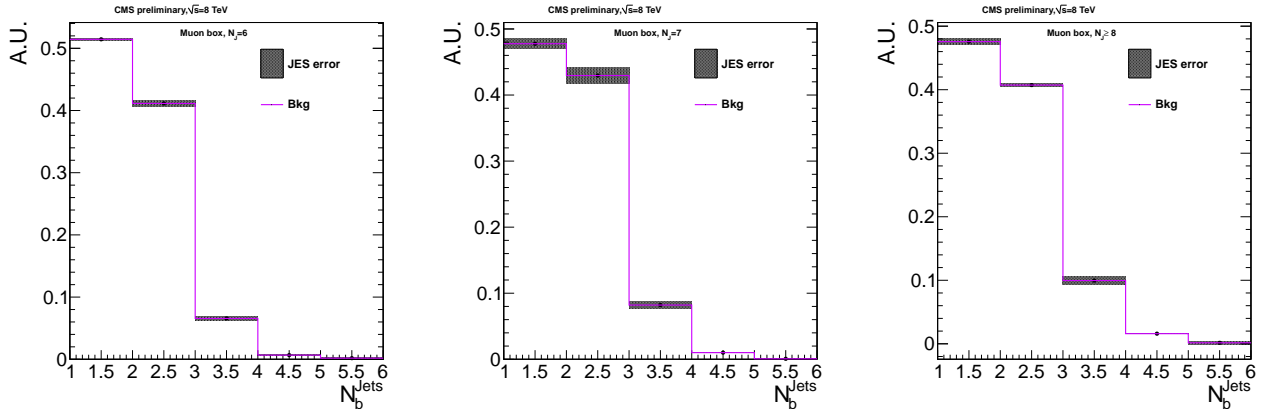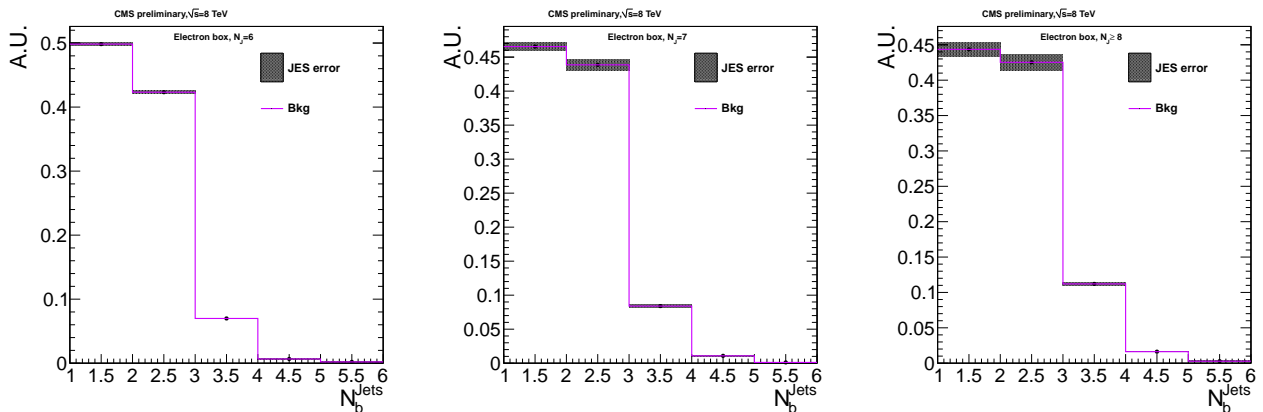
Figure C.1: Distribution of the number of b-jets, in the muon box, after applying the baseline selection and rescaling the Monte Carlo using the b-tagging scale factors, for the $= 6$ (left), $= 7$ jets (middle) and ≥ 8 jets (right) signal regions. The black band in the figures corresponds to the systematic error obtained varying the JES by $\pm 1\sigma$.

Figure C.2: Distribution of the number of b-jets, in the electron box, after applying the baseline selection and rescaling the Monte Carlo using the b-tagging scale factors, for the $= 6$ (left), $= 7$ jets (middle) and ≥ 8 jets (right) signal regions. The black band in the figures corresponds to the systematic error obtained varying the JES $\pm 1\sigma$.

C.3   ISR and FSR

In typical SUSY analyses an ISR systematic plays an important role close to the diagonal of the mother particle$-$LSP plane. In our case, also in absence of an LSP, the large number of jets in the final state requires some attention. The signal, once one of the W's from the tops decays leptonically, has eight partons that can potentially be reconstructed as jets. However a significant fraction of the events that we select has one or two outside of the acceptance ($|\eta| < 2.5$) as can
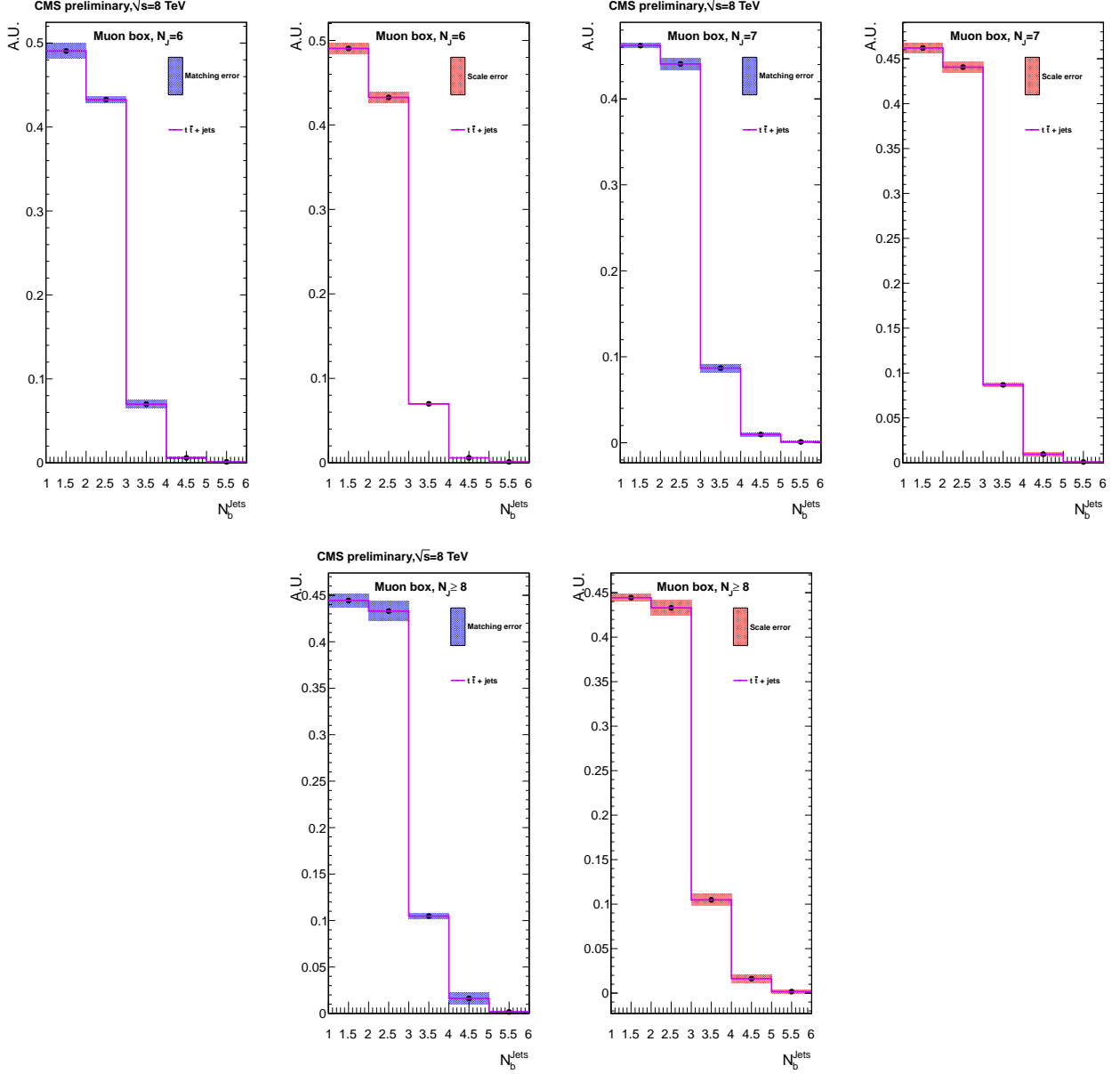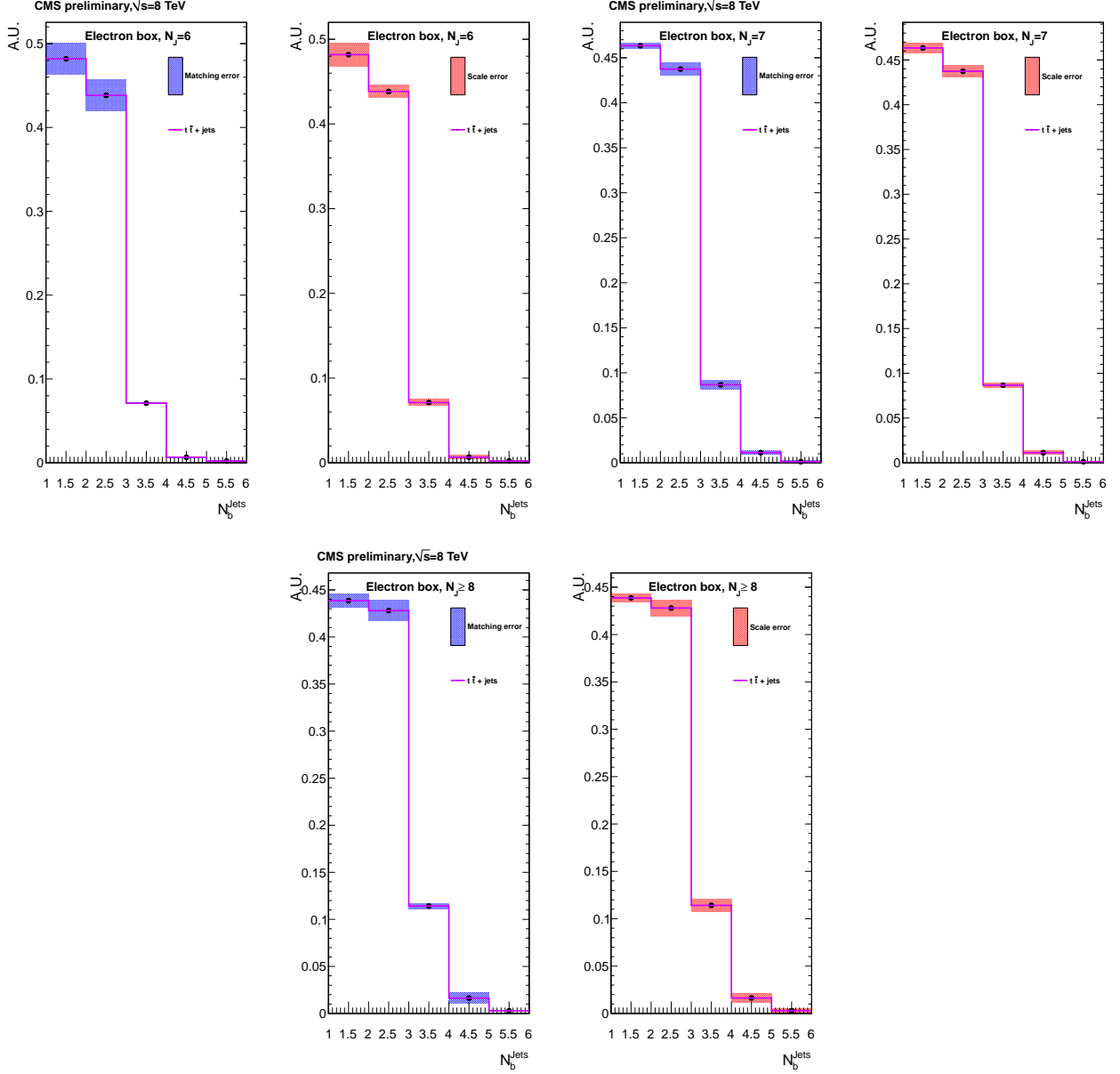
Figure C.3: Systematic error due to the matching threshold (blue) and renormalization and factorization scales (red) in the muon box, after the baseline selection. For events with exactly 6 jets (top left), 7 jets (top right) and ≥8 jets (bottom) in the MC $t\bar{t}$ sample.

be seen from the left panel of figure C.5. If we further impose a 30 GeV p_T cut on the partons the fraction of selected events with as many partons as reconstructed jets decreases even more as it is shown in the right panel of the same figure.

Figure C.4: Systematic error due to the matching threshold (blue) and renormalization and factorization scales (red) in the electron box, after the baseline selection. For events with exactly 6 jets (top left), 7 jets (top right) and ≥ 8 jets (bottom) in the MC $t\bar{t}$ sample.

For this reason we include in the analysis the uncertainty from the MC modeling of ISR and FSR. We divide the events in bins of p_T of the mother particles and assign to each event the uncertainty in table C.1. The resulting impact on the signal efficiency can be see in figures 6.6
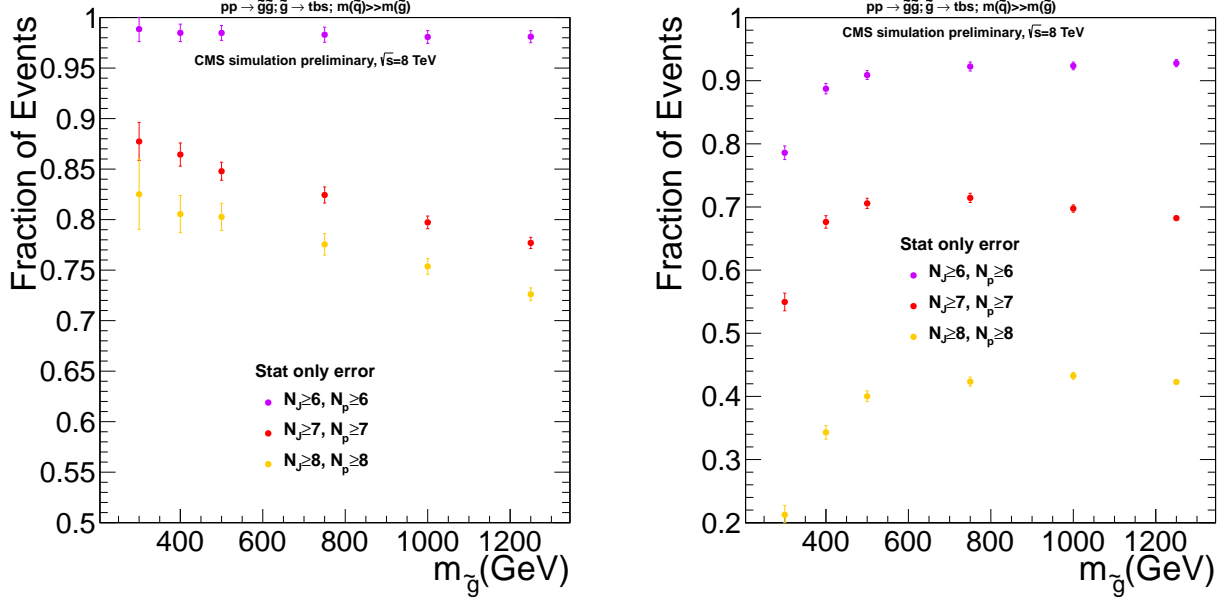
Figure C.5: Fraction of events selected in the three signal regions: 6 (purple), 7 (red), ≥ 8 jets (orange) with all the partons contained within the acceptance $|\eta| < 2.5$ (left) and with all the partons within the acceptance and above a 30 GeV p_T threshold (right).

$p_T^{\tilde{g}_1} + p_T^{\tilde{g}_2}$	Uncertainty
$(40, 100]$ GeV	6%
$(100, 150]$ GeV	10%
$(150, \infty]$ GeV	15%

Table C.1: Uncertainty in the Pythia modeling of ISR and FSR as determined from CMS in a separate study.

and 6.7. The effect is larger for a larger number of jets and becomes more important at small gluino masses, where additional radiation is needed for most events to pass our selection. Going from intermediate masses to larger ones the error increases slightly again, reflecting the growth of the average p_T of the system with the gluino mass.

Appendix D

Results of the five dimensional fit to Higgs couplings

This appendix collects the one dimensional profiles of the χ^2 obtained from the five dimensional fit described in section 7.6.3. In figures D.2 and D.1 we show them with the 68% and 95% intervals marked in orange. The details of the profiling are discussed in section 7.6.1. r_t, entering only at loop level in well measured rates, is essentially unconstrained due to the compensating effect of r_G and r_γ.
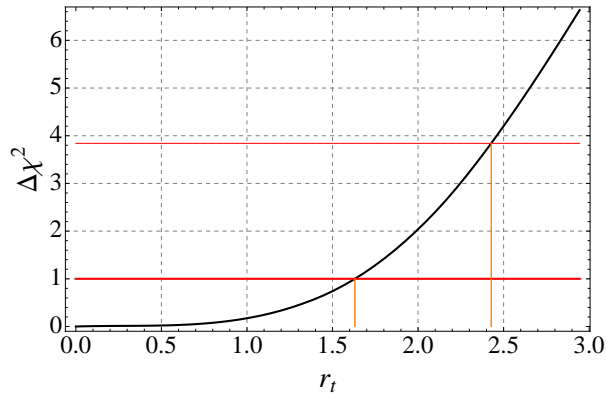

Figure D.1: $\Delta\chi^2$ profiles for the fifth parameter of the fit: r_t. Heights corresponding to the 68% and 95% confidence levels are marked in red.
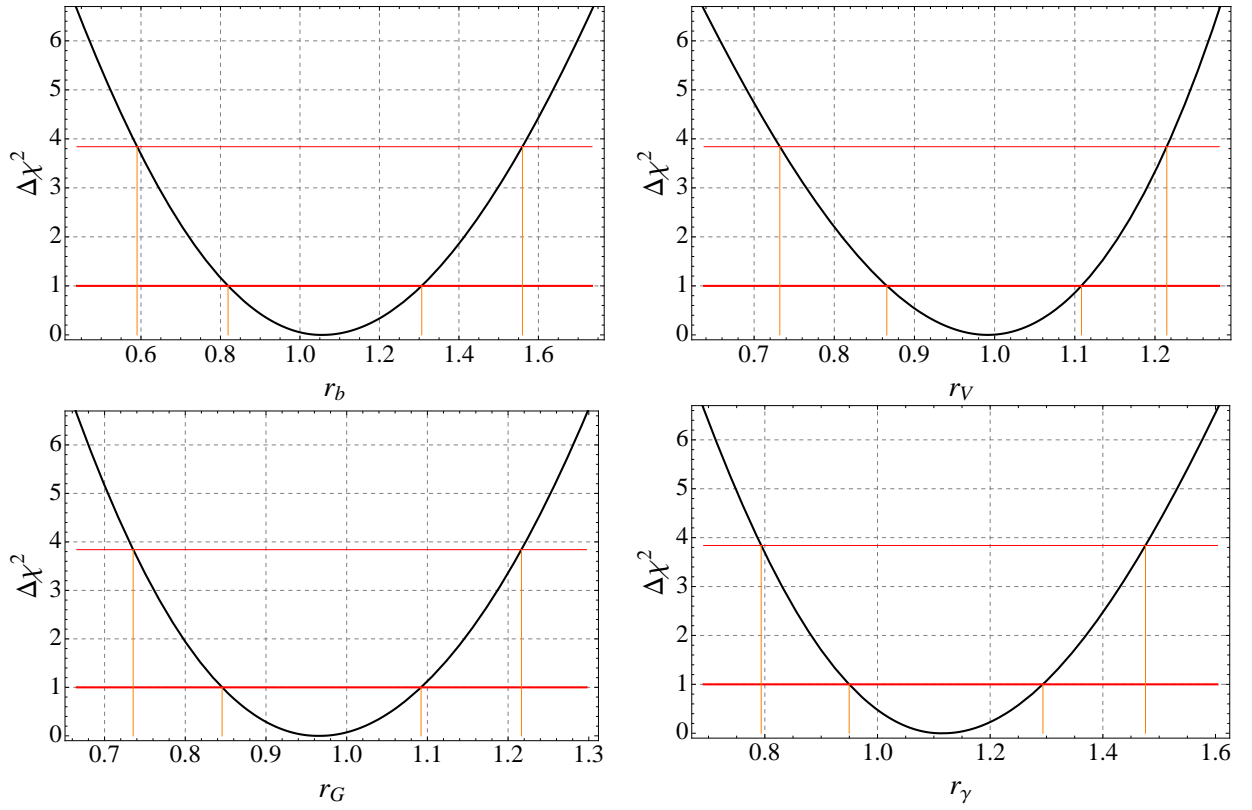
Figure D.2: $\Delta\chi^2$ profiles for four of the five parameters of the fit $(r_G, r_\gamma, r_V, r_b)$. Heights corresponding to the 68% and 95% confidence levels are marked in red.

Appendix E

Renormalization group equations for Yukawa couplings

Here we list the renormalization group equations for Yukawa couplings for theories constructed by adding to the SM extra leptonic multiplets. These results are relevant to chapter 8.

Vector doublets + singlets ("vector-like lepton"). For our "vector-like lepton" scenario in chapter 8, allowing for an additional neutral singlet $n \sim (1,1)_0$ with Yukawa couplings $\mathcal{L} = -y_n H^\dagger \psi n - y_n H \psi^c n + \text{h.c.}$, and including $\mathcal{N}$ copies with identical couplings, the relevant RGEs read [291, 292]

$$
\begin{aligned}
16\pi^2 \frac{dy}{dt} &= y \left(\frac{3}{2} \left(y^2 - y_n^2 \right) + \mathcal{N} \left(y^2 + y^{c2} + y_n^2 + y_n^{c2} \right) + 3y_t^2 - \frac{9g_2^2}{4} - \frac{9g_1^2}{4} \right), \\
16\pi^2 \frac{dy_n}{dt} &= y_n \left(\frac{3}{2} \left(y_n^2 - y^2 \right) + \mathcal{N} \left(y^2 + y^{c2} + y_n^2 + y_n^{c2} \right) + 3y_t^2 - \frac{9g_2^2}{4} - \frac{9g_1^2}{20} \right), \\
16\pi^2 \frac{dy_t}{dt} &= y_t \left(\mathcal{N} \left(y^2 + y^{c2} + y_n^2 + y_n^{c2} \right) + \frac{9y_t^2}{2} - 8g_3^2 - \frac{9g_2^2}{4} - \frac{17g_1^2}{20} \right), \\
16\pi^2 \frac{d\lambda}{dt} &= \lambda \left(24\lambda - 9g_2^2 - \frac{9g_1^2}{5} + 12y_t^2 + 4\mathcal{N} \left(y_n^2 + y_n^{c2} + y^2 + y^{c2} \right) \right) - \\
&\quad -2\mathcal{N} \left(y^4 + y^{c4} + y_n^4 + y_n^{c4} \right) - 6y_t^4 + + \frac{3}{8} \left(2g_2^4 + \left(g_2^2 + \frac{3g_1^2}{5} \right)^2 \right). \quad \text{(E.0.1)}
\end{aligned}
$$

The RGEs for y^c and y_n^c are similar to that for y and y_n. The gauge beta functions are

$$
b_1 = \frac{41}{10} + \frac{6\mathcal{N}}{5}, \quad b_2 = -\frac{19}{6} + \frac{2\mathcal{N}}{3}, \quad b_3 = -7. \quad \text{(E.0.2)}
$$

Vector doublets + triplet ("wino-higgsino"). For our "wino-higgsino" scenario, including $\mathcal{N}$ copies with identical couplings and allowing for an additional singlet n, the relevant RGEs

read [293]

$$16\pi^2 \frac{dy}{dt} = y^c y_n y_n^c + y \left(\frac{5}{4} y^2 + \frac{1}{4} y_n^2 - \frac{1}{2} y^{c2} + \frac{\mathcal{N}}{2} \left(3y^2 + 3y^{c2} + y_n^2 + y_n^{c2} \right) + 3y_t^2 - \frac{9}{20} g_1^2 - \frac{33}{4} g_2^2 \right),$$

$$16\pi^2 \frac{dy_n}{dt} = 3y_n^c y y^c + y_n \left(\frac{3}{4} y_n^2 + \frac{3}{2} y_n^{c2} + \frac{3}{4} y^2 + \frac{\mathcal{N}}{2} \left(3y^2 + 3y^{c2} + y_n^2 + y_n^{c2} \right) + 3y_t^2 - \frac{9}{20} g_1^2 - \frac{9}{4} g_2^2 \right),$$

$$16\pi^2 \frac{dy_t}{dt} = y_t \left(\frac{\mathcal{N}}{2} \left(3y^2 + 3y^{c2} + y_n^2 + y_n^{c2} \right) + \frac{9}{2} y_t^2 - 8g_3^2 - \frac{17}{20} g_1^2 - \frac{9}{4} g_2^2 \right),$$

$$16\pi^2 \frac{d\lambda}{dt} = \lambda \left(24\lambda + 2\mathcal{N} \left(3y^2 + 3y^{c2} + y_n^2 + y_n^{c2} \right) + 12y_t^2 \right) - \frac{\mathcal{N}}{2} \left(5y^4 + 5y^{c4} + y_n^4 + y_n^{c4} \right) -$$
$$- 2\mathcal{N} y_n y_n^c y y^c - \mathcal{N}(y^2 + y_n^{c2})(y^{c2} + y_n^2) - 6y_t^4 -$$
$$- 9\lambda \left(\frac{g_1^2}{5} + g_2^2 \right) + \frac{27}{200} g_1^4 + \frac{9}{20} g_2^2 g_1^2 + \frac{9}{8} g_2^4. \tag{E.0.3}$$

$$b_1 = \frac{41}{10} + \frac{2\mathcal{N}}{5}, \quad b_2 = -\frac{19}{6} + 2\mathcal{N}, \quad b_3 = -7. \tag{E.0.4}$$

We take as initial conditions, at a scale $\mu = 100$ GeV,

$$g_1 = 0.36\sqrt{5/3}, \ g_2 = 0.65, \ g_3 = 1.2, \ y_t = 0.99, \ \lambda = \frac{m_h^2}{2v^2} = 0.129. \tag{E.0.5}$$

The vacuum stability cutoff scale Λ_{UV} is determined by [294]

$$\lambda(\Lambda_{UV}) = \frac{2\pi^2}{3 \log\left(\frac{H}{\Lambda_{UV}} \right)} = -0.065 \left(1 - 0.02 \log_{10} \left(\frac{\Lambda_{UV}}{100 \text{ GeV}} \right) \right), \tag{E.0.6}$$

with the Hubble constant $H = 70 \, \text{km/s/Mpc} = 1.5 \cdot 10^{-42}$ GeV. We comment that for the problem under study, Landau poles of the Yukawa couplings appear at much higher scales, beyond the scale where the vacuum instability sets in, posing no additional constraint.

Appendix F

Estimates of the collider constraints on charged leptons

In this appendix we present our estimates of the LHC bounds on $\sigma \times \epsilon$ for new charged leptons, where ϵ includes acceptance, trigger and identification efficiencies, efficiencies of the kinematical cuts and the branching ratio to the relevant final state. We use a standard CLs technique to obtain the bounds and we take the number of observed events and the predicted background with its error from the CMS mulitlepton search at 8 TeV performed with an integrated luminosity of 9.2 fb^{-1} [282]. To get the excluded cross section, we first construct the likelihood as

$$L(n|n_s + n_b) = \mathcal{P}(n|n_s + n_b)G(n_b|n_b^{obs}, \sigma_b)\,, \tag{F.0.1}$$

where $\mathcal{P}$ is a Poisson distribution and we take a gaussian ansatz G for the background. Then we compute the CL$_s$,

$$\mathrm{CL}_s = \frac{\mathrm{CL}_{s+b}}{\mathrm{CL}_b} = \frac{P(n \leq n_d|n_s + n_b)}{P(n \leq n_d|n_b)}\,, \tag{F.0.2}$$

where P is the probability obtained marginalizing the likelihood, n_d is the number of events observed in the data, n_b the number of background events and n_s the number of signal events. Requiring CL$_s \leq 0.05$ fixes n_s to its 95% C.L. excluded value. In this way we obtain the cross section limits in Table F.1.

Selection	obs	background	$(\sigma\epsilon)_{\mathrm{excl}}$(fb)
$4l$, $S_T < 300$ GeV, Z	0	1.20 ± 0.38	0.4
$3l+1\tau$, $S_T < 300$ GeV, Z	18	18.0 ± 5.2	1.6

Table F.1: Estimated bounds on $(\sigma\epsilon)_{\mathrm{excl}}$ of multi-lepton final states [282] (see Sec. 8.3). l refers to electrons or muons and Z denotes two opposite sign leptons from a Z decay.

Bibliography

[1] T. Anderson, *An Introduction to Multivariate Statistical Analysis*. Wiley, third ed., 2003.

[2] e. Evans, Lyndon and e. Bryant, Philip, *LHC Machine*, *JINST* **3** (2008) S08001.

[3] **CMS** Collaboration, S. Chatrchyan *et. al.*, *Observation of a new boson at a mass of 125 GeV with the CMS experiment at the LHC*, *Phys.Lett.* **B716** (2012) 30–61, [`arXiv:1207.7235`].

[4] **ATLAS** Collaboration, G. Aad *et. al.*, *Observation of a new particle in the search for the Standard Model Higgs boson with the ATLAS detector at the LHC*, *Phys.Lett.* **B716** (2012) 1–29, [`arXiv:1207.7214`].

[5] **ALEPH Collaboration, CDF Collaboration, D0 Collaboration, DELPHI Collaboration, L3 Collaboration, OPAL Collaboration, SLD Collaboration, LEP Electroweak Working Group, Tevatron Electroweak Working Group, SLD Electroweak and Heavy Flavour Groups** Collaboration, *Precision Electroweak Measurements and Constraints on the Standard Model*, `arXiv:1012.2367`.

[6] S. Weinberg, *Anthropic Bound on the Cosmological Constant*, *Phys.Rev.Lett.* **59** (1987) 2607.

[7] **CMS** Collaboration, G. Bayatian *et. al.*, *CMS technical design report, volume II: Physics performance*, *J.Phys.* **G34** (2007) 995–1579.

[8] K. Blum, R. T. D'Agnolo, and J. Fan, *Natural SUSY Predicts: Higgs Couplings*, *JHEP* **1301** (2013) 057, [`arXiv:1206.5303`].

[9] R. T. D'Agnolo, E. Kuflik, and M. Zanetti, *Fitting the Higgs to Natural SUSY*, *JHEP* **1303** (2013) 043, [`arXiv:1212.1165`].

[10] N. Arkani-Hamed, K. Blum, R. T. D'Agnolo, and J. Fan, *2:1 for Naturalness at the LHC?*, *JHEP* **1301** (2013) 149, [`arXiv:1207.4482`].

[11] R. Barbieri, *Ten Lectures on the ElectroWeak Interactions*, `arXiv:0706.0684`.

[12] R. T. D'Agnolo, *Bounds from flavour physics on heavy fermions in higgsless models*, 2009. INFN Thesis Server.

[13] C.-N. Yang and R. L. Mills, *Conservation of Isotopic Spin and Isotopic Gauge Invariance*, *Phys.Rev.* **96** (1954) 191–195.

[14] W. Pauli, *Relativistic Field Theories of Elementary Particles*, *Rev.Mod.Phys.* **13** (1941) 203–232.

[15] M. E. Peskin and D. V. Schroeder, *An Introduction to quantum field theory*. Westview Press, 1995.

[16] A. V. Manohar, *Effective field theories*, `hep-ph/9606222`.

[17] J. Callan, Curtis G., *Broken scale invariance in scalar field theory*, *Phys.Rev.* **D2** (1970) 1541–1547.

[18] K. Symanzik, *Small distance behavior in field theory and power counting*, *Commun.Math.Phys.* **18** (1970) 227–246.

[19] K. Symanzik, *Small distance behavior analysis and Wilson expansion*, *Commun.Math.Phys.* **23** (1971) 49–86.

[20] G. Altarelli, *Partons in Quantum Chromodynamics*, *Phys.Rept.* **81** (1982) 1.

[21] C. Baker, D. Doyle, P. Geltenbort, K. Green, M. van der Grinten, *et. al.*, *An Improved experimental limit on the electric dipole moment of the neutron*, *Phys.Rev.Lett.* **97** (2006) 131801, [`hep-ex/0602020`].

[22] R. Peccei and H. R. Quinn, *CP Conservation in the Presence of Instantons*, *Phys.Rev.Lett.* **38** (1977) 1440–1443.

[23] S. Glashow, *Partial Symmetries of Weak Interactions*, *Nucl.Phys.* **22** (1961) 579–588.

[24] S. Weinberg, *A Model of Leptons*, *Phys.Rev.Lett.* **19** (1967) 1264–1266.

[25] F. Englert and R. Brout, *Broken Symmetry and the Mass of Gauge Vector Mesons*, *Phys.Rev.Lett.* **13** (1964) 321–323.

[26] P. W. Higgs, *Broken symmetries, massless particles and gauge fields*, *Phys.Lett.* **12** (1964) 132–133.

[27] P. W. Higgs, *Broken Symmetries and the Masses of Gauge Bosons*, *Phys.Rev.Lett.* **13** (1964) 508–509.

[28] P. W. Higgs, *Spontaneous Symmetry Breakdown without Massless Bosons, Phys.Rev.* **145** (1966) 1156–1163.

[29] P. W. Anderson, *Plasmons, Gauge Invariance, and Mass, Phys.Rev.* **130** (1963) 439–442.

[30] S. Weinberg, *The quantum theory of fields. Vol. 2: Modern applications.* Cambridge University Press, 1996.

[31] **Particle Data Group** Collaboration, J. Beringer *et. al.*, *Review of Particle Physics (RPP), Phys.Rev.* **D86** (2012) 010001.

[32] P. Huet, *Electroweak baryogenesis and the standard model*, `hep-ph/9406301`.

[33] B. W. Lee, C. Quigg, and H. Thacker, *The Strength of Weak Interactions at Very High-Energies and the Higgs Boson Mass, Phys.Rev.Lett.* **38** (1977) 883–885.

[34] A. Djouadi, *The Anatomy of electro-weak symmetry breaking. I: The Higgs boson in the standard model, Phys.Rept.* **457** (2008) 1–216, [`hep-ph/0503172`].

[35] **Particle Data Group** Collaboration, C. Amsler *et. al.*, *Review of Particle Physics, Phys.Lett.* **B667** (2008) 1–1340.

[36] G. Altarelli and R. Barbieri, *Vacuum polarization effects of new physics on electroweak processes, Phys.Lett.* **B253** (1991) 161–167.

[37] M. E. Peskin and T. Takeuchi, *A New constraint on a strongly interacting Higgs sector, Phys.Rev.Lett.* **65** (1990) 964–967.

[38] M. E. Peskin and T. Takeuchi, *Estimation of oblique electroweak corrections, Phys.Rev.* **D46** (1992) 381–409.

[39] S. Weinberg, *Implications of Dynamical Symmetry Breaking, Phys.Rev.* **D13** (1976) 974–996.

[40] S. Weinberg, *Implications of Dynamical Symmetry Breaking: An Addendum, Phys.Rev.* **D19** (1979) 1277–1280.

[41] E. Gildener, *Gauge Symmetry Hierarchies, Phys.Rev.* **D14** (1976) 1667.

[42] L. Susskind, *Dynamics of Spontaneous Symmetry Breaking in the Weinberg-Salam Theory, Phys.Rev.* **D20** (1979) 2619–2625.

[43] G. 't Hooft, *Naturalness, chiral symmetry, and spontaneous chiral symmetry breaking, NATO Adv.Study Inst.Ser.B Phys.* **59** (1980) 135.

[44] R. Barbieri and A. Strumia, *The 'LEP paradox'*, `hep-ph/0007265`.

[45] G. Isidori, Y. Nir, and G. Perez, *Flavor Physics Constraints for Physics Beyond the Standard Model, Ann.Rev.Nucl.Part.Sci.* **60** (2010) 355, [`arXiv:1002.0900`].

[46] F. Wilczek, *Decays of Heavy Vector Mesons Into Higgs Particles, Phys.Rev.Lett.* **39** (1977) 1304.

[47] H. Georgi, S. Glashow, M. Machacek, and D. V. Nanopoulos, *Higgs Bosons from Two Gluon Annihilation in Proton Proton Collisions, Phys.Rev.Lett.* **40** (1978) 692.

[48] J. R. Ellis, M. K. Gaillard, and D. V. Nanopoulos, *A Phenomenological Profile of the Higgs Boson, Nucl.Phys.* **B106** (1976) 292.

[49] M. A. Shifman, A. Vainshtein, M. Voloshin, and V. I. Zakharov, *Low-Energy Theorems for Higgs Boson Couplings to Photons, Sov.J.Nucl.Phys.* **30** (1979) 711–716.

[50] R. Dermisek and I. Low, *Probing the Stop Sector and the Sanity of the MSSM with the Higgs Boson at the LHC, Phys.Rev.* **D77** (2008) 035012, [`hep-ph/0701235`].

[51] **CMS** Collaboration, S. Chatrchyan *et. al.*, *Observation of a new boson at a mass of 125 GeV with the CMS experiment at the LHC, Phys.Lett.* **B716** (2012) 30–61, [`arXiv:1207.7235`].

[52] **ATLAS** Collaboration, G. Aad *et. al.*, *Observation of a new particle in the search for the Standard Model Higgs boson with the ATLAS detector at the LHC, Phys.Lett.* **B716** (2012) 1–29, [`arXiv:1207.7214`].

[53] "https://twiki.cern.ch/twiki/bin/view/CMSPublic/PhysicsResultsHIG."

[54] "https://twiki.cern.ch/twiki/bin/view/AtlasPublic/HiggsPublicResults."

[55] **CMS** Collaboration, *Updated results on the new boson discovered in the search for the standard model higgs boson in the zz to 4 leptons channel in pp collisions at $\sqrt{s} = 7$ and 8 tev*, CMS Physics Analysis Summary, CMS-PAS-HIG-12-041, 2012.

[56] **TEVNPH (Tevatron New Phenomena and Higgs Working Group), CDF, D0** Collaboration, *Combined CDF and D0 Search for Standard Model Higgs Boson Production with up to 10.0 fb^{-1} of Data*, `arXiv:1203.3774`.

[57] S. R. Coleman and J. Mandula, *All Possible Symmetries of the S Matrix, Phys.Rev.* **159** (1967) 1251–1256.

[58] R. Haag, J. T. Lopuszanski, and M. Sohnius, *All Possible Generators of Supersymmetries of the s Matrix, Nucl.Phys.* **B88** (1975) 257.

[59] Y. Golfand and E. Likhtman, *Extension of the Algebra of Poincare Group Generators and Violation of p Invariance, JETP Lett.* **13** (1971) 323–326.

[60] P. Ramond, *Dual Theory for Free Fermions*, *Phys.Rev.* **D3** (1971) 2415–2418.

[61] A. Neveu and J. Schwarz, *Factorizable dual model of pions*, *Nucl.Phys.* **B31** (1971) 86–112.

[62] J.-L. Gervais and B. Sakita, *Field Theory Interpretation of Supergauges in Dual Models*, *Nucl.Phys.* **B34** (1971) 632–639.

[63] J. Wess and B. Zumino, *Supergauge Transformations in Four-Dimensions*, *Nucl.Phys.* **B70** (1974) 39–50.

[64] J. Wess and J. Bagger, *Supersymmetry and supergravity*. Princeton University Press, 1992.

[65] S. Weinberg, *The quantum theory of fields. Vol. 3: Supersymmetry*. Cambridge University Press, 2000.

[66] S. P. Martin, *A Supersymmetry primer*, `hep-ph/9709356`.

[67] L. Girardello and M. T. Grisaru, *Soft Breaking of Supersymmetry*, *Nucl.Phys.* **B194** (1982) 65.

[68] A. Salam and J. Strathdee, *Supergauge Transformations*, *Nucl.Phys.* **B76** (1974) 477–482.

[69] R. Barbier, C. Berat, M. Besancon, M. Chemtob, A. Deandrea, *et. al.*, *R-parity violating supersymmetry*, *Phys.Rept.* **420** (2005) 1–202, [`hep-ph/0406039`].

[70] J. E. Kim and H. P. Nilles, *The mu Problem and the Strong CP Problem*, *Phys.Lett.* **B138** (1984) 150.

[71] G. Giudice and A. Masiero, *A Natural Solution to the mu Problem in Supergravity Theories*, *Phys.Lett.* **B206** (1988) 480–484.

[72] E. Chun, J. E. Kim, and H. P. Nilles, *A Natural solution of the mu problem with a composite axion in the hidden sector*, *Nucl.Phys.* **B370** (1992) 105–122.

[73] G. Dvali, G. Giudice, and A. Pomarol, *The Mu problem in theories with gauge mediated supersymmetry breaking*, *Nucl.Phys.* **B478** (1996) 31–45, [`hep-ph/9603238`].

[74] J. Jacobs, W. Klipstein, S. Lamoreaux, B. Heckel, and E. Fortson, *Testing time-reversal symmetry using Hg-199*, *Phys.Rev.Lett.* **71** (1993) 3782–3785.

[75] E. D. Commins, S. B. Ross, D. DeMille, and B. Regan, *Improved experimental limit on the electric dipole moment of the electron*, *Phys.Rev.* **A50** (1994) 2960–2977.

[76] D. Cho, K. Sangster, and E. Hinds, *Search for time reversal symmetry violation in thallium fluoride using a jet source*, *Phys.Rev.* **A44** (1991) 2783–2799.

[77] I. Altarev, Y. Borisov, N. Borovikova, S. Ivanov, E. Kolomensky, *et. al.*, *New measurement of the electric dipole moment of the neutron*, *Phys.Lett.* **B276** (1992) 242–246.

[78] K. Smith, N. Crampin, J. Pendlebury, D. Richardson, D. Shiers, *et. al.*, *A Search for the Electric Dipole Moment of the Neutron*, *Phys.Lett.* **B234** (1990) 191–196.

[79] J. R. Ellis, S. Ferrara, and D. V. Nanopoulos, *CP Violation and Supersymmetry*, *Phys.Lett.* **B114** (1982) 231.

[80] W. Buchmuller and D. Wyler, *CP Violation and R Invariance in Supersymmetric Models of Strong and Electroweak Interactions*, *Phys.Lett.* **B121** (1983) 321.

[81] S. M. Barr, *A Review of CP violation in atoms*, *Int.J.Mod.Phys.* **A8** (1993) 209–236.

[82] **MEG** Collaboration, J. Adam *et. al.*, *New limit on the lepton-flavour violating decay* $\mu^+ \to e^+\gamma$, *Phys.Rev.Lett.* **107** (2011) 171801, [`arXiv:1107.5547`].

[83] R. Barbieri, G. Isidori, J. Jones-Perez, P. Lodone, and D. M. Straub, *U(2) and Minimal Flavour Violation in Supersymmetry*, *Eur.Phys.J.* **C71** (2011) 1725, [`arXiv:1105.2296`].

[84] R. Barbieri, P. Campli, G. Isidori, F. Sala, and D. M. Straub, *B-decay CP-asymmetries in SUSY with a* $U(2)^3$ *flavour symmetry*, *Eur.Phys.J.* **C71** (2011) 1812, [`arXiv:1108.5125`].

[85] H. Georgi, H. R. Quinn, and S. Weinberg, *Hierarchy of Interactions in Unified Gauge Theories*, *Phys.Rev.Lett.* **33** (1974) 451–454.

[86] S. Dimopoulos, S. Raby, and F. Wilczek, *Supersymmetry and the Scale of Unification*, *Phys.Rev.* **D24** (1981) 1681–1683.

[87] U. Amaldi, W. de Boer, and H. Furstenau, *Comparison of grand unified theories with electroweak and strong coupling constants measured at LEP*, *Phys.Lett.* **B260** (1991) 447–455.

[88] G. Giudice and A. Romanino, *Split supersymmetry*, *Nucl.Phys.* **B699** (2004) 65–89, [`hep-ph/0406088`].

[89] N. Arkani-Hamed and S. Dimopoulos, *Supersymmetric unification without low energy supersymmetry and signatures for fine-tuning at the LHC*, *JHEP* **0506** (2005) 073, [`hep-th/0405159`].

[90] N. Arkani-Hamed, S. Dimopoulos, G. Giudice, and A. Romanino, *Aspects of split supersymmetry*, *Nucl.Phys.* **B709** (2005) 3–46, [`hep-ph/0409232`].

[91] G. Bhattacharyya, *Electroweak Symmetry Breaking and BSM Physics (A Review)*, *Pramana* **72** (2009) 37–54, [`arXiv:0807.3883`].

[92] **Planck** Collaboration, P. Ade *et. al.*, *Planck 2013 results. XVI. Cosmological parameters*, `arXiv:1303.5076`.

[93] **WMAP** Collaboration, G. Hinshaw *et. al.*, *Five-Year Wilkinson Microwave Anisotropy Probe (WMAP) Observations: Data Processing, Sky Maps, and Basic Results*, *Astrophys.J.Suppl.* **180** (2009) 225–245, [`arXiv:0803.0732`].

[94] N. Arkani-Hamed, A. Delgado, and G. Giudice, *The Well-tempered neutralino*, *Nucl.Phys.* **B741** (2006) 108–130, [`hep-ph/0601041`].

[95] N. Arkani-Hamed, S. Dimopoulos, and S. Kachru, *Predictive landscapes and new physics at a TeV*, `hep-th/0501082`.

[96] R. Mahbubani and L. Senatore, *The Minimal model for dark matter and unification*, *Phys.Rev.* **D73** (2006) 043510, [`hep-ph/0510064`].

[97] **XENON100** Collaboration, E. Aprile *et. al.*, *Dark Matter Results from 225 Live Days of XENON100 Data*, *Phys.Rev.Lett.* **109** (2012) 181301, [`arXiv:1207.5988`].

[98] **IceCube** Collaboration, M. Danninger, *Searches for dark matter with the IceCube detector*, *J.Phys.Conf.Ser.* **375** (2012) 012038.

[99] **XENON1T** Collaboration, E. Aprile, *The XENON1T Dark Matter Search Experiment*, `arXiv:1206.6288`.

[100] C. Cheung, L. J. Hall, D. Pinner, and J. T. Ruderman, *Prospects and Blind Spots for Neutralino Dark Matter*, `arXiv:1211.4873`.

[101] F. D. Steffen, *Gravitino dark matter and cosmological constraints*, *JCAP* **0609** (2006) 001, [`hep-ph/0605306`].

[102] R. Barbieri and G. Giudice, *Upper Bounds on Supersymmetric Particle Masses*, *Nucl.Phys.* **B306** (1988) 63.

[103] S. Dimopoulos and G. Giudice, *Naturalness constraints in supersymmetric theories with nonuniversal soft terms*, *Phys.Lett.* **B357** (1995) 573–578, [`hep-ph/9507282`].

[104] R. Kitano and Y. Nomura, *Supersymmetry, naturalness, and signatures at the LHC*, *Phys.Rev.* **D73** (2006) 095004, [`hep-ph/0602096`].

[105] M. Papucci, J. T. Ruderman, and A. Weiler, *Natural SUSY Endures*, `arXiv:1110.6926`.

[106] I. Low, *Polarized Charginos (and Tops) in Stop Decays*, `arXiv:1304.0491`.

[107] W. Beenakker, R. Hopker, and M. Spira, *PROSPINO: A Program for the production of supersymmetric particles in next-to-leading order QCD*, `hep-ph/9611232`.

[108] "http://resonaances.blogspot.ch/2011/02/more-susy-limits.html."

[109] **CMS** Collaboration, "Interpretation of Searches for Supersymmetry." CMS-PAS-SUS-11-016. `http://cdsweb.cern.ch/record/1445580`.

[110] **ATLAS** Collaboration, *Search for squarks and gluinos using final states with jets and missing transverse momentum with the atlas detector in $\sqrt{s} = 7$ tev proton-proton collisions*, ATLAS Conference Note, ATLAS-CONF-2012-033.

[111] R. Barbieri and D. Pappadopulo, *S-particles at their naturalness limits*, *JHEP* **0910** (2009) 061, [`arXiv:0906.4546`].

[112] **CMS** Collaboration, *Search for supersymmetry using events with a single lepton, multiple jets, and b-tags*, CMS Physics Analysis Summary, CMS-PAS-SUS-13-007, 2013.

[113] J. de Blas, A. Delgado, and B. Ostdiek, *The Least Supersymmetric Signals at the LHC*, `arXiv:1304.1946`.

[114] M. Lisanti, P. Schuster, M. Strassler, and N. Toro, *Study of LHC Searches for a Lepton and Many Jets*, `arXiv:1107.5055`.

[115] C. T. Hill and R. J. Hill, T^- *parity violation by anomalies*, *Phys.Rev.* **D76** (2007) 115014, [`arXiv:0705.0697`].

[116] K. Kumar, T. M. Tait, and R. Vega-Morales, *Manifestations of Top Compositeness at Colliders*, *JHEP* **0905** (2009) 022, [`arXiv:0901.3808`].

[117] A. De Simone, O. Matsedonskyi, R. Rattazzi, and A. Wulzer, *A First Top Partner's Hunter Guide*, *JHEP* **1304** (2013) 004, [`arXiv:1211.5663`].

[118] C. Csaki, Y. Grossman, and B. Heidenreich, *MFV SUSY: A Natural Theory for R-Parity Violation*, `arXiv:1111.1239`.

[119] R. S. Chivukula and H. Georgi, *Composite Technicolor Standard Model*, *Phys.Lett.* **B188** (1987) 99.

[120] L. Hall and L. Randall, *Weak scale effective supersymmetry*, *Phys.Rev.Lett.* **65** (1990) 2939–2942.

[121] A. Buras, P. Gambino, M. Gorbahn, S. Jager, and L. Silvestrini, *Universal unitarity triangle and physics beyond the standard model*, *Phys.Lett.* **B500** (2001) 161–167, [`hep-ph/0007085`].

[122] G. D'Ambrosio, G. Giudice, G. Isidori, and A. Strumia, *Minimal flavor violation: An Effective field theory approach*, *Nucl.Phys.* **B645** (2002) 155–187, [`hep-ph/0207036`].

[123] C. Frugiuele and T. Gregoire, *Making the Sneutrino a Higgs with a $U(1)_R$ Lepton Number*, *Phys.Rev.* **D85** (2012) 015016, [`arXiv:1107.4634`].

[124] E. Bertuzzo and C. Frugiuele, *Fitting Neutrino Physics with a $U(1)_R$ Lepton Number*, *JHEP* **1205** (2012) 100, [`arXiv:1203.5340`].

[125] **Super-Kamiokande** Collaboration, K. Abe *et. al.*, *The Search for $n - \bar{n}$ oscillation in Super-Kamiokande I*, `arXiv:1109.4227`.

[126] F. Takayama and M. Yamaguchi, *Gravitino dark matter without R-parity*, *Phys.Lett.* **B485** (2000) 388–392, [`hep-ph/0005214`].

[127] C. T. Hill and E. H. Simmons, *Strong dynamics and electroweak symmetry breaking*, *Phys.Rept.* **381** (2003) 235–402, [`hep-ph/0203079`].

[128] G. Cacciapaglia, R. Chierici, A. Deandrea, L. Panizzi, S. Perries, *et. al.*, *Four tops on the real projective plane at LHC*, *JHEP* **1110** (2011) 042, [`arXiv:1107.4616`].

[129] **CMS** Collaboration, S. Chatrchyan *et. al.*, *The CMS experiment at the CERN LHC*, *JINST* **3** (2008) S08004.

[130] "http://public.web.cern.ch/public/en/research/AccelComplex-en.html."

[131] **CMS** Collaboration, *CMS luminosity based on pixel cluster counting, summer 2012 update*, CMS Physics Analysis Summary, CMS-PAS-LUM-12-001, 2012.

[132] "https://twiki.cern.ch/twiki/bin/view/CMSPublic/LumiPublicResults."

[133] M. Atac, Y. Kozhevnikov, E. Bartz, J. Doroshenko, T. Koeth, *et. al.*, *Beam test results of the US - CMS forward pixel detector*, *Nucl.Instrum.Meth.* **A488** (2002) 271–281.

[134] **CMS** Collaboration, *Studies of tracker material in the CMS detector*, CMS Physics Analysis Summary, CMS-PAS-TRK-10-003, 2010.

[135] "https://twiki.cern.ch/twiki/bin/view/CMSPublic/TrackerMaterialBudgetplots."

[136] **CMS** Collaboration, *Tracking and primary vertex results in first 7 TeV collisions*, CMS Physics Analysis Summary, CMS-PAS-TRK-10-005, 2010.

[137] **CMS** Collaboration, S. Chatrchyan *et. al.*, *Performance of CMS muon reconstruction in pp collision events at $\sqrt{s} = 7$ TeV*, *JINST* **7** (2012) P10002, [`arXiv:1206.4071`].

[138] **CMS** Collaboration, S. Chatrchyan *et. al.*, *Time Reconstruction and Performance of the CMS Electromagnetic Calorimeter*, *JINST* **5** (2010) T03011, [`arXiv:0911.4044`].

[139] P. Adzic, R. Alemany-Fernandez, C. Almeida, N. Almeida, G. Anagnostou, *et. al.*, *Energy Resolution Performance of the CMS Electromagnetic Calorimeter*, .

[140] **CMS** Collaboration, G. Bayatian *et. al.*, *CMS physics: Technical design report*, tech. rep., 2006. CERN-LHCC-2006-001, CMS-TDR-008-1.

[141] **USCMS, ECAL/HCAL** Collaboration, S. Abdullin *et. al.*, *The CMS barrel calorimeter response to particle beams from 2-GeV/c to 350-GeV/c*, *Eur.Phys.J.* **C60** (2009) 359–373.

[142] **CMS** Collaboration, *Jet energy resolution in cms at $\sqrt{s} = 7$ TeV*, CMS Physics Analysis Summary, CMS-PAS-JME-10-014, 2010.

[143] **CMS** Collaboration, *Missing transverse energy performance in minimum-bias and jet events from proton-proton collisions at $\sqrt{s} = 7$ TeV*, CMS Physics Analysis Summary, CMS-PAS-JME-10-004, 2010.

[144] **CMS** Collaboration, CMS Collaboration, *Jet performance in pp collisions at $\sqrt{s}$=7 TeV*, CMS Physics Analysis Summary, CMS-PAS-JME-10-003, 2010.

[145] **CMS** Collaboration, S. Chatrchyan *et. al.*, *Performance of CMS Muon Reconstruction in Cosmic-Ray Events*, *JINST* **5** (2010) T03022, [arXiv:0911.4994].

[146] "https://twiki.cern.ch/twiki/bin/view/CMSPublic/PhysicsResultsMUO."

[147] **CMS** Collaboration, S. Dasu *et. al.*, *CMS. The TriDAS project. technical design report, vol.1: The trigger systems*, Tech. Rep. CERN-LHCC-2000-038, 2000.

[148] **CMS** Collaboration, e. Sphicas, P., *CMS. The TriDAS project. technical design report, vol.2: Data acquisition and high-level trigger*, Tech. Rep. CERN-LHCC-2002-026, 2002.

[149] e. Bird, I., e. Bos, K., e. Brook, N., e. Duellmann, D., e. Eck, C., *et. al.*, *LHC computing Grid. Technical design report*, Tech. Rep. CERN-LHCC-2005-024, 2005.

[150] **CMS** Collaboration, *Particle–flow event reconstruction in CMS and performance for jets, taus, and met*, CMS Physics Analysis Summary, CMS-PAS-PFT-09-001, 2009.

[151] **CMS** Collaboration, *Commissioning of the particle-flow event reconstruction with the first LHC collisions recorded in the CMS detector*, CMS Physics Analysis Summary, CMS-PAS-PFT-10-001, 2010.

[152] M. Cacciari, G. P. Salam, and G. Soyez, *The Anti-k(t) jet clustering algorithm*, *JHEP* **0804** (2008) 063, [arXiv:0802.1189].

[153] **CMS** Collaboration, *Jet plus tracks algorithm for calorimeter jet energy corrections in CMS*, CMS Physics Analysis Summary, CMS-PAS-JME-09-002, 2009.

[154] **CMS** Collaboration, *Commissioning of trackjets in pp collisions at $\sqrt{s}=7$ TeV*, CMS Physics Analysis Summary, CMS-PAS-JME-10-006, 2010.

[155] T. Sjostrand, S. Mrenna, and P. Z. Skands, *PYTHIA 6.4 Physics and Manual*, *JHEP* **0605** (2006) 026, [hep-ph/0603175].

[156] J. Alwall, M. Herquet, F. Maltoni, O. Mattelaer, and T. Stelzer, *MadGraph 5 : Going Beyond*, *JHEP* **1106** (2011) 128, [arXiv:1106.0522].

[157] N. Davidson, G. Nanava, T. Przedzinski, E. Richter-Was, and Z. Was, *Universal Interface of TAUOLA Technical and Physics Documentation*, *Comput.Phys.Commun.* **183** (2012) 821–843, [arXiv:1002.0543].

[158] **GEANT4** Collaboration, S. Agostinelli *et. al.*, *GEANT4: A Simulation toolkit*, *Nucl.Instrum.Meth.* **A506** (2003) 250–303.

[159] M. Cacciari and G. P. Salam, *Pileup subtraction using jet areas*, *Phys.Lett.* **B659** (2008) 119–126, [arXiv:0707.1378].

[160] M. Cacciari and G. P. Salam, *Dispelling the N^3 myth for the k_t jet-finder*, *Phys.Lett.* **B641** (2006) 57–61, [hep-ph/0512210].

[161] M. Cacciari, G. P. Salam, and G. Soyez, *FastJet user manual*, *Eur.Phys.J.* **C72** (2012) 1896, [arXiv:1111.6097].

[162] **CMS** Collaboration, S. Chatrchyan *et. al.*, *Determination of Jet Energy Calibration and Transverse Momentum Resolution in CMS*, *JINST* **6** (2011) P11002, [arXiv:1107.4277].

[163] M. Bahr, S. Gieseke, M. Gigg, D. Grellscheid, K. Hamilton, *et. al.*, *Herwig++ Physics and Manual*, *Eur.Phys.J.* **C58** (2008) 639–707, [arXiv:0803.0883].

[164] **CMS** Collaboration, *Electron and photon energy calibration and resolution with the cms ecal at $\sqrt{s} = 7$ TeV*, CMS Physics Analysis Summary, CMS-PAS-EGM-11-001, 2011.

[165] **CMS** Collaboration, *Determination of the jet energy scale in CMS with pp collisions at $\sqrt{s} = 7$ TeV*, CMS Physics Analysis Summary, CMS-PAS-JME-10-010, 2010.

[166] S. Alioli, P. Nason, C. Oleari, and E. Re, *A general framework for implementing NLO calculations in shower Monte Carlo programs: the POWHEG BOX*, *JHEP* **1006** (2010) 043, [arXiv:1002.2581].

[167] **CMS** Collaboration, *Description and performance of cms track reconstruction*, CMS Physics Analysis Summary, CMS-PAS-TRK-11-001, 2011.

[168] V. Blobel, *Software alignment for tracking detectors*, *Nucl.Instrum.Meth.* **A566** (2006) 5–13.

[169] G. Flucke, P. Schleper, G. Steinbruck, and M. Stoye, *CMS silicon tracker alignment strategy with the Millepede II algorithm*, JINST **3** (2008) P09002.

[170] **CMS** Collaboration, S. Chatrchyan *et. al.*, *Identification of b-quark jets with the CMS experiment*, `arXiv:1211.4462`.

[171] **CMS** Collaboration, *Algorithms for b jet identification in CMS*, CMS Physics Analysis Summary, CMS-PAS-BTV-09-001, 2009.

[172] **CMS** Collaboration, *Performance of cms muon reconstruction in pp collisions at $\sqrt{s} = 7$ TeV*, CMS Physics Analysis Summary, CMS-PAS-MUO-10-004, 2010.

[173] "http://root.cern.ch/drupal/."

[174] **CMS** Collaboration, *Performance of b-jet identification in CMS*, CMS Physics Analysis Summary, CMS-PAS-BTV-11-001, 2011.

[175] e. Bartalini, Paolo and e. Fano, Livio, *Multiple partonic interactions at the LHC. Proceedings, 1st International Workshop, MPI'08, Perugia, Italy, October 27-31, 2008*, `arXiv:1003.4220`.

[176] M. Botje, J. Butterworth, A. Cooper-Sarkar, A. de Roeck, J. Feltesse, *et. al.*, *The PDF4LHC Working Group Interim Recommendations*, `arXiv:1101.0538`.

[177] **CMS** Collaboration, S. Chatrchyan *et. al.*, *Measurement of the ttbar production cross section in the all-jet final state in pp collisions at sqrt(s) = 7 TeV*, `arXiv:1302.0508`.

[178] **CMS** Collaboration, S. Chatrchyan *et. al.*, *Measurement of the top-antitop production cross section in the tau+jets channel in pp collisions at sqrt(s) = 7 TeV*, `arXiv:1301.5755`.

[179] **CMS** Collaboration, S. Chatrchyan *et. al.*, *Measurement of the $t\bar{t}$ production cross section in pp collisions at $\sqrt{s} = 7$ TeV with lepton + jets final states*, `arXiv:1212.6682`.

[180] **CMS** Collaboration, *Measurement of the b-tagging efficiency using $t\bar{t}$ events*, CMS Physics Analysis Summary, CMS-PAS-BTV-11-003, 2011.

[181] L. Lyons, D. Gibaut, and P. Clifford, *How to Combine Correlated Estimates of a Single Physical Quantity*, Nucl.Instrum.Meth. **A270** (1988) 110.

[182] **CMS** Collaboration, S. Chatrchyan *et. al.*, *Inclusive b-jet production in pp collisions at $\sqrt{s} = 7$ TeV*, JHEP **1204** (2012) 084, [`arXiv:1202.4617`].

[183] **CMS** Collaboration, S. Chatrchyan *et. al.*, *Measurement of the Inclusive Jet Cross Section in pp Collisions at $\sqrt{s} = 7$ TeV*, Phys.Rev.Lett. **107** (2011) 132001, [`arXiv:1106.0208`].

[184] **CMS** Collaboration, D. Orbaker, *Fast simulation of the CMS detector, J.Phys.Conf.Ser.* **219** (2010) 032053.

[185] **CMS** Collaboration, *Search for the standard model Higgs boson decaying to a W pair in the fully leptonic final state in pp collisions at sqrt(s) = 8 TeV*, CMS Physics Analysis Summary, CMS-PAS-HIG-12-038, 2012.

[186] **CMS** Collaboration, S. Chatrchyan *et. al.*, *Particle-Flow Event Reconstruction in CMS and Performance for Jets, Taus, and MET*, CMS Physics Analysis Summary, CMS-PAS-PFT-09-001, 2009.

[187] **CMS** Collaboration, *Measuring Electron Efficiencies at CMS with Early Data*, CMS Physics Analysis Summary, CMS-PAS-EGM-07-001, 2007.

[188] **CMS** Collaboration, S. Chatrchyan *et. al.*, *Commissioning of the Particle-Flow reconstruction in Minimum-Bias and Jet Events from pp Collisions at 7 TeV*, CMS Physics Analysis Summary, CMS-PAS-PFT-10-002, 2010.

[189] J. Alwall, P. Demin, S. de Visscher, R. Frederix, M. Herquet, *et. al.*, *MadGraph/MadEvent v4: The New Web Generation*, *JHEP* **0709** (2007) 028, [`arXiv:0706.2334`].

[190] S. Hoeche, F. Krauss, N. Lavesson, L. Lonnblad, M. Mangano, *et. al.*, *Matching parton showers and matrix elements*, `hep-ph/0602031`.

[191] **CMS** Collaboration, *CMS luminosity based on pixel cluster counting, summer 2013 update*, CMS Physics Analysis Summary, CMS-PAS-LUM-13-001, 2013.

[192] D. Bourilkov, R. C. Group, and M. R. Whalley, *LHAPDF: PDF use from the Tevatron to the LHC*, `hep-ph/0605240`.

[193] L. Moneta, K. Belasco, K. S. Cranmer, S. Kreiss, A. Lazzaro, *et. al.*, *The RooStats Project*, *PoS* **ACAT2010** (2010) 057, [`arXiv:1009.1003`].

[194] **CMS** Collaboration, S. Chatrchyan *et. al.*, *Search for supersymmetry in hadronic final states with missing transverse energy using the variables α_T and b-quark multiplicity in pp collisions at $\sqrt{s} = 8$ TeV*, `arXiv:1303.2985`.

[195] **ATLAS** Collaboration, *Search for squarks and gluinos with the ATLAS detector using final states with jets and missing transverse momentum and 5.8 fb^{-1} of $\sqrt{s}$=8 TeV proton-proton collision data*, ATLAS Conference Note, ATLAS-CONF-2012-109, ATLAS-COM-CONF-2012-140, 2012.

[196] Y. Kats, P. Meade, M. Reece, and D. Shih, *The Status of GMSB After 1/fb at the LHC*, *JHEP* **1202** (2012) 115, [`arXiv:1110.6444`].

[197] C. Brust, A. Katz, S. Lawrence, and R. Sundrum, *SUSY, the Third Generation and the LHC*, *JHEP* **1203** (2012) 103, [arXiv:1110.6670].

[198] R. Essig, E. Izaguirre, J. Kaplan, and J. G. Wacker, *Heavy Flavor Simplified Models at the LHC*, *JHEP* **1201** (2012) 074, [arXiv:1110.6443].

[199] **ATLAS** Collaboration, G. Aad *et. al.*, *Search for scalar bottom pair production with the ATLAS detector in pp Collisions at sqrts = 7 TeV*, *Phys. Rev. Lett.* **108** (2012) 181802, [arXiv:1112.3832].

[200] **ATLAS** Collaboration, G. Aad *et. al.*, *Search for scalar top quark pair production in natural gauge mediated supersymmetry models with the ATLAS detector in pp collisions at sqrt(s) = 7 TeV*, arXiv:1204.6736.

[201] P. Draper, P. Meade, M. Reece, and D. Shih, *Implications of a 125 GeV Higgs for the MSSM and Low-Scale SUSY Breaking*, arXiv:1112.3068.

[202] L. J. Hall, D. Pinner, and J. T. Ruderman, *A Natural SUSY Higgs Near 126 GeV*, *JHEP* **1204** (2012) 131, [arXiv:1112.2703].

[203] M. Drees, R. Godbole, and P. Roy, *Theory and phenomenology of sparticles: An account of four-dimensional N=1 supersymmetry in high energy physics*. World Scientific, 2004.

[204] J. Ellis, T. Hahn, S. Heinemeyer, K. Olive, and G. Weiglein, *WMAP-Compliant Benchmark Surfaces for MSSM Higgs Bosons*, *JHEP* **0710** (2007) 092, [arXiv:0709.0098].

[205] J. F. Gunion and H. E. Haber, *The CP conserving two Higgs doublet model: The Approach to the decoupling limit*, *Phys.Rev.* **D67** (2003) 075019, [hep-ph/0207010].

[206] G. Branco, P. Ferreira, L. Lavoura, M. Rebelo, M. Sher, *et. al.*, *Theory and phenomenology of two-Higgs-doublet models*, arXiv:1106.0034.

[207] K. Blum and R. T. D'Agnolo, *2 Higgs or not 2 Higgs*, *Phys.Lett.* **B714** (2012) 66–69, [arXiv:1202.2364].

[208] L. Randall, *Two Higgs Models for Large Tan Beta and Heavy Second Higgs*, *JHEP* **0802** (2008) 084, [arXiv:0711.4360].

[209] M. S. Carena, J. Espinosa, M. Quiros, and C. Wagner, *Analytical expressions for radiatively corrected Higgs masses and couplings in the MSSM*, *Phys.Lett.* **B355** (1995) 209–221, [hep-ph/9504316].

[210] L. J. Hall, R. Rattazzi, and U. Sarid, *The Top quark mass in supersymmetric SO(10) unification*, *Phys.Rev.* **D50** (1994) 7048–7065, [hep-ph/9306309].

[211] P. Batra, A. Delgado, D. E. Kaplan, and T. M. Tait, *The Higgs mass bound in gauge extensions of the minimal supersymmetric standard model*, *JHEP* **0402** (2004) 043, [hep-ph/0309149].

[212] A. Maloney, A. Pierce, and J. G. Wacker, *D-terms, unification, and the Higgs mass*, *JHEP* **0606** (2006) 034, [hep-ph/0409127].

[213] N. Craig, S. Dimopoulos, and T. Gherghetta, *Split families unified*, *JHEP* **1204** (2012) 116, [arXiv:1203.0572].

[214] M. Cvetic, D. A. Demir, J. Espinosa, L. Everett, and P. Langacker, *Electroweak breaking and the mu problem in supergravity models with an additional U(1)*, *Phys.Rev.* **D56** (1997) 2861, [hep-ph/9703317].

[215] D. E. Morrissey and J. D. Wells, *The Tension between gauge coupling unification, the Higgs boson mass, and a gauge-breaking origin of the supersymmetric mu-term*, *Phys.Rev.* **D74** (2006) 015008, [hep-ph/0512019].

[216] M. Dine, N. Seiberg, and S. Thomas, *Higgs physics as a window beyond the MSSM (BMSSM)*, *Phys.Rev.* **D76** (2007) 095004, [arXiv:0707.0005].

[217] R. S. Chivukula, H.-J. He, J. Howard, and E. H. Simmons, *The Structure of electroweak corrections due to extended gauge symmetries*, *Phys.Rev.* **D69** (2004) 015009, [hep-ph/0307209].

[218] K. Blum, C. Delaunay, and Y. Hochberg, *Vacuum (Meta)Stability Beyond the MSSM*, *Phys.Rev.* **D80** (2009) 075004, [arXiv:0905.1701].

[219] U. Ellwanger and C. Hugonie, *Higgs bosons near 125 GeV in the NMSSM with constraints at the GUT scale*, arXiv:1203.5048.

[220] S. King, M. Muhlleitner, and R. Nevzorov, *NMSSM Higgs Benchmarks Near 125 GeV*, *Nucl.Phys.* **B860** (2012) 207–244, [arXiv:1201.2671].

[221] A. Arvanitaki and G. Villadoro, *A Non Standard Model Higgs at the LHC as a Sign of Naturalness*, *JHEP* **1202** (2012) 144, [arXiv:1112.4835].

[222] **Heavy Flavor Averaging Group** Collaboration, D. Asner *et. al.*, *Averages of b-hadron, c-hadron, and tau-lepton Properties*, arXiv:1010.1589.

[223] M. Benzke, S. J. Lee, M. Neubert, and G. Paz, *Factorization at Subleading Power and Irreducible Uncertainties in B to Xs gamma Decay*, *JHEP* **1008** (2010) 099, [arXiv:1003.5012].

[224] M. Misiak, H. Asatrian, K. Bieri, M. Czakon, A. Czarnecki, *et. al.*, *Estimate of B(anti-B toX(s) gamma) at O(alpha(s)**2)*, *Phys.Rev.Lett.* **98** (2007) 022002, [`hep-ph/0609232`].

[225] M. Perelstein and C. Spethmann, *A Collider signature of the supersymmetric golden region*, *JHEP* **0704** (2007) 070, [`hep-ph/0702038`].

[226] E. Lunghi and J. Matias, *Huge right-handed current effects in B to K*(K pi)l+l- in supersymmetry*, *JHEP* **0704** (2007) 058, [`hep-ph/0612166`].

[227] J. Gunion, G. Gamberini, and S. Novaes, *Can the Higgs Boson of the Minimal Supersymmetric Standard Model Be Detected at Hadron Collider via Two Photon Decays?*, *Phys.Rev.* **D38** (1988) 3481.

[228] A. Djouadi, V. Driesen, W. Hollik, and J. I. Illana, *The Coupling of the lightest SUSY Higgs boson to two photons in the decoupling regime*, *Eur.Phys.J.* **C1** (1998) 149–162, [`hep-ph/9612362`].

[229] M. A. Diaz and P. Fileviez Perez, *Can we distinguish between h(SM) and h0 in split supersymmetry?*, *J.Phys.G* **G31** (2005) 563–569, [`hep-ph/0412066`].

[230] **Particle Data Group** Collaboration, K. Nakamura *et. al.*, *Review of particle physics*, *J.Phys.G* **G37** (2010) 075021.

[231] M. Carena, S. Gori, N. R. Shah, and C. E. Wagner, *A 125 GeV SM-like Higgs in the MSSM and the gamma gamma rate*, *JHEP* **1203** (2012) 014, [`arXiv:1112.3336`].

[232] M. Carena, S. Gori, N. R. Shah, C. E. Wagner, and L.-T. Wang, *Light Stau Phenomenology and the Higgs gamma gamma rate*, `arXiv:1205.5842`.

[233] **CMS** Collaboration, *Combination of standard model Higgs boson searches and measurements of the properties of the new boson with a mass near 125 GeV*, CMS Physics Analysis Summary, CMS-PAS-HIG-13-005, 2013.

[234] **ATLAS** Collaboration, *Measurements of the properties of the Higgs-like boson in the $WW^{(*)} \to l\nu l\nu$ decay channel with the ATLAS detector using 25 fb1 of proton-proton collision data*, ATALS Conference Note, ATLAS-CONF-2013-030, 2013.

[235] **ATLAS** Collaboration, *Measurements of the properties of the Higgs-like boson in the four lepton decay channel with the ATLAS detector using 25 fb−1 of proton-proton collision data*, ATALS Conference Note, ATLAS-CONF-2013-013, 2013.

[236] **ATLAS** Collaboration, *Measurements of the properties of the Higgs-like boson in the two photon decay channel with the ATLAS detector using 25 fb1 of proton-proton collision data*, ATALS Conference Note, ATLAS-CONF-2013-012, 2013.

[237] **ATLAS** Collaboration, *Combined coupling measurements of the Higgs-like boson with the ATLAS detector using up to 25 fb−1 of proton-proton collision data*, ATALS Conference Note, ATLAS-CONF-2013-013, 2013.

[238] **ATLAS** Collaboration, *SM H to tautau 2012 for HCP*, ATLAS Conference Note, ATLAS-CONF-2012-160, 2012.

[239] **ATLAS** Collaboration, *SM H to bb 2012 for HCP*, ATLAS Conference Note, ATLAS-CONF-2012-161, 2012.

[240] D. Carmi, A. Falkowski, E. Kuflik, T. Volansky, and J. Zupan, *Higgs After the Discovery: A Status Report*, `arXiv:1207.1718`.

[241] J. Espinosa, C. Grojean, M. Muhlleitner, and M. Trott, *First Glimpses at Higgs' face*, `arXiv:1207.1717`.

[242] M. S. Carena and H. E. Haber, *Higgs boson theory and phenomenology*, *Prog.Part.Nucl.Phys.* **50** (2003) 63–152, [`hep-ph/0208209`].

[243] A. Djouadi, *The Anatomy of electro-weak symmetry breaking. II. The Higgs bosons in the minimal supersymmetric model*, *Phys.Rept.* **459** (2008) 1–241, [`hep-ph/0503173`]. And references therein.

[244] **CMS** Collaboration, *Search for MSSM Neutral Higgs Bosons Decaying to Tau Pairs in pp Collisions*, CMS Physics Analysis Summary, CMS-PAS-HIG-12-050, 2012.

[245] **ALEPH Collaboration, DELPHI Collaboration, L3 Collaboration, OPAL Collaboration, LEP Working Group for Higgs Boson Searches** Collaboration, S. Schael *et. al.*, *Search for neutral MSSM Higgs bosons at LEP*, *Eur.Phys.J.* **C47** (2006) 547–587, [`hep-ex/0602042`].

[246] M. S. Carena, S. Heinemeyer, C. Wagner, and G. Weiglein, *Suggestions for benchmark scenarios for MSSM Higgs boson searches at hadron colliders*, *Eur.Phys.J.* **C26** (2003) 601–607, [`hep-ph/0202167`].

[247] **ATLAS** Collaboration, *Search for neutral MSSM Higgs bosons in $\sqrt{s} = 7$ TeV pp collisions with the ATLAS detector*, ATLAS Conference Note, ATLAS-CONF-2012-094, 2012.

[248] **CMS** Collaboration, S. Chatrchyan *et. al.*, *MSSM Higgs production in association with b quarks - semileptonic*, CMS Physics Analysis Summary, CMS-PAS-HIG-12-027.

[249] **CMS** Collaboration, S. Chatrchyan *et. al.*, *MSSM Higgs production in association with b quarks - all hadronic*, CMS Physics Analysis Summary, CMS-PAS-HIG-12-026.

[250] M. S. Carena, S. Heinemeyer, C. Wagner, and G. Weiglein, *MSSM Higgs boson searches at the Tevatron and the LHC: Impact of different benchmark scenarios*, *Eur.Phys.J.* **C45** (2006) 797–814, [`hep-ph/0511023`].

[251] R. Barbieri, D. Buttazzo, K. Kannike, F. Sala, and A. Tesi, *Exploring the Higgs sector of a most natural NMSSM*, `arXiv:1304.3670`.

[252] **ATLAS** Collaboration, *Search for a Higgs boson decaying to four photons through light CP-odd scalar coupling using 4.9 fb−1 of 7 TeV pp collision data taken with ATLAS detector at the LHC*, ATALS Conference Note, ATLAS-CONF-2012-079, 2012.

[253] **CMS Collaboration** Collaboration, S. Chatrchyan *et. al.*, *Search for heavy resonances in the W/Z-tagged dijet mass spectrum in pp collisions at 7 TeV*, `arXiv:1212.1910`.

[254] I. Low, R. Rattazzi, and A. Vichi, *Theoretical Constraints on the Higgs Effective Couplings*, *JHEP* **1004** (2010) 126, [`arXiv:0907.5413`].

[255] M. Carena, I. Low, and C. E. Wagner, *Implications of a Modified Higgs to Diphoton Decay Width*, `arXiv:1206.1082`.

[256] D. Choudhury, T. M. Tait, and C. Wagner, *Beautiful mirrors and precision electroweak data*, *Phys.Rev.* **D65** (2002) 053002, [`hep-ph/0109097`].

[257] D. Morrissey and C. Wagner, *Beautiful mirrors, unification of couplings and collider phenomenology*, *Phys.Rev.* **D69** (2004) 053001, [`hep-ph/0308001`].

[258] S. Dawson and E. Furlan, *A Higgs Conundrum with Vector Fermions*, *Phys.Rev.* **D86** (2012) 015021, [`arXiv:1205.4733`].

[259] N. D. Christensen and C. Duhr, *FeynRules - Feynman rules made easy*, *Comput.Phys.Commun.* **180** (2009) 1614–1641, [`arXiv:0806.4194`].

[260] **CMS** Collaboration, S. Chatrchyan *et. al.*, *Search for heavy long-lived charged particles in pp collisions at sqrt(s)=7 TeV*, `arXiv:1205.0272`.

[261] **CMS** Collaboration, *Searches for long-lived charged particles*, CMS Physics Analysis Summary, CMS-PAS-EXO-12-026, 2013.

[262] **CMS** Collaboration, *Search in the displaced lepton channel for heavy resonances decaying to long-lived neutral particles*, CMS Physics Analysis Summary, CMS-PAS-EXO-11-101.

[263] **CDF** Collaboration, D. Acosta *et. al.*, *Search for long-lived doubly-charged Higgs bosons in $p\bar{p}$ collisions at $\sqrt{s} = 1.96$ TeV*, *Phys.Rev.Lett.* **95** (2005) 071801, [`hep-ex/0503004`].

[264] **CDF** Collaboration, A. L. Scott, *Search for long-lived parents of the Z^0 boson*, *Int.J.Mod.Phys.* **A20** (2005) 3263–3266, [`hep-ex/0410019`].

[265] **D0** Collaboration, V. Abazov *et. al.*, *Search for Resonant Pair Production of long-lived particles decaying to b anti-b in p anti-p collisions at s**(1/2) = 1.96-TeV*, *Phys.Rev.Lett.* **103** (2009) 071801, [`arXiv:0906.1787`].

[266] **D0** Collaboration, V. Abazov *et. al.*, *Search for long-lived particles decaying into electron or photon pairs with the D0 detector*, *Phys.Rev.Lett.* **101** (2008) 111802, [`arXiv:0806.2223`].

[267] **D0** Collaboration, V. Abazov *et. al.*, *Search for neutral, long-lived particles decaying into two muons in $p\bar{p}$ collisions at $\sqrt{s}$ = 1.96 TeV*, *Phys.Rev.Lett.* **97** (2006) 161802, [`hep-ex/0607028`].

[268] **ATLAS** Collaboration, *Search for direct slepton and gaugino production in final states with two leptons and missing transverse momentum with the ATLAS detector in pp collisions at 7 TeV*, ATALS Conference Note, ATLAS-CONF-2012-076.

[269] **CDF** Collaboration, Shalhout *et. al.*, *A search for dark matter in the monojet plus missing transverse energy signature in 6.7 Inverse fb*, . `http://www-cdf.fnal.gov/physics/exotic/r2a/20111124.monojetdarkmatter/index.html`.

[270] **CMS** Collaboration, S. Chatrchyan *et. al.*, *Search for dark matter and large extra dimensions in monojet events in pp collisions at sqrt(s)= 7 TeV*, `arXiv:1206.5663`.

[271] **CMS** Collaboration, S. Chatrchyan *et. al.*, *Search for Dark Matter and Large Extra Dimensions in pp Collisions Yielding a Photon and Missing Transverse Energy*, `arXiv:1204.0821`.

[272] **ATLAS** Collaboration, *Search for dark matter candidates and large extra dimensions in events with a jet and missing transverse momentum with the ATLAS detector*, ATLAS Conference Note, ATLAS-CONF-12-084.

[273] **ATLAS** Collaboration, *Search for dark matter candidates and large extra dimensions in events with a photon and missing transverse momentum in pp collision data at $\sqrt{s} = 7$ TeV with the ATLAS detector*, ATLAS Conference Note, ATLAS-CONF-12-085.

[274] **CMS** Collaboration, *Search for new physics in monojet events in pp collisions at sqrt(s)= 8 tev*, CMS Physics Analysis Summary, CMS-PAS-EXO-12-048, 2013.

[275] **ATLAS** Collaboration, G. Aad *et. al.*, *Search for New Phenomena in Monojet plus Missing Transverse Momentum Final States using 10/fb of pp Collisions at sqrt(s) = 8 TeV with the ATLAS detector at the LHC*, ATLAS Conference Note, ATLAS-CONF-2012-147, 2013.

[276] H. K. Dreiner and M. K. J. Tattersall, *How low can SUSY go? Matching, monojets and compressed spectra*, `arXiv:1207.1613`.

[277] G. Belanger, M. Heikinheimo, and V. Sanz, *Model-Independent Bounds on Squarks from Monophoton Searches*, `arXiv:1205.1463`.

[278] M. Ibe, T. Moroi, and T. Yanagida, *Possible Signals of Wino LSP at the Large Hadron Collider*, Phys.Lett. **B644** (2007) 355–360, [`hep-ph/0610277`].

[279] G. F. Giudice, T. Han, K. Wang, and L.-T. Wang, *Nearly Degenerate Gauginos and Dark Matter at the LHC*, Phys.Rev. **D81** (2010) 115011, [`arXiv:1004.4902`].

[280] **CMS** Collaboration, *Search for supersymmetry with the razor variables at CMS*, CMS Physics Analysis Summary, CMS-PAS-SUS-12-005.

[281] P. J. Fox, R. Harnik, R. Primulando, and C.-T. Yu, *Taking a Razor to Dark Matter Parameter Space at the LHC*, `arXiv:1203.1662`.

[282] **CMS** Collaboration, *Search for RPV supersymmetry with three or more leptons and b-tags*, CMS Physics Analysis Summary, CMS-PAS-SUS-12-027, 2013.

[283] E. Contreras-Campana, N. Craig, R. Gray, C. Kilic, M. Park, *et. al.*, *Multi-Lepton Signals of the Higgs Boson*, JHEP **1204** (2012) 112, [`arXiv:1112.2298`].

[284] *Private communication with Scott Thomas and Sunil Somalwar*, .

[285] CMS Collaboration, *Performance of τ-lepton reconstruction and identification in CMS*, J. Instrum. **7** (2012) 1001, [`arXiv:1109.6034`].

[286] **CMS** Collaboration, *Study of tau reconstruction algorithms using pppp collisions data collected at $\sqrt{s} = 7\,TeV$*, CMS Physics Analysis Summary, CMS-PAS-PFT-10-004, 2010.

[287] **CMS** Collaboration, *Cms strategies for tau reconstruction and identification using particle-flow techniques*, CMS Physics Analysis Summary, CMS-PAS-PFT-08-001, 2009.

[288] S. P. Martin, K. Tobe, and J. D. Wells, *Virtual effects of light gauginos and higgsinos: A Precision electroweak analysis of split supersymmetry*, Phys.Rev. **D71** (2005) 073014, [`hep-ph/0412424`].

[289] N. Maekawa, *Vector - like strong coupling theory with small S and T parameters*, Prog.Theor.Phys. **93** (1995) 919–926, [`hep-ph/9406375`].

[290] M. Baak, M. Goebel, J. Haller, A. Hoecker, D. Ludwig, *et. al.*, *Updated Status of the Global Electroweak Fit and Constraints on New Physics*, Eur.Phys.J. **C72** (2012) 2003, [`arXiv:1107.0975`].

[291] G. D. Kribs, T. Plehn, M. Spannowsky, and T. M. Tait, *Four generations and Higgs physics*, Phys.Rev. **D76** (2007) 075016, [`arXiv:0706.3718`].

[292] K. Ishiwata and M. B. Wise, *Higgs Properties and Fourth Generation Leptons, Phys.Rev.* **D84** (2011) 055025, [`arXiv:1107.1490`].

[293] G. F. Giudice and A. Strumia, *Probing High-Scale and Split Supersymmetry with Higgs Mass Measurements, Nucl.Phys.* **B858** (2012) 63–83, [`arXiv:1108.6077`].

[294] G. Isidori, G. Ridolfi, and A. Strumia, *On the metastability of the standard model vacuum, Nucl.Phys.* **B609** (2001) 387–409, [`hep-ph/0104016`].